Investigating the Impact of Ligand Modification on Luminescent Lanthanide Complexes

Charlie H. Simms

Supervisors: Prof. S. Faulkner and Prof. M. Langton

Trinity college, University of Oxford



A Thesis submitted for the degree of Doctor of Philosophy

Department of Inorganic Chemistry

October 2024

Investigating the Impact of Ligand Modification on Luminescent Lanthanide Complexes

Charlie H. Simms, Trinity College, University of Oxford

Abstract of thesis submitted for the degree of Doctor of Philosophy, October 2024

This thesis describes

Chapter 1 introduces the field of lanthanide chemistry, from electronic structure to the influence of coordinating ligands, with a particular focus on the luminescent properties. It describes the various methods in which ligand choice and modification has allowed for the development of responsive luminescent lanthanide probes.

Chapter 2 describes the synthesis, and optical properties of kinetically stable, photoswitchable, emissive lanthanide complexes, which are controlled by four orthogonal wavelengths of light. The complete orthogonality achieved between the photoswitching and the excitation and emission of the lanthanide has allowed for applications in optical information storage to be realised.

Chapter 3 details the preparation of a family of related binuclear lanthanide probes for the detection of redox environments *via* magnetic resonance or optical imaging. Common classes of compounds including nitrophenyl, azide and azobenzenes were incorporated into binuclear lanthanide complexes, which upon complete reduction, yielded a shared product, the corresponding aniline. This reduction for Gd(III) complexes resulted in a change in realxivity, and for Tb(III) complexes, an impressive turn on of long lived bright green emission.

Chapter 4 investigates the structure and speciation of common heptadentate lanthanide complexes in solution. The isomeric distribution of twisted square antiprismatic and square antiprismatic geometries were determined independently by detailed and robust analysis of the

luminescence spectra, and by ^{1}H NMR spectroscopy. This novel methodology highlights the structural information available from lanthanide luminescence.

Chapter 5 explores the structure and speciation in solution of binuclear lanthanide complexes introduced in **Chapter 3**, in detail. Particularly focussing on the speciation as a function of pH. This allowed insight into the structure in solution of complex and exciting binuclear complexes.

Chapter 6 summarises the conclusions of this thesis.

Chapter 7 describes the experimental procedures used in this work, including the synthesis and characterisation of all complexes studied in **Chapters 2-5**.

Acknowledgements

Disclaimer: This is going to be very long! I have been supported by a whole village of people throughout my DPhil and I hold in my heart love for them all, for without them this thesis could not have been written (and I would have less friends).

Firstly, I would like to thank my two amazing supervisors Professor Steve Faulkner and Professor Matt Langton. Steve, your knowledge, fairness and patience has been overwhelming, not only have you taught me so much about my now beloved lanthanides, you have also taught me that even with great responsibility there is space for kindness. Matt, your kindness, openness and motivation has been a driving force for me during this degree. You have taught me to be practical, detailed and curious, but also about how to build a wonderful and diverse research culture which I hope to take with me in the future.

Next, I would like to thank Professor Thomas Just Sørensen for hosting me in his group at the University of Copenhagen for three months. In this short time, I learnt more than I could have imagined and from Thomas I learnt to be critical and passionate about my work. I also learnt how much Fernet Branca I could drink in one night, although I would say this is a limit and not a target…

Of course, I have to thank the amazing members of the Langton and Faulkner groups over the years who have been my friends and teachers throughout my DPhil. Firstly, to Aaron, my day 1, thank you for teaching me how to be a research scientist and for coming all the way down from Edinburgh to keep me company in the Langton group. Aidan and Laura, thank you for welcoming me into the lab and teaching me some amazing synthetic tips and tricks! Toby, my desk buddy, thank you for everything, talking to you every day kept me sane and I will always appreciate your input on what colours I should use in my graphs. Shaun, my northern counterpart, thank you for everything but mostly thank you for annoying Xiangyu. Xiangyu, I

love u bby forever and always. Kel, thank you for being such an inspiration. Manzoor, thank you for sharing your incredible knowledge with me. Elin, thank you for having fantastic music taste and being my favourite proof reader. Martin, because of you I tried new things, I will miss your lab hugs a lot. Elba, thank you for being the most wonderful Part II student I could have imagined, working closely with you was one of the highlights of my DPhil. You are truly incredible, and I have loved watching you grow into a magnificent researcher. I am so happy to call you, my friend. Thank you to all the other wonderful Part II students in the Langton group, particularly, Amir, Dom, Srija and Amy. Thank you also to Anna, Gurshinder and Chiara, you all make the Langton group a great place to work.

Now on to the Faulkner group! First and foremost, thank you to Dani, thank you for taking me under your wing and teaching me everything from synthesis to analysis. Thank you for also being a wonderful person to vent to, and for all your advice over the years! Thank you to Carlson, you were so kind to me when I started and taught me so much, for which I am ever grateful. To Debs, I was so nervous when I started and I remember after my very first conversation with you, I felt more confident, thank you for giving me confidence when I needed it most. Matt A. thank you for making the huge trek across the world to be our post doc, you are fantastic! I am so glad I got to spend the last few months learning from you, it has been really fun! To Charlotte, Jonny and Ceri, thank you for always making me laugh and for being able to come to you with anything, you have been such rocks to me in this last year! Thank you also to Emily, Cam, Rhodri, Clara, Laura, Euan, Marie, Shitong and Jevon for all the great conversations.

I would also like to say a huge thank you to the incredible members of the Sørensen group who instantly made me welcome on my visit to Copenhagen, with who I shared one of the best parts of my DPhil. First and foremost thank you to Villads, I am not sure I can put into words how much I want to thank you… Thank you for making time, having patience and for teaching me

so much of what I know about Lanthanide spectroscopy. I absolutely loved working with you both in Copenhagen and Oxford, without you this thesis would be in much worse shape. I would also like to thank Nicolaj and Kirstine for being the best office buddies, and for all the wonderful food recommendations. I would like to thank Vassilis for being such a ray of sunshine and immediately welcoming me to Copenhagen. Sabina, thank you so much for your endless supply of tea and cakes. Magnus, Kirill and Gustav thank you for always making me laugh!

I would also like to thank Professor Paul Beer, and all the beer group members over the years, especially Jamie, Hui, Andrew and Arya, for all their support and advice in group meetings and in the labs. Additionally, thank you to Professor Ester Hammond and Lina for being such wonderful collaborators.

My time in Oxford is not only defined by my DPhil but also by PERIODically, the Oxford Period Podcast. Creating this Podcast has been my lifeline, I have loved and cherished every moment and for that I want to thank Dr Michael O'Neill for unwavering support and guidance. I would also like to thank all the amazing guests, Nick at the podcast studio, all of our thousands of listeners. This has been one of the most rewarding projects I have had the pleasure of being involved in. Of course, none of this would be possible without Elba, Sofia, Lottie, Felicity, Josie, Manami and Amy, you all put your heart and soul into this project. I am in awe of every single one of you and I am so proud to call you my friends. I would also like to thank all the Staff in the Chemistry Teaching Lab, the MPLS Equality, Inclusion and Diversity team, Sue Henderson, Janice French and Maitane Fernandez Chento for always supporting PERIODically.

Thank you to the OxICFM CDT team for the support to carry out this thesis, especially thank you to my fellow course mates, for keeping me sane in lockdown and for endless pub trips.

Thank you to my best friends who I met at Oxford, to Chloé, Helen, Maya and Xiangyu thank you for teaching me about the world and for the emotional support. Thank you to Joe, Liam and Aisling for all the trips to the flamb and lag and impromptu and delicious meals that inevitably followed. Thank you to Aaron K. for morning chats and cat pictures!

Thank you to my best friends Sophie, Diana and Nic, without you I would have no one to complain to and get advice on what I should make for my dinner. Thank you to Carole and Anthony for letting me crash at your house to write this thesis, the delicious meals have been motivating me through this process. Thank you to my mum and dad for all the love and support you have given me over the years, the endless moving trips and tasty meals out, you have been a huge support! Thank you to my Aunty Lou, the best godmum there could be! You calmed me down and supported me before my interview 4 years ago and the support you have given me throughout my time in Oxford has really kept me going! I have loved spending more time with you, Flo, Bertie and Lucy.

To my grandma and granddad, you taught me to be a chemist and a physicist. I am honoured that I get to do both now, you are both my biggest inspirations, always.

Finally, and most importantly, thank you to Matt, I love you so much! I whole-heartedly could not have done this without you! Thank you for all your love, cups of tea and delicious food which has sustained me over the past four years! I am so happy to have had the pleasure to watch you become an incredibly successful researcher and also the most important person in my life. Now, let's go on a big holiday!

"Thank you for support" – Darwin Núnez, 27.08.2023

Previously Published Work

1. **Binuclear lanthanide complexes as magnetic resonance and optical imaging probes for redox sensing** C. Simms, Charlie, D. Kovacs, L. Hacker, E. Sarson, D. Sokolova, K. Christensen, A. Khrapichev, L. Martin, K. Vincent, S. Conway, E. Hammond, M. Langton, S. Faulkner, submitted September 2024.

2. **Photoswitchable luminescent lanthanide complexes controlled and interrogated by four orthogonal wavelengths of light** C. Simms, V. R. M. Nielsen, T. J. Sørensen, S. Faulkner and M. J. Langton, Phys. Chem. Chem. Phys., 2024, **26**, 18683-18691

3. **Periods and practicals: how to help your students** E. Feo, S. Olendraru, M. O'Neill and C. H. Simms, Trends Chem., 2023, **5**, 789-791.

4. **Representations of women and men in popular chemistry textbooks in the United Kingdom and Republic of Ireland** C. Murray, Y. Anderson, C. H. Simms and M. K. Seery, Chem. Educ. Res. Pract., 2022, **23**, 373-384.

Oral Presentations

"Turn on Lanthanide Luminescence Probes for Imaging in Hypoxic Environments"

1. Chemistry Research Seminar, University of Copenhagen, November 2023

2. OxICFM CDT Science Day, University of Oxford, July 2023

3. Dalton Inorganic Chemistry Conference, University of Warwick, April 2023

Poster Presentations

"Investigating the structure of Kinetically Stable Nd(III) complexes in solution"

1. Centre for Rare Earth and Actinides Research Summer School, CNRS, Aussois, June 2024

"Turn on Lanthanide Luminescence Probes for Imaging in Hypoxic Environments"

1. International Conference of f-elements 2023, University of Strasbourg, August 2023

"Photoswitchable Luminescent Lanthanide Complexes"

1. OxICFM CDT Science Day 2022, University of Oxford, July 2022

2. 1st International Supramolecular Chemistry Summer school, Cagliari, June 2022

Abbreviations

ISC	intersystem crossing
FRET	Forster resonance energy transfer
MLCT	metal-to-ligand charge transfer
MR	magnetic resonance
NMR	nuclear magnetic resonance
PSS	photostationary state
SMM	single molecule magnet
HPLC	high performance liquid chromatography
ROS	reactive oxygen species
Ln	Lanthanide
Abs	absorbance
eT	energy transfer
PCA	principal component analysis
δ	chemical shift
Δ	change in
μ	micro
μW	microwave
d	deuterated
K_a	association constant
T_1	longitudinal relaxation time
T_2	transverse relaxation time
q	number of water molecules in the inner-coordination sphere
Φ	quantum yield
pH	$-\log_{10}[H^+]$
pK_a	$-\log_{10}K_a$
br	broad
s	singlet
d	doublet
t	triplet
m	multiplet
λ_{ex}	excitation wavelength
λ_{em}	emission wavelength
τ	luminescence lifetime
SHE	standard hydrogen electrode
PeT	photoinduced electron transfer
OTf	trifluoromethane sulfonate
UV	Ultraviolet
Vis	visible
DCM	dichloromethane
DMF	*N*,*N*-dimethylformamide
DMSO	dimethylsulfoxide

TFA	trifluoroacetic acid
SAP	square antiprismatic
TSAP	twisted-square antiprismatic
TLC	thin layer chromatography
HRMS	high resolution mass spectrometry
LRMS	low resolution mass spectrometry
cyclen	1,4,7,10-tetraazacyclododecane
DOTA	1,4,7,10-tetraazacyclododecane-*N,N′,N″,N‴*-tetraacetic acid
DO3A	1,4,7,10-tetraazacyclododecane-1,4,7-triacetic acid
pDO3A	2,2',2"-(10-(prop-2-yn-1-yl)-1,4,7,10-tetraazacyclododecane-1,4,7-triyl)triacetic acid
DOTAM	1,4,7,10-*tetrakis*(2-carbamoylethyl)-1,4,7,10-tetraazacyclododecane
DIPEA	*N,N*-diisopropylethylamine
PBS	phosphate buffered saline
GSH	Glutathione
NCS	N-chlorosuccinimide
NBS	N-bromosuccimide
DTE	Diarylethene
DBU	1,8-Diazabicyclo(5.4.0)undec-7-ene
Hyd-1/C	Nickel Hydrogenase supported on carbon
DTMA	1,4,7,10-tetrakis[(*N*-methylcarbamoyl)methyl]-1,4,7,10-tetraaza-cyclododecane)
p-TsCl	4- toluenesulfonyl chloride
K	Kelvin
m/z	mass to charge ratio
℃	degrees Celsius
Bu	Butyl
Et	Ethyl
Me	Methyl
rt	room temperature

Table of Contents

CHAPTER 1 ..... **1**
INTRODUCTION 1
1.1 Introduction *1*
1.2 Electronic Structure of Lanthanides *1*
1.3 Lanthanide Luminescence *6*
1.3.1 Sensitised Luminescence 6
1.3.2 Förster Resonance Energy Transfer 8
1.3.3 Dexter Exchange 9
1.3.4 Quenching 9
1.4 Influence of Ligand Modification on Lanthanide Luminescence *11*
1.4.1 Ligand Design 11
1.4.2 Inner Sphere Contributions 11
1.4.2.1 Symmetry 12
1.4.2.2 Equilibria of DOTA/DO3A complexes 13
1.4.2.3 Inner Sphere Effects: pH 14
1.4.2.4 Influence of Anions on the Electronic Properties 15
1.4.2.5 Direct Antenna Coordination 18
1.4.3 Reversible Modification of Ligand Constitution 19
1.4.3.1 Cation Binding 19
1.4.3.2 π-π interactions 21
1.4.3.3 pH and O_2 dependence 21
1.4.3.4 Viscosity 23
1.4.4 Irreversible Modification of Ligand Constitution 24
1.4.4.1 Analyte Responsive Reduction 25
1.4.4.2 Analyte Triggered Decaging 26
1.4.4.3 *In-situ* Reactions 27
1.5 Scope and Aims *29*
1.6 References for Chapter 1 ..... *30*
CHAPTER 2 ..... **35**
PHOTOSWITCHABLE LUMINESCENT LANTHANIDE COMPLEXES 35
2.1 Introduction *35*
2.1.1 Optical Information Storage 35
2.1.2 Photoswitchable Lanthanide Complexes in the Literature 36
2.2 Design of Novel Photoswitchable Lanthanide Complexes *40*
2.3 Synthesis *43*
2.4 Characterisation *45*
2.4.1 ^{1}H NMR 45
2.4.2 High Performance Liquid Chromatography 47
2.5 Photoswitching Properties *48*
2.5.1 Absorbance Spectroscopy 48
2.5.1.1 $2{\cdot}L_a$ and $2{\cdot}L_b$ 49
2.5.1.2 Ln(III) complexes 50
2.5.2 HPLC Analysis 51
2.6 Photophysical Properties of Eu(III) and Nd(III) Complexes *53*
2.6.1 Luminescent Properties of Ligands 53
2.6.2 Eu(III) Luminescence 56
2.6.2.1 Steady State Spectra of Eu(III) Complexes 56
2.6.2.2 Time-gated Luminescence of Eu(III) Complexes 65
2.6.2.3 Understanding the Photophysical Mechanisms of the Eu(III) Complexes 66
2.6.3 Nd(III) Luminescence 68
2.6.3.1 Understanding the Photophysical Mechanisms of Nd(III) Complexes 75
2.7 Conclusions *77*
2.8 References for Chapter 2 ..... *78*
CHAPTER 3 ..... **81**
BINUCLEAR LANTHANIDE COMPLEXES FOR REDOX SENSING 81
3.1 Introduction *81*
3.1.1 Understanding Redox Environments 81
3.1.2 Lanthanide(III) Redox Probes in the Literature 83
3.2 Design of Binuclear Ln(III) Probes *87*
3.3 Synthesis of Binuclear Ln(III) Probes *89*
3.4 Characterisation of Binuclear Ln(III) complexes *91*

3.4.1 ^{1}H NMR 91
3.4.1.1 Influence of *para*-Substituents on the ^{1}H NMR of Binuclear Eu(III) Complexes 94
3.4.2 High Performance Liquid Chromatography (HPLC) 95
3.5 Relaxivity *96*
3.6 Luminescent Properties of Tb(III) Analogues *98*
3.6.1 Absorbance Spectra 98
3.6.2 Steady State Spectra 99
3.6.2.1 Emission Spectra 100
3.6.2.2 Excitation Spectra (λ_{em} = 545 nm) 101
3.6.2.3 Comparison of Luminescent Properties of Binuclear Tb(III) Complexes 103
3.6.2.4 Quantum Yields 106
3.6.3 Time-gated Luminescence 107
3.6.3.1 Luminescence Lifetimes 107
3.7 Chemical Reduction *110*
3.7.1 ^{1}H NMR Response 110
3.7.2 Luminescence Response 113
3.8 Electrochemical Reduction *115*
3.9 Detecting Hydrogen Sulphide in Solution *119*
3.10 Biocatalytic Reduction *121*
3.11 Cell Studies *123*
3.12 Conclusions *124*
3.13 References for Chapter 3 ..... *126*
CHAPTER 4 ..... **130**
INVESTIGATING THE STRUCTURE OF KINETICALLY STABLE ND(III) COMPLEXES IN SOLUTION 130
4.1 Introduction *130*
4.1.1 Lanthanides in Solution 130
4.1.2 Neodymium Properties and Applications 131
4.1.3 Kinetic Stability of Ln(III) Complexes 131
4.1.4 Structure Property Relationships of Isomers 132
4.1.5 Speciation of Ln(III) Complexes in Solution 133
4.1.6 Principal Component Analysis (PCA) 134
4.1.7 Aims 135
4.2 Synthesis of Nd(III) propargyl-DO3A *135*
4.3 Characterisation of Nd(III) propargyl-DO3A *136*
4.3.1 Solid State Structure of Ln(III) propargyl-DO3A 136
4.3.2 ^{1}H NMR Spectrum 137
4.3.3 Optical Spectroscopy 138
4.4 Determination of Multiple Species in Solution *140*
4.4.1 Steady State Luminescence 140
4.4.2 Time-gated Luminescence 143
4.5 Principal Component Analysis *144*
4.6 Spectral Fitting and Isomeric Distribution *149*
4.7 Spectral Reconstruction *151*
4.8 Determination of Energy levels *152*
4.9 Conclusions *154*
4.10 References for Chapter 4 ..... *155*
CHAPTER 5 ..... **158**
SPECIATION OF BINUCLEAR LN(III) COMPLEXES IN SOLUTION 158
5.1 Introduction *158*
5.1.1 Binuclear Ln(III) Complexes 158
5.1.2 Influence of Paramagnetic Ions on ^{1}H NMR Spectra 159
5.2 Aims *161*
5.3 ^{1}H NMR of Binuclear Ln(III) Complexes *162*
5.3.1 Experimental Details 162
5.3.2 Tb(III) Binuclear Complexes 163
5.3.3 Eu(III) Binuclear complexes 169
5.4 Conclusions *170*
5.5 References for Chapter 5 ..... *171*
CHAPTER 6 ..... **173**
CONCLUSIONS AND FUTURE WORK 173
CHAPTER 7 ..... **175**
EXPERIMENTAL PROCEDURES 175
7.1 General Methods and Reagents *175*

7.1.1 Synthesis and Purification 175
7.1.2 Characterisation Information 176
7.1.2.1 Mass Spectrometry 176
7.1.2.2 NMR Spectrometry 176
7.1.2.3 Liquid Chromatography Mass Spectrometry (LCMS) 176
7.1.2.4 High Performance Liquid Chromatography (HPLC) 177
7.1.2.5 Absorption Spectra 177
7.1.2.6 Optical Spectroscopy 177
7.2 Experimental for Chapter 2 179
7.2.1 Synthesis and Characterisation of Complexes 179
7.2.1.1 Procedures for Asymmetric Azobenzenes 179
7.2.1.2 General Procedure for Tosyl Protection 181
7.2.1.3 General Procedure for *Tert*-butyl Ester Protection 182
7.2.1.4 General Procedure for *Tert*-butyl Ester Deprotection 183
7.2.1.5 General Procedure for Lanthanide Coordination 184
7.2.2 Photoswitching experiments 185
7.2.3 Optical Spectroscopy 188
7.2.3.1 Time-Resolved Luminescence Spectroscopy 191
7.3 Experimental for Chapter 3 193
7.3.1 Synthesis and Characterisation 193
7.3.1.1 General Procedure for TBS Protection 193
7.3.1.2 General Procedure for Radical Dibromination 194
7.3.1.3 Procedures for the Protected Macrocycles 195
7.3.1.4 General Procedure for *Tert*-butyl Ester Deprotection 197
7.3.1.5 General Procedure for Obtaining the Binuclear Complexes 198
7.3.2 X-ray Crystal Structures 200
7.3.3 Optical Spectroscopy 203
7.3.3.1 Steady State Luminescence 203
7.3.3.2 Luminescence Lifetimes 204
7.3.3.3 Triplet Energies 204
7.3.4 Relaxivity 205
7.3.5 Cyclic Voltammetry (CV) 206
7.3.6 General Procedure for Reduction Assay (Plate Reader) 207
7.3.7 General Procedure for Reduction Assay (^{1}H NMR) 207
7.3.8 NaHS Reduction 208
7.3.9 Cell Studies 210
7.3.9.1 Cell Culture 210
7.3.9.2 Hypoxia Exposure 210
7.3.9.3 Fluorescent Microscopy 210
7.3.10 Biocatalytic Reduction 210
7.4 Experimental for Chapter 4 213
7.4.1 Characterisation 4.Nd 213
7.4.2 PCA for Spectral Reconstruction 214
7.5 Experimental for Chapter 5 217
7.5.1 General Method for ^{1}H NMR pH titration 217
7.6 References for Chapter 7 218

Chapter 1

Introduction

This thesis outlines a number of ways in which the luminescence of lanthanide complexes has been modified as a result of the ligand it is coordinated within. This focusses on the three main classes of ligand modification; inner sphere coordination, reversible and irreversible effects. In this thesis, examples of each modification are described and their influence on the optical and magnetic properties of the coordinated lanthanide.

1.1 Introduction

This introduction will detail the fundamental understanding and phenomena which dictate the electronic structure of the lanthanides. Particular focus will be on the influence of crystal field splitting and the role of nuclear magnetic resonance (NMR) and luminescence spectroscopy in determining the electronic structure. This introduction will further detail the possible modifications to the crystal field that induce a spectroscopic response and the utility of such modifications in the development of stimuli responsive probes.

1.2 Electronic Structure of Lanthanides

The chemistry and physics of the lanthanides are defined by the electronic structure and properties of these elements. The electronic properties result from the filling/partial filling of the radially contracted 4f orbitals which are shielded by the more diffuse 5s and 5p orbitals.[1, 2] As a result, the chemistry of the lanthanides is dominated by the ions in the +3 oxidation state,

where removing electrons from the 6s and 5d orbitals is favourable and removing an electron from the contracted and core-like 4f orbitals requires significantly higher ionisation energies ($I_4 > I_3 + I_2 + I_1$).[3] The core-like nature of the 4f orbitals means they are less available to interact covalently, and thus the bonding of lanthanides is dictated by electrostatic interactions. Across the series, the Ln(III) ionic radii decrease with increasing atomic number, this is known as the lanthanide contraction, arising from the poor screening of effective nuclear charge by the 4f electrons. This contraction dictates the coordination number of Ln(III) ions, where earlier lanthanides tend to adopt an 8-coordinate geometry whereas the later lanthanides prefer a 9-coordinate geometry.[4]

There are seven 4f orbitals which can each be filled with 2 electrons and are described by 4 quantum numbers, the principal quantum number (n), the orbital angular momentum (l), the magnetic quantum number (m_l) and the spin quantum number (m_s). In the case of the 4f orbitals n = 4 and l = 3, the values of these quantum numbers describe the shape of the f-orbitals. Additionally, for a specific configuration of n electrons the number of microstates can be determined by the following equation:

$$\frac{(4l+2)!}{n!\,(4l+2-n)!} = \frac{14!}{n!\,(14-n)!}\ if\ l = 3$$

(1. 1)

For example, Tb(III) ($4f^8$) contains 3003 microstates. However, this degeneracy can be lifted as a result of electronic repulsion, spin-orbit coupling, and exposure to crystal and magnetic fields (Figure 1.1).

Electronic repulsion describes the fundamental spectroscopic term defined by Hund's rule, depending on the maximum spin multiplicity, S and the maximum orbital multiplicity, L. Importantly, relativistic effects must also be considered, due to the high mass of the lanthanide elements and therefore the angular dependence of the f-orbitals and strong spin-orbit coupling.[5]

Russel and Saunders described this in an approximation with overall angular momentum, which is not strictly true for lanthanides, where the quantum number J (total angular momentum) is comprised of L+S (when the shell is more than half filled) and L-S (when the shell is less than half filled). This results in a description of the microstates by a term symbol $^{2S+1}L_J$ where 2S+1 describes the spin multiplicity and L describes the value of angular momentum quantum number as represented by a letter (0 = S, 1 = P, 2 = D, 3 = F, 4 = G, 5 = H, 6 =I).

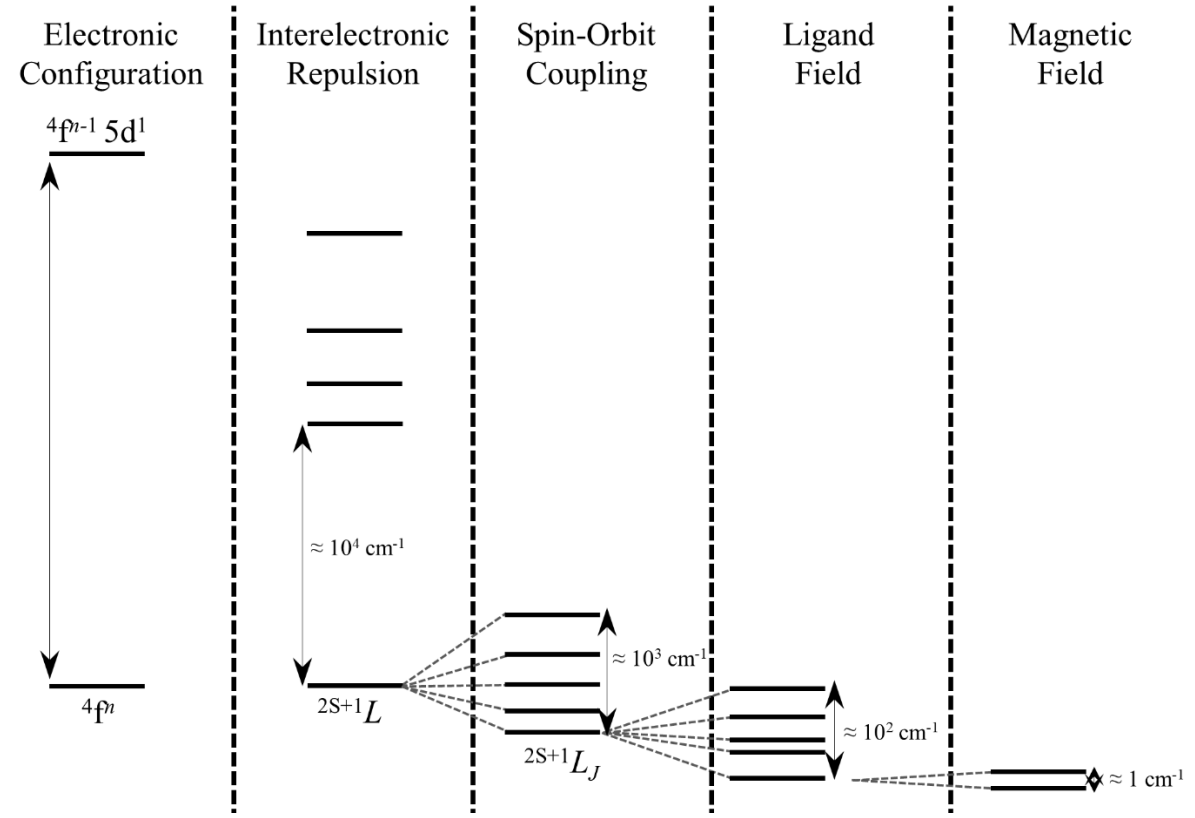


Figure 1.1: Factors which influence the splitting of the electronic states within the f-elements.

Upon exposure to a chemical environment, the spherical symmetry of the electronic structure is compromised, removing the degeneracy of the spin-orbit coupling (2J+1).[6] This is dependent on the symmetry and nature of the lanthanide coordination environment and referred to as the crystal field splitting. As a result of the contracted f-orbitals, mixing of these orbitals with neighbouring orbitals is small and therefore the splitting as a result of crystal field is small (1-

100 cm^{-1}).[7, 8] The effects of electronic repulsion, spin-obit coupling and crystal field effects underpin the electronic properties of the lanthanides and can be described using a Hamiltonian operator (Equation 1.2).[9]

$$H = \sum_{i=1}^{n}(-\frac{Z'}{r_i} - \frac{1}{2}\Delta_i) + \sum_{i\neq j}^{n}\frac{1}{r_{ij}} + \lambda \cdot \vec{L} \cdot \vec{S} + \sum_{k,q,i} B_q^k \, C_q^{(k)}(i) \; where \; \lambda = \pm\frac{\xi}{2S}$$

(1. 2)

In equation 1.2, the first and second term describe the electronic configuration, electronic interactions (repulsion between electrons at a distance, r_{ij}) and the screened nuclear charge (Z'). The third term describes the spin orbit coupling and the Russel-Saunders approximation (total angular momentum J = L + S). The final term describes the crystal field effect, where B_q^k is a crystal field parameter in which *k* and *q* are defined by the symmetry of the complex. The crystal field parameter, B_0^2 in axially symmetric complexes Eu(III) complexes can be derived from the splitting of the ΔJ = 1 band of the Eu(III) centred emission, where the true value of B_0^2 is directly proportional to the observed splitting. The sign and magnitude of the crystal field parameter details information about the effect of the crystal field on the magnetic anisotropy of the Ln(III) centre.[10] C_q is a tensor operator related to the spatial expansion of the 4f orbitals and Slater determinants.[11, 12] Kramer's ions occur where there are an odd number of electrons (half integer total spin) in which the degeneracy of the orbitals is not completely removed by the crystal field, and in low symmetry the energy levels of the Kramer's ions split into doubly degenerate states (Kramer's doublets).[13] This degeneracy can only be removed in the presence of a magnetic field (Zeeman effect).[14] The intensities of transitions, between these electronic states, in both absorption and emission spectra of Ln(III) complexes can be described by Judd-Ofelt theory.[15, 16] With this information, the ground state and excited state energies can then be determined as demonstrated by the work of Carnall (Fig. 1.2), showing the energy level diagrams for the aquo Ln(III) ions.[17-22] Work by Stein and Wurzburg combined earlier studies

on the spectra of Ln(III) ions to determine the principal emissive states of each lanthanide (red).[23] Since then, extensive investigations at low temperature and exploiting up-conversion mechanisms have revealed additional emissive states (orange).[24-48]

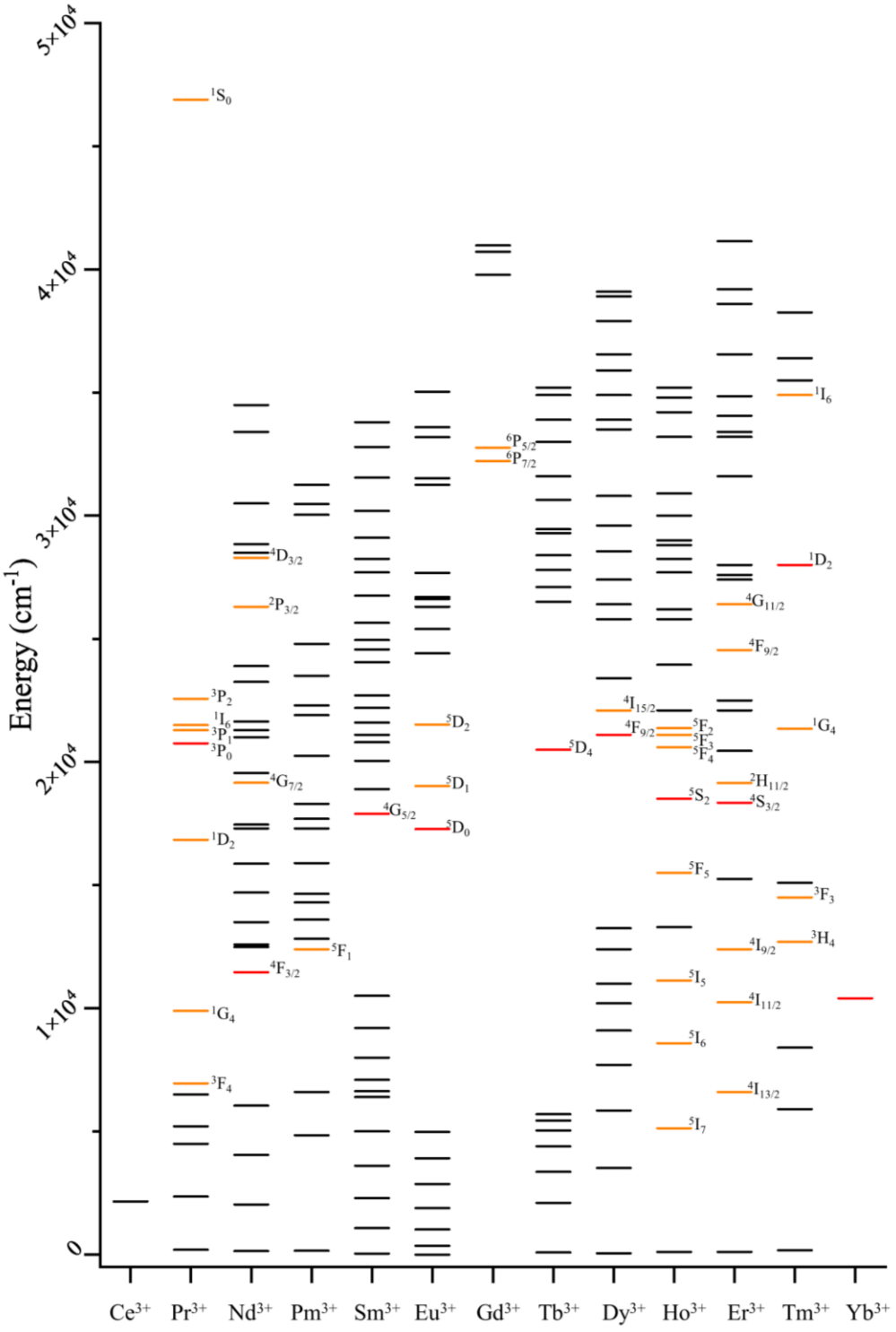


Figure 1.2: Updated energy level diagram for the Ln(III) aquo ions, as determined by Carnall, where primary emissive states are highlighted in red, and other possible emissive states are highlighted in orange.[14-45]

1.3 Lanthanide Luminescence

Lanthanide luminescence can be exploited as a tool to investigate the electronic transitions that can occur in lanthanide complexes, and thus ascertain the electronic structure. These transitions include; f→f transitions which are sharp and line like, f→d transitions which are broader, and both metal to ligand and ligand to metal charge transfers which are again both broad transitions.[49] These transitions can be characterised through absorption spectroscopy, in which a ground state electron is promoted to a higher energy excited state. Additionally, the reverse process can be investigated using emission spectroscopy, in which the excited state electron relaxes back into the lower energy ground state. In comparison to transition metals, lanthanide luminescence spectra contain many transitions relating to the large number of microstates available as determined by the number of electrons in the ground state.

f→f transitions are characteristic for individual lanthanide ions, however they usually occur with weak intensities. f→f transitions are formally forbidden by Laporte's selection rules, despite this, the transitions can occur *via* the mixing of electronic states under a crystal field known as vibronic coupling. The core like nature of the 4f electrons means vibronic coupling is much weaker, in comparison to transition metals, therefore these f→f transitions occur with lower absorption coefficients and reduced intensity.[50] However, the forbidden nature of the f→f transitions gives rise to the desirable long-lived emission lifetimes (μs - ms) observed as a result of low transition probabilities and long-lived excited states.[51]

Another characteristic property of lanthanide luminescence is the line-like spectra. The shielded f-electrons experience only a small influence from the surrounding environment and thus promotion or relaxation of an electron between the ground and excited state only weakly perturbs the interaction with the crystal field (as it is dominated by electrostatics) and so the geometry in the excited state remains almost unchanged, generating narrow bands with a small

stokes shift. These narrow line-like transitions are characteristic to each Ln(III) ion and can be used to characterise lanthanide complexes. Additionally, fine structure of the transitions in lanthanide luminescence spectra contains electronic information regarding, the geometry, symmetry and impact of crystal and magnetic field of the complex.

1.3.1 Sensitised Luminescence

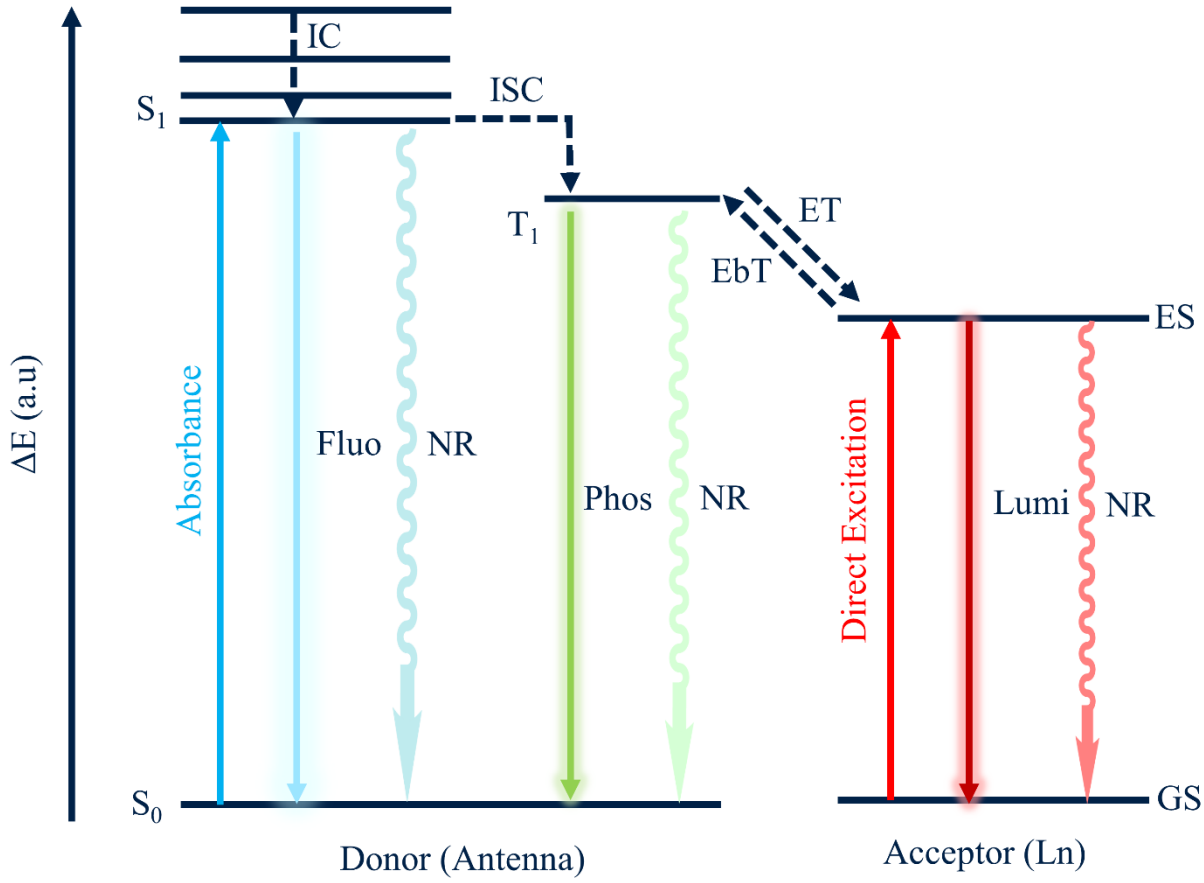


Figure 1.3: Schematic energy level diagram dipicting antenna sensitisation and the possible non-radiative and radiative pathways available for sensitised Ln(III) complexes. Fluo = fluorecence, Phos = phosphorescence, Lumi = luminescence, N.R = non-raditave decay,IC = internal conversion, ISC = intersystem crossing, ET = energy transfer and EbT = back energy transfer.

Direct excitation into a f→f transition usually yields emission with low intensity as a result of the forbidden nature of the transition. Sensitisation or the antenna effect modifies the environment around the lanthanide, generating pathways for the indirect population of the lanthanide excited state (Ln^{*}) thus increasing the probability of radiative emission.[52, 53] This can occur using inorganic phosphors,[54, 55] transition metal complexes[56-58] or most commonly

organic chromophores,[59] incorporated into the ligand design. The process works by taking advantage of the Laporte and spin allowed transitions of the antenna, exciting electrons from the ground state into the ^{1}S excited state. The system then undergoes intersystem crossing (ISC) to populate the ^{3}T state of the antenna, which can in turn populate the Ln* *via* energy transfer (Fig. 1.3). In order for this process to be efficient, there must be sufficient energy transfer between the antenna and the lanthanide, this is described by Fermi's golden rule:

$$W_{DA} = \left(\frac{4\pi^2}{h}\right) \cdot \left| < D^* A \left| \mathcal{H}' \right| DA^* > \right|^2 \cdot \Omega_{DA} \qquad (1.3)$$

In equation 1.3, W_{DA} describes the probability of energy transfer, D represents the donor and donor excited state (D^*), A represents the acceptor an acceptor excited state (A^*) and Ω_{DA} is the integral of spectral overlap between the donor and acceptor. $\mathcal{H}'$ represents the perturbation operator. Therefore, in order to have efficient energy transfer the spectral overlap between the energy levels of the donor and acceptor must be large.[1] Another aspect which determines the efficiency of the sensitiser is the probability of non-radiative decay from both the ^{1}S and ^{3}T excited states. The energy transfer can occur either *via* Förster resonance energy transfer (FRET) or by Dexter exchange.

1.3.2 Förster Resonance Energy Transfer

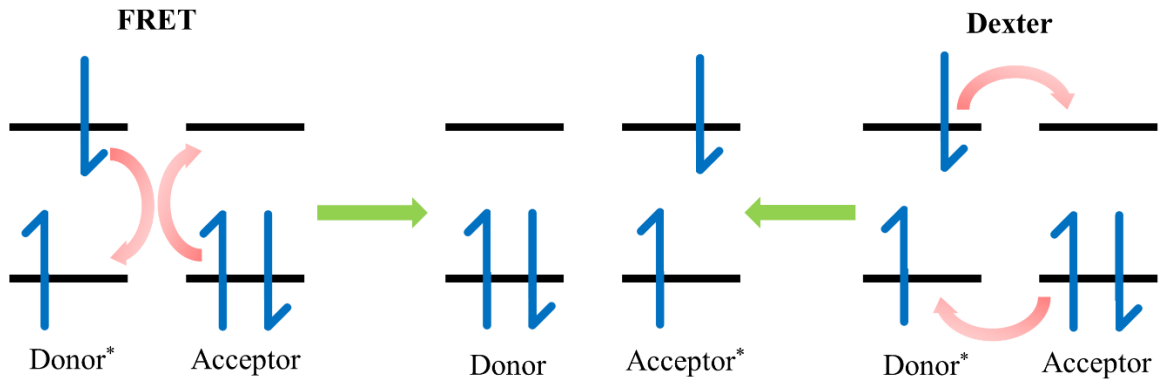


Figure 1.4: Schematic diagram depicting the mechanism of Förster Resonance Energy Transfer (FRET) and Dexter exchange.

Förster resonance energy transfer (FRET) occurs *via* an electrostatic, through space interaction (Figure 1.4). In FRET, the donor and acceptor are treated as dipoles and the electronic transitions are allowed. The efficiency of the energy transfer between the donor and acceptor can be described as:

$$\eta_{et} = \frac{1}{1 + (\frac{R_{DA}}{R_0})^6}$$

(1. 4)

Where R_0 is the critical distance at which 50% of energy transfer occurs. FRET is a distance dependent phenomenon, the probability of energy transfer is dependent on R_{DA}^{-6} as a result, FRET occurs up to 1000 pm and is considered a long-range interaction.[60-62]

1.3.3 Dexter Exchange

Dexter exchange depends on a double electron exchange interaction which is dependent on the overlap of molecular orbitals. For this reason, Dexter exchange is often considered as a through bond interaction (Figure 1.4). The rate of Dexter exchange is described by:

$$k_{et} = KJ' e^{[\frac{-2R_{DA}}{L}]}$$

(1. 5)

Where K is a spectroscopic constant, J' is the normalised spectral overlap integral, R_{DA} is the distance between donor and acceptor and L is the sum of the van der Waals radii of the donor and acceptor. Here the distance dependence is much shorter and typically between 30-50 pm.[63]

1.3.4 Quenching

The overall quantum yield can be described as a combination of the intrinsic quantum yield and the efficiency of sensitisation from the ligand to the lanthanide, eq. 1.6.[1, 64]

$$\phi_{ln} = \eta_{sens} \cdot \phi_{Ln}^{Ln} = \eta_{sens} \cdot \frac{\tau_{obs}}{\tau_{rad}}$$

(1. 6)

Non-radiative pathways offer a route for the luminescence to be quenched, by dissipating the excited state energy through a series of vibrations. These can be in the complex itself or via solvent molecules and anions in solution. Particularly, for lanthanides the intrinsic quantum yield is correlated to the difference in energy between the ground and excited state energies as this gap is similar in energy to that of common O-H, N-H and C-H oscillations. Therefore, deactivation through these non-radiative pathways is common and further reduces the probability of emission. This is particularly true for NIR emitting lanthanides.[65, 66] The intrinsic quantum yield can be determined by measuring the observed lifetime, as this accounts for both radiative and non-radiative components. A method to determine the impact of quenching as a result of the inner sphere coordinated solvent molecules is described by the modified Horrocks equation, (equation 1.7).[67, 68]

$$q = A(\tau_{H_2O} - \tau_{D_2O} - B)$$

(1. 7)

In the modified Horrocks equation, q is the number of bound water molecules in the first co-ordination sphere, A is a constant describing the sensitivity of the lanthanide ion to vibronic quenching by O-H oscillators, B is a constant that accounts for outer-sphere quenching and τ is the observed luminescent lifetimes of the lanthanide complex in water and deuterated equivalent. The q value is particularly useful in determining the contribution of solvent and anions as luminescence quenchers.

Quenching can also occur *via* back energy transfer resulting from a small difference in energy between the antenna excited state and the Ln(III) excited state ($\Delta E \sim 2000\ cm^{-1}$).[2] Photoinduced electron transfer (PeT) is also an efficient quencher of lanthanide luminescence. Upon

photoexciting, a redox reaction occurs where the antenna becomes oxidised and the Ln(III) is reduced, this is common for Eu(III) as Eu(II) is easily accessible (E_{red} = -0.35 V vs SHE), but is also possible for Em, Dy or Yb.[69]

1.4 Influence of Ligand Modification on Lanthanide Luminescence

1.4.1 Ligand Design

The application of a luminescent lanthanide complex is often dependent on careful engineering of the ligand surrounding the lanthanide. The ligand or ligands dictate the coordination sphere, symmetry, thermodynamic and kinetic stability, the availability of quenching pathways and the presence/efficiency of an antenna. Each of these can be optimised for a particular application. In solution, the stability of the complex in the presence of competing solvent/anions is of paramount importance. To ensure stability, preorganised and often macrocyclic ligands which saturate the coordination sphere of the lanthanide and exploit the chelate and macrocyclic effect are targeted. These ligands commonly contain hard donors such as oxygen and nitrogen to exploit the favourable electrostatic interactions with hard Ln(III) centres. A popular motif based on these principles is the DOTA ligand, in which a cyclen ring containing 4 nitrogen atoms are flanked by 4 carboxylate arms. These arms are free to wrap around and encapsulate the lanthanide ion in an octadentate coordination environment (Fig. 5a).[70] This system has been further modified by the removal of one carboxylate arm to give the DO3A ligand in which one arm is free to be functionalised for a specific application.[71] Modification of both the inner sphere coordination environment and the surrounding ligand can influence the properties of lanthanide luminescence.

1.4.2 Inner Sphere Contributions

Despite the less pronounced effects afforded by crystal field in comparison to that of spin-orbit coupling in lanthanide complexes, the influence of crystal field on the electronic structure can

be measured spectroscopically. Thus, the spectra recorded are dependent on the chemical make-up, geometry, symmetry, coordination number and number of bound solvent molecules.

1.4.2.1 Symmetry

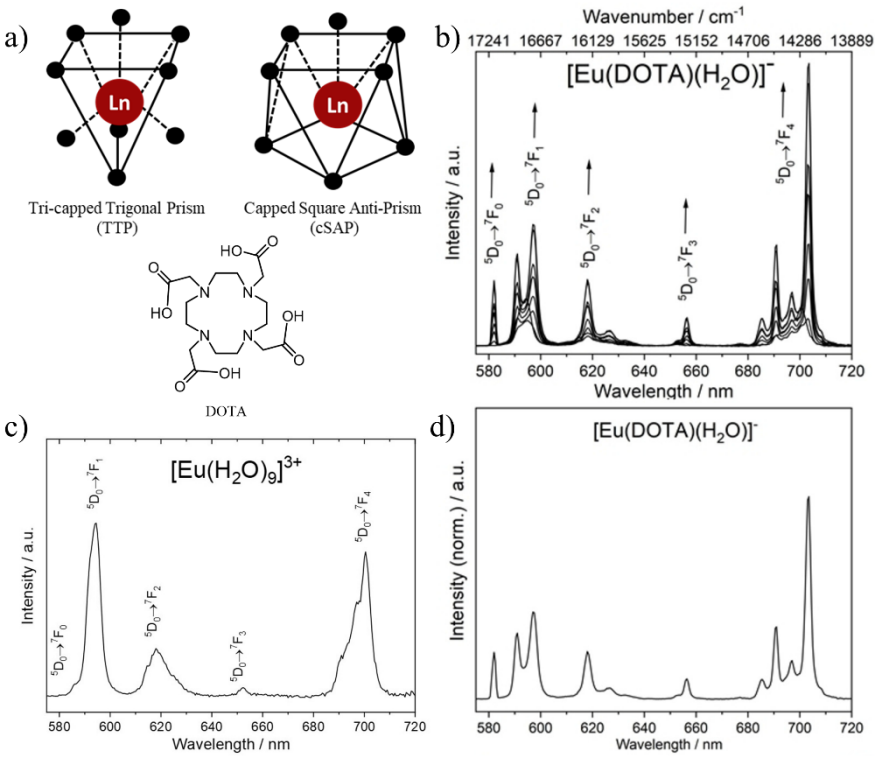


Figure 1.5: a) Possible geometries available for 9-coordinate lanthanides in solution b) change in Eu (III) emission upon addition of DOTA to $[Eu(H_2O)_9]^{3+}$ in water c) the emission spectra of $[Eu(H_2O)_9]^{3+}$ in water d) the emission spectra of $[Eu(DOTA)(H_2O)]^-$ in water. λ_{ex} = 394 nm. Reproduced with permission from Sørensen and co-workers.[72]

The impact of symmetry upon the electronic transitions has been extensively researched with regards to Ln(III) complexes.[73, 74] Sørensen and co-workers demonstrated the importance of symmetry and coordination environment with Eu(III) complexes in solution (Fig. 1.5).[72] The Eu(III) aquo ion adopts a 9-coordinate tri-capped trigonal prismatic geometry with point group symmetry corresponding to D_{3h}. Additionally, Eu(III) predominantly emits from $^5D_0$ excited state upon radiative decay to the lower lying ^7F_J (J = 0,1,2,3,4) ground states (Figure 1.5c). Upon addition of DOTA, a strong, octadentate, macrocyclic ligand, complexation occurs to form the $[Eu(DOTA)(H_2O)]^-$, as observed in Figure 1.5b. Upon complexation they observed

two changes; an increase in the intensity of the europium emission and increased splitting of transitions. The increase in emission intensity is attributed to the removal of inner sphere water molecules upon complexation (q = 9 $[Eu(H_2O)_9]^{3+}$ to q = 1 $[Eu(DOTA)(H_2O)]^-$) , which are efficient quenchers of Eu(III) emission. The increased number of lines describes a change in crystal field and the splitting shows a non-uniform crystal field where the original degeneracy has been removed. Particularly, the presence of a strong and defined $^5D_0 \rightarrow {}^7F_0$ transition in $[Eu(DOTA)(H_2O)]^-$ suggests there is no mirror plane orthogonal to the primary axis and the splitting of the $^5D_0 \rightarrow {}^7F_1$ relates to the rotational symmetry.[72] Recent work in the group has further assessed the importance of point group symmetry in lanthanide complexes, using a computational approach.[75]

1.4.2.2 Equilibria of DOTA/DO3A complexes

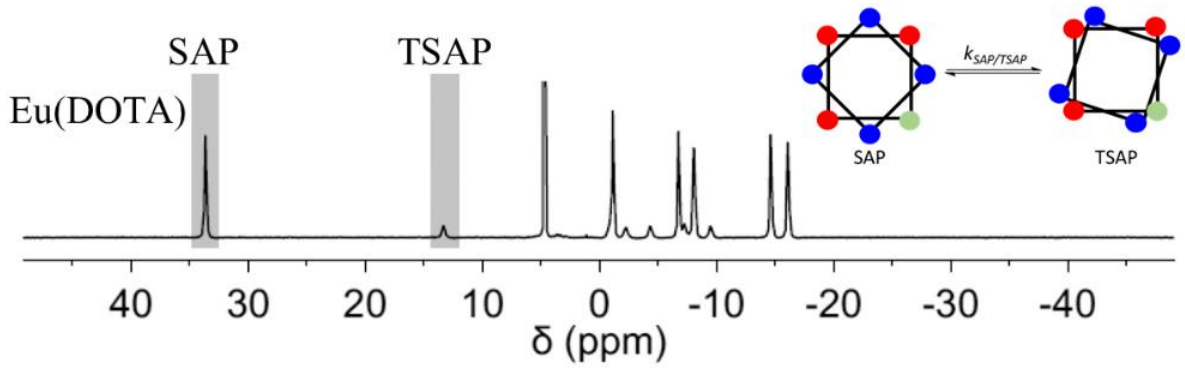


Figure 1.6: ^1H NMR of Eu(DOTA) in D_2O, highlighting the presence of SAP and TSAP axial protons at their respective chemical shifts. Reproduced from Sørensen and co-workers.[76]

$[Ln(DOTA)(H_2O)]^-$, complexes can adopt either the square anti-prism (SAP) or the twisted square antiprism (TSAP) geometry in solution. SAP and TSAP are in equilibrium with each other, and the solvent capped and uncapped forms of each, leading to 8 different possible structures in solution.[77-79] Sørensen and co-workers further investigated the solution state structure of $[Eu(DOTA)(H_2O)]^-$, particularly the influence of isomers on the electronic structure. They determined that for all measured spectra, the spectrum observed describes the

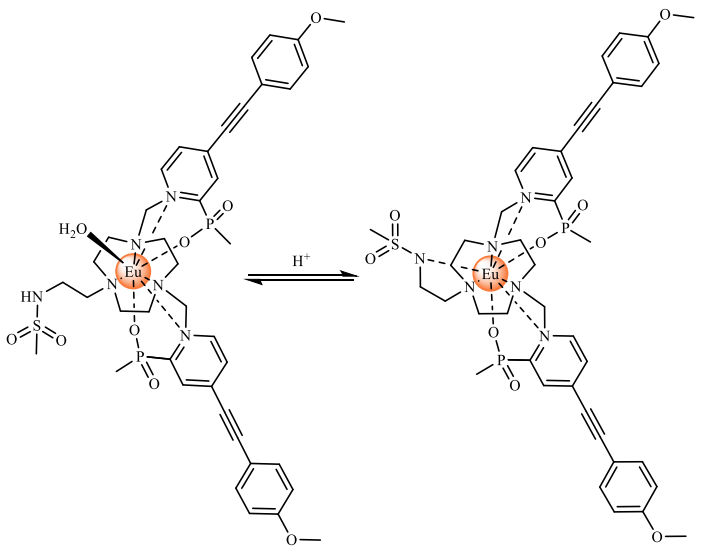
weighted average of all equilibrium species in solution, the species in equilibria observed is dependent on the time-scale of the experiment. For $[Eu(DOTA)(D_2O)]^-$, ^1H NMR describes distribution of isomers in solution as the interconversion between TSAP and SAP isomers can range from (25- 72 s^{-1}), which is within the time frame of a typical ^1H. NMR experiment (Fig. 1.6).[80] Both TSAP and SAP have distinct and predictable chemical shifts, integration of the axial proton peak of each, normalised to the total integration, can approximate the isomeric distribution in solution. However, for asymmetrical and more complex systems the peaks in ^1H NMRs become broad due to fluxionality of the ligand and it becomes much harder to isomeric distributions. Unfortunately, comparative to ^1H NMR, the differences between the TSAP and SAP isomer in luminescence spectra are much smaller (~ 100 cm^{-1}) and usually cannot be well resolved with current instrumentation.[76, 81]

1.4.2.3 Inner Sphere Effects: pH

Changes in pH can induce a change in coordination geometry and symmetry around a Ln(III) metal centre. This was demonstrated by Parker and co-workers using an Eu(III) complex containing a methyl substituted sulphonamide arm which can bind reversibly to the Eu(III) centre upon deprotonation/protonation of the amide.

Upon deprotonation of the amide, the ligand reversibly switches from heptadentate to octadentate. At low pH where the heptadentate ligand is present, the emission intensity of the Eu(III) $^5D_0 \rightarrow {}^7F_J$ transitions are considerably reduced, suggesting the presence of a quenching solvent molecule in the inner sphere. At high pH, the emission intensity is much greater, suggesting that the deprotonated nitrogen, displaces the bound water and coordinates directly to the Eu(III) centre. Notably, not only does the emission intensity change but also the shape and splitting of the $^5D_0 \rightarrow {}^7F_J$ transitions. This is a direct consequence of the change in crystal field between the heptadentate and octadentate ligand conformations. Importantly, we must

also consider equilibria in this system, the emission spectrum observed at the pK_a value (6.52) describes a weighted average of both the protonated and deprotonated complexes in solution. This phenomenon has been exploited readily in the development of Ln(III) based optical probes for monitoring pH. [82, 83]



Scheme 1.1: Change in structure of a Eu(III) probe upon protonation/deprotonation of the methyl substituted sulphonamide arm. Reproduced from Parker and co-workers.[83]

1.4.2.4 Influence of Anions on the Electronic Properties

Many luminescent Ln(III) complexes, in solution, contain an axial site occupied by a solvent molecule. This is the case for most DOTA, and DO3A containing Ln(III) complexes. In competitive media this neutral solvent molecule can be replaced by competing anions, the electron density, electronegativity and hard/soft nature of the coordinating anion influences the crystal field experienced by the lanthanide.[71, 84-86]

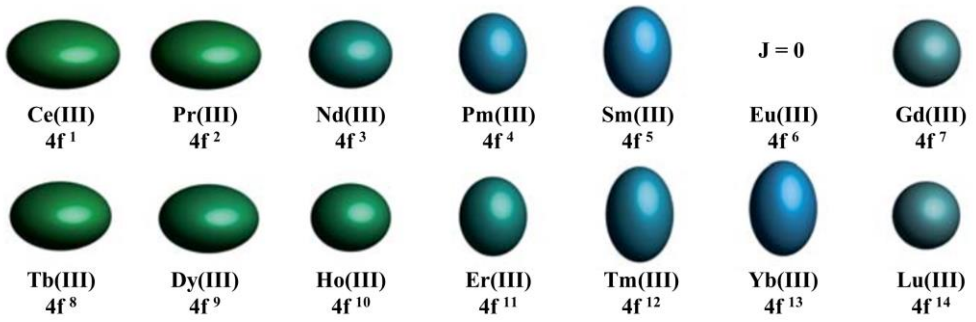


Figure 1.7: Shape of the f-electron distribution in the ground state of Ln(III) ions. Reproduced from Long and Rinehart.[87]

Additionally, the lanthanide in question is important, as the influence of anions is also dependent on the shape of the lanthanide ground state. The distribution of the 4f electrons in the ground state was approximated by Long and Rinehart using the total angular momentum quantum number, the stevens coefficient and the radius of the 4f shell squared. This gave a range of distributions from prolate (Tb(III) and Dy(III)) to oblate (Tm(III) and Yb(III)), Fig. 1.7.[87] Therefore, if electron density is pointing in the axial position (oblate) and anions bind axially, then electronic repulsion is strong and the change in electronic structure is large compared to the axial binding of an anion to a prolate Ln(III) centre.

This effect was demonstrated by Faulkner and co-workers, investigating the influence of axial fluoride binding on a series of Ln(III) tetraamide (DTMA) complexes (Figure. 1.8).[88-90] First, they investigated the influence of fluoride on Yb(III) complexes using ^{1}H NMR. Upon addition of fluoride there was a considerable change in the proton chemical shifts of the Yb(III) complex, which was conveniently expressed using the Bleany equation (Equation. 1.8) and dependent on the crystal field parameter D_1 (a constant describing the crystal field, temperature and Boltzman distribution).[11, 12]

$$\delta_{PC} = D_1 \frac{(3cos^2\theta - 1)}{r^3}$$

(1. 8)

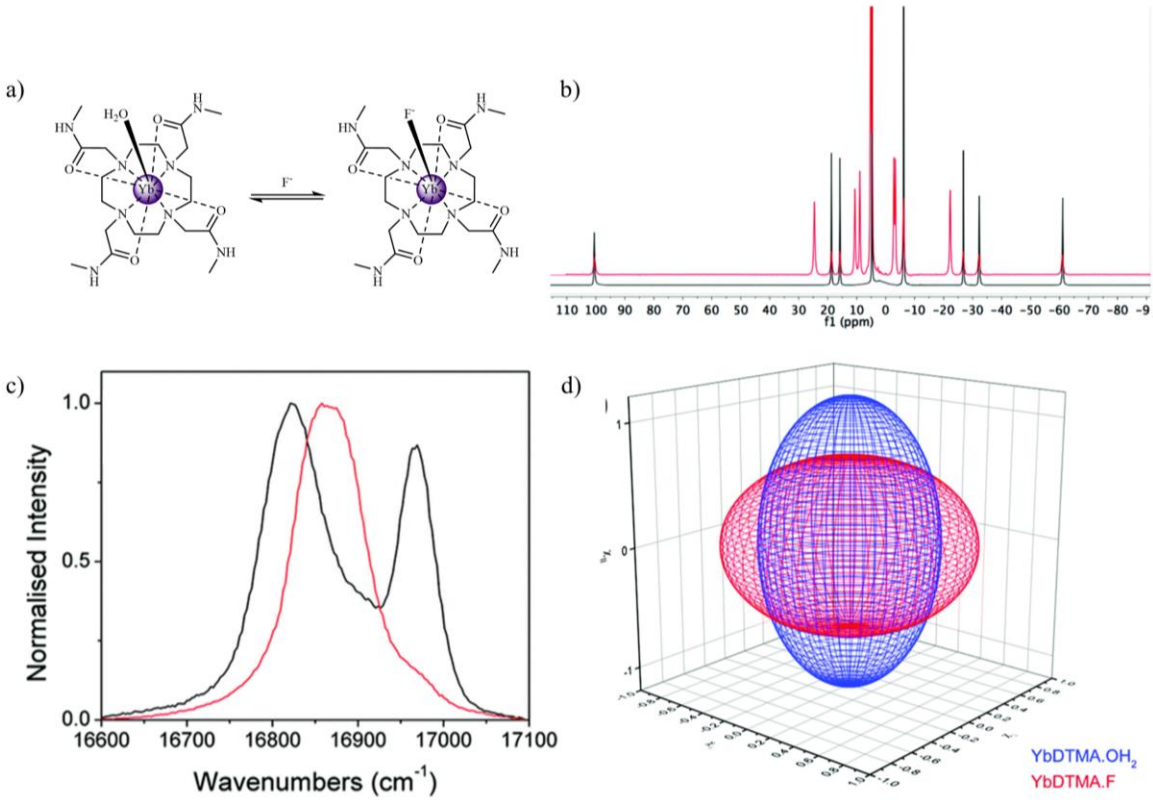


Figure 1.8: Influence of axial flouride binding on Ln(III) tetraamide complexes a) ^{1}H NMR of Yb(DTMA) in D_2O (black), with the addition of fluoride (red) b) the emission of Eu(DTMA) in D_2O upon excitation at 394 nm (black) and upon addition of fluoride (red) c) the approximated anisotropy of the Yb(DTMA).OH_2 (blue) and upon addition of fluoride (red). Reproduced from Faulkner and co-workers.[90]

D_1 represents the gradient of the line upon plotting the chemical shift vs $(3\cos^2\theta - 1)/r^3$, where $\delta_{PC} = \delta_{obs} - 2.9$ ppm (average shift, accounting for diamagnetic contribution) and $(3\cos^2\theta - 1)/r^3$ values were taken from a closely related crystal structure (Equation 1.9). This information was then used to approximate the anisotropy of each complex where the χ_{av} is estimated as 2.5 $cm^3\ mol^{-1}\ K$.

$$\delta_{PC} = \frac{1}{2N_A}\left[\frac{(3cos^2\theta - 1)}{r^3}(\chi_{\parallel} - \chi_{av})\right]$$

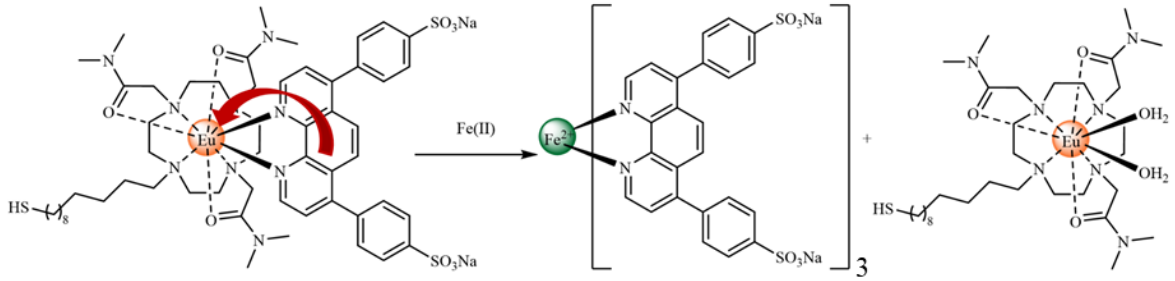
(1. 9)

This is summarised in Figure 1.8d, where the $Yb(DTMA)^-$ displayed oblate anisotropy, where upon binding of a fluoride, this anisotropy switched to prolate. This is supported by ^{1}H NMR studies on Eu(III) complexes and additional luminescent studies. In the case of luminescence, the addition of fluoride considerably changed the shape and splitting of the $^{5}D_0 \rightarrow {}^{7}F_2$

transition, further implying a significant change in electronic structure upon anion binding of fluoride at the axial position. Additionally, the luminescent lifetimes increase upon the binding of fluoride, as the number of O-H oscillators present in the inner coordination sphere is reduced.

1.4.2.5 Direct Antenna Coordination

Another modification to the inner sphere coordination environment is the reversible coordination of a sensitiser directly to the Ln(III) metal centre. This has been used to develop probes for sensing chromophores in solution[91] or more commonly in displacement assays.[92]



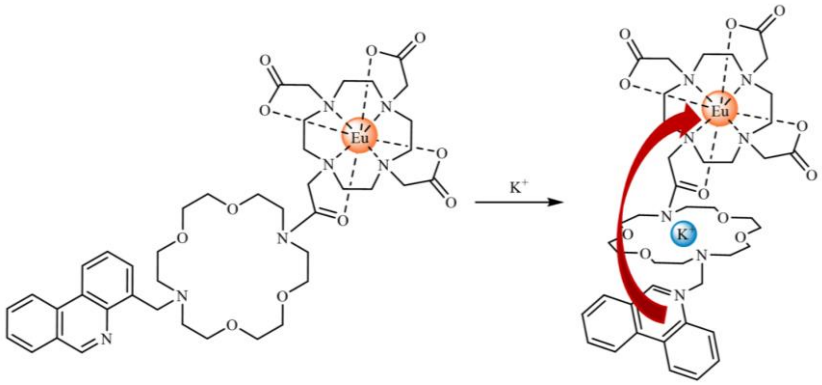
Scheme 1.2: Displacement assay for the detection of Fe(II) in solution with an emissive Eu(III) probe. Reproduced from Gunnlaugsson and co-workers.[93]

Gunnlaugsson and co-workers demonstrated the sensing of Fe(II) in a displacement assay, utilising a ternary Eu(III) complex comprising of a heptadentate DO3A-based ligand and a bidentate 4,7-diphenyl-1,10-phenanthroline-disulfonate (BPS) antenna (Scheme 1.2).[93] Initially the BPS antenna is directly coordinated to the Eu(III) centre and acts as an efficient sensitiser (λ_{ex} = 278 nm) for Eu(III) emission. However, upon addition of Fe(II), the Eu(III) is outcompeted and the BPS unit coordinates to the Fe(II). This displacement results in i) a change in crystal field around the Eu(III), ii) an increase in number of bound solvent molecules (q) at the Eu(III) centre, iii) removal of an efficient sensitiser. Both the removal of the sensitiser and the increase in bound solvent molecules drastically quenches the luminescence, resulting in a "turn off" probe for Fe(II) in solution. This example demonstrates the impact of a combination of inner sphere effects on Ln(III) luminescence.

1.4.3 Reversible Modification of Ligand Constitution

Reversible modification of the antenna, can also induce changes in the lanthanide luminescence, this can include anion binding, supramolecular interactions or in response to changing pH and O_2 levels. Each of these interactions can reversibly manipulate the photophysics of the antenna and thus the lanthanide luminescence. [94, 95]

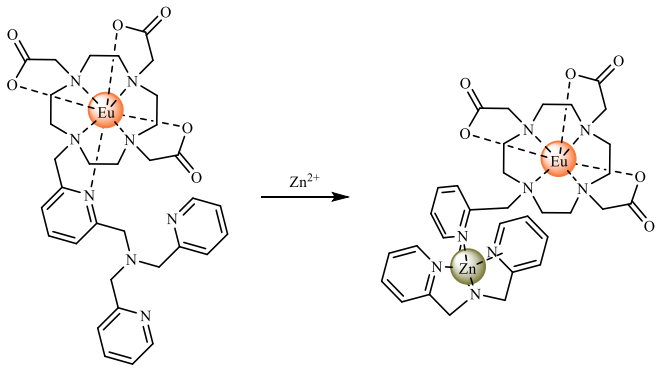
1.4.3.1 Cation Binding



Scheme 1.3: A Eu(III) probe for K^+. Reproduced from Pierre and co-workers.[96]

Pierre and co-workers incorporated both an antenna and a cation binding site (crown ether) into a kinetically stable Eu(III) complex.[96] Importantly, they designed the compound so that the cation binding site was between the Eu(III) centre and the phenanthridine antenna (Scheme 1.3). In the absence of cations, K^+, the ligand is flexible and the antenna is further away from the Eu(III) centre. Upon binding of K^+ within the crown ether, the nitrogen on the phenanthridine can consequently coordinate with the encapsulated potassium ion. This both increases the conjugation of the ligand system, and decreases the distance between the Eu(III) centre and the antenna. Notably, this system displays ratiometric probing of the K^+ concentration in solution, the UV region of the excitation spectra (λ_{em} = 593 nm) is sensitive to K^+ concentration whereas excitation in the blue region of the visible spectra (λ_{ex} = 263 nm) yields the Eu(III) centred emission, which is independent of the concentration of K^+. They attribute the dependence of the ligand-based emission on the concentration of K^+, to the

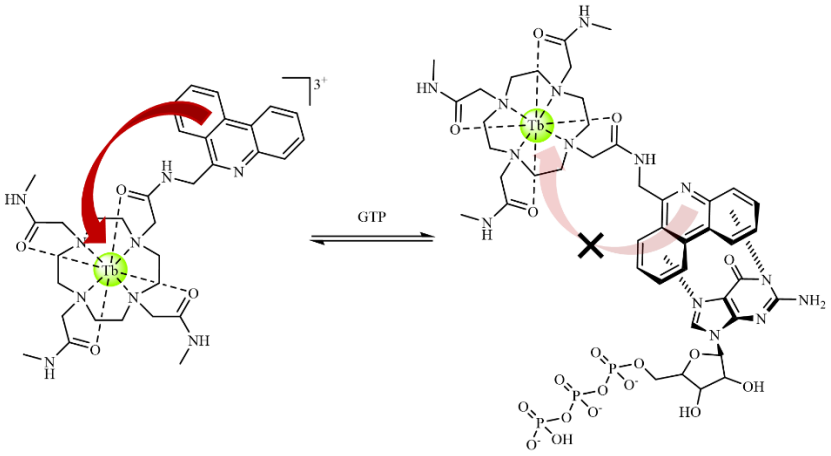
efficiency of energy transfer from the phenanthridine to the Eu(III) centre. In this case, the antenna is brought closer to the Eu(III) upon coordination of K^+, thus increasing the probability of FRET from the antenna to the metal centre, resulting in brighter emission.



Scheme 1.4: Eu(III) picolyl probe for the detection of Zn^{2+}. Reproduced from Pope and co-workers.[97]

Pope and co-workers developed a luminescent Eu(III) sensor for Zn(II), exploiting both inner sphere and antenna modulation in their design (Scheme 1.4).[97] They synthesised a kinetically stable DO3A based ligand in which the free arm was functionalised with a bis-picolyl amine, capable of encapsulating Zn(II) ions. Upon complexation of Eu(III), in the absence of Zn(II), an octadentate coordination environment is satisfied, seven donors from DO3A and an additional nitrogen from the pyridine of the bis-picolyl arm. Upon addition of Zn(II), this pyridine nitrogen favours binding to the Zn(II) encapsulating it within the tetradentate site. Consequently, the Eu(III) is coordinated through 7 ligand donor atoms and thus additional solvent molecules can coordinate. Ultimately upon addition of Zn(II) the Eu(III) centred emission was found to decrease in intensity. This is a result of a combination of two factors: i) increasing the distance between Eu(III) metal centre and the antenna and, ii) removal of a Dexter exchange pathway through the pyridine nitrogen. Additionally, they observed changes in the intensity and shape of $^5D_0 \rightarrow {}^7F_J$ transitions of the Eu(III) emission, due to the change in crystal field, by the removal of the coordinating pyridine nitrogen upon addition of Zn(II).

1.4.3.2 π-π interactions



Scheme 1.5: A Tb(III) phenanthridine probe for the sensing of purine nucleotides in solution Reproduced from Pierre and co-workers.[98]

Pierre and co-workers investigated the impact of π-π interactions, between the antenna and analyte, on the lanthanide luminescence.[98] They exploited the well-known phenanthridine antenna and incorporated it into the design of kinetically stable Eu(III) and Tb(III) complexes (Scheme 1.5). The extended aromatic phenanthridine is not only an efficient antenna, it also favours hydrophobic interactions and π-π stacking. In the absence of purine nucleotides, the Ln(III) phenanthridine complex is highly emissive. However, in the presence of purine nucleotides, the lanthanide luminescence is dominated by the static quenching caused by formation of a stacked phenanthridine–purine complex. Upon formation of the stacked complex, photoelectron transfer (PeT) can occur from the purine nucleotide to phenanthridine, reducing the phenanthridine ligand, resulting in quenching of the Ln(III) emission.

1.4.3.3 pH and O_2 dependence

Parker and co-workers designed and synthesised a Ln(III) phenanthridine complex in which the Tb/Eu(III) emission intensity and lifetime decreased upon increased acidity.[99, 100] A pH titration revealed that the pK_a of the Tb(III) phenanthridine complex was 5.75, corresponding to the protonation of the nitrogen on the phenanthridine, Figure 1.9a. In the Tb(III) system,

upon protonation, the triplet energy gap between the ligand and Tb(III) $^5D_4$ emissive state decreased from 1500 cm^{-1} to 800 cm^{-1}, therefore back energy transfer dominated for the protonated system, reducing the emission intensity and lifetime of the Tb(III) $^5D_4$ emissive state.

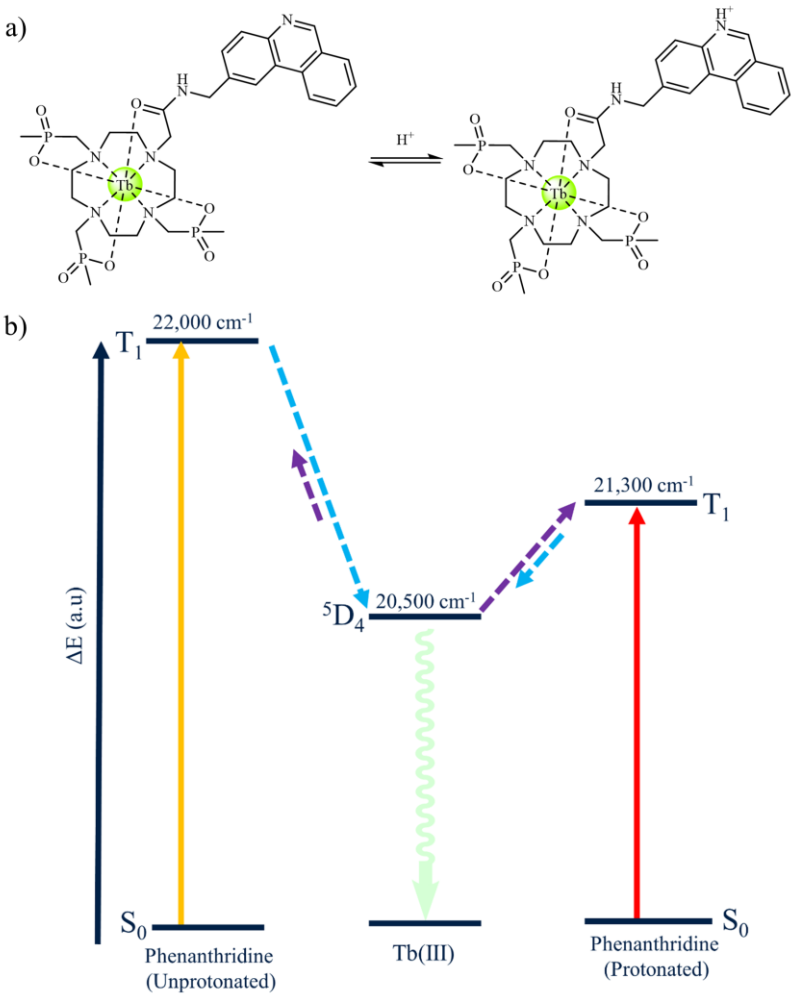
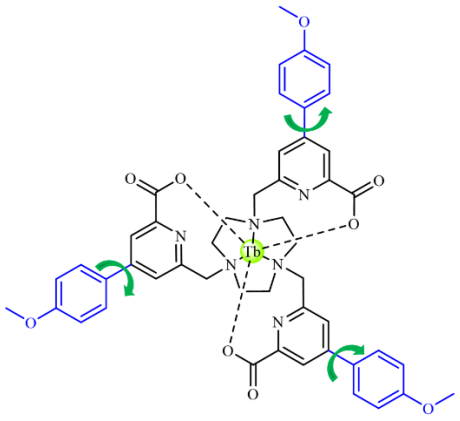


Figure 1.9: a) structure of the pH and oxygen responsive Tb(III)phenanthridine probe b) simplified Jablonski diagram of triplet state dependence on pH, absorbance in block lines (orange and red), back energy transfer (purple, dashed), energy transfer (blue, dashed) and emission (green, wavy). Reproduced from parker and co-workers.[101]

Additionally, the rate of back energy transfer and the rate of oxygen quenching of triplet states are competitive and thus, in low oxygen environments both the emission lifetime and quantum yield increased. Additionally, with methyl substituted phenanthridine complexes, the addition of halide ions leads to a decrease in luminescence intensity of both the ligand and Eu(III) emission as a result of collisional (Stern-Volmer) quenching of the excited states.[101]

1.4.3.4 Viscosity

Viscosity can dictate the availability of non-radiative decay pathways via the restriction of molecular motion and thus influence the efficiency of emissive complexes.[102, 103]



Scheme 1.6: A viscosity sensitive emissive Tb(III) probe, based on rotations around the ligand arms b) Reproduced from Maury and co-workers.[104]

Maury and co-workers investigated the influence of viscosity on the luminescent properties of an emissive Tb(III) 1,4,7-triazacyclononane complex (Scheme 1.6). They assessed the quantum yield of the complex in various media with differing viscosities, observing that in high viscosity media, such as glycerol, quantum yields of $\Phi = 67\%$ were achieved. This was a significant increase on the sample in methanol, which exhibited a $\Phi = 15\%$. Additionally, the luminescent lifetimes increased with increasing viscosity. Both these observations were explained by the reduction in molecular motion of the internal biaryl antenna. The Gd(III) analogue was synthesised to investigate the ligand excited states. Low temperature emission experiments determined the antenna triplet state energy as ~ 22,000 cm^{-1}. This is close in energy to the Tb(III) $^5D_4$ emissive state and the energy difference is small enough such that back energy transfer can occur ($^5D_4 \rightarrow {}^3T$). They hypothesised that this energy gap, and thus the equilibrium with back energy transfer, allowed for the observed changes in luminescent intensities and lifetimes in different viscosity media. To ensure this, they synthesised the Eu(III) analogue which has a much larger energy gap between the antenna triplet and emissive

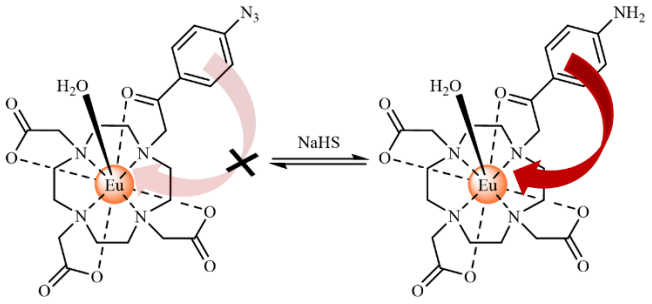
$^5D_0$ state and consequently observed no dependence of luminescent properties with viscosity. Therefore, they proposed that the reversibility of the energy transfer between the $^5D_4 \leftrightarrow {}^3T$ underpins, the dependence of the luminescent properties with viscosity.[104]

However, upon review the authors released a correction. The influence of dissolved oxygen within the different samples had been underestimated, therefore they repeated the investigation in air-equilibrated and degassed methanol and glycerol solutions. In methanol, very strong enhancement of luminescence properties was observed as oxygen concentration decreased; In contrast, a modest increase was observed in glycerol upon degassing. Therefore, although their initial measurements were correct, the interpretation that the changes were due to viscosity were incorrect, and should instead be described as a system which reports on the concentration of dissolved oxygen.

1.4.4 Irreversible Modification of Ligand Constitution

Responsive luminescent lanthanide sensors can also result from irreversible modifications of the antenna upon interaction with an external stimulus. This interaction with analytes can trigger functional group interconversions, decaging reactions, cyclisation and catalytic transformations.[105, 106] An irreversible change in ligand constitution is often accompanied by a pronounced change in the luminescent properties of the lanthanide, resulting in efficient probes with good contrast between states.

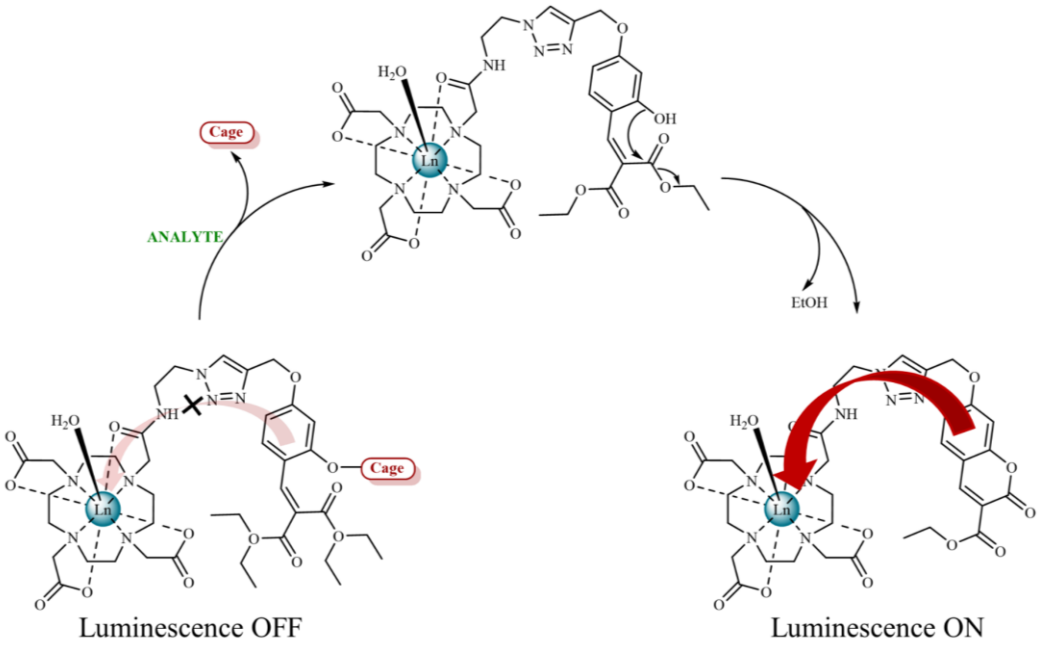
1.4.4.1 Analyte Responsive Reduction



Scheme 1.7: A kinetically stable Eu(III) azido-acetophenone containing luminescent probe for the sensing of hydrogen sulphide in solution. Reproduced from Faulkner and co-workers.[107]

Faulkner and co-workers developed a kinetically stable, turn-on Eu(III) probe which selectively responds to the presence of hydrogen sulphide in solution. They synthesised an azido-acetophenone containing Eu(III) probe which undergoes rapid reduction in the presence of hydrogen sulphide yielding the corresponding aniline (Scheme 1.7). Modification at the *para* position, from an azide (weakly electron withdrawing) to an aniline (strongly electron donating) resulted in a 20-fold increase in Eu(III) emission when excited with 350 nm light. This is a result of improved energy transfer between the antenna chromophore and the Eu(III) centre upon reduction. Additionally, the luminescent lifetime remains mostly unchanged throughout the reaction, suggesting that the inner sphere coordination environment remains unchanged upon reduction. Therefore, the observed increase in intensity of the Eu(III) emission results from improved energy transfer from the ligand to the metal centre and is not due to inner sphere contributions such as sulphide coordination or solvent displacement at the Eu(III) centre. They also demonstrated the selectivity which is afforded by irreversible ligand modification by testing the reductive stability of the azide probe with other biologically relevant reductive species and anions, where they found the biggest and most prominent change in the presence of hydrogen sulphide.[107]

1.4.4.2 Analyte Triggered Decaging



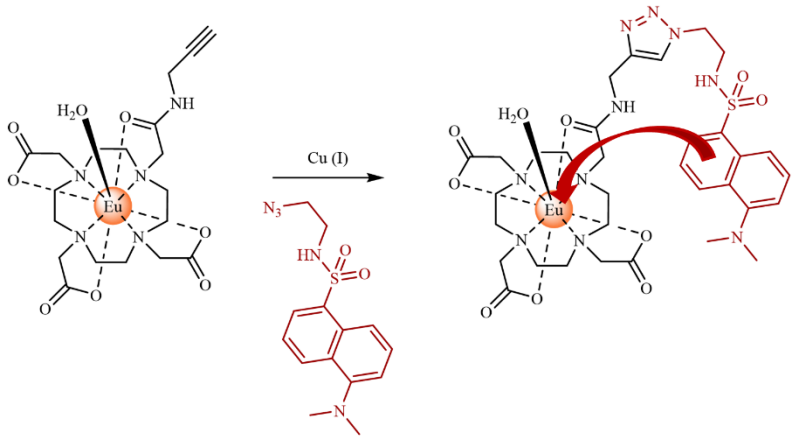
Scheme 1.8: Framework of design for a coumarin containing emissive Ln(III) probe triggered by the sensing of specific analytes.[108]

Another popular irreversible ligand modification utilises caged chromophores, where a protecting group, the cage, can be removed upon exposure to a specific analyte, in turn producing the active chromophore. These are highly selective transformations and have been demonstrated in a plethora of applications including targeted drug activation,[109] ion transport across lipid membranes[110-112] and in the development of responsive probes.[113, 114]

Borbas and co-workers designed a framework in which a kinetically stable Ln(III) complex was functionalised with a caged-coumarin (Scheme 1.8). Here, the choice of cage could be tailored to respond selectively to the presence of specific analytes including organic reductants, inorganic anions and cations and targeted enzymes. Upon release of the cage by the analyte, the ligand underwent an intramolecular ring-closing, via a transesterification, to yield the coumarin sensitiser. They developed a number of cages with different analyte triggers, specifically phenylboronic acid (hydrogen peroxide), triisopropylsilane (fluoride), allyl (Pd^{2+}) and galactose (β-galactosidase). The caged compounds were essentially non emissive when

excited at 365 nm however, upon cleavage of the cage, the emission intensity of both Eu(III) and Tb(III) complexes increased. This demonstrates the utility of an emissive lanthanide framework for the sensing of a multitude of species in solution.

1.4.4.3 *In-situ* Reactions



Scheme 1.9: A schematic describing the mechanisms underpinning a successful Eu(III) probe for sensing Cu(I) in solution, a DO3A based Eu(III) complex functionalised with a propargyl group, which can undergo the copper click reaction with azide in the presence of Cu(I). Reproduced from Hulme and co-workers.[115]

Since the development of the copper click reaction, *in-situ* functionalisation of kinetically stable Ln(III) complexes has been realised. The copper click reaction has been utilised in combination with lanthanide complexes for a variety of applications including the synthesis of luminescent complexes,[116-118] to create multimetallic arrays,[119-121] including d-f hybrid complexes,[58] sensing Cu(I) in solution,[115] appending lanthanide complexes to surfaces,[122] as a tool to measure DNA in cells[123] and in protein labelling.[124] Importantly, upon formation of the click product, the constitution of the ligand is irreversibly modified and thus the electronic properties of the ligand.

The utility of *in-situ* reactions, particularly the Cu(I) click reaction, was demonstrated by Hulme and co-workers in which the formation of a luminescent probe was generated through the Huisgen 1,3-dipolar cycloaddition reaction between a Eu(III) complex and dansyl azide, catalysed by the presence of Cu(I)-GSH (Scheme 1.9). Upon formation of the triazole in the

presence of Cu(I) the dansyl group was appended to the ligand. Dansyl groups are efficient antennas for Eu(III) emission, thus by attaching the dansyl group covalently to the ligand the pathway of sensitisation was realised. This introduction of an antenna drastically changes the ability to populate the emissive $^5D_0$ state *via* excitation at 350 nm (through the dansyl group), thus the intensity of the Eu(III) centred emission is drastically increased. This reaction is specifically catalysed in the presence of micromolar concentration of Cu(I) thus, this increase in emission is attributed to the presence of Cu(I) in solution.

Faulkner and co-workers also utilised the Cu(I) click reaction for the preparation of a pair of heterobimetallic Ln(III) complexes with interesting photophysical properties (Figure 1.10). Here, two separate and unique, kinetically inert Ln(III) complexes (one containing a propargyl group and the second containing an azide-acetophenone group) were covalently linked *via* a triazole as a result of the Cu(I) click reaction. By utilising the click reaction, the system was altered by, i) the acetophenone antenna now being conjugated to a triazole and, ii) the addition of another, different, lanthanide ion in close proximity to the first. The distance from each lanthanide, in both complexes, to the acetophenone antenna was found to dictate the luminescent properties.

The closer the Ln(III) metal centre was to the acetophenone, especially through direct coordination of the ketone, increased the emission intensity of that particular metal centre with respect to the second metal centre in the complex. It is also noted that the intensity and shape of the Eu/Yb(III) emission was dependent on the binding pocket it resided in. For the same Ln(III) metal in each binding site, the resulting fine structure in the emission spectra differed. This corresponds to the different crystal field experienced by the Ln(III) ion in each binding pocket, each pocket is octadentate with seven donors from a shared DO3A motif. However, the final coordination site differs as a result of coordination of the oxygen (from the acetophenone) in one pocket and the nitrogen (from the triazole) in the other pocket. This

example highlights that not only can irreversible modification of the antenna lead to changes in the sensitising efficiency, but also the influence of Ln(III) ions in close proximity.[119]

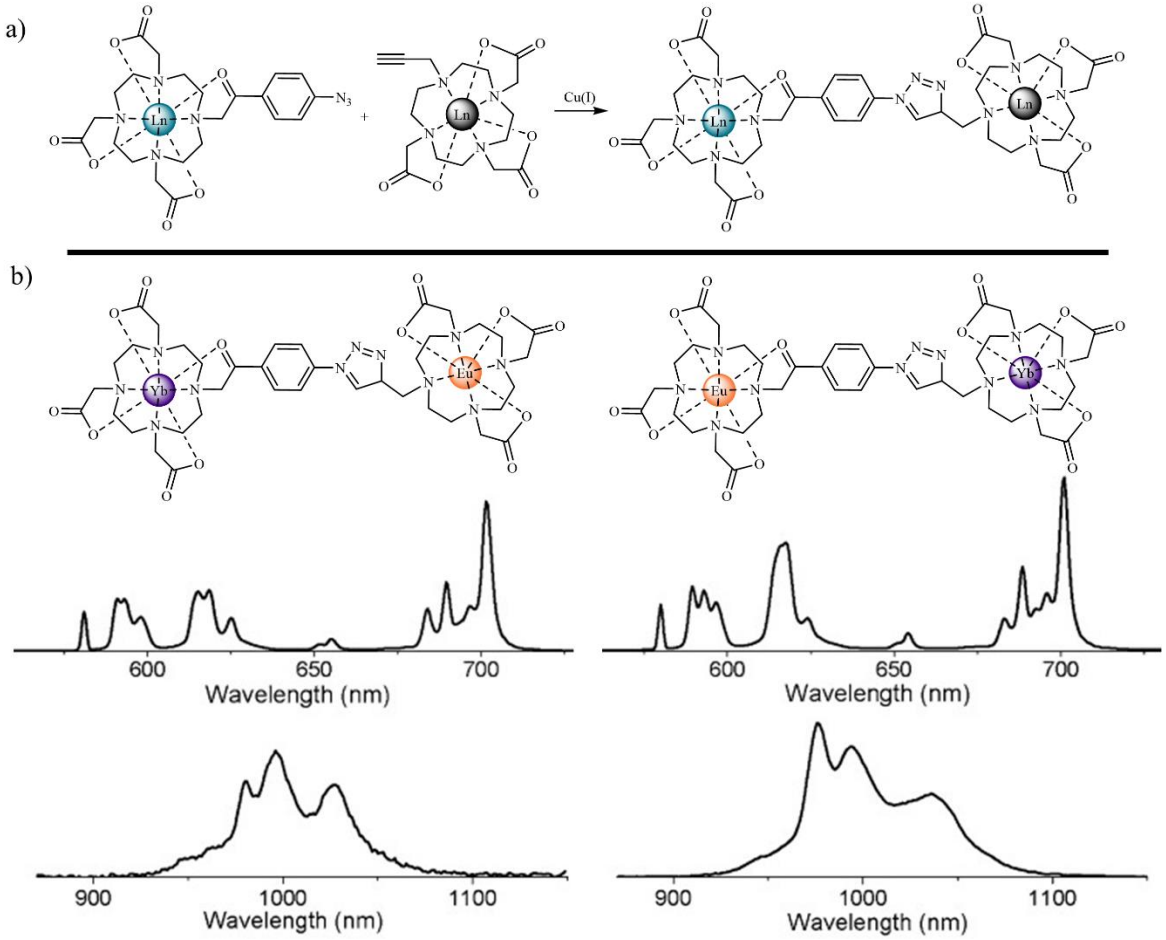


Figure 1.10: a) Synthesis to afford heterobimetallic complexes b)structure of two similar heterobimetallic complexes with the correponding Eu (III) and Yb (III) centred emission for each compound, differing by the position of the Ln (III) in each binding pocket. Reproduced from Faulkner and co-workers.[119]

1.5 Scope and Aims

The aim of this project was to investigate novel methods for the modification of Ln(III) luminescence for applications as responsive probes.

Chapter 2 describes the synthesis and optimisation of reversible photo-switchable ligands to investigate the luminescent properties of Eu(III) and Nd(III) complexes for applications in read-write optical information storage.

Chapter 3 highlights the development of binuclear lanthanide complexes as magnetic resonance and optical imaging probes for redox sensing.

Chapter 4 investigates the structure of kinetically stable Nd(III) complexes in solution, focusing on the role of inner sphere coordination (TSAP and SAP) on luminescence spectroscopy.

Chapter 5 describes the investigation of binuclear Ln(III) complexes in solution.

Chapter 6 concludes the work presented in this thesis and possible future research avenues.

Chapter 7 outlines the experimental procedures used throughout the work presented in this thesis.

1.6 References for Chapter 1

1. Bünzli, JC.G., Eliseeva, S.V. (2010). Basics of Lanthanide Photophysics. In: Hänninen, P., Härmä, H. (eds) Lanthanide Luminescence. Springer Series on Fluorescence, vol 7. Springer, Berlin, Heidelberg. https://doi.org/10.1007/4243_2010_3
2. J. C. G. Bünzli and C. Piguet, *Chem. Soc. Rev.*, 2005, **34**, 1048-1077.
3. R. Z. W.C Martin, Lucy Hagan, *Atomic Energy Levels—The Rare-Earth Elements The Spectra of Lanthanum, Cerium, Praseodymium,Neodymium, Promethium, Samarium, Europium,Gadolinium, Terbium, Dysprosium, Holmium, Erbium,Thulium, Ytterbium, and Lutetium*, Institute for basic standards, Washington D.C, 1978.
4. K. N. Raymond, D. L. Wellman, C. Sgarlata and A. P. Hill, *C. R. Chim.*, 2010, **13**, 849-852.
5. P. Pyykko, *Chem. Rev.*, 1988, **88**, 563-594.
6. J. G. Conway and B. G. Wybourne, *Phys.l Rev.*, 1963, **130**, 2325-2332.
7. D. J. Newman, *Adv. Phys.*, 1971, **20**, 197-256.
8. G. H. Dieke and H. M. Crosswhite, *Appl. Optics*, 1963, **2**, 675-686.
9. B. G. Wybourne, *Spectroscopic properties of rare earths*, Interscience Publishers, New York, 1965.
10. O. A. Blackburn, R. M. Edkins, S. Faulkner, A. M. Kenwright, D. Parker, N. J. Rogers and S. Shuvaev, *Dalton Trans*, 2016, **45**, 6782-6800.
11. B. Bleaney, *J. Mag. Reson.*, 1972, **8**, 91.
12. B. Bleaney, R. J. P. Williams, A. V. Xavier, R. B. Martin, B. A. Levine and C. M. Dobson, *J. Chem. Soc. Chem. Comm.*, 1972, 791-793.
13. M. J. Klein, *Am. J. Phys.*, 1952, **20**, 65-71.
14. H. Bethe, *Z. Phys.*, 1930, **60**, 218-233.
15. B. R. Judd, *Phys. Rev.*, 1962, **127**, 750-761.
16. G. S. Ofelt, *J. Chem. Phys.*, 1962, **37**, 511-520.
17. W. T. Carnall, P. R. Fields and K. Rajnak, *J. Chem. Phys.*, 1968, **49**, 4424-4442.

18. W. T. Carnall, P. R. Fields and K. Rajnak, *J. Chem. Phys.*, 1968, **49**, 4450-4455.
19. W. T. Carnall, P. R. Fields and K. Rajnak, *J. Chem. Phys.* 1968, **49**, 4412-&.
20. W. T. Carnall, P. R. Fields and K. Rajnak, *J. Chem. Phys.*, 1968, **49**, 4443-&.
21. W. T. Carnall, P. R. Fields and K. Rajnak, *J. Chem. Phys.*, 1968, **49**, 4450-&.
22. W. T. Carnall, P. R. Fields and K. Rajnak, *J. Chem. Phys.*, 1968, **49**, 4447-&.
23. G. Stein and E. Würzberg, *J. Chem. Phys.*, 1975, **62**, 208-213.
24. H. L. Yin, P. J. Carroll, J. M. Anna and E. J. Schelter, *J. Am. Chem. Soc.*, 2015, **137**, 9234-9237.
25. Y. Wang, G. Sun, Q. Su, Y. Xie, F. Xing, H. Zhang and L. Sun, *Chem. Eur. J.*, 2024, **30**.
26. R. Piramidowicz, I. Pracka, W. Wolinski and M. Malinowski, *J. Phys. Condens. Matter*, 2000, **12**, 709-718.
27. R. S. Yadav, R. K. Verma, A. Bahadur and S. B. Rai, *Spectrochim. Acta A*, 2015, **137**, 357-362.
28. W. Wang, Y. Xue, J. Dong, C. Zhang, J. Liu, W. Hou, Q. Wang, X. Xu, H. Tang, H. Lin, D. Li, Z. Wang and J. Xu, *Opt. Mater. Express*, 2023, **13**, 1267.
29. L. D. Merkle, Z. Fleischman, E. E. Brown, J. L. Allen, U. Hommerich and M. Dubinskii, *Opt. Express*, 2021, **29**, 39001.
30. P. Boutinaud, R. Mahiou, N. Martin and M. Malinowski, *J. Lumin.*, 1997, **72-4**, 809-811.
31. R. Balda, M. Sanz, A. Mendioroz, J. Fernández, L. S. Griscom and J. L. Adam, *Phys. Rev. B*, 2001, **64**.
32. C.-K. Duan, P. A. Tanner, V. N. Makhov and M. Kirm, *Phys. Rev. B*, 2007, **75**.
33. X. J. Zhou, X. Q. Zhao, C. S. K. Mak, L. Li, Q. X. Li and P. A. Tanner, *Opt. Mater.*, 2014, **37**, 24-27.
34. M. Yin, Y. F. Li, N. Dong, V. N. Makhov, N. M. Khaidukov and J. C. Krupa, *J. Alloys Compd.*, 2003, **353**, 95-101.
35. U. Vetter, J. B. Gruber, A. S. Nijjar, B. Zandi, G. Öhl, U. Wahl, B. De Vries, H. Hofsäss, M. Dietrich and I. Collaboration, *Phys. Rev. B*, 2006, **74**.
36. N. Kofod, R. Arppe-Tabbara and T. J. Sorensen, *J. Phys. Chem. A*, 2019, **123**, 2734-2744.
37. J. L. Adam, A. D. Docq and J. Lucas, *J. Solid State Chem.*, 1988, **75**, 403-412.
38. E. Erol, O. Kıbrıslı, N. Vahedigharehchopogh, M. Çelikbilek Ersundu and A. E. Ersundu, *Phys. Chem. Chem. Phys.*, 2020, **22**, 25963-25972.
39. S. Balaji, G. Gupta, K. Biswas, D. Ghosh and K. Annapurna, *Sci. Rep.*, 2016, **6**, 29203.
40. B. Suresh, Y. Zhydachevskii, M. G. Brik, A. Suchocki, M. S. Reddy, M. Piasecki and N. Veeraiah, *J. Alloys Compd.*, 2016, **683**, 114-122.
41. A. Kumari and V. K. Rai, *Mater. Res. Bull.*, 2015, **72**, 168-175.
42. M. J. Lo Faro, A. A. Leonardi, F. Priolo, B. Fazio, M. Miritello and A. Irrera, *Sci. Rep.*, 2020, **10**.
43. L. A. Jacob, S. Sisira, K. P. Mani, K. Thomas, D. Alexander, P. R. Biju, N. V. Unnikrishnan and C. Joseph, *SN Appl. Sci.*, 2020, **2**.
44. X. Wang, X. Yan and C. Kan, *J. Mater. Chem.*, 2011, **21**, 4251.
45. M. N. Azlan, Y. Azlina, H. R. Shaari, S. N. Nazrin, N. M. Al-Hada, I. Boukhris, S. A. Umar, M. H. M. Zaid, R. Hisam, S. M. Iskandar and B. K. Kenzhaliyev, *J. Mater. Sci.: Mater. Electron.*, 2021, **32**, 24415-24428.
46. M. S. Meijer, P. A. Rojas-Gutierrez, D. Busko, I. A. Howard, F. Frenzel, C. Würth, U. Resch-Genger, B. S. Richards, A. Turshatov, J. A. Capobianco and S. Bonnet, *Phys. Chem. Chem. Phys.*, 2018, **20**, 22556-22562.

47. D. Gao, X. Zhang, H. Zheng, P. Shi, L. Li and Y. Ling, *Dalton Trans.*, 2013, **42**, 1834-1841.
48. L. Singh and R. Singh, *Chem. Pap.*, 2014, **68**.
49. J. H. Van Vleck, *Am. J. Phys. Chem.*, 1937, **41**, 67-80.
50. O. Laporte and W. F. Meggers, *J. Opt. Soc. Am. Rev. Sci.*, 1925, **11**, 459-463.
51. A. J. Amoroso and S. J. A. Pope, *Chem. Soc. Rev.*, 2015, **44**, 4723-4742.
52. S. I. Weissman, *J. Chem. Phys.*, 1942, **10**, 214-217.
53. A. K. R. Junker, L. R. Hill, A. L. Thompson, S. Faulkner and T. J. Sorensen, *Dalton Trans.*, 2018, **47**, 4794-4803.
54. L. D. Carlos, R. A. S. Ferreira, V. De Zea Bermudez, B. Julián-López and P. Escribano, *Chem. Soc. Rev.*, 2011, **40**, 536-549.
55. U. A. Bawane, A. R. Kadam, A. Nande and S. J. Dhoble, *J. Phys.: Conf. Ser.*, 2021, **1913**, 012030.
56. R. C. Knighton, J. M. Beames and S. J. A. Pope, *Inorg. Chem.*, 2023, **62**, 19446-19456.
57. S. J. A. Pope, B. J. Coe, S. Faulkner, E. V. Bichenkova, X. Yu and K. T. Douglas, *J. Am. Chem. Soc.*, 2004, **126**, 9490-9491.
58. M. Tropiano, C. J. Record, E. Morris, H. S. Rai, C. Allain and S. Faulkner, *Organometallics*, 2012, **31**, 5673-5676.
59. Y. Hasegawa, Y. Kitagawa and T. Nakanishi, *NPG Asia Mater.*, 2018, **10**, 52-70.
60. T. Forster, *Naturwissenschaften*, 1946, **33**, 166-175.
61. T. Főrster, *Discuss. Faraday Soc.*, 1959, **27**, 7-17.
62. T. FöRster, *J. Biomed. Opt.*, 2012, **17**, 011002.
63. D. L. Dexter, *J. Chem. Phys.*, 1953, **21**, 836-850.
64. A. Aebischer, F. Gumy and J.-C. G. Bünzli, *Phys. Chem. Chem. Phys.*, 2009, **11**, 1346.
65. N. B. D. Lima, S. M. C. Gonçalves, S. A. Júnior and A. M. Simas, *Sci. Rep.*, 2013, **3**.
66. A. Beeby, I. M. Clarkson, R. S. Dickins, S. Faulkner, D. Parker, L. Royle, A. S. de Sousa, J. A. G. Williams and M. Woods, *J. Chem. Soc. Perkin Trans. 2*, 1999, DOI: DOI 10.1039/a808692c, 493-503.
67. W. D. Horrocks and D. R. Sudnick, *J. Am. Chem. Soc.*, 1979, **101**, 334-340.
68. R. M. Supkowski and W. D. Horrocks, *Inorg. Chim. Acta*, 2002, **340**, 44-48.
69. S. Shuvaev, M. Starck and D. Parker, *Chem. Eur. J.*, 2017, **23**, 9974-9989.
70. E. Toth and E. Brucher, *Inorg. Chim. Acta*, 1994, **221**, 165-167.
71. S. E. Bodman and S. J. Butler, *Chem. Sci.*, 2021, **12**, 2716-2734.
72. M. S. Thomsen, P. R. Nawrocki, N. Kofod and T. J. Sorensen, *Eur. J. Inorg. Chem.*, 2022, **2022**.
73. D. Parker, E. A. Suturina, I. Kuprov and N. F. Chilton, *Acc. Chem. Res.*, 2020, **53**, 1520-1534.
74. N. M. Shavaleev, S. V. Eliseeva, R. Scopelliti and J. C. G. Bünzli, *Inorg. Chem.*, 2015, **54**, 9166-9173.
75. V. R. M. Nielsen, B. Le Guennic and T. J. Sorensen, *J. Phys. Chem. A*, 2024, **128**, 28, 5740-5751.
76. L. G. Nielsen and T. J. Sorensen, *Inorg. Chem.*, 2020, **59**, 94-105.
77. S. Aime, M. Botta and G. Ermondi, *Inorg. Chem.*, 1992, **31**, 4291-4299.
78. S. Aime, A. Barge, J. I. Bruce, M. Botta, J. A. K. Howard, J. M. Moloney, D. Parker, A. S. de Sousa and M. Woods, *J. Am. Chem. Soc.*, 1999, **121**, 5762-5771.
79. G. Tircso, B. C. Webber, B. E. Kucera, V. G. Young and M. Woods, *Inorg. Chem.*, 2011, **50**, 7966-7979.
80. J. Blahut, P. Hermann, Z. Tošner and C. Platas-Iglesias, *Phys. Chem. Chem. Phys.*, 2017, **19**, 26662-26671.

81. M. Storm Thomsen, H. O. B. Andersen and T. J. Sørensen, *Dalton Trans.*, 2022, **51**, 14118-14124.
82. D. G. Smith, B. K. Mcmahon, R. Pal and D. Parker, *Chem. Commun.*, 2012, **48**, 8520.
83. B. K. Mcmahon, R. Pal and D. Parker, *Chem. Commun.*, 2013, **49**, 5363.
84. R. Pal, D. Parker and L. C. Costello, *Org. Biomol. Chem.*, 2009, **7**, 1525.
85. S. E. Bodman, C. Breen, S. Kirkland, S. Wheeler, E. Robertson, F. Plasser and S. J. Butler, *Chem. Sci.*, 2022, **13**, 3386-3394.
86. S. R. Kiraev, R. R. Weber, J. A. L. Wells, A. Orthaber, D. Kovacs and K. E. Borbas, *Anal. Sens.*, 2022, **2**.
87. J. D. Rinehart and J. R. Long, *Chem. Sci.*, 2011, **2**, 2078.
88. O. A. Blackburn, J. D. Routledge, L. B. Jennings, N. H. Rees, A. M. Kenwright, P. D. Beer and S. Faulkner, *Dalton Trans.*, 2016, **45**, 3070-3077.
89. O. A. Blackburn, N. F. Chilton, K. Keller, C. E. Tait, W. K. Myers, E. J. L. McInnes, A. M. Kenwright, P. D. Beer, C. R. Timmel and S. Faulkner, *Angew. Chem. Int. Ed.*, 2015, **54**, 10783-10786.
90. O. A. Blackburn, A. M. Kenwright, P. D. Beer and S. Faulkner, *Dalton Trans.*, 2015, **44**, 19509-19517.
91. S. E. Page, K. T. Wilke and V. C. Pierre, *Chem. Commun.*, 2010, **46**, 2423.
92. S. Comby, S. A. Tuck, L. K. Truman, O. Kotova and T. Gunnlaugsson, *Inorg. Chem.*, 2012, **51**, 10158-10168.
93. O. Kotova, S. Comby and T. Gunnlaugsson, *Chem. Commun.*, 2011, **47**, 6810.
94. J. A. Tilney, T. J. Sørensen, B. P. Burton-Pye and S. Faulkner, *Dalton Trans.*, 2011, **40**, 12063.
95. B. K. Mcmahon and T. Gunnlaugsson, *Tetrahedron Lett.*, 2010, **51**, 5406-5410.
96. E. A. Weitz and V. C. Pierre, *Chem. Commun.*, 2011, **47**, 541-543.
97. S. J. A. Pope and R. H. Laye, *Dalton Trans.*, 2006, DOI: 10.1039/b605837j, 3108-3113.
98. E. A. Weitz, J. Y. Chang, A. H. Rosenfield, E. A. Morrow and V. C. Pierre, *Chem. Sci.*, 2013, **4**, 4052.
99. D. Parker, *Coord. Chem. Rev.*, 2000, **205**, 109-130.
100. D. Parker, K. Senanayake and J. A. Gareth Williams, *Chem. Commun.*, 1997, DOI: 10.1039/a704318j, 1777-1778.
101. D. Parker, P. K. Senanayake and J. A. Gareth Williams, *J. Chem. Soc. Perkin Trans. 2*, 1998, DOI: 10.1039/a801270i, 2129-2140.
102. Z. Yang, J. Cao, Y. He, J. H. Yang, T. Kim, X. Peng and J. S. Kim, *Chem. Soc. Rev.*, 2014, **43**, 4563-4601.
103. M. K. Kuimova, *Phys. Chem. Chem. Phys*, 2012, **14**, 12671.
104. A. T. Bui, A. Grichine, A. Duperray, P. Lidon, F. Riobé, C. Andraud and O. Maury, *J. Am. Chem. Soc.*, 2017, **139**, 7693-7696.
105. D. Parker, J. D. Fradgley and K.-L. Wong, *Chem. Soc. Rev.*, 2021, **50**, 8193-8213.
106. M. C. Heffern, L. M. Matosziuk and T. J. Meade, *Chem. Rev.*, 2014, **114**, 4496-4539.
107. M. Tropiano and S. Faulkner, *Chem. Commun.*, 2014, **50**, 4696-4698.
108. E. Pershagen, J. Nordholm and K. E. Borbas, *J. Am. Chem. Soc.*, 2012, **134**, 9832-9835.
109. S. Davies, B. J. Stenton and G. J. L. Bernardes, *Chimia.*, 2018, **72**, 771.
110. S. B. Salunke, J. A. Malla and P. Talukdar, *Angew. Chem. Int. Ed.*, 2019, **58**, 5354-5358.
111. S. A. Gartland, T. G. Johnson, E. Walkley and M. J. Langton, *Angew. Chem. Int. Ed.*, 2023, **62**.
112. M. Ahmad, S. A. Gartland and M. J. Langton, *Angew. Chem. Int. Ed.*, 2023, **62**.
113. H. Q. Zhao, Y. L. He, Y. T. Lo, H. Z. Song and J. Z. Lu, *Trac. Trend Anal. Chem.*, 2023, **169**.

114. K. K. W. Lo, *Acc. Chem. Res.*, 2020, **53**, 32-44.
115. R. F. H. Viguier and A. N. Hulme, *J. Am. Chem. Soc.*, 2006, **128**, 11370-11371.
116. G. J. Stasiuk and M. P. Lowe, *Dalton Trans.*, 2009, DOI: 10.1039/b918891f, 9725.
117. N. Wang, J. W. Wang, D. Zhao, S. K. Mellerup, T. Peng, H. B. Wang and S. N. Wang, *Inorg. Chem.*, 2018, **57**, 10040-10049.
118. H. Akiba, J. Sumaoka, K. Tsumoto and M. Komiyama, *Anal. Chem.*, 2015, **87**, 3834-3840.
119. M. Tropiano, A. M. Kenwright and S. Faulkner, *Chem. Eur. J.*, 2015, **21**, 5697-5699.
120. C. Szíjjártó, E. Pershagen and K. E. Borbas, *Dalton Trans.*, 2012, **41**, 7660.
121. T. J. Sorensen and S. Faulkner, *Acc. Chem. Res.*, 2018, **51**, 2493-2501.
122. S. N. A. Jenie, S. Pace, B. Sciacca, R. D. Brooks, S. E. Plush and N. H. Voelcker, *ACS Appl. Mater. Inter.*, 2014, **6**, 12012-12021.
123. J. Shaklee, K. Srivastava, H. Brown, E. A. Arriaga, V. C. Pierre and J. H. Van Berlo, *Sci. Rep.*, 2018, **8**.
124. N. Candelon, N. D. Hădade, M. Matache, J.-L. Canet, F. Cisnetti, D. P. Funeriu, L. Nauton and A. Gautier, *Chem. Commun.*, 2013, **49**, 9206.

Chapter 2

Photoswitchable Luminescent Lanthanide Complexes

2.1 Introduction

The work in this chapter highlights a newly developed, innovative method of reversibly modifying ligand constitution, through the use of organic photoswitches, investigating the influence of photoisomerisation on the Ln(III) centred luminescence. This has important applications in the field of optical information storage. The focus of this chapter will include, the design, synthesis, photophysical properties and applications of a series of novel photoswitchable lanthanide complexes. The work in this chapter has already been published as a full paper and can be found here: ***Phys. Chem. Chem. Phys.***, 2024, **26**, 18683-18691.

2.1.1 Optical Information Storage

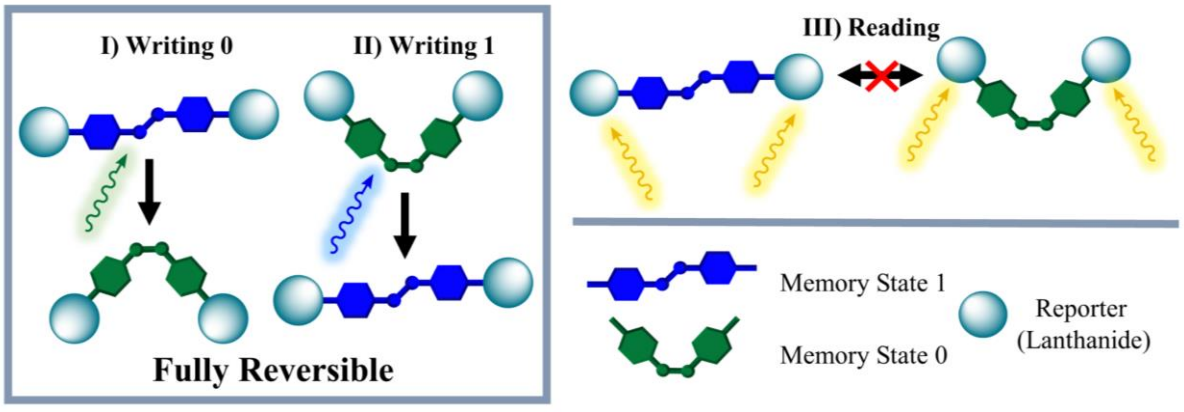


Figure 2.1: Design of an optical information storage system, where two photoswitchable memory states can be written by orthogonal wavelengths of light in a fully reversible manner, steps (I) and (II). Step (III) describes the reading of this optical data via orthogonal emission of a lanthanide, which itself does not perturb the system state.

Optical information storage requires light to both read and write data for storage in optical media such as CDs and DVDs. Efficient systems require exceptional photocontrol with

multiple wavelengths of light, to achieve a binary system. One wavelength of light is required to "write" the optical information by changing the system's state *via* a photochemical process. A second wavelength of light allows for this optical information to be "read". For effective, reversible read and write steps, these processes must be orthogonal and reversible.[125, 126]

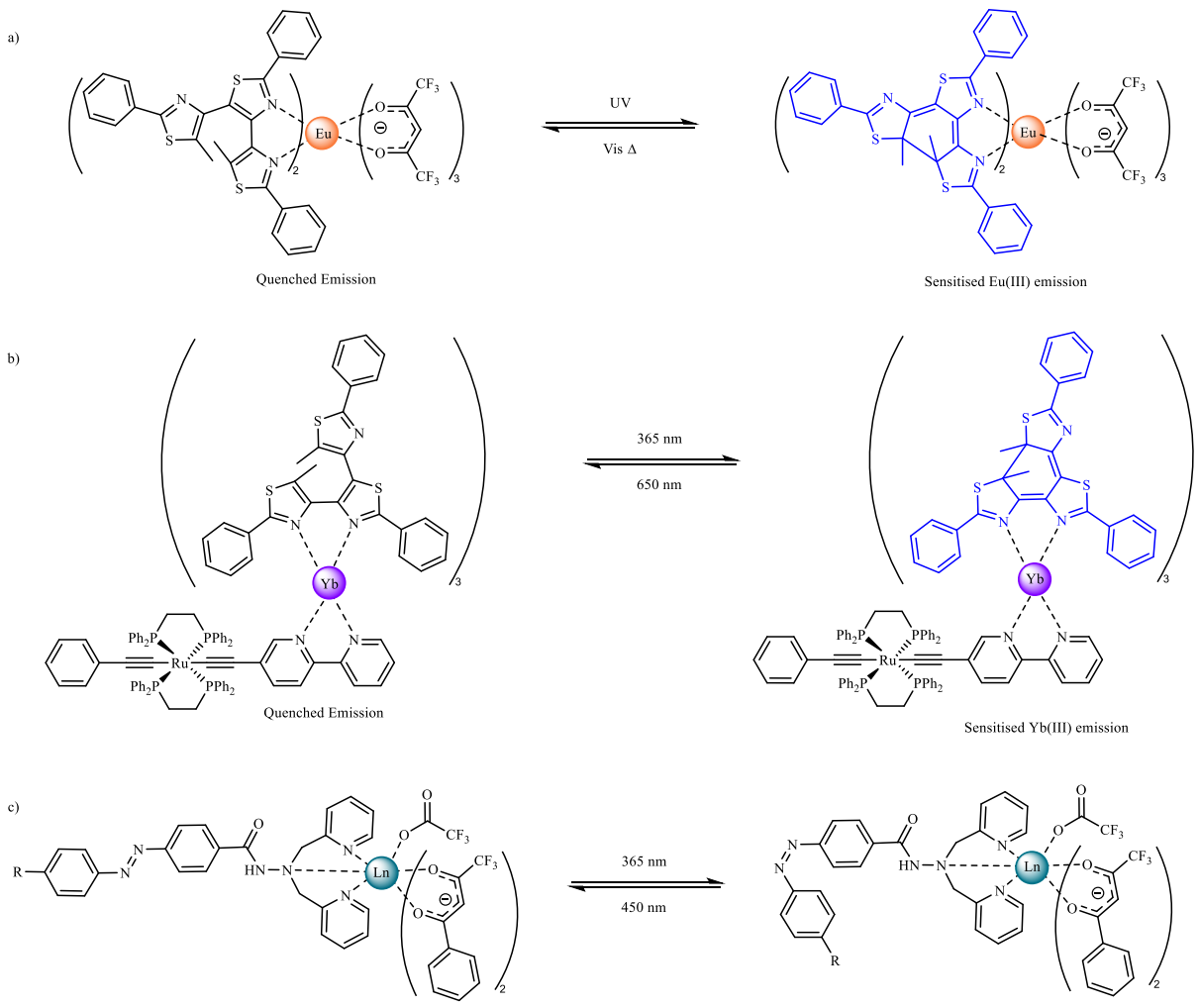
While organic fluorophores are commonly utilised in imaging applications, the broad absorbance bands of organic photoswitches and fluorophores often overlap, and as a result, reading the data without perturbing the system's state is difficult to achieve.[127] One solution to this challenge is to employ lanthanide complexes as the emissive moiety, with a judicious choice of ligand enabling its decoupling from the lanthanide luminescence (Figure 2.1).[2] Furthermore, the narrow bandwidth of lanthanide emission also allows for insight into molecular structure,[17-20, 22] while long emission lifetimes may be exploited in time-gated imaging.[1]

2.1.2 Photoswitchable Lanthanide Complexes in the Literature

Despite the numerous examples of photoswitchable systems and materials,[128-135] there are only a handful of examples where these have been incorporated into systems with luminescent lanthanide complexes.[126, 136-150]

Diarylethene (DTE) photoswitches can undergo a reversible ring-closing/opening upon irradiation with light, with good photochromic reversibility, excellent thermal stability and resistance to fatigue upon multiple cycles.[151] Nakagawa and co-workers designed and investigated a series of Ln(III) complexes containing DTE photoswitches. In these systems, the DTE ligand is directly coordinated in a bidentate manner, from two thiazoles to the Eu(III) metal centre (Scheme 2.1a). Upon irradiation with 365 nm light, the DTE ligand undergoes a photoinduced cyclisation, producing a coloured complex (closed form), in which the Eu(III) emission is quenched relative to the open form when excited through the DTE antenna. Eu(III)

emission could still be observed, albeit with lower intensity, for both forms upon direct excitation into the $^7F_0 \rightarrow {}^5L_6$ transition. Notably, the splitting of the hypersensitive $^5D_0 \rightarrow {}^7F_2$ transition remained unchanged upon photoswitching. This lack of change in crystal field splitting suggests that the symmetry and geometry of the Eu(III) centre is retained upon reversible cyclisation of the ligand, this was further supported by the luminescence lifetimes which were also unchanged upon photoisomerisation. Interestingly, they did observe a change in intensity of the Eu(III) transitions between the open and closed form, due to the availability of non-radiative decay pathways in each isomer.[141, 142, 152]

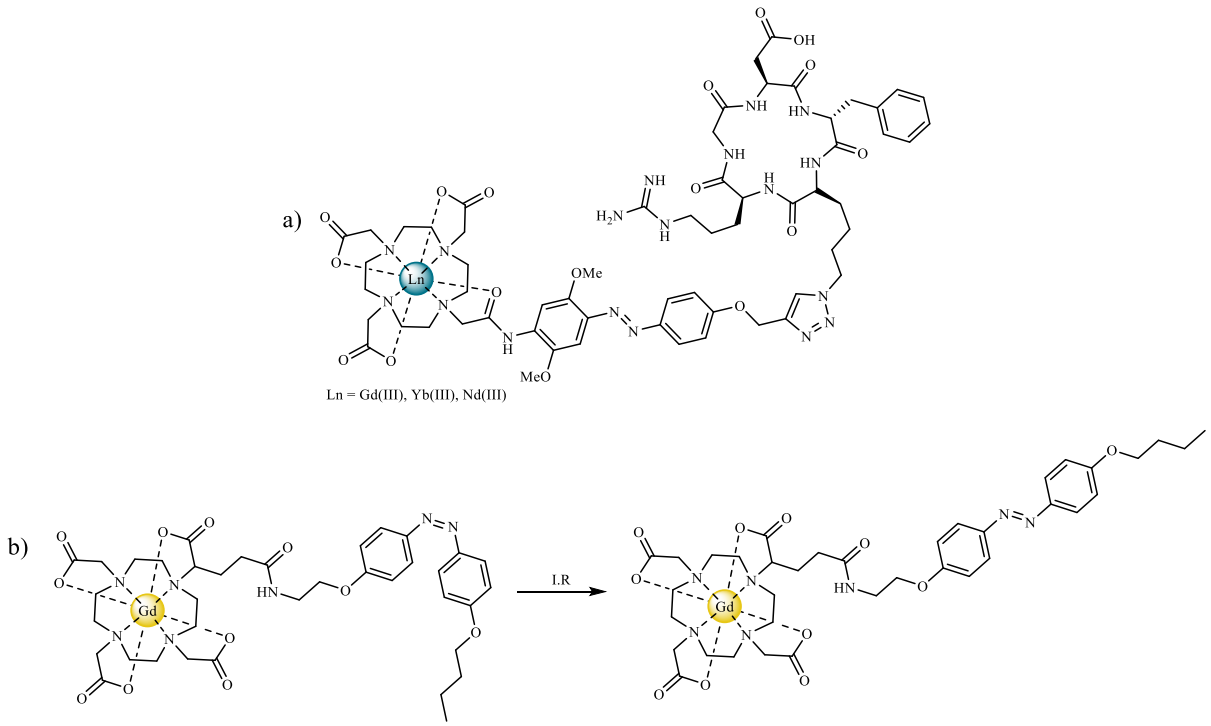


Scheme 2.1: Photoswitchable Ln(III) systems reported in the literature a) diarylethene (DTE) Eu(III) complex[126, 141, 142] b) d-f hybrid system based on a DTE photoswitch, ruthenium sensitiser and Yb(III) emissive centre,[139, 140, 147, 153] c) Ln(III)containing an azobenzene photoswitch.[144, 147]

Norel and co-workers have developed a system in which the DTE photoswitch is coupled to a d-f hybrid system.[153] In this complex, a Yb(III) metal centre is flanked by three bidentate DTE ligands, and a single bipyridine is in conjugation with the ruthenium centre (Scheme 2.1b). In the open form, they observed a MLCT band originating from the ruthenium centre, upon excitation into this transition (λ_{ex} = 450 nm), the $^2F_{5/2} \rightarrow {}^2F_{7/2}$ transition of the Yb(III) centre was observed, confirming the ruthenium complex acts as an efficient sensitiser for Yb(III) emission. However, subsequent irradiation with 350 nm light to access the closed confirmation revealed no observable Yb(III) centred emission. Impressively, the Yb(III) emission could be recovered upon photoisomerisation to the open form (λ_{irr} = 650 nm), thus demonstrating a near-infrared (NIR) emissive photoswitchable system. Unfortunately, the applications of this system are limited by the lack of kinetic stability and reduced contrast between both states as a result of low photostationary state (PSS) distributions (~ 75%). [137-140]

Azobenzenes are a class of photoswitch in which reversible photoisomerisation around the N=N interconverts between the *trans*- (*E*) and the *cis*- (*Z*) form. This isomerisation results in a change in dipole, geometry and photochromic properties.[154] Tang and co-workers first incorporated an azobenzene photoswitch into a Ln(III) complex (Scheme 2.1c). They developed a tridentate ligand which coordinates to the Ln(III) metal centre through three flanking nitrogen atoms, the second nitrogen is in direct conjugation to the azobenzene *via* an amide bond. Upon coordination to Ln(III) metal ions, the PSS distribution and fatigue resistance of the azobenzene were found to increase, as a result of the communication between the Ln(III) and the azobenzene through the conjugated system. Even with this improvement of the PSS distributions upon coordination to a Ln(III) centre, the maximum PSS achieved was 75% due to the spectral overlap between the *E* and *Z* isomers. In an attempt to increase the PSS distribution of the system further, they modified the azobenzene with the addition of an electron-donating group in the *para*-position (R= $N(CH_3)_2$), in the hope of separating both the

n → π* and π → π* transitions of each isomer. Unfortunately, they found the modified azobenzene to be unstable to UV light. For both Eu(III) analogues where R = H and R = $N(CH_3)_2$, Eu(III) centred emission was observed upon excitation into the sensitising *β*-diketonate. However, they observed no Eu(III) emission resulting from excitation into the azobenzene.[144, 147]



Scheme 2.2: Kinetically stable Ln(III) complexes containing an azobenzene.[148, 149]

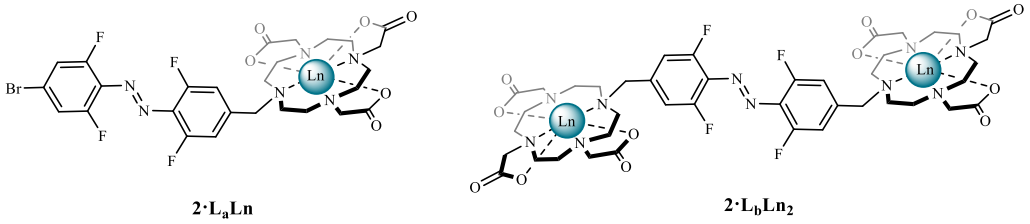
In the literature, there are only two reports of kinetically stable lanthanide complexes containing an azobenzene photoswitch (Scheme 2.2). One example, by Petoud and co-workers, is the development of NIR emitting lanthanide(III) complexes as prototypes of optical imaging agents with peptide targeting ability (Scheme 2.2a).[148] In this example, they utilised the azobenzene as a functional handle in which a targeting peptide can be attached for drug delivery and cancer imaging. They also suggest that the azobenzene can act as a sensitiser, for the emission of Yb(III) and Nd(III). The azobenzene in this example was not optimised for use as a photoswitch, and no details were supplied on the photoswitching ability of this complex.

Additionally, Bort and co-workers developed a kinetically stable, azobenzene-containing Gd(III) complex (Scheme 2.2b).[149] Their aim was to develop a system in which the cytotoxic effects elicited by the isomerisation of the azobenzenes,[135, 155-158] could be triggered upon photoisomerisation with an energy source with deeper tissue penetration, which addresses the limitations associated with UV/visible light as a stimulus in clinical settings. They postulated that ionising radiation could be used to photoswitch the azobenzene, if it was coupled to a moiety that interacts well with high-energy photons. For this reason, Gd(III) was chosen as a photosensitiser. Upon interaction with ionising radiation, Gd(III) releases lower energy photons. The low energy photons then triggered the $Z \rightarrow E$ isomerisation of the azobenzene. When this system was applied in cellular studies, the complex was found to accumulate in the membrane, where upon exposure to ionising radiation, the isomerisation occurred and the membrane was disrupted, leading to cell death. This is an interesting example where the Ln(III) complex acts as the photosensitizer for the isomerisation; this is the opposite as described by Petoud's system. However, until now, there are no examples of kinetically stable Ln(III) complexes which are optimised to achieve good PSS distributions and visible light isomerisation. Additionally, it is crucial to understand the influence of photoswitching on the optical properties of the luminescent Ln(III) within the complex.

2.2 Design of Novel Photoswitchable Lanthanide Complexes

The orthogonality of photocontrol underpins the utility of a photoswitchable lanthanide complex for applications in optical information storage. Therefore, the choice of the emissive Ln(III) ion, the nature of the photoswitchable ligand and the electronic communication between the two are integral to the functionality of the system. Regarding the choice of emissive lanthanides, Eu(III) has relatively high quantum yields, long luminescent lifetimes (ms) and emits in the red region, making it easy to detect using conventional spectrometers or

fluorescence microscopes.[72, 159-161] However, Eu(III) suffers from low molar absorption coefficients and absorbs well in the UV/blue region, which can result in unwanted spectral overlap with organic ligands and an increased likelihood of back energy transfer.[162] Neodymium(III) complexes, on the other hand, have higher molar absorption coefficients and absorb light across a wider range of UV, visible and NIR wavelengths, albeit with shorter (ns) luminescent lifetimes and low quantum yields. Furthermore, the low-lying excited states of Nd(III) inhibit back energy transfer.[3, 163-165] To ensure kinetic stability in this work, the Ln(III) cations were coordinated within a macrocyclic DO3A framework, in which the free arm was functionalised with a photoswitchable moiety.[58, 119, 166, 167]



Scheme 2.3: Novel kinetically stable ortho-fluoroazobenzene containing Ln(III) complexes synthesised and investigated in this work.

Azobenzene photoswitches are particularly amenable to functionalisation and display a significant change in geometry and photophysical properties upon reversible isomerisation between the *E* and *Z* isomers. Thus, they are promising photoswitches for the development of responsive materials.[168] *Ortho*-fluoro functionalisation in particular leads to improved photoswitching properties over the parent azobenzene.[169-171] In the *Z* isomer, the repulsive interactions between the nitrogen lone pairs and the *ortho* substituents destabilise the n orbital and thus red-shift the n→π* transition, enabling visible light to be used to control the photochemical isomerisation. This destabilisation is reduced in the *E* isomer, enhancing the separation between the transitions of the isomers and improving PSS distributions. Notably, the introduction of fluorine in the *ortho* positions of the azobenzene stabilises the *Z* isomer enabling thermal half-lives of up to 2 years.[172-174]

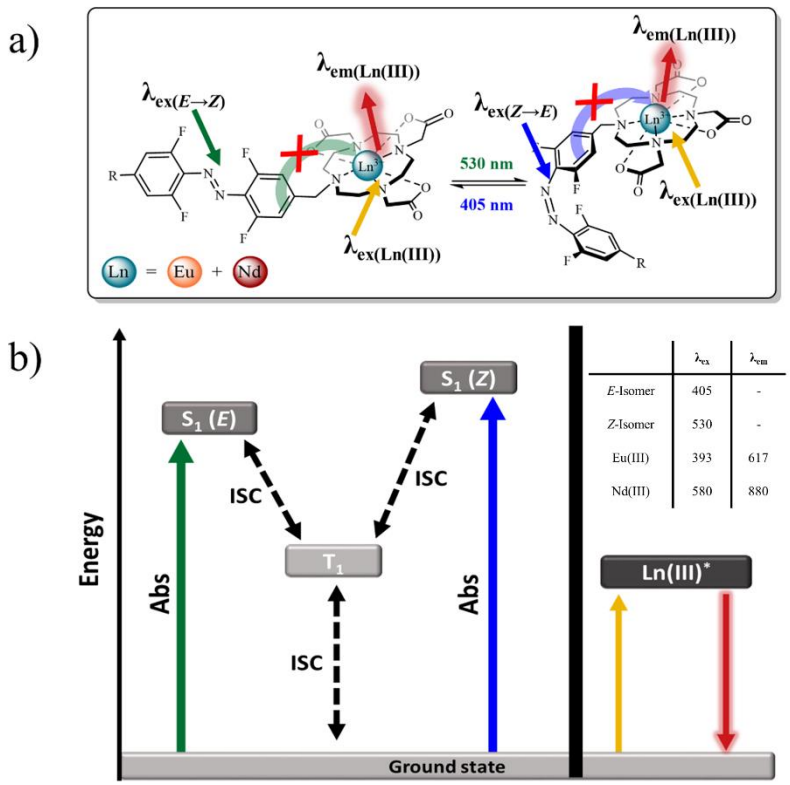


Figure 2.2: a) schematic to describe the orthogonal photocontrol of ***2·L$_a$Ln*** *and* ***2·L$_b$Ln$_2$****, using visible and NIR light b) Jablonski diagram to represent the important energy pathways for orthogonal control of both the photoswitchable azobenzene ligand and the Ln(III) luminescence.*

The photoswitchable lanthanide complexes prepared and studied in this chapter are shown in Scheme 2.3. This system combines the tetra-*ortho*-fluoroazobenzene and kinetically stable DO3A macrocycle in the design of both mono-/binuclear Ln(III) complexes. In summary, this system can be photocontrolled with four orthogonal wavelengths of light, dependent on the choice of Ln(III) cation (Figure 2.2a). The tetra-*ortho*-fluoroazobenzene is efficiently photoisomerised using orthogonal visible light wavelengths of 405 nm ($Z \rightarrow E$) and 530 nm ($E \rightarrow Z$). The Eu(III) and Nd(III) complexes are directly excited with violet light and yellow light, respectively, resulting in the emission of red light from europium(III) and NIR light from neodymium(III). Figure 2.2b describes the dominating pathways required for orthogonal control of the Ln(III) complexes for applications in optical information storage.

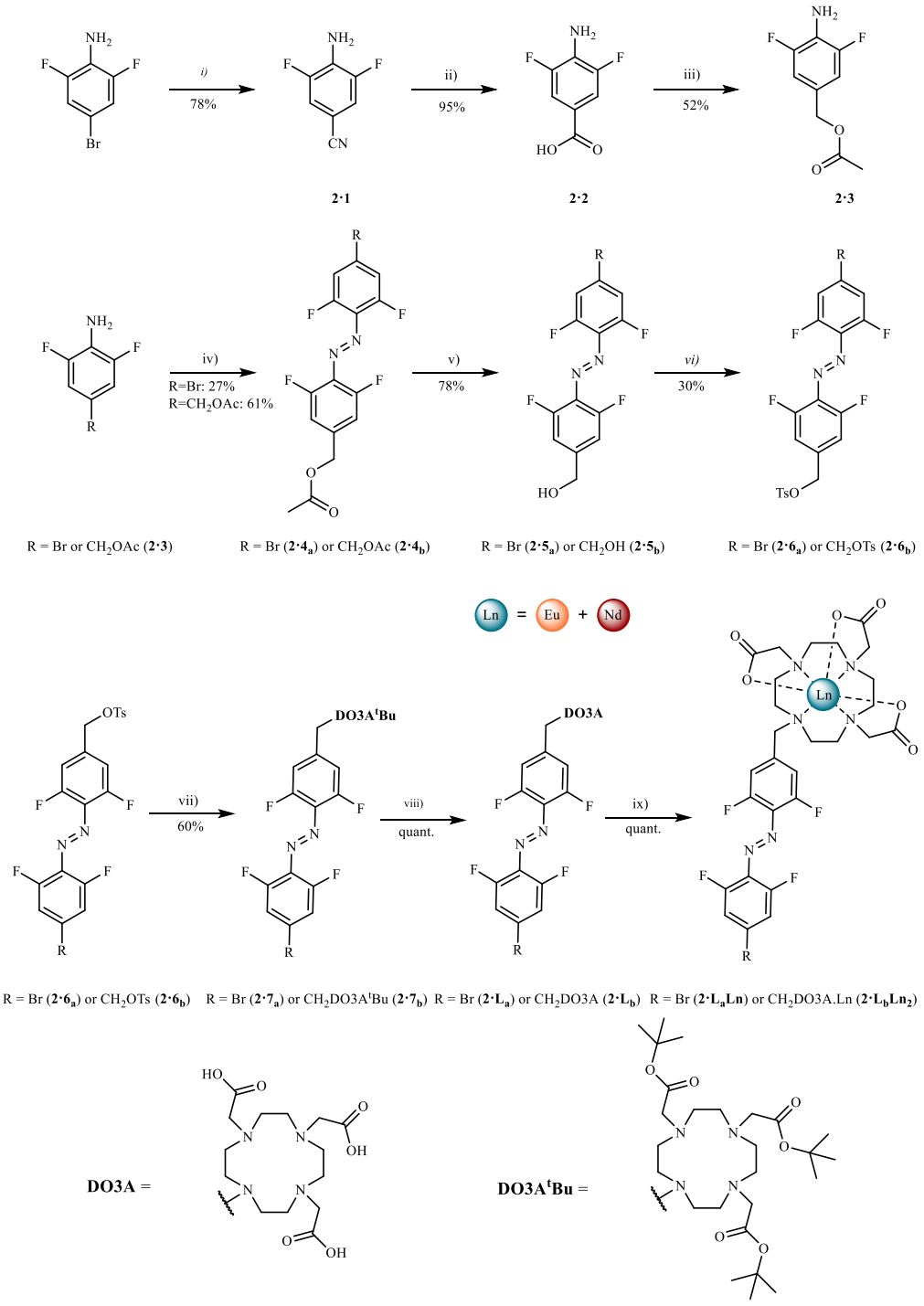
2.3 Synthesis

The synthetic route to access **2·L$_a$Ln** and **2·L$_b$Ln$_2$** is shown in Scheme 2.4. Full experimental details and characterisation can be found in **Chapter 7**.

Firstly, experimental attempts concentrated on the synthesis of the azobenzene core for both the symmetric and asymmetric ligands. Both required the common intermediate **2·3**, which was synthesised from commercially available 4-bromo-2,6-difluoroaniline in four steps.[168] This involved the initial cyanation of 4-bromo-2,6-difluoroaniline to access compound **2·1**, followed by hydrolysis of the cyanide group to yield the *para*-carboxylate **2·2** in good yields. The carboxylate group was subsequently reduced with lithium aluminium hydride, to the corresponding alcohol, which was immediately protected as an acetic acid ester, yielding **2·3**. Importantly, the acetic acid ester protection of the *para*-methanol group allowed for the subsequent azo-coupling reactions to proceed successfully.

The symmetric azobenzene, **2·4$_b$**, was prepared *via* oxidative dimerization of **2·3**, in the presence of NCS and DBU. The asymmetric **2·4$_a$** was formed *via* the Mills reaction, whereby 4-bromo-2,6-difluoroaniline was oxidised *in situ* to form the corresponding nitroso derivative, to which **2·3** was added and upon condensation, **2·4$_a$** was formed. All reactions and purification proceeding the formation of an azobenzene were carried out in the dark, to reduce the possibility of visible light photoswitching. Upon successfully synthesising the symmetric and asymmetric units, the focus turned towards the *para*-functionalisation of the azobenzenes. Both systems were treated in a similar manner, where the acetic acid ester was first removed under acidic conditions to yield the *para*-benzyl alcohol derivative, **2·5$_{a/b}$**. Initial attempts to brominate this position with PBr_3 and *N*-bromosuccinimde were unsuccessful, due to the common over-bromination and the challenges in purifying the corresponding mixture with

column chromatography. Subsequently, activation of the alcohol using a *p*-tosyl group was attempted and successfully produced **2·6$_{a/b}$** in good yields.



Scheme 2.4: Synthetic scheme for the synthesis of ***2·L$_a$Ln*** *and* ***2·L$_b$Ln$_2$*** *(i) copper cyanide, N-methyl -2-pyrrolidone, 202 °C, 90 minutes, microwave radiation. (ii) potassium hydroxide (30%), 100 °C, 12 hours, (iii) (1) lithium aluminum hydride, tetrahydrofuran, 60 °C, 12 hours; (2) acetic anhydride, pyridine, 25 °C, 12 hours. (iv) for R = Br: oxone, dichloromethane: acetone, 25 °C, 12 hours; if R = CH$_2$OAc: N-chlorosuccinimide, DBU, dichloromethane, −78 °C, 10 minutes. (v) Hydrochloric acid (37%) in methanol, 40 °C, 72 hours. (vi) p-tosyl chloride, tetrahydrofuran: water, sodium hydroxide 25 °C, 30 minutes. (vii) DO3A^{t}Bu, acetonitrile, sodium carbonate, 70 °C, 12 hours. (viii) Trifluoroacetic acid, dichloromethane, 25 °C, 12 hours. (ix) Ln(OTf)$_3$, ethanol: water, 50 °C, 72 hours.*

The *p*-tosyl group is an efficient leaving group in S_N2 reactions, and thus reaction with either 1 or 2 eq. of ^{t}butyl-ester DO3A yielded **2·7$_{a/b}$**. Subsequently, acid deprotection with TFA of both **2·7$_{a/b}$** yielded the free carboxylate arms of ligands **2·L$_a$** and **2·L$_b$**. Finally, the lanthanide coordination by the macrocyclic framework was achieved by stirring with the appropriate triflate salt, to yield complexes **2·L$_a$Eu**, **2·L$_b$Eu$_2$**, **2·L$_a$Nd** and **2·L$_b$Nd$_2$**. Any excess lanthanide salt was removed by dialysis in Milli-Q water over a period of 3 days, with the water changed daily.

2.4 Characterisation

This section will detail the characterisation techniques evidencing the successful synthesis of **2·L$_a$Eu**, **2·L$_b$Eu$_2$**, **2·L$_a$Nd** and **2·L$_b$Nd$_2$**. To confirm the presence of the Ln(III) complexes, high-resolution electrospray ionisation mass spectrometry (HR-ESI-MS) was performed; see **Chapter 7** for details.

2.4.1 ^{1}H NMR

The solubility of the complexes was poor in both polar and non-polar solvents as result of the *ortho*-fluoroazobenzene unit. Difficulties arose with NMR characterisation as the concentration required to obtain a good spectrum was hard to reach. In particular, the Nd(III) analogues were more insoluble than the Eu(III) complexes, perhaps due to the increased size of the Ln(III) ion. ^{1}H NMR spectra could be obtained for Eu(III) complexes in DMSO-d_6; however, the Nd(III) analogues were insoluble at the concentrations required for NMR.

The ^{1}H NMR spectrum of **2·L$_a$Eu** is shown in Figure 2.3. The chemical shifts of the protons extend up to ± 40.00 ppm, which is indicative of the formation of a mononuclear Eu(III) complex, in which the protons on the ligand experience the magnetic field provided by the paramagnetic Eu(III) centre.

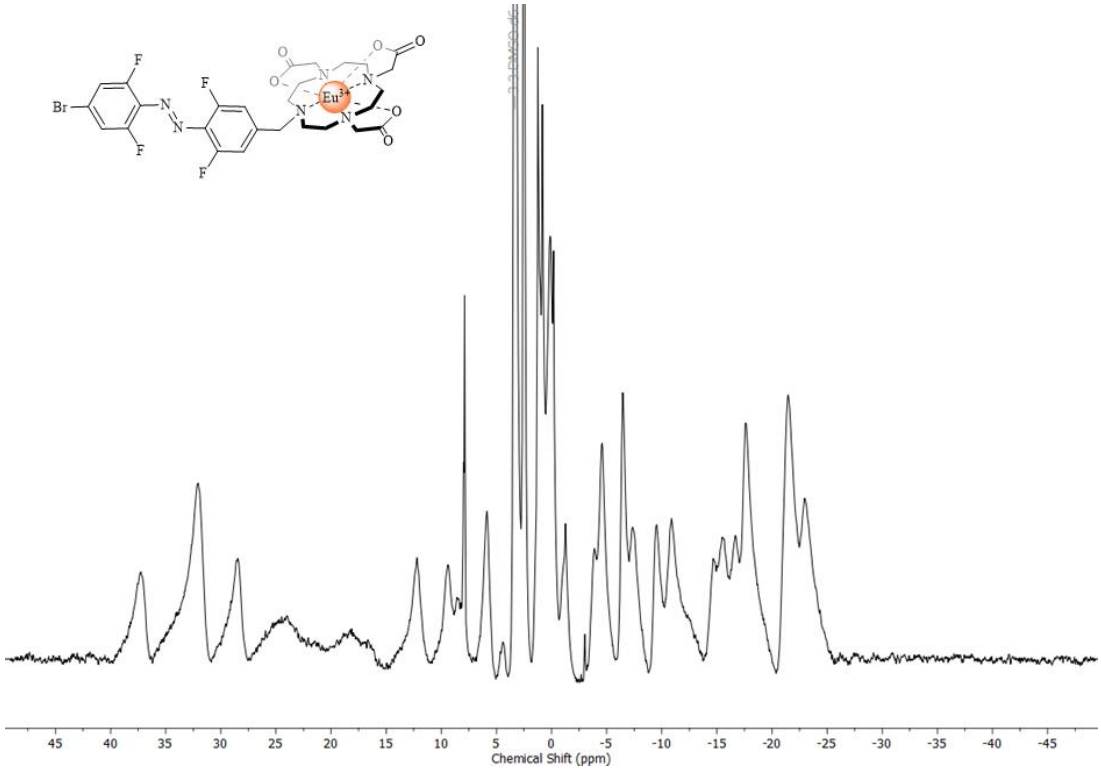


*Figure 2.3: ^{1}H NMR spectrum of compound **2·L$_a$Eu** D_2O, 400 MHz, 298 K.*

The ^{1}H NMR spectrum of **2·L$_b$Eu$_2$** is shown in Figure 2.4. The chemical shifts of the protons extend up to ± 50.00 ppm. This is ± 10.00 ppm greater than the mononuclear complex, suggesting that the presence of two Eu(III) centres further enhances the magnetic field experienced by the protons in the complex, providing additional evidence for the formation of a binuclear Eu(III) complex.

In both ^{1}H NMR spectra, there is significant overlap and broadening of the peaks. This is due to the presence of both *E*/*Z* isomers of the azobenzene ($k_{E\rightarrow Z} \approx$ 2 years)[171] and, fluxionality in the DO3A macrocycle. DO3A macrocycles can adopt both twisted square anti-prism (TSAP) or square anti-prism (SAP) geometries in solution ($k_{TSAP\leftrightarrow SAP} \approx$ minutes). Additionally, both TSAP and SAP forms are in equilibrium with each other and also their solvent uncapped and capped forms, resulting in numerous possible species in solution on the ^{1}H NMR timescale (16 possible species for **2·L$_a$Eu** and 128 possible species for **2·L$_b$Eu$_2$)**.[76]

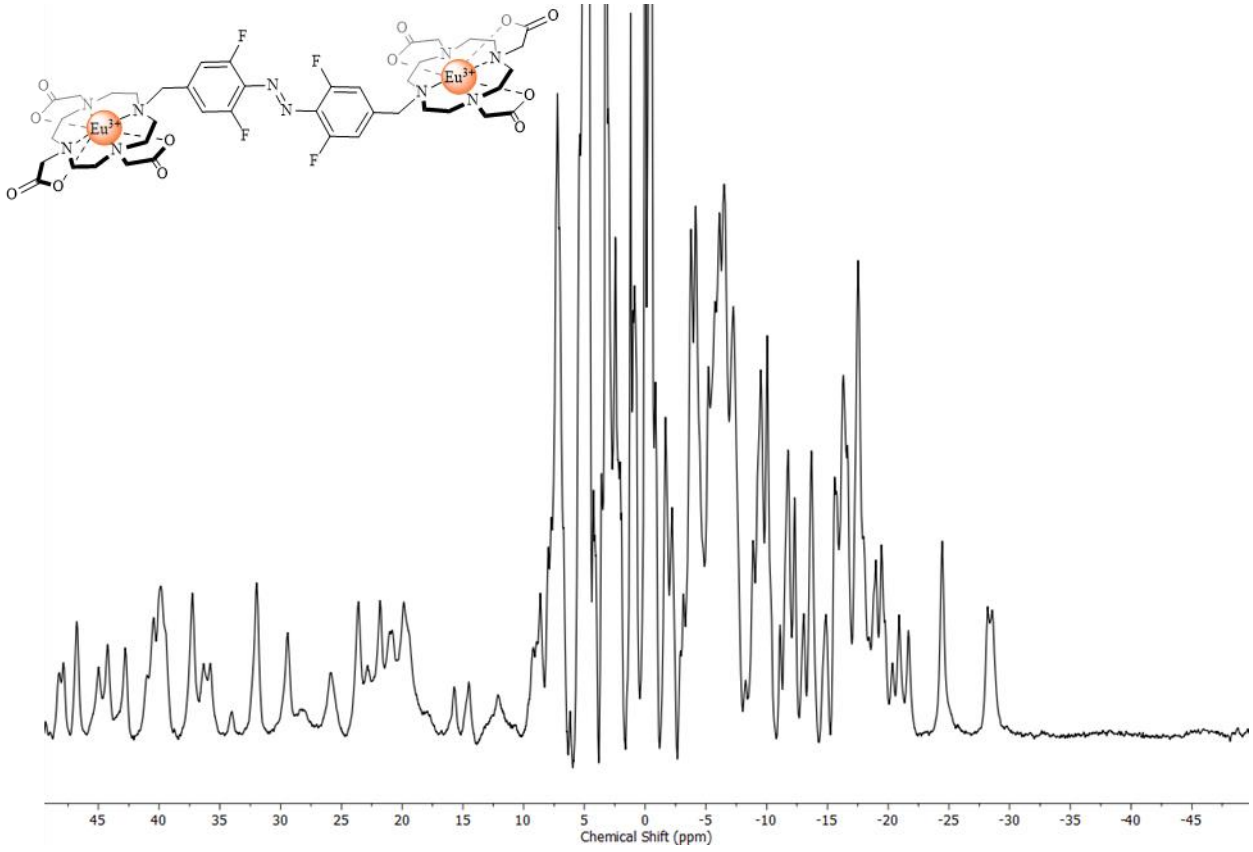


*Figure 2.4: ^{1}H NMR spectrum of compound **2·L$_b$Eu$_2$** in D_2O, 400 MHz, 298 K.*

2.4.2 High Performance Liquid Chromatography

High-performance liquid chromatography (HPLC) was used to determine the purity of the Ln(III) complexes (Figure 2.5). Using method 1, as detailed in **Chapter 7,** the HPLC traces for all Ln(III) complexes were obtained.

Figure 2.5 shows the HPLC traces for **2·L$_a$Eu** and **2·L$_b$Eu$_2$**. The presence of three significant peaks in each trace can be assigned the solvent front (denoted with a *) and both *E* and *Z* isomers of each complex in solution, determined upon irradiation of the sample with 405 and 530 nm light, followed by HPLC; for more details see **Section 2.5.2**. From the HPLC, we determined that Ln(III) complexes synthesised were ≥ 98% pure. The binuclear system had a shorter retention time due to the increased polarity in comparison to the mononuclear complex. Further investigation into the influence of isomers on the HPLC traces is detailed in **Section 2.5.2**.

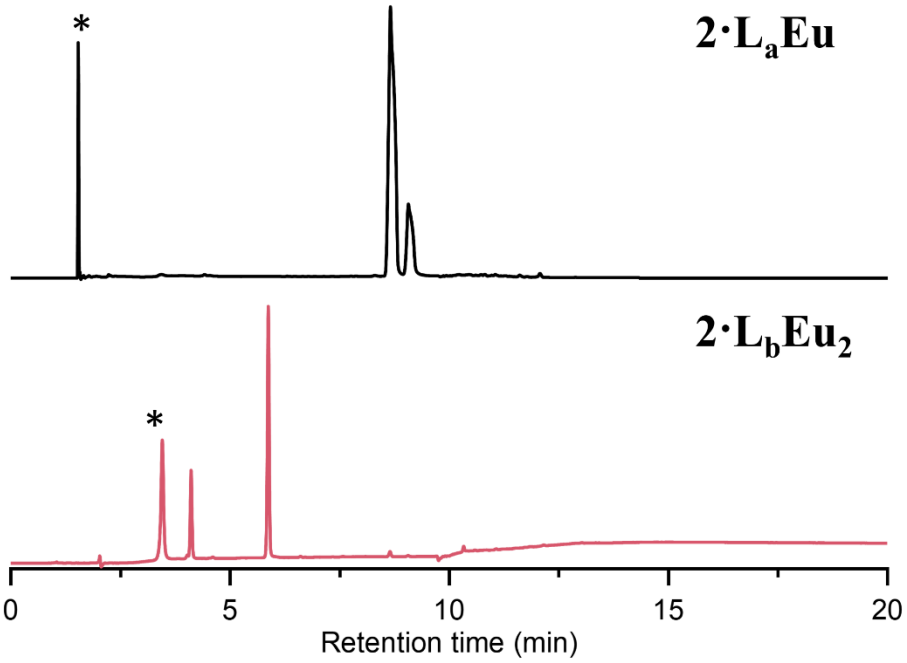


*Figure 2.5: HPLC trace of **2·L$_a$Eu** and **2·L$_b$Eu$_2$** upon irradiation with 530 nm for 10 minutes, respectively, recorded at 272 nm using method 1 where * represents the solvent front.*

2.5 Photoswitching Properties

It is known that efficient photoisomerisation occurs for *ortho*-fluoroazobenzenes. Selective irradiation into the n → π* transition of each isomer can generate the enriched photostationary state (PSS) of *E*/*Z* isomers. Blue light (λ = 405 nm) can selectively excite the *Z* isomer allowing for *Z* → *E* isomerisation, yielding the *E*-enriched state. Green light (λ = 530 nm) can selectively excite the *E* isomer allowing for the *E* → *Z* isomerisation, yielding the *Z*-enriched state.[170, 171]

2.5.1 Absorbance Spectroscopy

The UV-visible absorption spectra were recorded at room temperature from 280 – 700 nm. Due to the low solubility of both ligands and Ln(III) complexes, all spectra were recorded in DMSO.

2.5.1.1 2·L_a and 2·L_b

Photostationary state distributions of each ligand (**2·L_a** and **2·L_b**) were investigated upon irradiation with blue light (405 nm, ~0.9 W LED) and green light (530 nm, ~1.1 W LED) for 10 minutes, the photostationary state was confirmed when the absorbance spectra remained unchanged upon continued irradiation. UV-Vis absorbance spectra of each isomer enriched state were recorded (Figure 2.6).

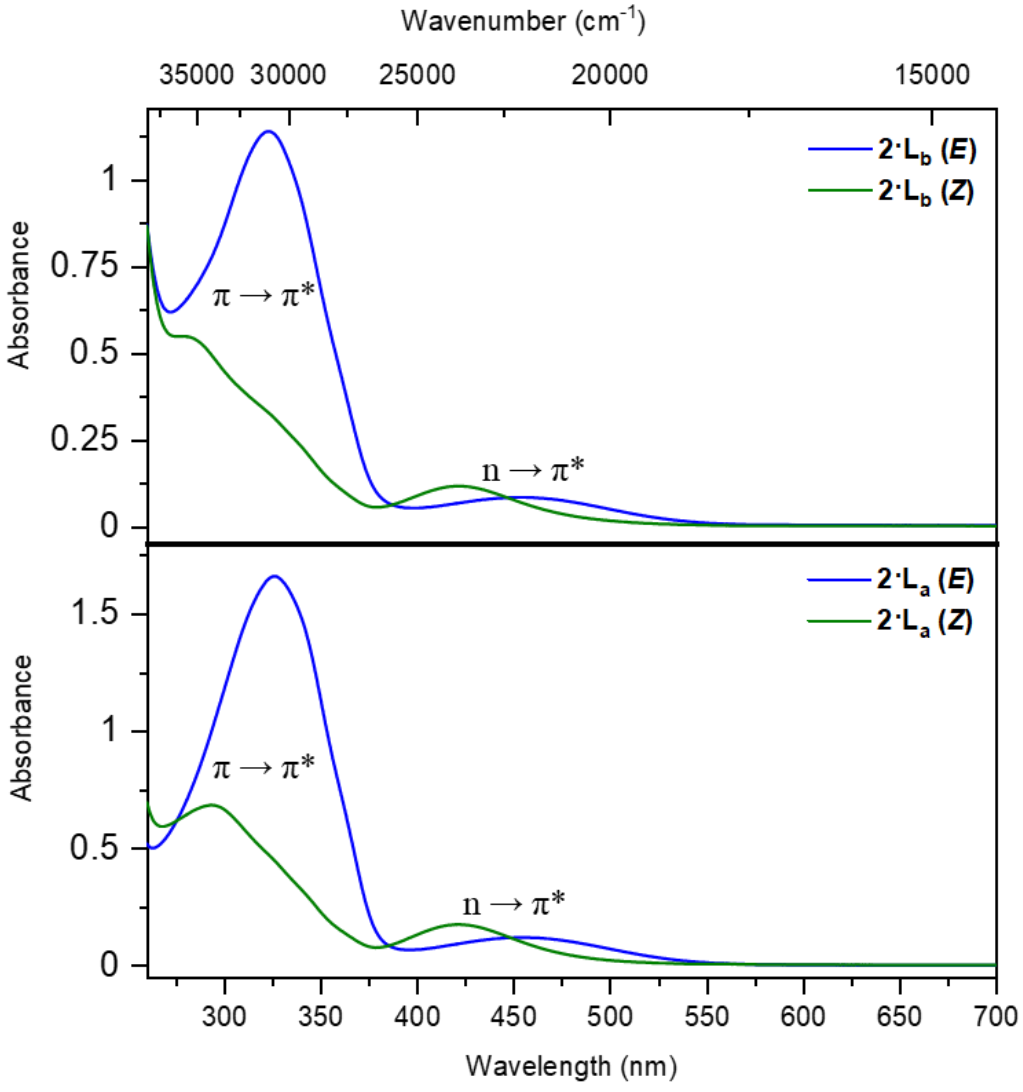


*Figure 2.6: Absorbance spectra of top) **2·L_b** and bottom) **2·L_a** where the E-isomer enriched PSS is represented in blue (λ_{irr} = 405 nm, 10 minutes) and the Z-isomer enriched PSS represented in green (λ_{irr} = 530 nm, 10 minutes).*

For both ligands, **2·L_a** and **2·L_b**, the absorbance spectra of the corresponding PSS are similar. For the *E*-enriched PSS (λ_{irr} = 405 nm), in both ligands the highly absorbing $\pi \rightarrow \pi^*$ transition

around 325 nm (λ_{max} = 326 nm, **2·L$_a$** λ_{max} = 323 nm, **2·L$_b$**) is observed, in addition to the lower lying n → π* transition at 445 nm (**2·L$_a$** and **2·L$_b$**). In the *Z*-enriched PSS, for both ligands, the π → π* transition is blue-shifted in comparison to the *E*-enriched PSS (λ_{max} = 283 nm, **2·L$_a$** λ_{max} = 294 nm, **2·L$_b$**) and the n → π* transition is also blue-shifted to 422 nm (**2·L$_a$** and **2·L$_b$**). Interestingly, the λ_{max} of the π → π* transition of both *E*/*Z* isomers varies slightly between **2·L$_a$** and **2·L$_b$** whilst the λ_{max} of the n → π* transition remains unchanged. This is likely a result of the different groups in the *para*-position influencing the electronics of the azobenzene core. The significant separation between the n → π* transition between *E* and *Z* isomers allowed for efficient and orthogonal switching with visible light in both directions. Importantly, Figure 2.6 shows an isosbestic point (λ_{iso} = 377 nm), where both *E* and *Z* isomers absorb light with the same efficiency, for both **2·L$_a$** and **2·L$_b$.** This allowed for investigation of the PSS distributions using HPLC (**Section 2.5.2**).

2.5.1.2 Ln(III) complexes

Tang and co-workers reported that for their system, the PSS distribution of the *E*-enriched and *Z*-enriched states of the azobenzene ligand changed upon the coordination to a Ln(III) metal centre *via* a *β*-diketonate chelator. To investigate the same phenomenon for the Ln(III) complexes developed in this chapter, the normalised absorbance spectra of both *E*-enriched (λ_{irr} = 405 nm, 10 minutes) and *Z*-enriched states (λ_{irr} = 530 nm, 10 minutes) of the free ligands were compared with that of the Ln(III) complexes (Figure 2.7). Negligible difference in the normalised absorption spectra of the ligands **2·L$_a$** and **2·L$_b$** and their corresponding Ln(III) complexes for each enriched PSS's was observed, suggesting that, unlike Tang and co-workers' system, the PSS distribution of isomers remains unchanged upon coordination of the ligand to a Ln(III) metal. In Tang's ligand, the azobenzene is directly conjugated to the Ln(III) metal centre *via* an amide bond, whereas in both **2·L$_a$** and **2·L$_b$** a *para*-methylene linker prevents direct conjugation between the azobenzene and the Ln(III) metal centre. Therefore,

the π→π* and n→π* transitions of the azobenzene are not significantly influenced by the presence of Ln(III) ions within these complexes.

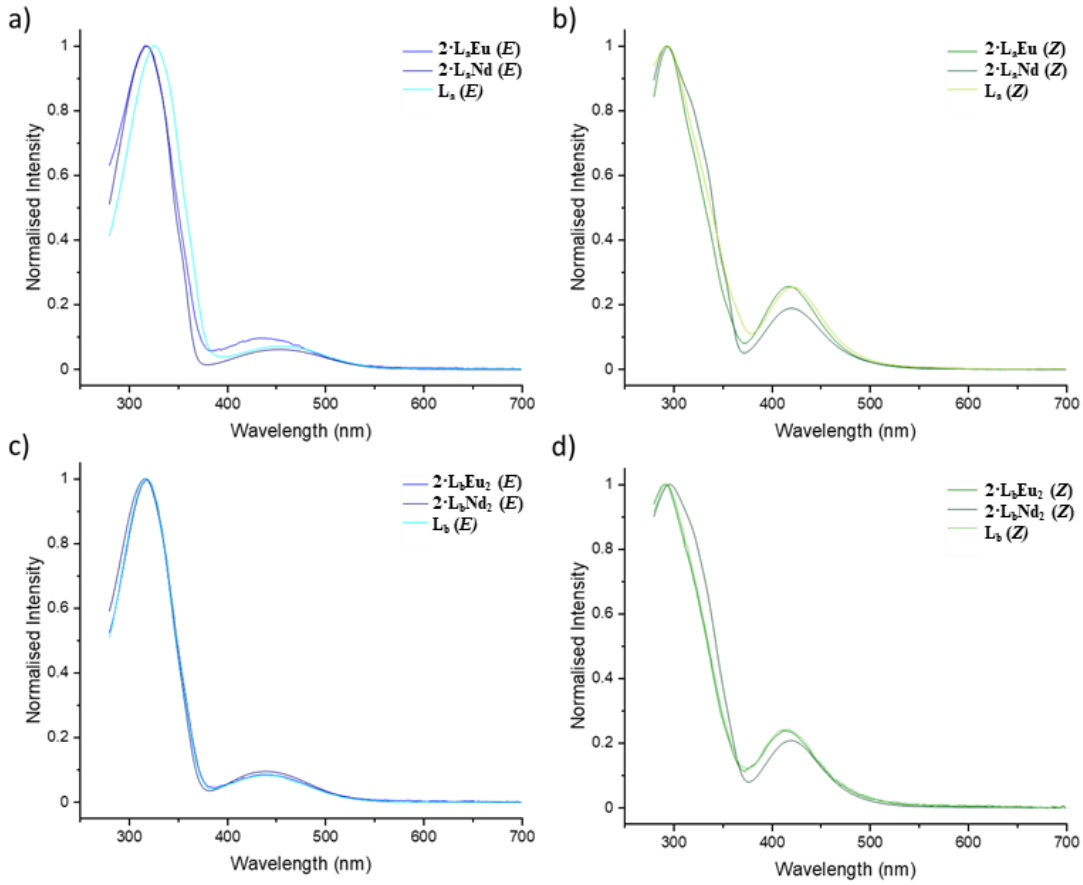


Figure 2.7: Normalised absorbance spectra in DMSO a) ***2·LaEu***, ***2·LaNd*** *and* ***2·La*** *after each sample was irradiated with 405 nm light for 10 minutes b)* ***2·LaEu***, ***2·LaNd*** *and* ***2·La*** *after each sample was irradiated with 530 nm light for 10 minutes c)* ***2·LbEu2***, ***2·LbNd2*** *and* ***2·Lb*** *after each sample was irradiated with 405 nm light for 10 minutes d)* ***2·LbEu2***, ***2·LbNd2*** *and* ***2·Lb*** *after each sample was irradiated with 530 nm light for 10 minutes.*

2.5.2 HPLC Analysis

Typically, the PSS distributions for organic molecules can be calculated from the integration of peaks in ^{1}H NMR and the ratio of the integrations corresponding to protons from the *trans* isomer compared with the *cis* isomer. However, in paramagnetic complexes such as those investigated here, the integrations of the proton's environments are not quantitative and the systems are more difficult to fully characterise. Therefore, to determine the PSS distributions for paramagnetic complexes, both HPLC and absorbance spectroscopy were required.

To determine the PSS distributions of both the *E*-enriched and *Z*-enriched states, each complex was irradiated for 10 minutes with 405 nm to achieve the *E*-enriched state, and 530 nm light to achieve the *Z*-enriched state. Upon reaching the PSS state *via* irradiation at 405 nm and 530 nm, the absorbance spectra were recorded, as shown for **2·L$_a$Eu** in Figure. 2.8. For details on the PSS analysis of all other complexes, see **Chapter 7**. From the absorbance spectra, the isosbestic point, where both isomers absorb light with the same efficiency, for both the *E* and *Z* enriched states was found to occur at 377 nm. Subsequently, the samples corresponding to the enriched states were analysed by HPLC, using method 1 (see **Chapter 7**), where the absorbance was set at 377 nm (Figure 2.8a). This resulted in two peaks in the HPLC trace of each enriched state. To ensure these two peaks related to the *E*/*Z* isomer, the samples were photoswitched to the other isomer, and again analysed with HPLC. This resulted in a change in the intensities of each peak; however, the retention times remained unchanged (Figure 2.8a). Therefore, the two peaks in each trace were integrated, and the overall area of integration was normalised to 1, revealing the distribution of each isomer in each enriched state. For **2·L$_a$Eu,** the PSS distribution of the *E*-enriched state was 92:8 (*E*:*Z),* whereas in the *Z*-enriched, the *E*:*Z* distribution was slightly lower, at 26:74 *(E*:*Z).* The higher PSS distribution in the *E*-enriched state could either be a result of steric clash in the *Z* isomer or reduced efficiency of 530 nm light pushing the photoisomerisation towards the formation of the *Z* isomer. Using the ratios determined from HPLC, and the corresponding absorbance spectra of the *E*/*Z*-enriched states, a theoretical absorption spectrum of pure *E* and pure *Z* (Figure 2.8b), could be determined using equations 2.1 and 2.2:

$$PSS_E = a[E] + b[Z] \quad (2.1)$$

$$PSS_Z = c[E] + d[Z] \quad (2.2)$$

Where a = percentage of *E* at PSS_E, b = percentage of *Z* at PSS_E, c = percentage of *E* at PSS_Z, d = percentage of *Z* at PSS_Z.

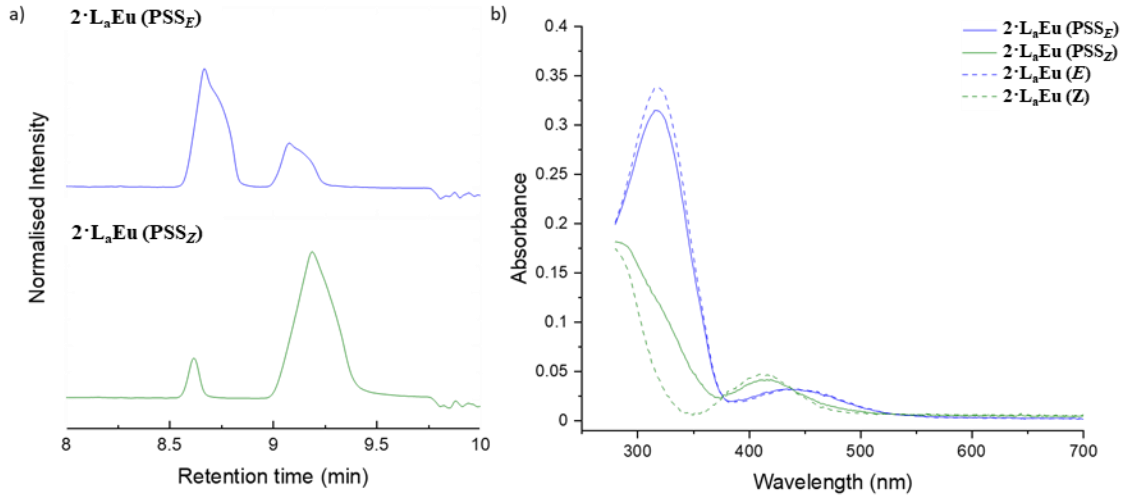


*Figure 2.8: a) HPLC trace of **2·LₐEu** (PSS_E and PSS_Z) using method 1, blue line represents the trace after irradiation of **2·LₐEu** with 405 nm light for 10 minutes, the green line represents the trace after irradiation of **2·LₐEu** with 530 nm light for 10 minutes. b) Absorbance of **2·LₐEu** (PSS_E, PSS_Z, E and Z) solid blue line represents the trace after irradiation of **2·LₐEu** with 405 nm light for 10 minutes, the solid green line represents the trace after irradiation of **2·LₐEu** with 530 nm light for 10 minutes, the dashed blue and green line represent the calculated absorbance of pure E and Z isomers respectively.*

2.6 Photophysical Properties of Eu(III) and Nd(III) Complexes

2.6.1 Luminescent Properties of Ligands

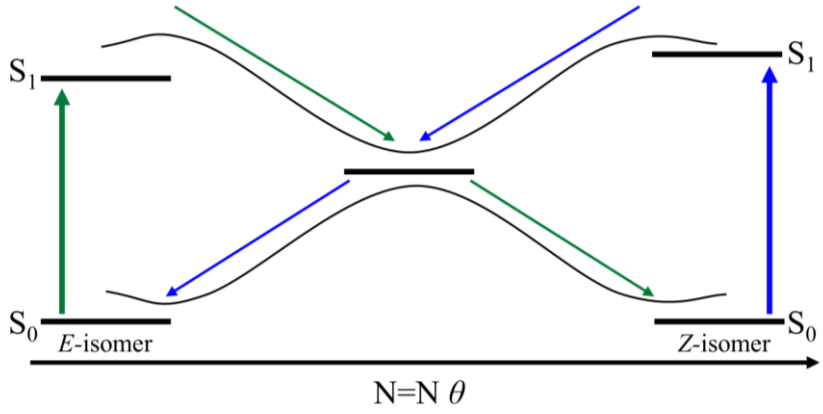


Figure 2.9: Schematic representation of the photoisomerisation pathway in ortho-fluoroazobenzene compounds as a function of the dihedral angle of the N=N bond.

The photophysical properties of azobenzenes are dictated by their photoisomerisation, in which the probability of the interconversion between isomers is a function of both the excitation

wavelength and the N=N dihedral angle (θ). Excitation of either *E* or *Z* isomer *via* the $S_0 \rightarrow S_1$ transition provides a pathway to overcome the barrier on the potential energy surface to rotation/inversion, resulting in the isomerisation (Figure 2.9).[175-180]

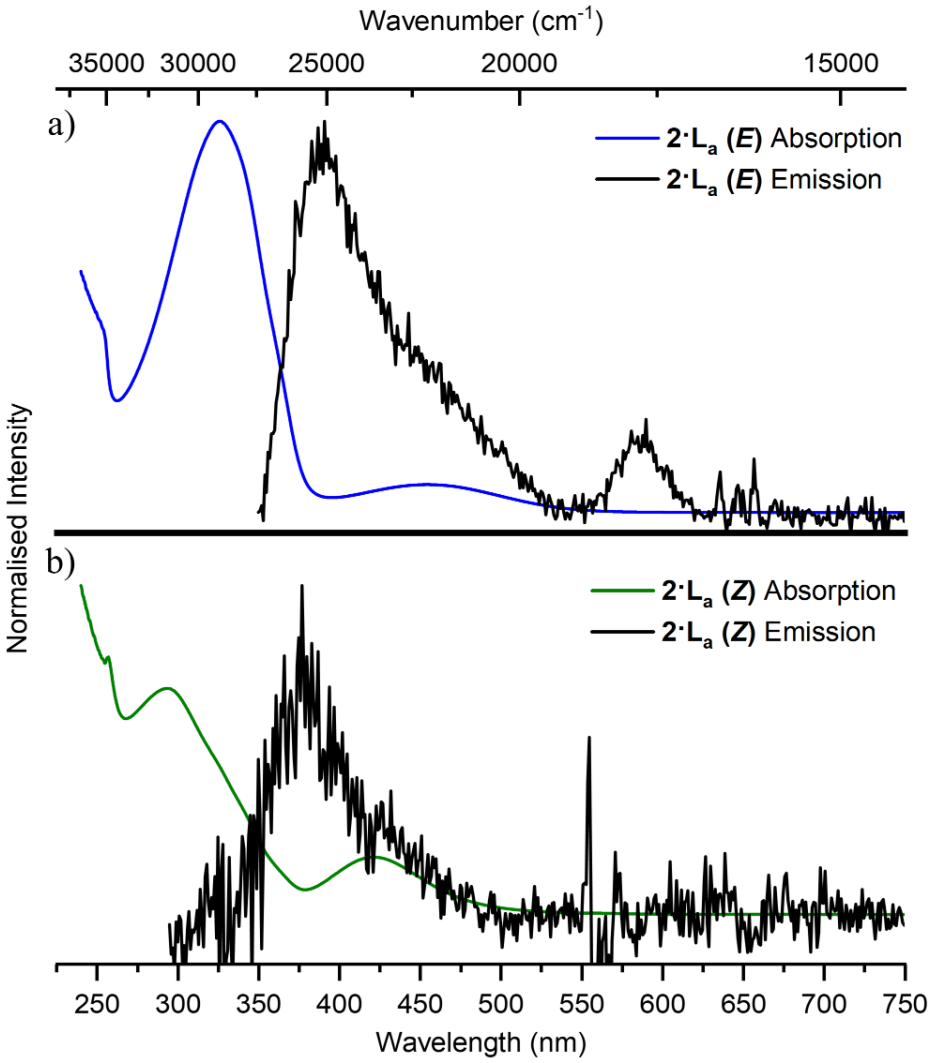


Figure 2.10: Luminescent properties of ***2·La*** *top) E-enriched PSS absorbance upon irradiation with 405 nm light for 10 minutes (blue line) and emission when excited into the n→π* transition at 325 nm (black line) bottom) Z-enriched PSS absorbance upon irradiation with 530 nm light for 10 minutes (green line) and emission when excited into the n→π* transition at 280 nm (black line). Excitation slit at 5 nm, emission slit at 1 nm, integration time 0.1 s. All spectra normalised.*

The absorbance s for the *E*-enriched PSS of **2·La** has a maximum intensity at 325 nm, corresponding to the $\pi \rightarrow \pi^*$ transition (Figure 2.10a). Excitation into this transition yielded a ligand-centred emission spectrum with the characteristic stokes shift. However, the intensity of the emission was extremely low, and the spectrum suffered from poor significant signal-to-noise ratio, suggesting that the ligand favours non-radiative relaxation from the S_1 excited state.

This is in concordance with the previously determined extremely low fluorescence quantum yields for both *E*-azobenzene (7.54×10^{-7} to 1.1×10^{-5}, S_1 state) and *Z*-azobenzene ($\sim 1 \times 10^{-6}$, S_1 state).[181, 182]

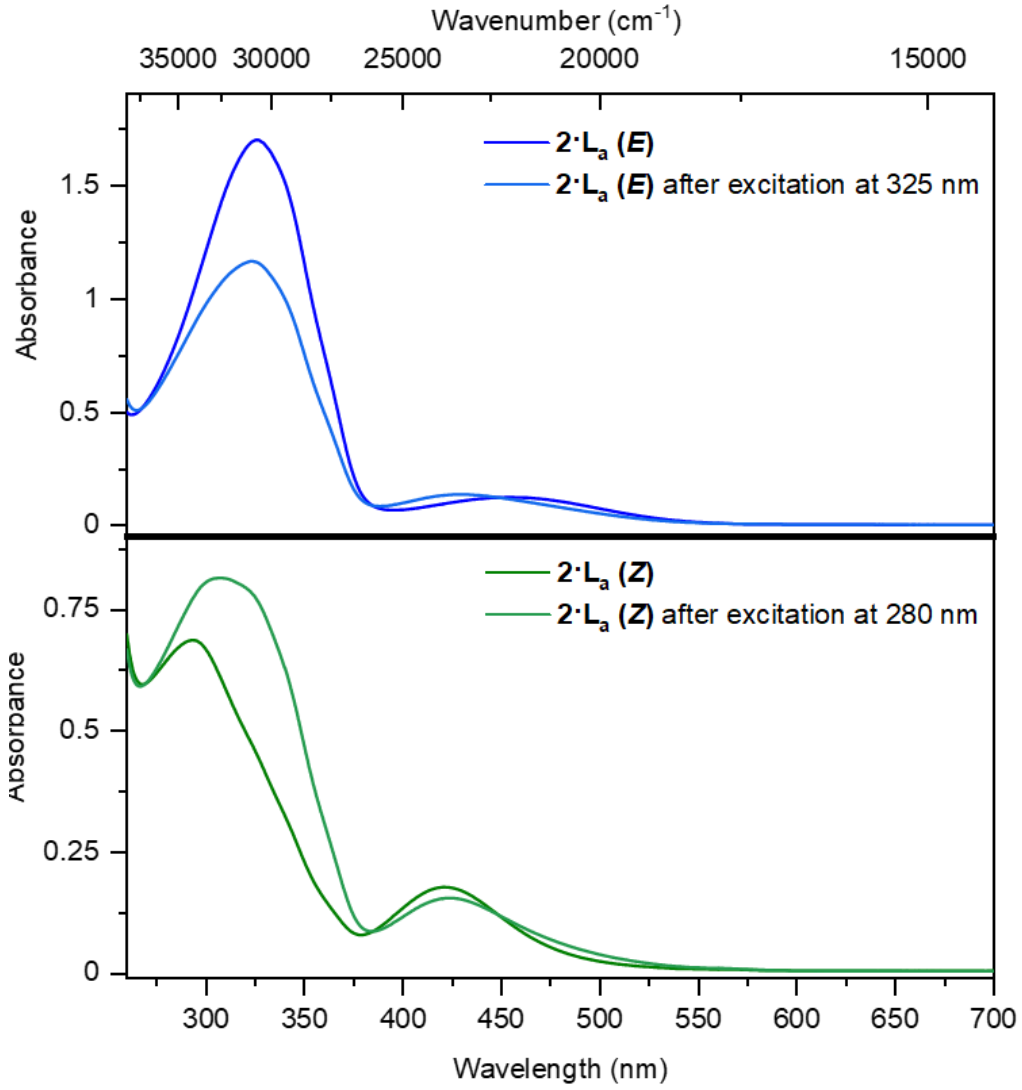


Figure 2.11: Absorption spectra of ***2·L**a* *the top) E-enriched state before and after irradiation at 325 nm and bottom) Z-enriched state before and after irradiation at 280 nm.*

Importantly, the absorbance spectra recorded immediately after the initial excitation at 325 nm differed in comparison to the *E*-enriched PSS. Upon excitation at 325 nm, the PSS distribution was perturbed with an increased proportion of the *Z* isomer. This demonstrates that the majority of energy absorbed by the *E* isomer is directed into the photoisomerisation pathway but not to radiative decay from the S_1 excited state (Figure 2.11). This was further supported by evidence

acquired upon excitation into the n → π^* transition (λ_{ex} = 450 nm), where the ligand emission intensity was much weaker and hard to distinguish from the baseline (**Chapter 7,** Figure 7.4). Similarly, the absorbance spectrum recorded after excitation at 450 nm again showed a change in PSS, with an increased proportion from the Z isomer (**Chapter 7,** Figure 7.5).

Additional investigations into the luminescence of the *Z* isomer of **2·L$_a$** upon excitation into both the $\pi \rightarrow \pi^*$ transition at 280 nm and n → π^* transition at 422 nm, again showed ligand emission with low intensity and characteristic stokes shift (Figure 2.10). After each excitation, the PSS distribution was perturbed with an increased proportion of the *E* isomer present (Figure 2.11), once again demonstrating that isomerisation is the favoured pathway in the azobenzene ligand, between the S_1 excited states of the *E* and *Z* isomers, in both directions.

2·L$_b$ was investigated in a similar manner, it was also found to be weakly emissive, where the energy absorbed by the ligand was directed towards the photoisomerisation, agreeing well with the observations in **2·L$_a$**. The presence of a second macrocycle had negligible effects on the emission observed. More details for the optical analysis of **2·L$_b$** can be found in **Chapter 7** (Figure 7.6 and 7.7).

2.6.2 Eu(III) Luminescence

2.6.2.1 Steady State Spectra of Eu(III) Complexes

Eu(III) steady-state emission and excitation spectra were recorded at 298 K, unless stated otherwise. For emission spectra, Eu(III) was directly excited into the $^4F_0 \rightarrow {}^5L_6$ transition (λ_{ex} = 393 nm), and emission and excitation slits were fixed at 1 and 5 nm, respectively, with a step size of 0.5 nm and integration time of 0.2 s. For excitation spectra, the $^5D_0 \rightarrow {}^7F_2$ transition was monitored (λ_{em} = 617 nm); emission and excitation slits were set at 5 and 1 nm, respectively; the step size was 0.5 nm, and the integration time is 0.2 s. For samples

recorded at 77 K, a constant nitrogen flow in the sample chamber was maintained to reduce condensation forming on the glass.

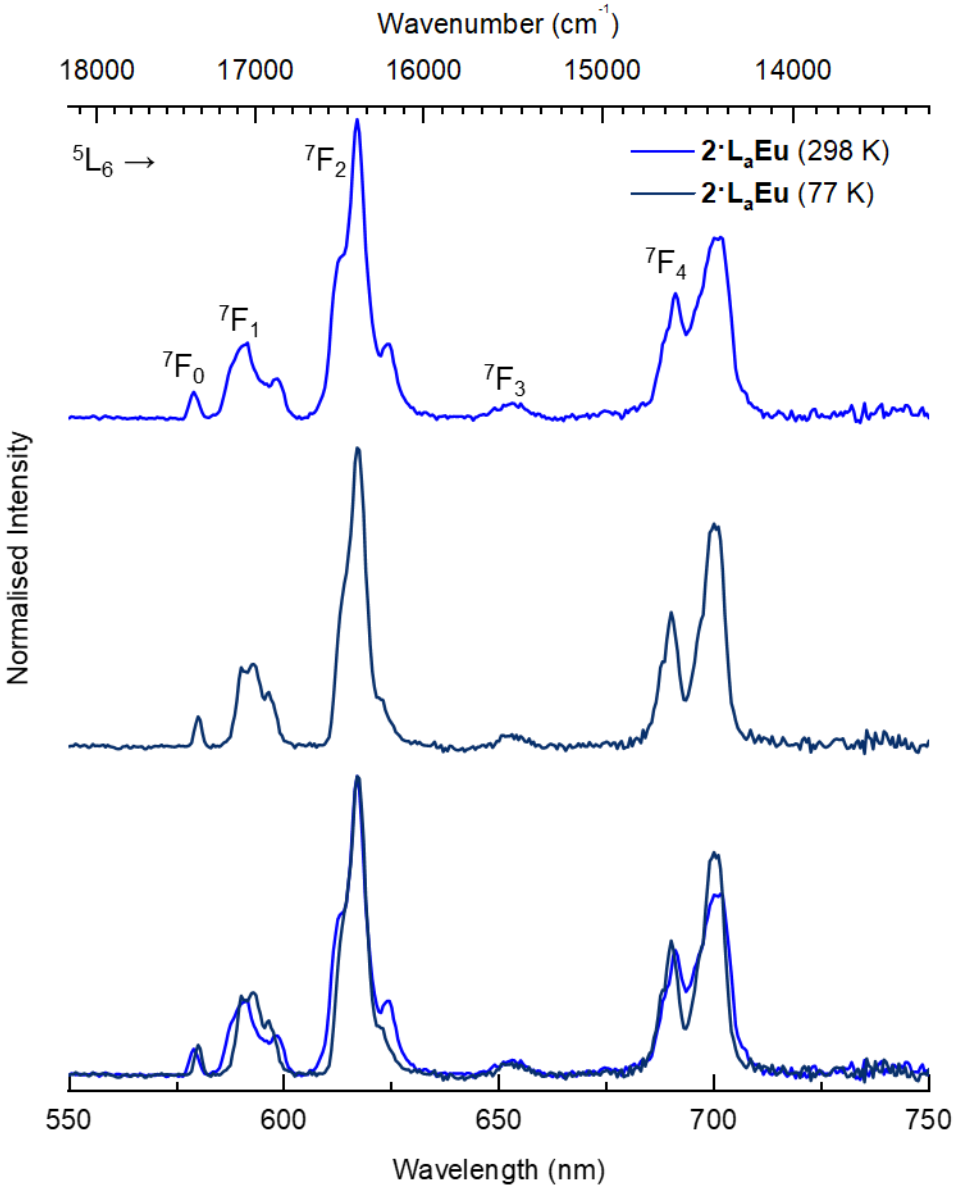


*Figure 2.12: normalised emission spectra of E-enriched PSS of **2·LaEu**, upon excitation into the $^4F_0 \rightarrow {}^5L_6$, transition ($\lambda_{ex}$ = 393 nm) of Eu(III) at both 298 K (royal blue) and 77 K (dark blue).*

Upon direct excitation into the $^4F_0 \rightarrow {}^5L_6$, transition ($\lambda_{ex}$ = 393 nm) of the *E*-enriched PSS of **2·LaEu**, red light emission was observed corresponding to the $^5D_0 \rightarrow {}^7F_J$ (J= 0, 1, 2, 3, 4) transitions. $^5D_0$ is the principle emissive state of Eu(III), which relaxes radiatively to the lower lying ^7F_J ground states, resulting in an emission spectrum, as shown in Figure 2.12. The splitting of these peaks is indicative of a non-uniform crystal field in which the original

degeneracy of the Eu(III) ion has been removed, arising from the coordination of Eu(III) within the heptadentate macrocyclic framework. Additionally, the strong and defined $^5D_0 \rightarrow {}^7F_0$ transition suggests a lack of mirror plane, orthogonal to the primary axis.

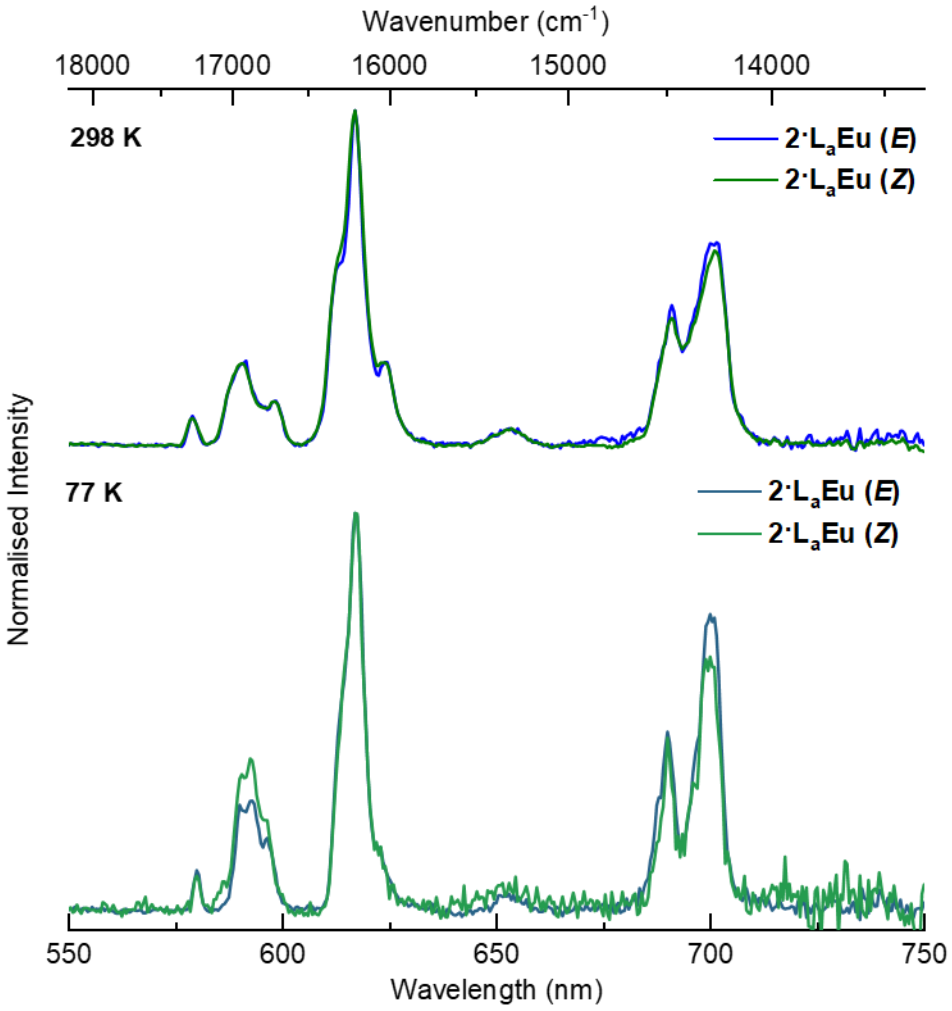


Figure 2.13: normalised emission spectra of E-enriched PSS (blue) and Z-enriched PSS (green) of ***2·LaEu****, upon excitation into the* $^4F_0 \rightarrow {}^5L_6$*, transition (*$\lambda_{ex}$ *= 393 nm) of Eu(III) at both 298 K (top) and 77 K (bottom).*

The splitting of the $^5D_0 \rightarrow {}^7F_1$ transition also suggests rotational symmetry within the coordination sphere. DO3A-based structures are known to have both TSAP and SAP isomers in solution, which can interconvert with each other and also with their capped/uncapped forms on the timescale of a luminescence measurement.[76] Upon cooling, the rate of exchange between isomers is reduced, and a slight perturbation in the emission spectra of **2·LaEu** was observed at 77 K. Additionally, at lower temperatures, the Boltzmann distribution is narrower, leading

to more defined, sharp peaks. However, the emission spectrum at 77 K remains largely unchanged compared with the room temperature spectrum, suggesting that the inner sphere coordination of Eu(III) remains largely unchanged upon cooling (Figure 2.12).

Upon direct excitation into the $^4F_0 \rightarrow {}^5L_6$, transition ($\lambda_{ex}$ = 393 nm) of the *Z*-enriched PSS of **2·L$_a$Eu**, red light emission was observed corresponding to the $^5D_0 \rightarrow {}^7F_J$ (J= 0, 1, 2, 3, 4) transitions. In comparison to the *E*-enriched PSS, there was no observable difference in the Eu(III) emission spectra upon isomerisation at either 298 K or 77 K (Figure 2.13), despite the significant change in geometry and dipole centred on the ligand. This is presumably because the photoisomerisation of the ligand occurs some distance away from the Eu(III) metal centre and does not impact the geometry and symmetry of the Eu(III) centre, such that isomerisation of the ligand is independent of crystal field splitting.

The excitation spectra recorded for **2·L$_a$Eu** are shown in Figure 2.14. The transitions observed in the excitation spectra include $^7F_0 \rightarrow {}^5D_4$, $^7F_0 \rightarrow {}^5D_{7,8,9}$, $^7F_0 \rightarrow {}^5L_6$, $^7F_0 \rightarrow {}^5D_2$ and $^7F_0 \rightarrow {}^5D_1$ of the Eu(III) metal centre, mirroring the absorption spectra of Eu(DOTA) in solution.[162] This is almost identical for *E* and *Z* isomers of **2·L$_a$Eu**, agreeing with the conclusions drawn from the emission spectra, namely that isomerisation of the ligand has no effect on the crystal field splitting of the Eu(III) centre, this is not surprising as the isomerisation of the ligand occurs away from the Eu(III) centre, with no change in the direct coordination around the Eu(III) centre. Comparison between the absorption spectra and the excitation spectra shows that although both isomers of the azobenzene ligand absorb efficiently in the range between 300 to 550 nm, there is no contribution of this ligand absorption in the Eu(III) emission for both *E*-enriched PSSs and *Z*-enriched PSSs. This demonstrates that, in this system, there is no energy transfer from either *E* or *Z* isomers of the ligand to the Eu(III) centre in **2·L$_a$Eu**, such that the Eu(III) centre and the photoswitchable ligand are essentially entirely decoupled from each other. This is particularly surprising considering the significant spectral overlap between the

absorption of the ligand ($S_0 \rightarrow S_1$) and the Eu(III) excitation spectra. Therefore, the lack of sensitisation is attributed to the availability of the non-radiative decay pathways (primarily photoisomerisation, Figure 2.9).

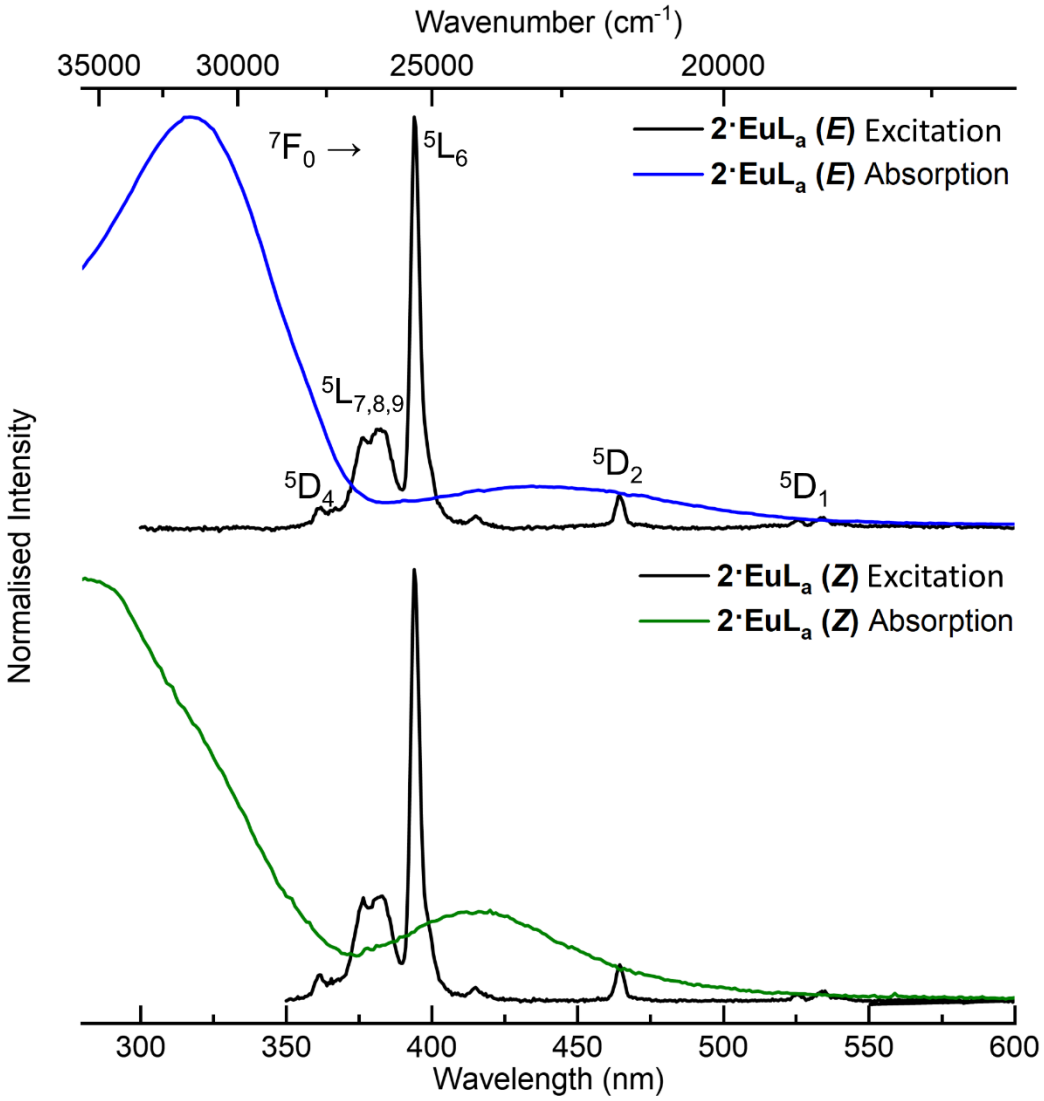


Figure 2.14: top) normalised absorbance spectra of E-enriched PSS (blue) and the corresponding normalised excitation spectra (black) bottom) normalised absorption spectra of Z-enriched PSS (green) and the corresponding normalised excitation spectra (black). Emission monitored at 616nm at 298 K.

For applications in optical information storage, one wavelength of light is required to "write" the optical information by changing the systems state, while irradiation with a second wavelength of light allows for this optical information to be "read". For effective, reversible read and write steps, these processes must be orthogonal and reversible: the excitation wavelength of the reporter in the "read" step does not perturb the system state (the

photochromic reaction), emission does not induce energy transfer to the switch, and the writing process does not itself lead to emission. Importantly, the reversibility of the system allows for data erasure and subsequent re-writing.

Unfortunately, in this Eu(III) system, there is slight spectral overlap between the excitation ("write" step) and the photochromic reaction ("read" step). Particularly, the direct excitation into the $^7F_0 \rightarrow {}^5L_6$ transition of the Eu(III) overlaps with the beginning of the absorbance of the $n \rightarrow \pi^*$ transition of both the azobenzene isomers (Figure 2.14). The degree of isomerisation upon direct excitation of the Ln(III) was calculated using equation 2.3:

$$ID = \frac{Abs_{Ex} - Abs_{PSS}}{Abs_{PSS}} \times 100 \qquad (2.3)$$

Where ID = Degree of isomerisation (%) Abs_{Ex} = Absorption after excitation of lanthanide, Abs_{PSS} = Abs at PSS (405 or 530 nm).

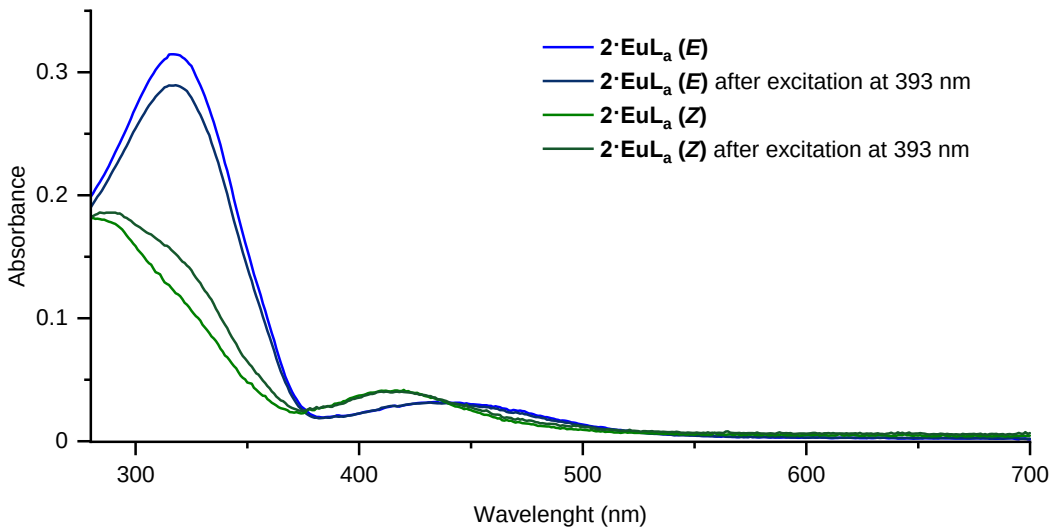


*Figure 2.15: Absorption spectra of the **2·L$_a$Eu** E and Z-enriched states before and after irradiation at 393 nm.*

The degree of isomerisation was calculated using the maximum absorbance wavelength of the $n \rightarrow \pi^*$ transition for both isomers and compared with the original distribution of isomers in each PSS to give the new isomer distribution. This analysis revealed that following excitation

of Eu(III) at 393 nm, the PSS is perturbed for both the enriched states, PSS_E = 4% reduction in *E* isomer, PPS_Z = 2% reduction in *Z* isomer.

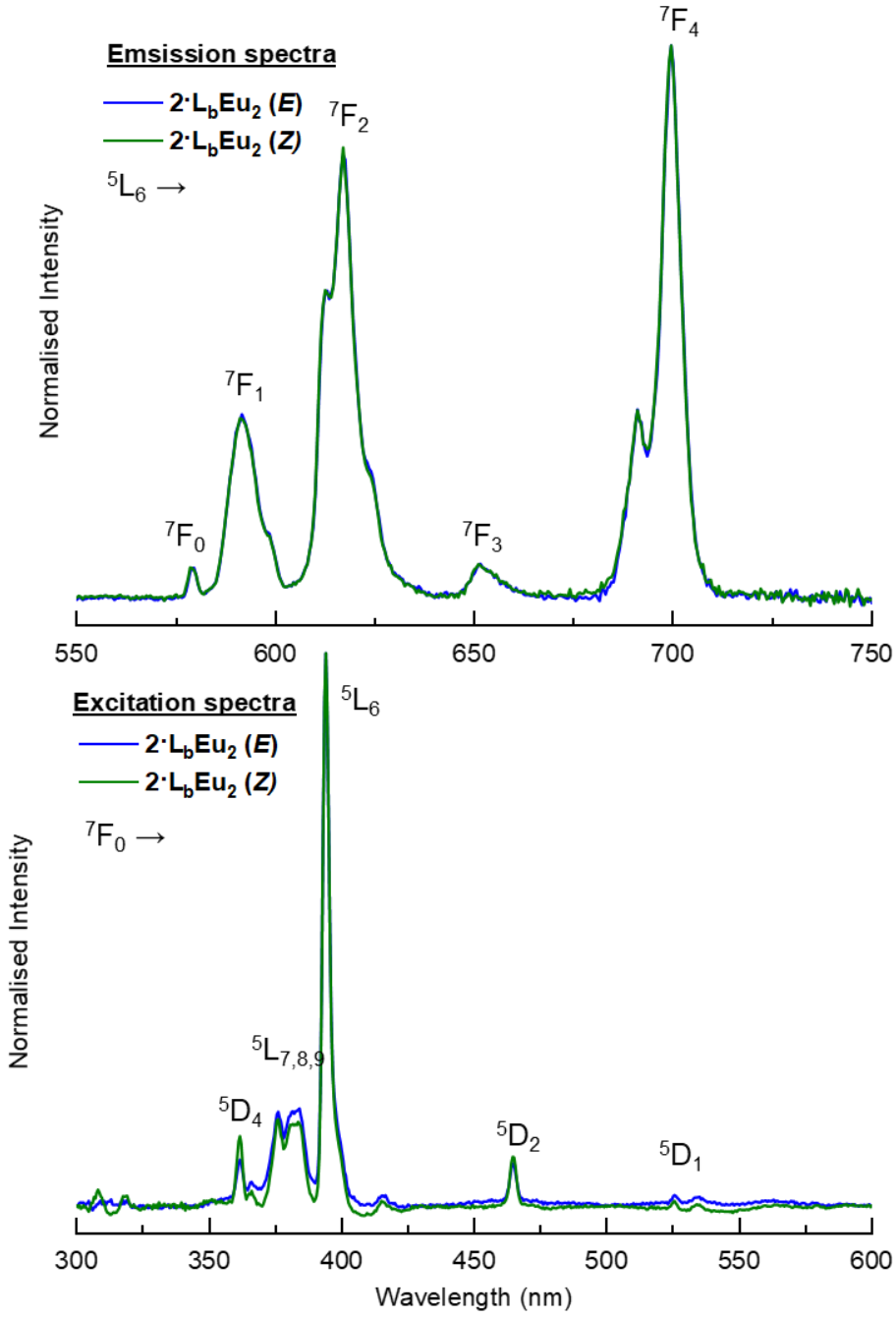


Figure 2.16: top) normalised emission spectra of E-enriched PSS (blue) and Z-enriched PSS (green) of ***2·LbEu2****,(*λ_{ex} *= 393 nm), 298 K. bottom)normalised excitation spectra of E-enriched PSS (blue) and Z-enriched PSS (green) of* ***2·LbEu2****, (*λ_{em} *= 616 nm), 298 K.*

Attention then turned to the investigation of the related binuclear complex **2·LbEu2**. Upon excitation into the $^7F_0 \rightarrow {}^5L_6$ transition (λ_{ex} = 393 nm), red light emission was observed for both

E and *Z* isomers corresponding to the $^5D_0 \rightarrow {}^7F_J$ (J= 0, 1, 2, 3, 4) transitions, and again there was no difference in the crystal field splitting observed. This was mirrored in the excitation spectra, where again there was no observable contribution from the ligand to Eu(III) emission, and no observable differences between isomers, similar to what was observed for **2·L$_a$Eu** (Figure 2.16).

Additionally, upon direct excitation at 393 nm into the Eu(III) centre, perturbations in the PSS distribution were observed for both *E* and *Z* isomers. At 393 nm, the efficiency at which the isomer absorbs light differs; as a consequence, this absorbed energy not only directly excites the $^7F_0 \rightarrow {}^5L_6$ transition, but it also can directly populate the excited states of each isomer. Therefore, both Eu(III) emission observed and also photoswitching of the ligand.

To understand the differences between the photophysical properties of the mononuclear and binuclear complex, **2·L$_a$Eu** and **2·L$_b$Eu$_2$**, the normalised emission and excitation spectra of the *E*-enriched states were compared at 77 K (Figure 2.17). The comparison of the normalised emission spectra (λ_{ex} = 393 nm) of the mono- and binuclear complexes revealed slight differences in the crystal field splitting of Eu(III). Considering that the coordination environment around the Eu(III) ions in each complex is dictated by the same heptadentate DO3A macrocycle, the changes observed in the crystal field at 77 K relate to the distribution of geometric isomers in solution. This was initially observed in the ^{1}H NMR of both complexes in section **2.4.2,** where the contribution of TSAP/SAP isomers and their solvent-capped and uncapped forms lead to a number of related species in solution. Since the binuclear complex has two identical Eu(III) coordination sites, the combination of isomers are increased 8-fold in comparison to the mononuclear complex. Thus, the mononuclear complex represents the weighted average of 16 species in solution, and the binuclear represents 128. Each isomer will have a slightly different crystal field splitting depending on the conformation around both Eu(III) cations. Therefore, the overall distribution varies compared with the mononuclear

complex. Similarly, the excitation spectrum (λ_{em} = 616 nm) also varies slightly between the mono- and binuclear complex, as a result of the varying number and conformation of species in solution.

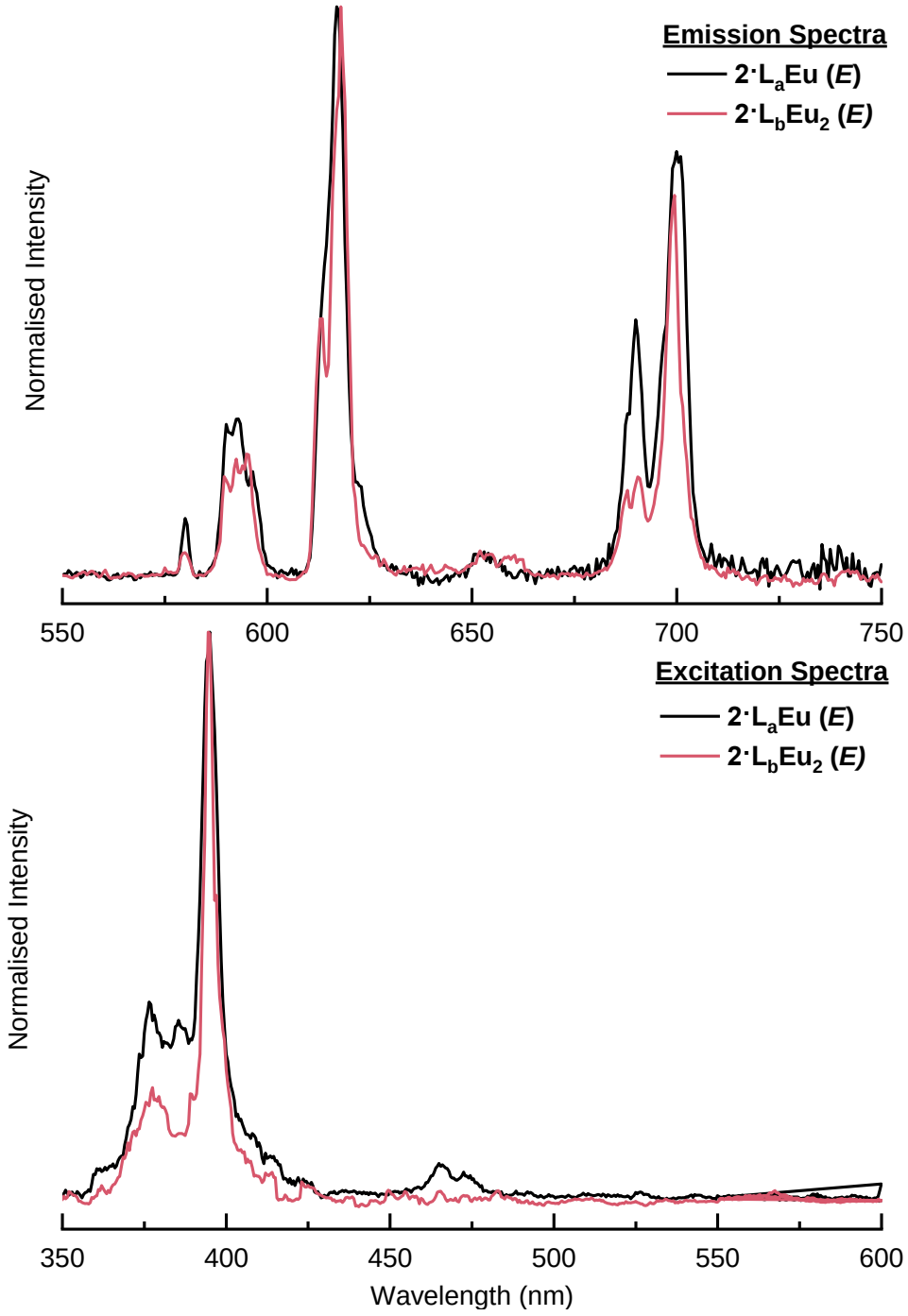


Figure 2.17: top) normalised emission spectra of E-enriched PSS of ***2·LaEu*** *(black) and* ***2·LbEu2*** *(mauve),* λ_{ex} *= 393 nm, 77 K. bottom) normalised excitation spectra of E-enriched PSS of* ***2·LaEu*** *(black) and* ***2·LbEu2*** *(mauve),* λ_{em} *= 616 nm, 77 K.*

Analysis of the non-normalised emission spectra (Figure 2.18) demonstrated that the emission intensity of the binuclear complex is higher than the mononuclear complex when excited under the same conditions. Integration of the area under the curves revealed that the emission intensity for the binuclear complex is 1.8 times greater than that of the mononuclear complex, consistent with the fact that, in the binuclear complex, there are two emissive Eu(III) centres which can be populated.

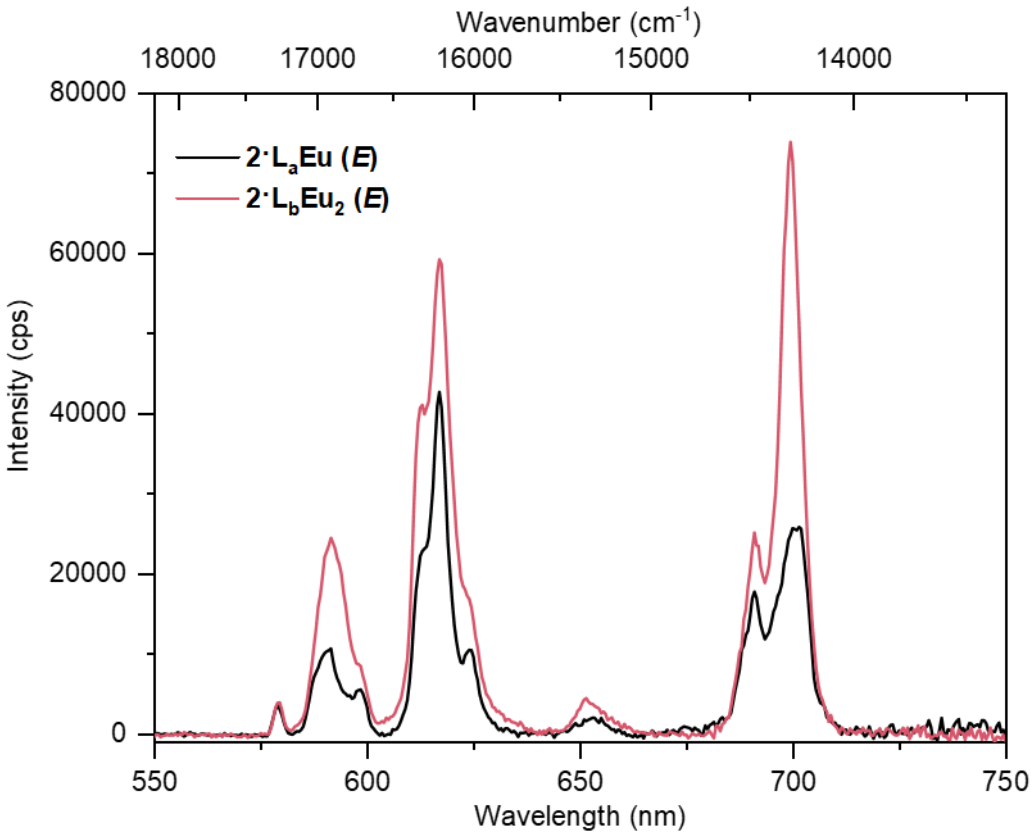


Figure 2.18: Emission spectra of E-enriched PSS of ***2·LaEu*** *(black) and* ***2·LbEu2*** *(mauve),* λ_{ex} *= 393 nm, 298 K.*

2.6.2.2 Time-gated Luminescence of Eu(III) Complexes

Luminescent lifetimes of both the *E*-enriched and *Z*-enriched PSS's of **2·LaEu** and **2·LbEu2** were measured by monitoring the emission intensity of the $^5D_0 \rightarrow {}^7F_2$ transition (λ_{em} = 616 nm) upon the excitation into the $^7F_0 \rightarrow {}^5L_6$ transition (λ_{ex} = 394 nm), with a time delay of 10 ms and measured at both 298 K and 77 K (**Chapter 7**, Figure 7.8 and 7.9). The lifetimes calculated upon fitting the luminescence decay are tabulated in Table 2.1. At 298 K, both isomers of each

Eu(III) complex could be fit to a mono-exponential decay profile, resulting in luminescence lifetimes around1-1.5 ms. Notably, the luminescent lifetimes of each isomer were comparable, suggesting that in each isomer the environment around the Eu(III) cation is unchanged upon isomerisation. However, at 77 K, a bi-exponential decay was required to adequately fit the emission decay profile, suggesting that at low temperature there are two species present. This is consistent with slow exchange between the twisted square antiprismatic (TSAP) and square antiprismatic (SAP) isomers of the DO3A ligands, which are otherwise in fast exchange at 298 K, resulting in a solution-state lifetime representing a weighted average of both isomers.[76, 79, 183] Unfortunately, the data quality of the lifetime recorded for the *Z*-enriched PSS of **2·L$_a$Eu** at 77 K was not well resolved enough to fit well to a biexponential decay.

*Table 2. 1: Luminescence lifetimes (τ) of **2·L$_a$Eu** E-enriched PSS and Z-enriched PSS at 298 K and 77 K (λ_{ex} = 395 nm, λ_{em} = 616 nm, 5 nm excitation and emission slits, delay time = 10 ms).*

		τ (298 K) (ms)	**τ $_1$(77 K) (ms)**	**τ $_2$(77 K) (ms)**
EuL$_a$	***E***	1.15	0.21	0.77
	Z	1.34	0.55	-
Eu$_2$L$_b$	***E***	1.51	0.34	1.18
	Z	1.48	0.31	0.95

2.6.2.3 Understanding the Photophysical Mechanisms of the Eu(III) Complexes

In summary, although there is a significant change in the absorbance spectra upon photoisomerisation, the photophysical properties of the Eu(III) centre remain unchanged in both **2·L$_a$Eu** and **2·L$_b$Eu$_2$** upon isomerisation of the ligand. This is due to a lack of energy transfer from the ligand to the Eu(III) centre, which is attributed to the favourable non-radiative decay pathways available in the ligand, including photoisomerisation. Azobenzenes are known to be highly efficient luminescent quenchers as a result of the photochemical isomerisation and dissipation of energy *via* heat (dark quenchers).[184] Additionally, the triplet state of the ligand

is expected to be low lying in the NIR region, which would be lower in energy than the emissive $^5D_0$ excited state of Eu(III) (~17,000 cm^{-1}),[18] and thus energy transfer from the $^3T \rightarrow {}^5D_0$ would be an uphill process. A schematic energy level diagram depicting the predominant pathways in this system is described in Figure 2.19.

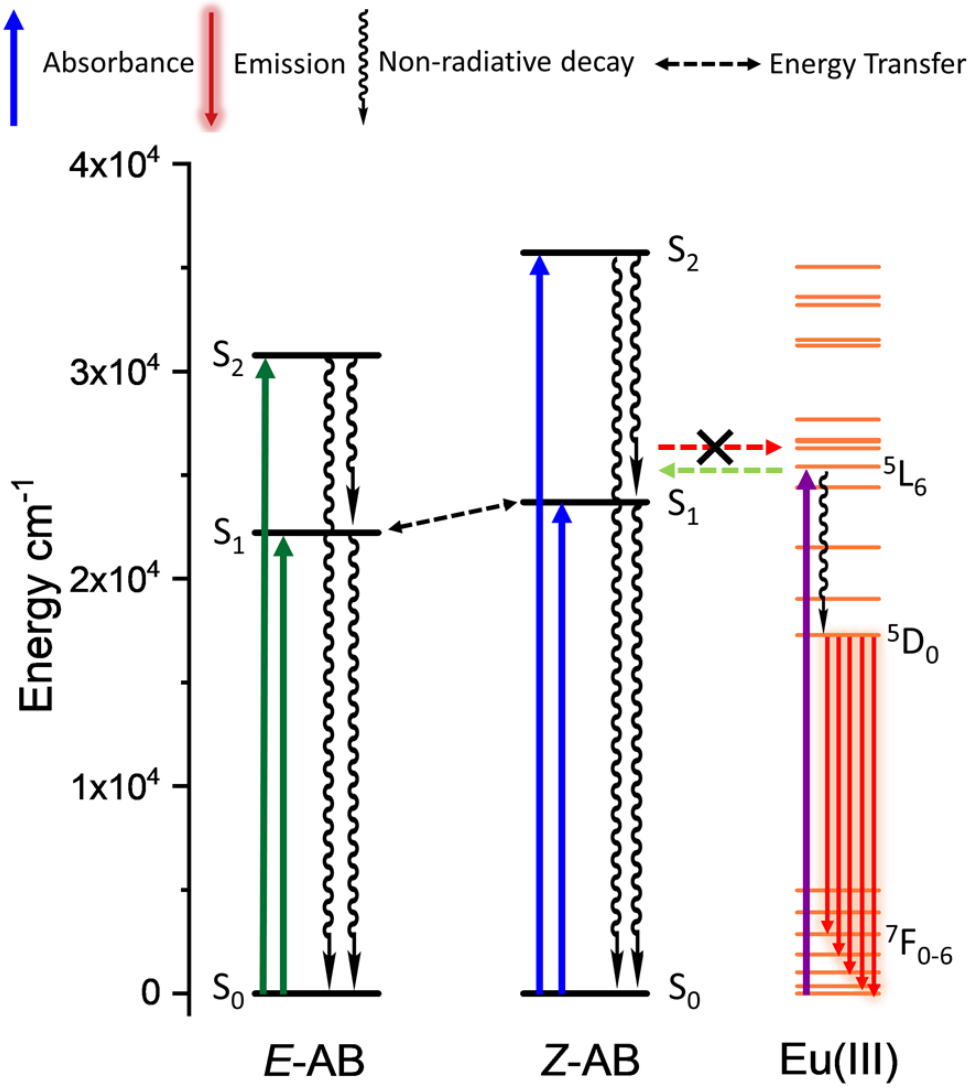


Figure 2.19: Jablonski diagram representing the energy levels of both the azobenzene and lanthanide components of the system. The azobenzene E and Z isomers can rapidly interconvert between each other upon excitation into both the S_2 and S_1 states, but cannot transfer energy into the excited states of Eu(III) in ***2·L$_a$Eu*** *and* ***2·L$_b$Eu$_2$*** *(as measured by Carnall et al).*[18]

Unfortunately, for both **2·L$_a$Eu** and **2·L$_b$Eu$_2$** direct excitation into the $^4F_0 \rightarrow {}^5L_6$, transition ($\lambda_{ex}$ = 393 nm) leads to slight perturbations in the PSS state distribution of *E* and *Z* isomers in solution due to spectra overlap. Therefore, the photoswitching is not completely orthogonal to the excitation of the Eu(III), Figure 2.19. To improve this orthogonality, a Ln(III) complex in

which the primary excitation of the Ln(III) lies outside that of the absorbance of both *E* and *Z* isomers of the photoswitch is required, and so attention was turned to the Nd(III) complexes, which can be excited at 580 nm, as the wavelength is outside the absorption range for the azobenzene.

2.6.3 Nd(III) Luminescence

Nd(III) steady-state emission and excitation spectra were recorded at 298 K, unless stated otherwise. For emission spectra, Nd(III) was directly excited into the $^4I_{9/2} \rightarrow {}^4G_{5/2}, {}^2G_{7/2}$ transition (λ_{ex} = 580 nm), a long-pass filter of 800 nm was used, and the centre wavelength of the detector was set to 880 or 1050 nm for the two regions of interest. The laser power was set to 90% with the maximum repetition rate (78 MHz). A 750B grating was used for measurements below the 950 nm point, and a 1200B grating was used for measurements above 950 nm. The emission slit was set to 25 μm for all measurements. For samples recorded at 77 K, a constant nitrogen flow in the sample chamber was maintained to avoid condensation on the cuvette.

Nd(III) has four emissive transitions occurring significantly into the NIR region at ~880 nm ($^4F_{3/2} \rightarrow {}^4I_{9/2}$), ~1060 nm ($^4F_{3/2} \rightarrow {}^4I_{11/2}$), ~1340 nm ($^4F_{3/2} \rightarrow {}^4I_{13/2}$) and ~1850 nm ($^4F_{3/2} \rightarrow {}^4I_{15/2}$).[163-165] Using a custom-built spectrometer in the group of Prof. Thomas Just Sørensen at the University of Copenhagen,[185] the maximum observable range is 500-1550 nm, and therefore the emission at ~1850 nm ($^4F_{3/2} \rightarrow {}^4I_{15/2}$) was not observable. Additionally, the emission at ~1340 nm ($^4F_{3/2} \rightarrow {}^4I_{13/2}$) for the Nd(III) complexes was extremely weak, and thus no high-quality emission spectra could be produced. For these reasons luminescent investigations concentrated on the emission spectra of both the higher energy transitions at ~880 nm ($^4F_{3/2} \rightarrow {}^4I_{9/2}$) and ~1060 nm ($^4F_{3/2} \rightarrow {}^4I_{11/2}$), Figure 2.20.

Upon direct excitation of the Nd(III) centre of the *E*-enriched state of **2·L$_a$Nd**, *via* the $^4I_{9/2} \rightarrow (^4G_{5/2}, ^2G_{7/2})$ transition (λ_{ex} = 580 nm) at 298 K, emission was observed from the $^4F_{3/2}$ state, corresponding to the $^4F_{3/2} \rightarrow {}^4I_{9/2}$ and $^4F_{3/2} \rightarrow {}^4I_{11/2}$ transitions (Figure 2.20). Nd(III) is a Kramer's ion, and in the absence of a magnetic field, both the $^4F_{3/2}$ and the $^4I_{9/2}$ ions split into 2 and 5 states, respectively (Figure 2.21).

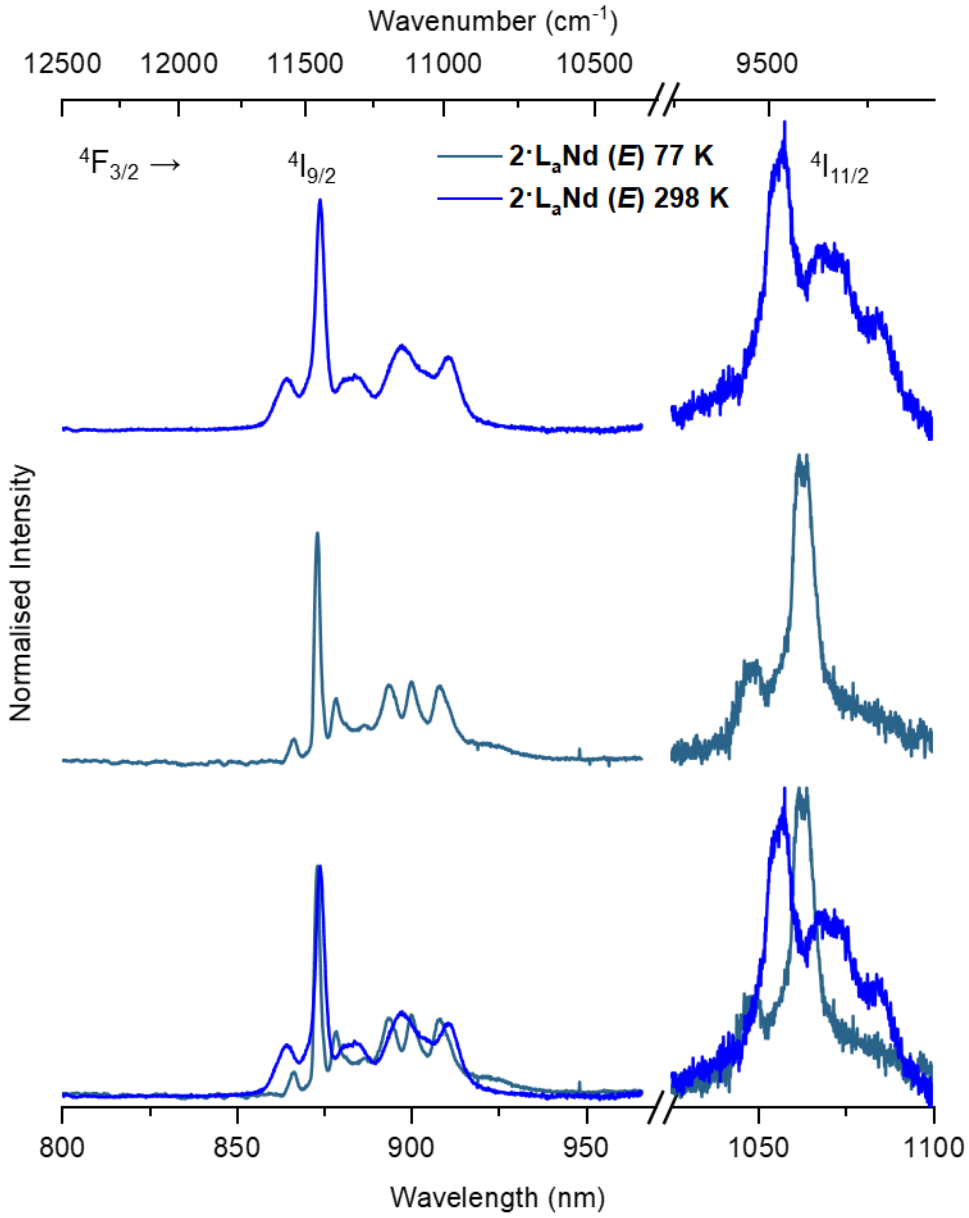


*Figure 2.20: Normalised emission spectra of E-enriched PSS of **2·L$_a$Nd**, upon excitation into the $^4I_{9/2} \rightarrow {}^4G_{5/2}, {}^2G_{7/2}$ transition (λ_{ex} = 580 nm) of Eu(III) at both 298 K (royal blue) and 77 K (dark blue).*

Therefore, a maximum of ten lines can be observed in the emission spectrum recorded around ~880 nm ($^4F_{3/2} \rightarrow {}^4I_{9/2}$). Additionally, the $^4I_{11/2}$ state can split into 6 states, so the emission at

~1060 nm ($^4F_{3/2} \rightarrow {}^4I_{11/2}$) can be described by 12 lines in the emission spectrum. In addition to the Kramer's ion splitting, there is a contribution from TSAP/SAP isomers and their capped and uncapped forms in solution, which further split the energy levels and increase the number of transitions. These transitions are very similar in energy (1-2 cm^{-1}), and overlap with other transitions. Therefore, the emission spectrum observed is an averaged spectrum describing all the transitions. To determine the crystal field splitting in more detail, the spectrum was obtained at 77 K, where the Boltzmann distribution was reduced and the transitions more defined (Figure 2.20).

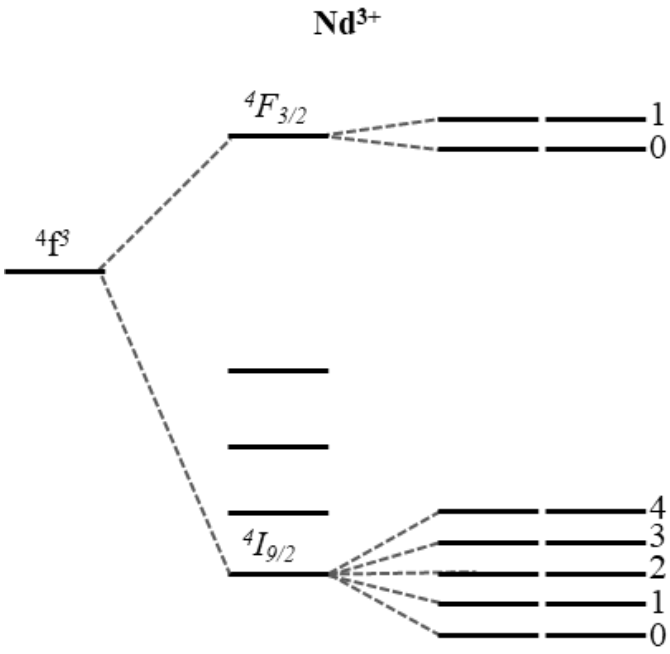


Figure 2.21: Splitting of the ground and excited state energy levels of Nd(III) as a result of Kramer's doublets in the absence of a magnetic field.

Similarly to that of the Eu(III) complexes, the Nd(III) emission of the *Z*-enriched state of **2·L$_a$Nd,** upon excitation at 580 nm, was almost identical to that of the *E* isomer (Figure 2.22). This demonstrates that the Nd(III) emission is dictated by the coordination environment around the Nd(III) centre, which remains unchanged upon photoisomerisation of the ligand.

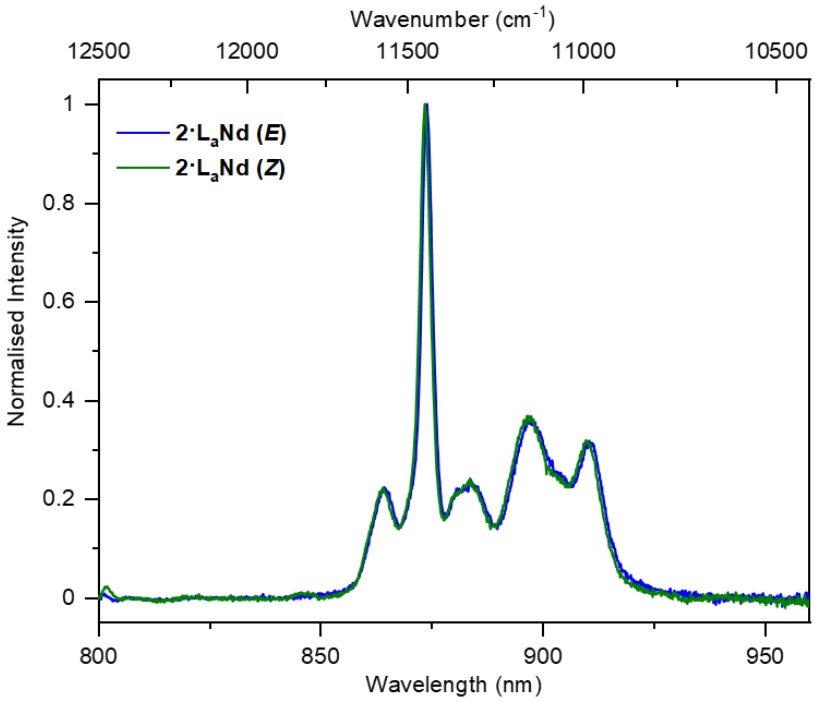


*Figure 2.22: Normalised emission spectra of E-enriched PSS (blue) and Z-enriched PSS (green) of **2·LaNd**, upon excitation (λ_{ex} = 580 nm).*

The excitation spectra (λ_{em} = 880 nm) of both the *E*-enriched and the *Z*-enriched states, along with the absorbance spectra of each isomeric state are shown in Figure 2.23. By monitoring the emission at 880 nm, the transitions observed describe the direct excitation of Nd(III) including the $^4I_{9/2} \rightarrow (^2K_{13/2}, {}^4G_{9/2})$, $^4I_{9/2} \rightarrow (^4G_{5/2}, {}^2G_{7/2})$, $^4I_{9/2} \rightarrow (^4F_{7/2}, {}^2S_{3/2})$, and $^4I_{9/2} \rightarrow (^4F_{5/2}, {}^2H_{9/2})$ transitions. Comparison of the excitation spectra of both the *E*-enriched and *Z*-enriched PSS of **2·LaNd** shows no significant difference upon photoisomerisation. This observation supports the conclusion that isomerisation of the ligand has no effect on the crystal field splitting of the Nd(III) centre. Notably, the absence of a broad peak in the blue region suggests that there is no contribution from an antenna in the excitation spectra, in agreement with the observations from the analogous Eu(III) complexes.

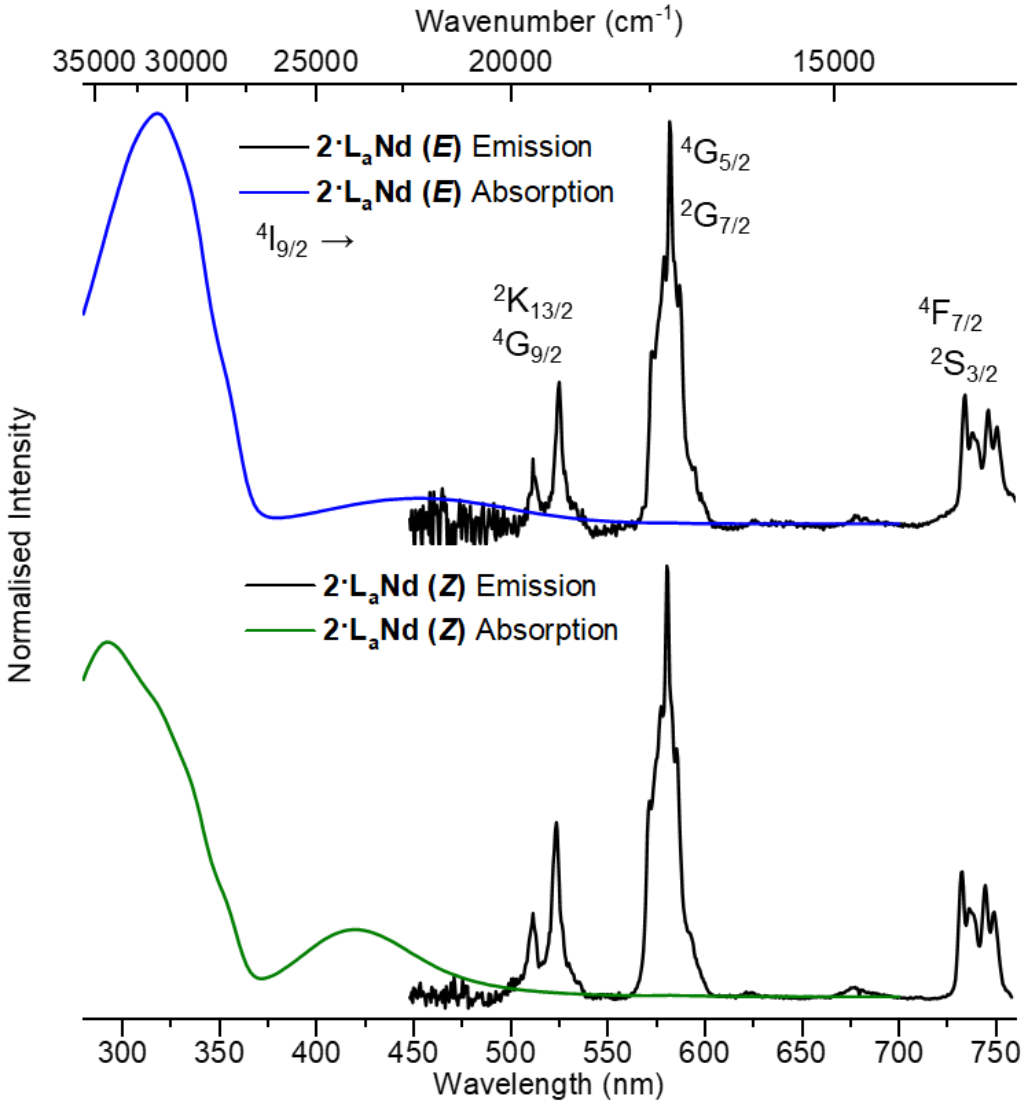


Figure 2.23: top) Absorption spectra of E-enriched PSS (blue) and the corresponding excitation spectra (black) bottom) Absorption spectra of Z-enriched PSS (green) and the corresponding excitation spectra (black). Emission monitored at 616nm at 298 K, all spectra normalised.

Analogous experiments were repeated for **2·L$_b$Nd$_2$**, which showed that there were no significant differences in the electronic transitions of the normalised emission (λ_{ex} = 580 nm) and excitation spectra (λ_{em} = 810 nm) between the mononuclear and binuclear complexes, and therefore the luminescent properties are defined by the coordination environment dictated by the DO3A macrocycle (Figure 2.24).

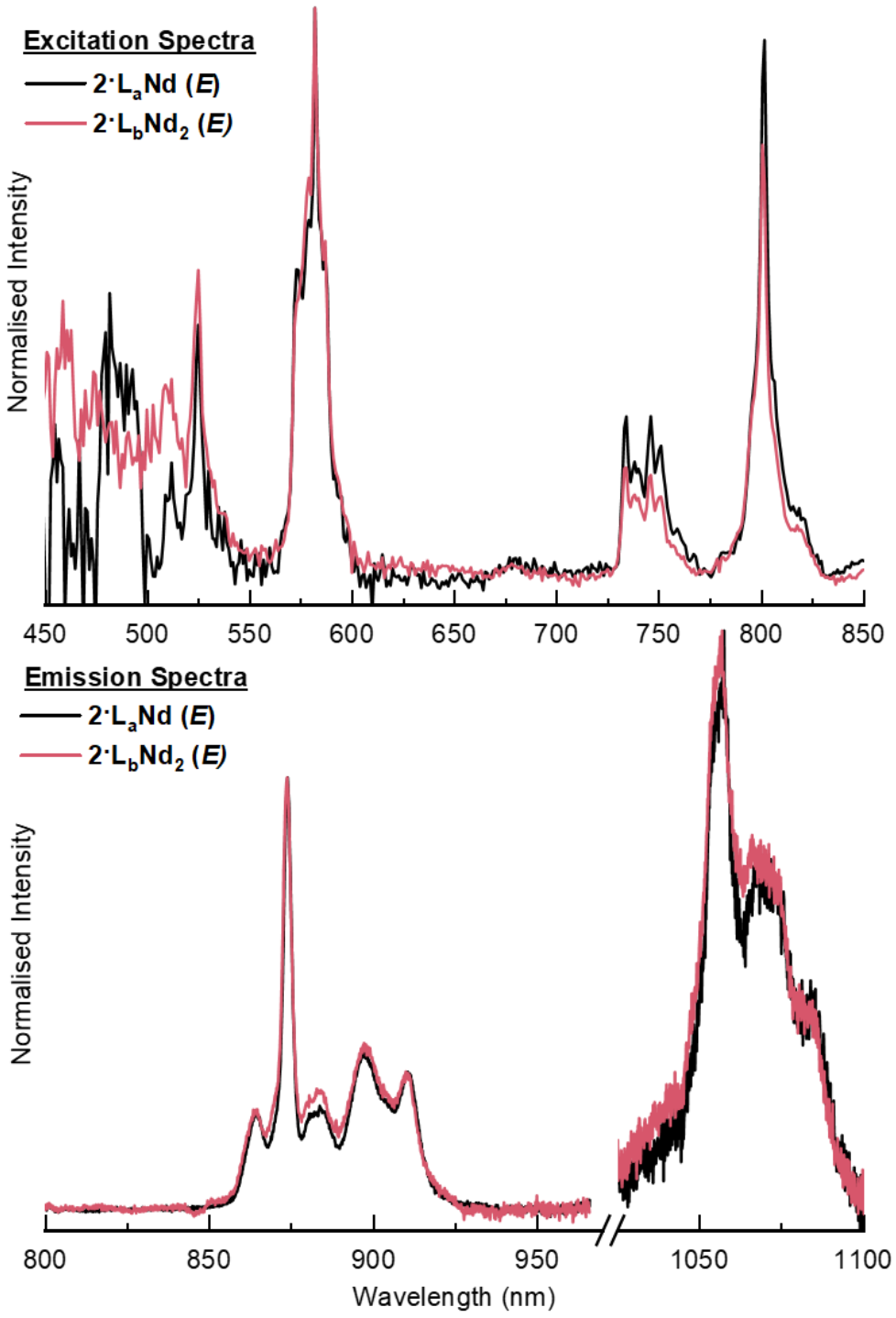


Figure 2.24: top) normalised excitation spectra of E-enriched PSS of ***2·L$_a$Nd*** *(black) and* ***2·L$_b$Nd$_2$*** *(mauve), λ_{em} = 880 nm, 77 K, bottom) normalised emission spectra of E-enriched PSS of* ***2·L$_a$Nd*** *(black) and* ***2·L$_b$Nd$_2$*** *(mauve), λ_{ex} = 580 nm, 77 K.*

Focussing on orthogonality, the choice of excitation wavelength for Nd(III) was carefully considered. The highest energy excitation into the $^4I_{9/2} \rightarrow (^2K_{13/2}, ^4G_{9/2})$ transition overlaps with the tail of the absorbance of the $n \rightarrow \pi^*$ transitions of the *E* and *Z* isomers, therefore this was considered to be not a good candidate for the orthogonal Nd(III) excitation. However, the

most intense transition of the $^4I_{9/2} \rightarrow (^4G_{5/2}, {}^2G_{7/2})$ occurs around 580 nm, which is beyond the absorbance of both isomeric forms of the azobenzene and, therefore, a good candidate to investigate the orthogonal switching and excitation (Figure 2.25).

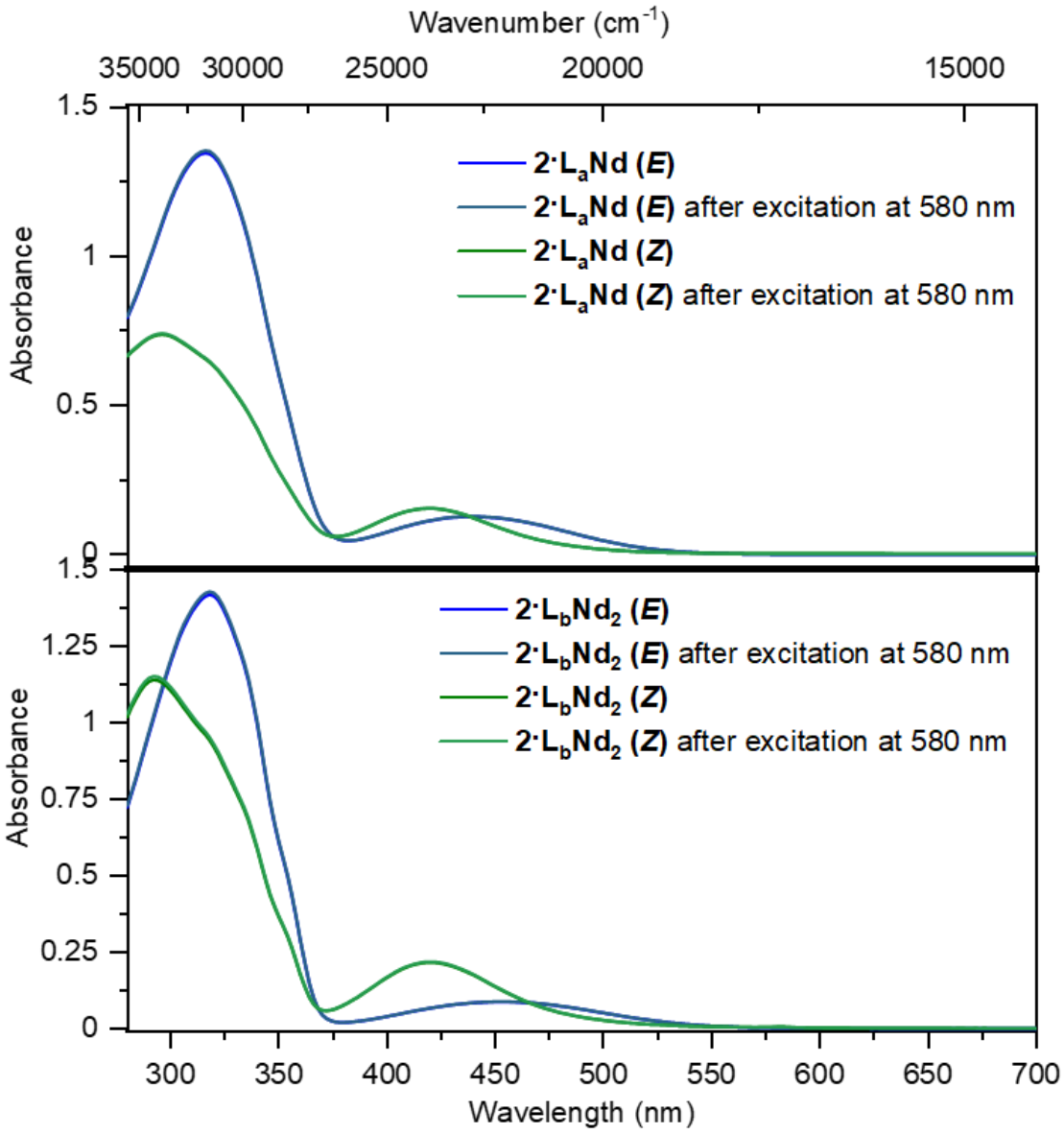


*Figure 2.25: top) absorption spectra of the **2·LaNd** E/Z-enriched states before and after irradiation at 580 nm, bottom) absorption spectra of the **2·LbNd2** E/Z-enriched states before and after irradiation at 580 nm*

To investigate the change in PSS distribution of both the *E*-enriched and *Z*-enriched states of **2·LaNd** and **2·LbNd2** upon excitation with 580 nm light, the absorbance spectra were recorded before and after excitation (Figure 2.25). Notably, there was no significant difference in the absorption before and after excitation for either mononuclear or binuclear complex in either

isomeric form. Therefore, in this system, the Nd(III) luminescent properties are completely decoupled and orthogonal to the azobenzene ligand.

2.6.3.1 Understanding the Photophysical Mechanisms of Nd(III) Complexes

In summary, the ligand showed no observable influence on the luminescent properties of the Nd(III) metal centres in each of the complexes studied. Additionally, upon excitation at 580 nm, directly into the $^4I_{9/2} \rightarrow (^4G_{5/2}, {}^2G_{7/2})$ transition, there was no change in the PSS distribution of the isomerically enriched states, and therefore, excitation at 580 nm does not contribute to the photoswitching of the azobenzene ligands in either direction (Figure 2.26).

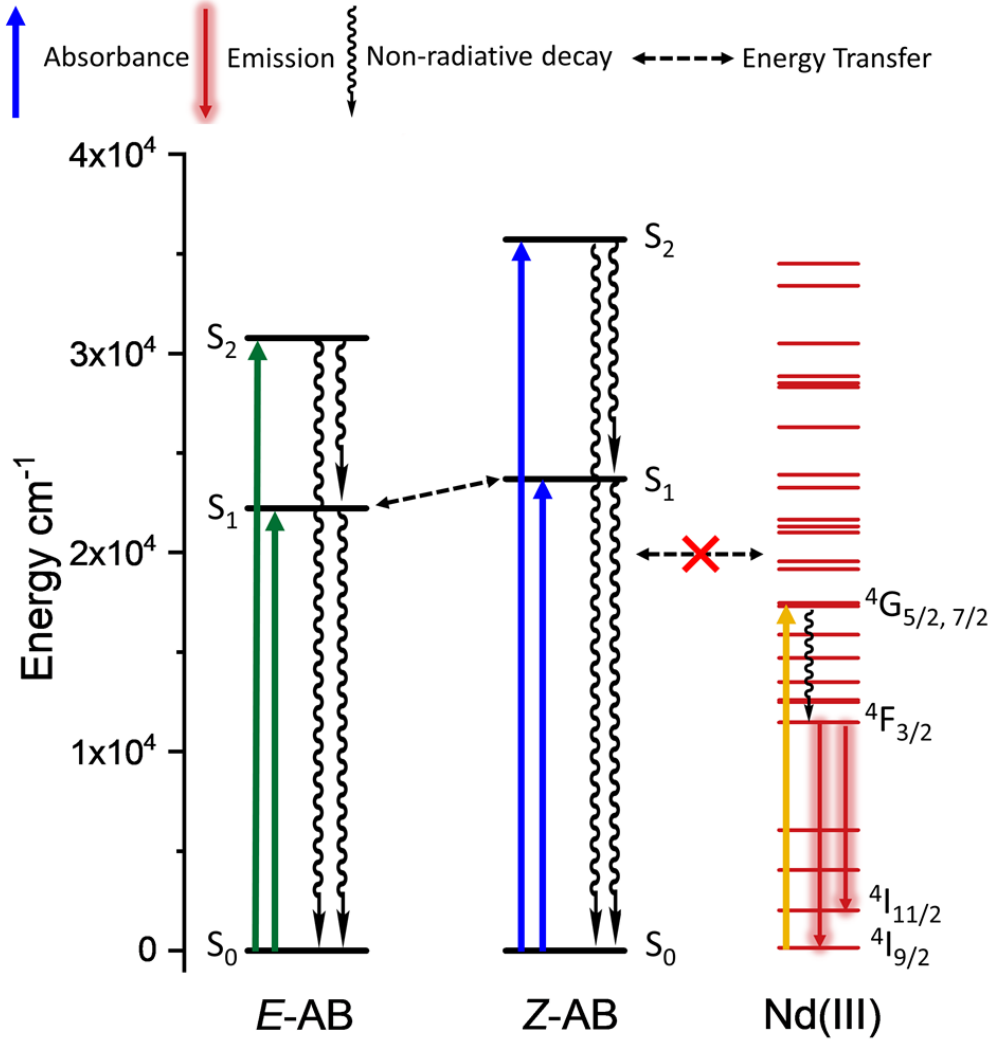


Figure 2.26: Jablonski diagram representing the energy levels of both the azobenzene and lanthanide components of the system. The azobenzene E and Z isomers can rapidly interconvert between each other upon excitation into both the S_2 and S_1 states, but cannot transfer energy into the excited states of Nd(III) in ***2·L$_a$Nd*** *and* ***2·L$_b$Nd$_2$*** *(as measured by Carnall et al).*[18]

The complete orthogonality of the system is somewhat unexpected as previous reports have determined that the triplet (T_1) state of a tetra-*ortho*-flouroazobenzene resides around ~12,000 cm^{-1}.[172, 173, 186] This would suggest that there should be sufficient spectral overlap of the azobenzene T_1 state with the excited states of Nd(III) (Figure 2.27). However, the excitation spectra of the Nd(III)-azobenzene complexes reveal that no emission is observed upon excitation into the azobenzene core, so presumably the lack of sensitisation in the Nd(III) complexes is a result of inefficient energy transfer. Previous studies have reported that the rate of intersystem crossing (ISC) between the S_1 and T_1 states is as fast as 10^{11} s^{-1} for azobenzenes.[180, 187] Therefore, it is speculated that the ISC between *E* and *Z* isomers is much faster than the rate of energy transfer from the T_1 state of the azobenzene ligand to the Nd(III) excited state, such that, despite sufficient spectral overlap between T_1 and Nd(III), the excited Nd(III) states are not populated to a significant degree *via* the T_1 state of the ligand.

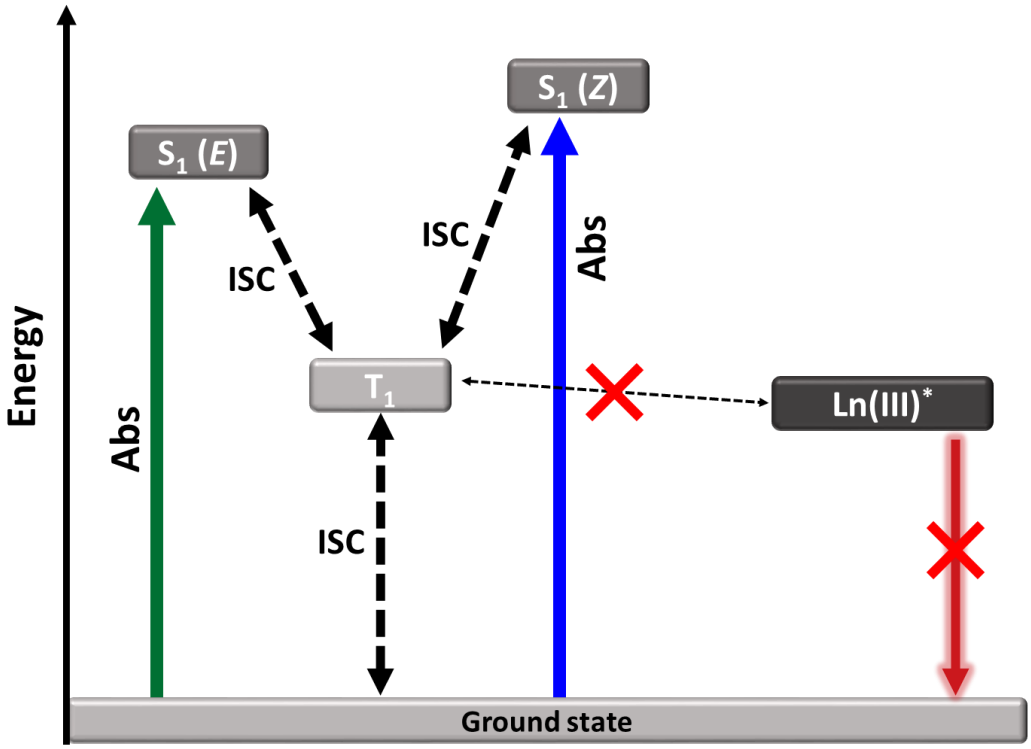


Figure 2.27: Schematic diagram describing the dominating processes underpinning the photophysics of ***2·L$_a$Nd*** *and* ***2·L$_b$Nd$_2$****, dashed lines represent intersystem crossing (ISC), with bolded dashed lines representing the fast and dominant ISC between S_1 and T_1. Solid lines represent absorbance into the azobenzene S_1 states.*

2.7 Conclusions

This chapter describes the first examples of kinetically stable photoswitchable emissive lanthanide complexes in which the system can be controlled and interrogated by orthogonal wavelengths of visible and near-IR light. The synthesis of a family of mono- and binuclear complexes, **2·L_aEu**, **2·$L_b$$Eu_2$**, **2·$L_a$Nd** and **2·$L_b$$Nd_2$,** was reported. Both the symmetric and asymmetric azobenzene photoswitches were initially synthesised, and subsequent functionalisation in the *para*-position with a DO3A macrocycle allowing for the coordination of Ln(III) cations ensured a kinetically stable complex in solution. Analysis of both the mono- and binuclear Eu(III) and Nd(III) photoswitchable complexes upon irradiation with 405 nm (blue) light and 530 nm (green) light for 10 minutes revealed high PSS distributions for both the *E*-enriched state and the *Z*-enriched state. In both Eu(III) and Nd(III) complexes, there was no contribution of the azobenzene ligand in the Ln(III) luminescence despite good spectral overlap, which is attributed to the rate and availability of non-radiative decay pathways, particularly the photoisomerisation of the azobenzene. In the Eu(III) complexes, upon direct excitation at 393 nm, there was a change in the PSS distribution of *E*-enriched and *Z*-enriched states due to spectral overlap with the absorbance of the *E*/*Z* isomers. However, moving to the Nd(III) analogues, in which direct excitation can occur outside of the absorbance of the ligand at 580 nm, there was no change in the PSS distribution upon excitation. This, therefore, represents an unprecedented fully orthogonal system, in which both visible light-mediated switching and lanthanide excitation and emission are entirely independent, allowing the system to be controlled and interrogated by four orthogonal wavelengths of light. This feature is requisite for applications in read/write optical information storage, and we anticipate that these results will pave the way for applications of such photoswitchable emissive complexes in this area, as well as more generally opening up new approaches to interrogating molecular photoswitchable devices by emission spectroscopy.

2.8 References for Chapter 2

1. P. Hong, N.-H. Xie, K. Xiong, J. Liu, M.-Q. Zhu and C. Li, *J. Mater. Chem. A*, 2023, **11**, 5703-5713.
2. T. Nakagawa, Y. Hasegawa and T. Kawai, *Chem. Commun.*, 2009, 5630-5632.
3. M. M. Lerch, M. J. Hansen, W. A. Velema, W. Szymanski and B. L. Feringa, *Nat. Commun.*, 2016, **7**, 12054.
4. J. C. G. Bünzli and C. Piguet, *Chem. Soc. Rev.*, 2005, **34**, 1048-1077.
5. W. T. Carnall, P. R. Fields and K. Rajnak, *J. Chem. Phys.*, 1968, **49**, 4424-4442.
6. W. T. Carnall, P. R. Fields and K. Rajnak, *J. Chem. Phys*, 1968, **49**, 4450-4455.
7. W. T. Carnall, P. R. Fields and K. Rajnak, *J Chem Phys*, 1968, **49**, 4412.
8. W. T. Carnall, P. R. Fields and K. Rajnak, *J Chem Phys*, 1968, **49**, 4443.
9. W. T. Carnall, P. R. Fields and K. Rajnak, *J Chem Phys*, 1968, **49**, 4447.
10. Bünzli, JC.G., Eliseeva, S.V. (2010). Basics of Lanthanide Photophysics. In: Hänninen, P., Härmä, H. (eds) Lanthanide Luminescence. Springer Series on Fluorescence, vol 7. Springer, Berlin, Heidelberg. https://doi.org/10.1007/4243_2010_3
11. P. Kobauri, F. J. Dekker, W. Szymanski and B. L. Feringa, *Angew. Chem. Int. Ed.*, 2023, **62**.
12. S. Crespi, N. A. Simeth and B. König, *Nat. Rev. Chem.*, 2019, **3**, 133-146.
13. J. Volarić, W. Szymanski, N. A. Simeth and B. L. Feringa, *Chem. Soc. Rev.*, 2021, **50**, 12377-12449.
14. D. H. Qu, Q. C. Wang, Q. W. Zhang, X. Ma and H. Tian, *Chem. Rev.*, 2015, **115**, 7543-7588.
15. A. Goulet-Hanssens, F. Eisenreich and S. Hecht, *Adv. Mater.*, 2020, **32**, 1905966.
16. E. R. Ruskowitz and C. A. Deforest, *Nat. Rev. Mater.*, 2018, **3**, 17087.
17. Y. Zhou, H. Ye, Y. B. Chen, R. Y. Zhu and L. C. Yin, *Biomacromolecules*, 2018, **19**, 1840-1857.
18. S. B. N., W. S. Yam and G. Hegde, *RSC Adv.*, 2019, **9**, 40588-40606.
19. Y. Hasegawa, T. Nakagawa and T. Kawai, *Coord. Chem. Rev.*, 2010, **254**, 2643-2651.
20. P. Selvanathan, E. Tufenkjian, O. Galangau, T. Roisnel, F. Riobé, O. Maury, L. Norel and S. Rigaut, *Inorg. Chem.*, 2023, **62**, 2049-2057.
21. H. Al Sabea, L. Norel, O. Galangau, T. Roisnel, O. Maury, F. Riobé and S. Rigaut, *Adv. Funct. Mater.*, 2020, **30**, 2002943.
22. H. Al Sabea, L. Norel, O. Galangau, H. Hijazi, R. Métivier, T. Roisnel, O. Maury, C. Bucher, F. Riobé and S. Rigaut, *J. Am. Chem. Soc.*, 2019, **141**, 20026-20030.
23. X. He, L. Norel, Y.-M. Hervault, R. Métivier, A. D'Aléo, O. Maury and S. Rigaut, *Inorg. Chem.*, 2016, **55**, 12635-12643.
24. T. Nakagawa, Y. Hasegawa and T. Kawai, *J. Phys. Chem. A*, 2008, **112**, 5096-5103.
25. T. Nakagawa, K. Atsumi, T. Nakashima, Y. Hasegawa and T. Kawai, *Chem. Lett.*, 2007, **36**, 372-373.
26. H. B. Cheng, H. Y. Zhang and Y. Liu, *J. Am. Chem. Soc.*, 2013, **135**, 10190-10193.
27. L.-R. Lin, X. Wang, G.-N. Wei, H.-H. Tang, H. Zhang and L.-H. Ma, *Dalton Trans.*, 2016, **45**, 14954-14964.
28. F. Hu, X. Li, Y. M. Leng, Y. H. Zhang, M. J. Zhou and Y. P. Ou, *Inorg. Chim. Acta*, 2017, **458**, 45-49.
29. Y.-G. Wang, Y.-Q. Li, H.-H. Tang, L.-R. Lin and L.-H. Ma, *ACS Omega*, 2018, **3**, 5480-5490.
30. L. R. Lin, H. H. Tang, Y. G. Wang, X. Wang, X. M. Fang and L. H. Ma, *Inorg. Chem.*, 2017, **56**, 3889-3900.

31. M. Cieslikiewicz-Bouet, S. V. Eliseeva, V. Aucagne, A. F. Delmas, I. Gillaizeau and S. Petoud, *RSC Adv.*, 2019, **9**, 1747-1751.
32. A. Guesdon-Vennerie, P. Couvreur, F. Ali, F. Pouzoulet, C. Roulin, I. Martínez-Rovira, G. Bernadat, F. X. Legrand, C. Bourgaux, C. L. Mazars, S. Marco, S. Trépout, S. Mura, S. Mériaux and G. Bort, *Nat. Commun.*, 2022, **13**.
33. P. P. Lima, M. M. Nolasco, F. A. A. Paz, R. A. S. Ferreira, R. L. Longo, O. L. Malta and L. D. Carlos, *Chem. Mater.*, 2013, **25**, 586-598.
34. M. Irie, T. Fulcaminato, K. Matsuda and S. Kobatake, *Chem. Rev.*, 2014, **114**, 12174-12277.
35. T. Nakagawa, Y. Hasegawa and T. Kawai, *Chem. Commun.*, 2009, 5630.
36. E. Di Piazza, L. Norel, K. Costuas, A. Bourdolle, O. Maury and S. Rigaut, *J. Am. Chem. Soc.*, 2011, **133**, 6174-6176.
37. H. M. D. Bandara and S. C. Burdette, *Chem. Soc. Rev.*, 2012, **41**, 1809-1825.
38. M. Di Martino, L. Sessa, R. Diana, S. Piotto and S. Concilio, *Molecules*, 2023, **28**.
39. T. Eom, W. Yoo, S. Kim and A. Khan, *Biomaterials*, 2018, **185**, 333-347.
40. Y. R. Choi, G. C. Kim, H.-G. Jeon, J. Park, W. Namkung and K.-S. Jeong, *Chem. Commun.*, 2014, **50**, 15305-15308.
41. A. A. Beharry and G. A. Woolley, *Chem. Soc. Rev.*, 2011, **40**, 4422.
42. M. H. V. Werts, R. T. F. Jukes and J. W. Verhoeven, *Phys. Chem. Chem. Phys.*, 2002, **4**, 1542-1548.
43. M. H. V. Werts, *Sci. Prog.*, 2005, **88**, 101-131.
44. N. Kofod, P. Nawrocki and T. J. Sorensen, *J. Phys. Chem. Lett.*, 2022, **13**, 3096-3104.
45. M. S. Thomsen, P. R. Nawrocki, N. Kofod and T. J. Sorensen, *Eur. J. Inorg. Chem.*, 2022, **2022**.
46. K. Binnemans, *Coordin. Chem. Rev.*, 2015, **295**, 1-45.
47. V. R. M. Nielsen, P. R. Nawrocki and T. J. Sorensen, *J. Phys. Chem. A*, 2023, **127**, 3577-3590.
48. P. R. Nawrocki and T. J. Sørensen, *Phys. Chem. Chem. Phys.*, 2023, **25**, 19300-19336.
49. A. Beeby and S. Faulkner, *Chem. Phys. Lett.*, 1997, **266**, 116-122.
50. R. Z. W.C Martin, Lucy Hagan, *Atomic Energy Levels—The Rare-Earth Elements The Spectra of Lanthanum, Cerium, Praseodymium,Neodymium, Promethium, Samarium, Europium,Gadolinium, Terbium, Dysprosium, Holmium, Erbium,Thulium, Ytterbium, and Lutetium*, Institute for basic standards, Washington D.C, 1978.
51. T. J. Sørensen and S. Faulkner, *Acc. Chem. Res.*, 2018, **51**, 2493-2501.
52. J. D. Routledge, M. W. Jones, S. Faulkner and M. Tropiano, *Inorg. Chem.*, 2015, **54**, 3337-3345.
53. M. Tropiano, A. M. Kenwright and S. Faulkner, *Chem. Eur. J.*, 2015, **21**, 5697-5699.
54. M. Tropiano, C. J. Record, E. Morris, H. S. Rai, C. Allain and S. Faulkner, *Organometallics*, 2012, **31**, 5673-5676.
55. A. L. Leistner, S. Kirchner, J. Karcher, T. Bantle, M. L. Schulte, P. Gödtel, C. Fengler and Z. L. Pianowski, *Chem. Eur. J.*, 2021, **27**, 8094-8099.
56. C. Knie, M. Utecht, F. L. Zhao, H. Kulla, S. Kovalenko, A. M. Brouwer, P. Saalfrank, S. Hecht and D. Bléger, *Chem. Eur. J.*, 2014, **20**, 16492-16501.
57. C. Knie, M. Utecht, F. Zhao, H. Kulla, S. Kovalenko, A. M. Brouwer, P. Saalfrank, S. Hecht and D. Bléger, *Chem. Eur. J.*, 2014, **20**, 16492-16501.
58. D. Bléger, J. Schwarz, A. M. Brouwer and S. Hecht, *J. Am. Chem. Soc.*, 2012, **134**, 20597-20600.
59. K. Kuntze, J. Viljakka, E. Titov, Z. Ahmed, E. Kalenius, P. Saalfrank and A. Priimagi, *Photochem. Photobio. Sci.*, 2022, **21**, 159-173.

60. J. Isokuortti, K. Kuntze, M. Virkki, Z. Ahmed, E. Vuorimaa-Laukkanen, M. A. Filatov, A. Turshatov, T. Laaksonen, A. Priimagi and N. A. Durandin, *Chem. Sci.*, 2021, **12**, 7504-7509.
61. Z. Ahmed, A. Siiskonen, M. Virkki and A. Priimagi, *Chem. Commun.*, 2017, **53**, 12520-12523.
62. L. G. Nielsen and T. J. Sorensen, *Inorg. Chem.*, 2020, **59**, 94-105.
63. I. C. D. Merritt, D. Jacquemin and M. Vacher, *Phys. Chem. Chem. Phys.*, 2021, **23**, 19155-19165.
64. T. Fujino, S. Y. Arzhantsev and T. Tahara, *J. Phys. Chem. A*, 2001, **105**, 8123-8129.
65. T. Fujino and T. Tahara, *J. Phys. Chem. A*, 2000, **104**, 4203-4210.
66. I. K. Lednev, T. Q. Ye, P. Matousek, M. Towrie, P. Foggi, F. V. R. Neuwahl, S. Umapathy, R. E. Hester and J. N. Moore, *Chem. Phys. Lett.*, 1998, **290**, 68-74.
67. I. K. Lednev, T. Q. Ye, R. E. Hester and J. N. Moore, *Am. J. Phys. Chem.*, 1996, **100**, 13338-13341.
68. E. R. Talaty and J. C. Fargo, *Chem. Commun.*, 1967, **0**, 65-66.
69. P. Bortolus and S. Monti, *Am. J. Phys. Chem.*, 1979, **83**, 648-652.
70. C. M. Stuart, R. R. Frontiera and R. A. Mathies, *J. Phys. Chem. A*, 2007, **111**, 12072-12080.
71. K. J. Miller, A. A. Saherwala, B. C. Webber, Y. Wu, A. D. Sherry and M. Woods, *Inorg. Chem.*, 2010, **49**, 8662-8664.
72. G. Tircso, B. C. Webber, B. E. Kucera, V. G. Young and M. Woods, *Inorg. Chem.*, 2011, **50**, 7966-7979.
73. A. Chevalier, C. Massif, P. Y. Renard and A. Romieu, *Chem. Eur. J.*, 2013, **19**, 1686-1699.
74. P. R. Nawrocki, V. R. M. Nielsen and T. J. Sorensen, *Methods Appl. Fluoresc.*, 2022, **10**.
75. S. Monti, E. Gardini, P. Bortolus and E. Amouyal, *Chem. Phys. Lett.*, 1981, **77**, 115-119
76. S. Axelrod, E. Shakhnovich and R. Gómez-Bombarelli, *ACS Cent. Sci.*, 2023, **9**, 166-176.

Chapter 3

Binuclear Lanthanide Complexes for Redox Sensing

3.1 Introduction

This chapter describes the design, synthesis and photophysical properties of a range of binuclear lanthanide(III) probes which respond to redox changes in an environment. These systems demonstrate the utility of irreversible ligand modification on the lanthanide luminescence in response to an external stimulus. In short, the binuclear Ln(III) complexes respond upon exposure to reductive environments *via* an irreversible reduction of the ligand. This in turn alters the fundamental optical and magnetic resonance properties of the Ln(III) complexes. Thus, this envisions both optical and magnetic resonance probes for the sensing of reductive environments. Two compounds in this chapter were previously synthesised and the luminescent properties studied by Dr Daniel Kovacs. Further analysis on these complexes were completed by myself and detailed in this chapter. This work in this chapter is currently under peer-review at JACS.

3.1.1 Understanding Redox Environments

Redox is a term that encompasses both reducing and oxidising environments. Oxidising environments, occur in the presence of oxygen and oxygen containing chemicals such as reactive oxygen species (ROS). In contrast, reductive environments occur predominantly at low levels of oxygen, often in the presence of hydrogen containing chemicals. The redox state of biological environments underpins a variety of important biological process, including cellular respiration.[188] Therefore, understanding the redox state of cells, tissues and organs in both plants and animals can allow detailed insight into the mechanisms that occur in biological

processes.[189-191] Importantly, biological tissues suffering from extreme redox environments can result in damaging processes and are often a sign of underlying disease.[192-194]

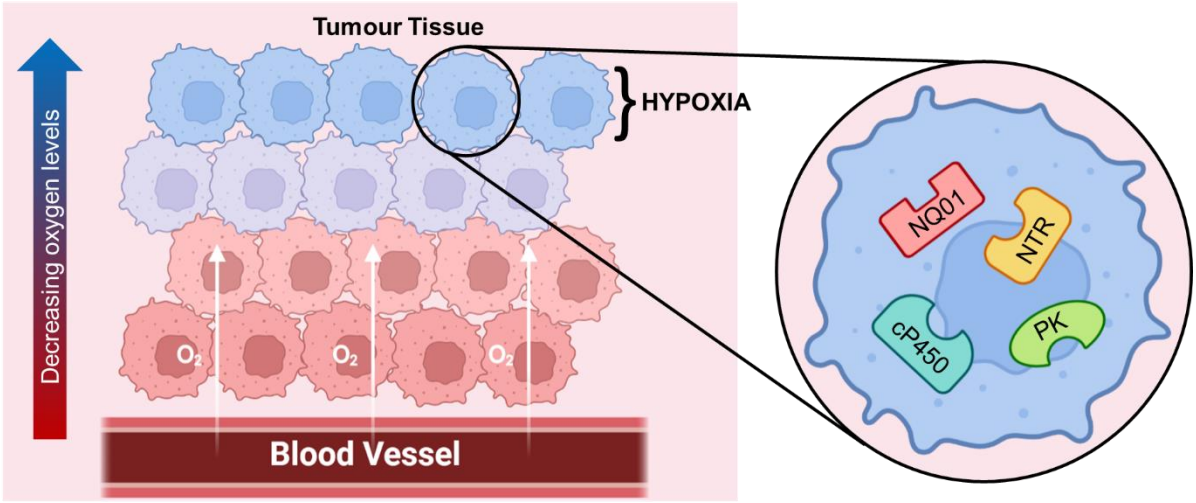
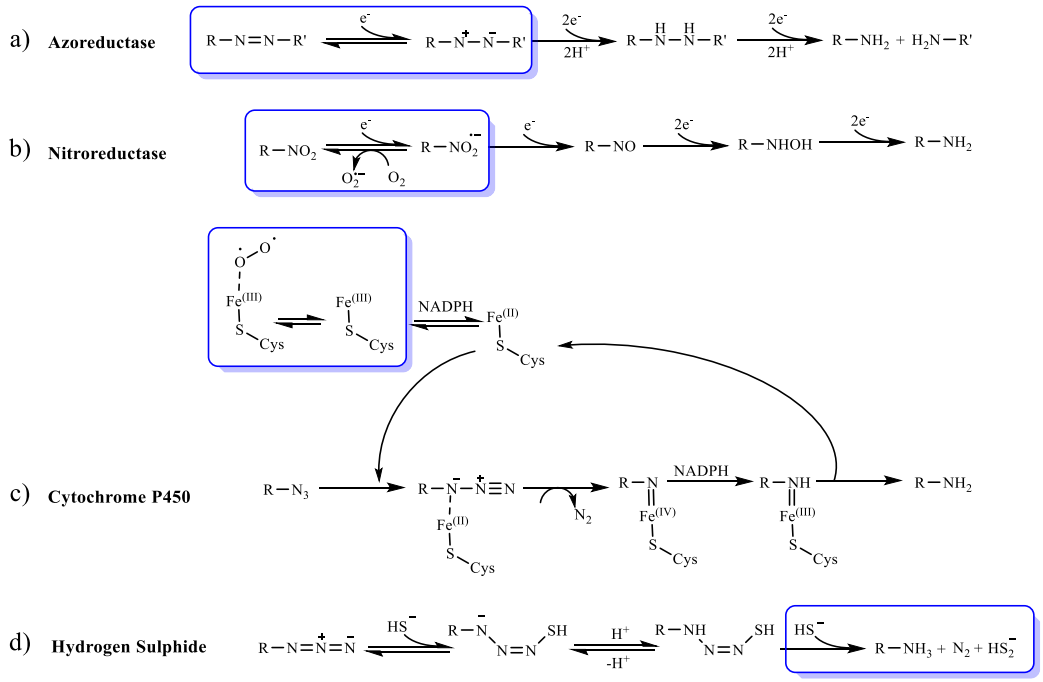


Figure 3.1: Diagram to describe hypoxia in cancerous tumours and thus the overexpression of common reductase enzymes: nitroquinone reductase 1 (NQ01), nitroreductase (NTR), cytochrome P450s (cP450) and pyruvate kinase (PK).[195]

Hypoxia, occurs when there are low levels of oxygen in biological tissues.[195] Hypoxia can occur naturally, in important processes such as menstruation, where it is important for endometrial repair, [196] or due to prolonged exposure to low levels of oxygen at high altitude.[197] Interestingly, chronic long term hypoxia has led to biological adaptations for communities living at high altitudes in which their red blood cells have increased capacity for absorbing oxygen.[198, 199] However, most commonly hypoxia is a sign of underlying disease, such as chronic obstructive pulmonary disease (COPD), diabetes, and cancer.[200]

In cancer, tumours can become hypoxic as a result of rapid cell proliferation and the disruption of tumour vasculature (Figure 3.1), these hypoxic tumours are particularly treatment resistant and result in poor patient prognosis.[201, 202] By understanding the role and mechanism of hypoxia in cancer tumours, they themselves can be more deeply understood and thus lead to better therapeutics and improved patient prognosis. Hypoxic tissues can also induce the overexpression of a range of reductase enzymes,[203] including cytochrome p450s,[204, 205] nitroreductases[206, 207] and azoreductases,[208] which can catalyse the oxygen dependent multi-

electron reduction of azides, nitroaromatics and azobenzenes respectively (Scheme 3.1).[209-211] By utilising these transformations, a number of chemical probes for sensing reductive environments have been developed.[212-218]



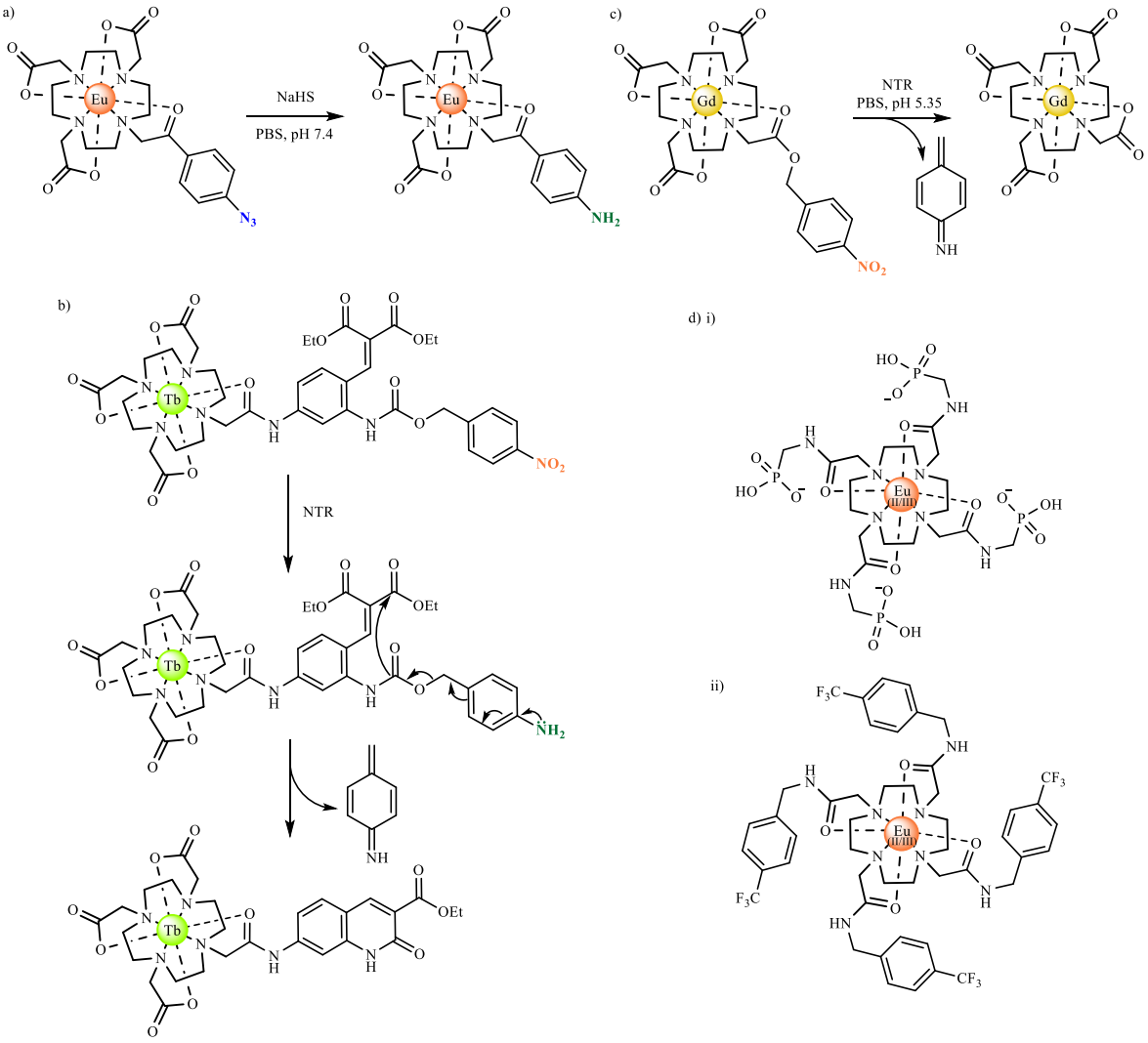
Scheme 3.1: Reduction mechanisms of commonly overexpressed reductase enzymes in hypoxic environments a) Azobenzene reduction via azoredcuctases,[208] b) nitroaryl reduction via nitroreductases c) Azide reduction via cytochrome P450s,[211] and d) Azide reduction via hydrogen sulphide.[219]

Hydrogen sulphide is a key endogenous gasotransmitter and a biomarker for hypoxia. Under hypoxic conditions hydrogen sulphide accumulates in biological tissues and subsequently inhibits mitochondrial respiration.[220] Hydrogen sulphide also selectively reduces aryl azides, to the corresponding aniline, and thus aryl azide based probes can be used to determine the levels of hydrogen sulphide in hypoxic environments.[107, 221]

3.1.2 Lanthanide(III) Redox Probes in the Literature

Lanthanide(III) cations have been used extensively in the development of chemical probes due to their intrinsic magnetic and optical properties. Particularly, Gd(III) complexes have been widely used in the development of magnetic resonance (MR) probes for applications in contrast

imaging and diagnostics.[222-224] By careful design of the ligand, responsive MR probes have been realised which target specific tissues or respond to biochemical stimuli.[106, 225]



Scheme 3.2:a) A Eu(III)-azide optical probe for the sensing of hydrogen sulphide,[107] b) A Tb(III)-caged carbostyril probe for the optical sensing of nitroreductase in bacteria,[207] c) A Gd(III)-caged DOTA magnetic resonance probe for the sensing of nitroreductase,[226] d)i) A Eu(II/III)-phosphonate magnetic resonance probe for sensing hypoxia,[227] ii) a ratiometric Eu(II/III)-^{19}F magnetic resonance probe for sensing hypoxia.[228]

Additionally, the intrinsic long lived luminescence of Ln(III) cations has led to the development of numerous optical imaging probes.[106] Many examples of luminescent lanthanide probes utilise the antenna effect for improved luminescence quantum yields by indirectly populating the lanthanide excited states *via* energy transfer from the ligand. Therefore, modification of the ligand as a result of a specific analyte or environment which subsequently leads to a change in the energy transfer pathway, allows for responsive Ln(III)

probes.[105, 229] Although there are numerous examples of both MR and optical probes based on Ln(III) complexes which respond to oxidative conditions,[230] there are only a handful of examples which respond to a reductive environment (Scheme 3.2).

Faulkner and co-workers developed an optical turn-on probe for the sensing of hydrogen sulphide in solution.[107] This system utilised a kinetically stable Eu(III) complex functionalised with an acetophenone in which the *para*-position on the ring featured an azide functional group (Scheme 3.2a). Upon exposure to sulphide in solution, the azide was rapidly reduced to the corresponding aniline. The Eu(III) emission recorded upon excitation at 350 nm for the aniline complex was 20-fold higher in intensity than that of the Eu(III)-azide complex. They attribute this impressive turn-on effect to a change in the energy transfer efficiency from the ligand to the Eu(III) metal centre upon reduction of the azide to the aniline. By comparison of the absorbance spectra of the Eu(III)-azide and Eu(III)-aniline complex significant blue shifting of the LMCT band upon reduction to the electron donating aniline is observed. Therefore, there is increased absorbance of the ligand at 350 nm compared with that of the azide containing complex. Thus, upon excitation at 350 nm energy transfer from the aniline to the Eu(III) is much more efficient. [107]

Additionally, Nazaré and co-workers developed an optical probe for the sensing of nitroreductase enzymes in bacteria.[207] This system is based on a cascade of reactions which occur at the ligand leading to the formation of an carbostryril group, an efficient sensitiser for Tb(III) luminescence (Scheme 3.2b). Initial reduction of the *para*-nitro group on the aromatic ring to the corresponding aniline triggered a reaction which resulted in the liberation of iminoquinone methide *via* self-immolation. The resulting amine then underwent intramolecular ring closure to form the carbostryril. The *in-situ* formation of carbostryril in solution allows for the efficient population of Tb(III) excited states *via* the antenna effect. Upon excitation at 355 nm into the carbostryril strong green light emission was observed, which

resulted from the radiative decay of the $^5D_4 \rightarrow {}^7F_J$ (J = 6, 5, 4, 3) transitions. The long lived Tb(III) luminescence (μs) allows for time-gated optical imaging to investigate nitroreductase activity in bacteria.[207]

Nazaré and co-workers also developed a MR probe which responds in the presence of nitroreductases, with a change in relaxivity (r_1).[226] To achieve this, the high spin of Gd(III) (S = 7/2) was utilised. Additionally, the Gd(III) cation was stabilised by complexation within a kinetically stable framework containing a *para*-nitro functionalised acetophenone unit (Scheme 3.2c). The reduction of the *para*-nitro group to the amino triggered the release both of iminoquinone methide and Gd(DOTA), a clinically used MR contrast agent. This reduction resulted in a change in the relaxivity (r_1) which increased from 3.51 mM^{-1} s^{-1} (masked probe) to 4.02 mM^{-1} s^{-1} (Gd-DOTA) in PBS (pH 5.35), measured on a 7 T magnet. This corresponds to a 15% increase in relaxivity in the presence of nitroreductase.[226]

A different approach was taken by Allen and co-workers, exploiting the Eu(II/III) redox couple to develop an MR probe to directly monitor the redox potential of hypoxic environments.[227, 228] Here, they coordinated a Eu(II) cation within a cyclen-based ligand functionalised with phosphonate arms (Scheme 3.2di). The phosphonate arms allowed the Eu(II) probe to be delivered *in-vivo* to hypoxic tissues. Upon arrival to the hypoxic environment, the Eu(II) was reduced to Eu(III) as a result of the redox potential of the tissue. This resulted in a change in the relaxivity.[227] Due to stability issues of Eu(II) within the original ligand framework they developed a family of second generation probes. Here, they modified the arms on the cyclen ring with fluorinated aromatic rings (Scheme 3dii). The combination of the Eu(II)/(III) redox couple and ^{19}F within the same complex allowed for ratiometric sensing of hypoxia by MR.[228]

The mechanisms and physiological effects of hypoxia are complex and further investigation is required to fully understand the generation and impact of hypoxic environments in biology. To

this end, it is desirable to have a series of molecular probes that respond to a broad variety of stimuli and which allow the biochemistry of hypoxia to be interrogated in detail. Importantly, there are no examples of Ln(III) complexes which report on the reduction of an azobenzene, which is a common organic transformation to monitor azoreductase, an overexpressed enzyme in hypoxic conditions.

3.2 Design of Binuclear Ln(III) Probes

Multiple Ln(III) cations within the same complex can have interesting and unusual photophysical and magnetic properties.[231-233] Previous work in the group, has investigated binuclear Ln(III) complexes for applications in host-guest chemistry and self-assembly.[234-237]

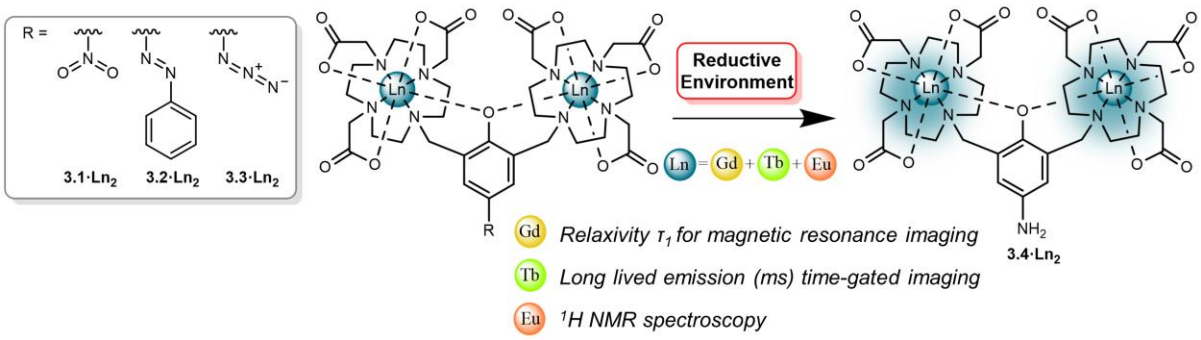


Figure 3.2: Redox-activated, luminescent lanthanide probes based on the reduction of nitro, azo and azide groups to a corresponding aniline. The Gd(III) complexes provide a magnetic resonance (MR) read-out of reductive conditions, whilst the reduction of the Tb(III) species affords turn-on luminescence sensors with long-lived green light emission.

A previously studied motif containing a *para*-bisphenol in which the 2 and 6 positions on the ring were functionalised with macrocyclic DO3A coordination sites was found to be particularly interesting. The crystal structure of a binuclear Eu(III) complex of this motif was determined by Kirsten Christensen (Figure 3.3). Importantly, this scaffold holds the two lanthanide metal centres in close proximity to each other through coordination of the phenolate to each Ln(III) centre. The distance between the two Ln(III) in this scaffold is 3.77 Å (further details can be found in **Chapter 7**). It was postulated that this short distance could lead to

interesting optical and magnetic properties and thus the bridging phenolate motif was included in the design of the probes discussed in this chapter (Figure 3.2).

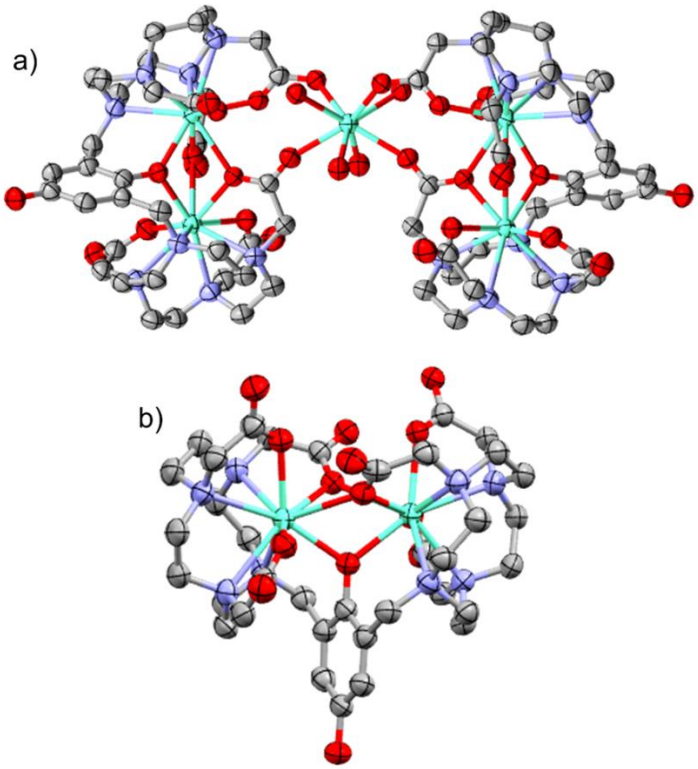


*Figure 3.3: Thermal displacement ellipsoid drawing (50% probability) of a) the full structure of the [[**3.5·Eu**$_2$]$_2$[Eu(H$_2$O)$_4$]]$^-$ anion, which co-crystallises with a hydrated Na$^+$ cation (not shown) and b) **3.5·Eu**$_2$. All H atoms (excluding OH protons) and non-coordinated solvent molecules have been omitted for clarity. Crystal grown by Dr Daniel Kovacs.*

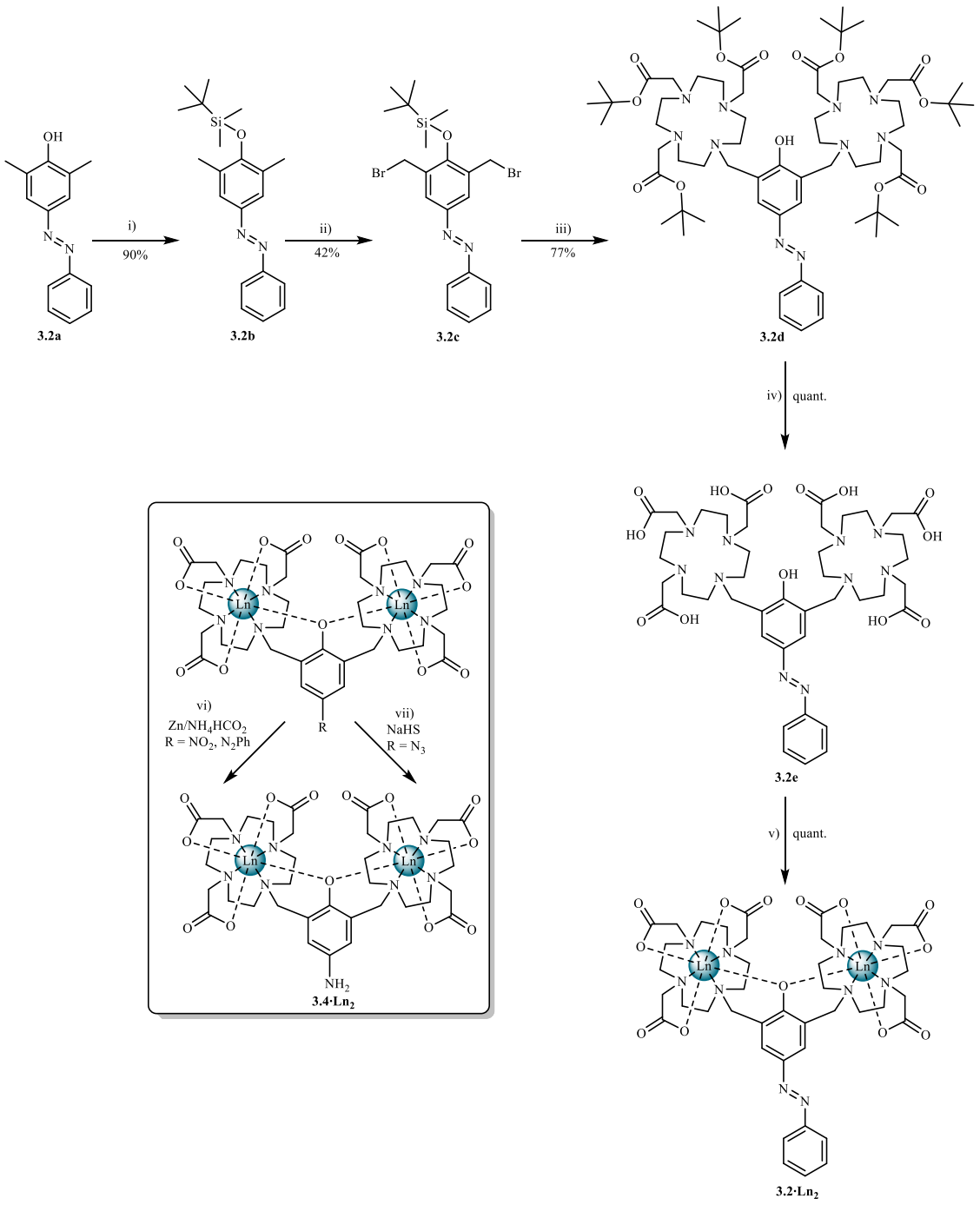
The design of responsive probes requires the inclusion of a moiety which responds to an external stimulus. In this case, for a redox active probe, the majority of the structure was retained from previous work, with the addition of redox active groups to the phenolate in the *para*-position. Therefore, a family of related binuclear Ln(III) complexes was suggested in which the *para*-position of the aromatic ring was functionalised as a nitro (**3.1·Ln**$_2$), azobenzene (**3.2·Ln**$_2$) and azide (**3.3·Ln**$_2$). It was postulated that upon complete reduction, all complexes would reveal the same shared reduction product, the aniline **3.4·Ln**$_2$ (Figure 3.3). Additionally, the choice of coordinating Ln(III) cation was important to elicit both optical and magnetic properties. Gd(III) was chosen for applications in MR, where it has been extensively investigated, as it is highly paramagnetic (S = 7/2). In contrast, Tb(III) was chosen to

investigate the optical properties as it is strongly emissive in comparison to other Ln(III) cations and emits in the green region. Finally, Eu(III) complexes were investigated to further understand the magnetic and chemical properties afforded by the binuclear ligands using ^{1}H NMR spectroscopy.

3.3 Synthesis of Binuclear Ln(III) Probes

The synthetic route to of **3.2·Ln$_2$** and **3.4·Ln$_2$** is described in Scheme 3.3. Full experimental details and characterisation can be found in **Chapter 7**. Complexes **3.1·Ln$_2$** and **3.3·Ln$_2$** were previously synthesised in the literature.[238]

3.2a was synthesised according to literature procedures *via* classic diazo coupling. Initially, aniline was suspended in hydrochloric acid and cooled to 0 °C, to this sodium nitrate was added to form the diazonium. Upon formation of the diazonium *in-situ* 2,6-dimethylphenol and sodium hydroxide were added to form the azobenzene, as a result the reaction mixture turned bright orange. Upon completion, the solution was acidified and a dark red precipitate formed which was isolated as **3.2a**.[239] The next step was to protect the alcohol: a *tert*-butyldimethylsilyl ester (TBS) protecting group was chosen as it can be selectively cleaved under basic conditions. **3.2a** was dissolved in DMF, to this *tert*-butyldimethylsilyl chloride was added along with base to yield **3.2b** in good yield (90%).[240] Once the alcohol was protected, the flanking methyl groups could then undergo radical bromination. **3.2b** was dissolved in tetrachloromethane, to which N-bromosuccinimide (NBS) was added along with a radical initiator, benzoyl peroxide. The reaction was heated to reflux and left for 3 hours after which the crude product purified by silica gel column chromatography. The purification was difficult as multiple bromination products were present including mono-, di-, tri-, and tetra-brominated compounds. Therefore, long silica columns were required and pentane was used as the eluent to reduce co-elution. After multiple columns **3.2c** was isolated as an orange oil in moderate yield (46 %).



Scheme 3.3 Synthesis of ***3.2·Ln₂*** *and* ***3.4·Ln₂*** *i) TBS-Cl, Imidazole, DMF, r.t., 16h. ii.) NBS, $(BzO)_2$, CCl_4, Δ, 3h iii.) DO3A^{t}Bu, Na_2CO_3, MeCN, 60°C, 48 h iv.) TFA:DCM (1:1), r.t., 18h v.) Ln(OTf)$_3$, $NaOH_{(aq)}$, H_2O, 50°C, 24 h vi) Zn/NH_4HCO_2, H_2O, 37 °C, 48 h vii) NaHS, H_2O, 37 °C, 2 h.*

Next, the *tert*-butyl ester protected macrocycles were appended *via* an S_N2 reaction under basic conditions. In this same step, fortuitously, the TBS protecting group was also removed *via* ester hydrolysis to yield **3.2d**. The final step in the synthesis of the ligand was deprotection of the *tert*-butyl ester protecting groups on the macrocycles with trifluoroacetic acid (TFA). This

deprotection yielded the free carboxylate arms required for coordination of Ln(III) ions and successive trituration allowed for the removal of excess TFA from the product. Finally, the lanthanide coordination by the macrocyclic framework was achieved by stirring with the appropriate triflate salt, to yield **3.2·Ln$_2$**. Any excess lanthanide salt was removed by dialysis in Milli-Q water over a period of 3 days during which the water was changed daily.

3.4·Ln$_2$ was produced by reduction of previously synthesised Ln(III) complexes (Scheme 3.3 inset). **3.1·Ln$_2$** and **3.3·Ln$_2$** (made previously by Dr Daniel Kovacs) were reduced in the presence of Zinc and ammonium formate to yield **3.4·Ln$_2$**.[218] More conveniently, **3.4·Ln$_2$** was the product of the rapid and efficient reduction of **3.3·Ln$_2$** with sodium hydrogen sulphide.[107] Much like complexation, any excess reducing agents were removed by dialysis in Milli-Q water.

3.4 Characterisation of Binuclear Ln(III) complexes

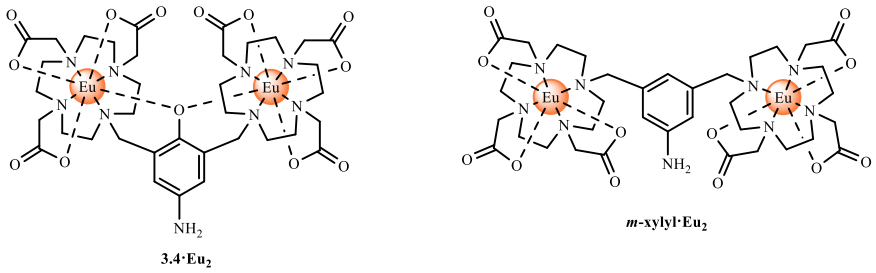
This section will detail the characterisation techniques evidencing the successful synthesis of **3.2·Ln$_2$** and **3.4·Ln$_2$**. Each complex was also confirmed by HR-ESI mass spectrometry, full details can be found in **Chapter 7**.

3.4.1 ^{1}H NMR

Due to difficulties in recording the ^{1}H NMR spectra of the Tb(III) analogues as a result of solubility and phasing issues, the Eu(III) analogues **3.2·Eu$_2$** and **3.4·Eu$_2$** were synthesised to investigate the structure of the complexes in solution by ^{1}H NMR.

The ^{1}H NMR spectra of both **3.2·Eu$_2$** and **3.4·Eu$_2$** in D_2O are shown in Figure 3.4. The spectra of both complexes exhibit sharp, well resolved peaks indicative of a rigid structure around the Eu(III) centres. The sharpness of the peaks suggests that each Eu(III) is coordinatively saturated, where seven donor atoms arise from the DO3A macrocycle and 1 donor from the

bridging phenolate. The usual range investigated for paramagnetic Eu(III) complexes is ± 50.00 ppm; however, when the complexes were measured with these settings the axial proton environment (labelled with *) extended out of the usual range, ± 50.00 ppm. Therefore, the range of the ^{1}H NMR experiment was extended to accommodate this highly shifted peak.



*Scheme 3.4: Comparison of related structures **3.4·Eu2** and **m-xylyl·Eu2**.* [238]

The axial proton environment is heavily shifted in both **3.2·Eu2** (δH_{ax} = 46.11 ppm) and **3.4·Eu2** (δH_{ax} = 49.12 ppm) in comparison to other previously reported binuclear complexes, ***m*-xylyl·Eu2** (δH_{ax} = 22.40 ppm) (Scheme 3.4) reported by Faulkner and co-workers. [235, 238] The structure of **3.4·Eu2** and ***m*-xylyl·Eu2** are identical except for the phenolate group present on **3.4·Eu2**, however, the chemical shifts differ by 26.72 ppm (54 % of δH_{ax} (**3.4·Eu2**)). Therefore, the effective magnetic field experienced by the protons in the phenolate bridged complexes is significantly higher than the analogous system with no bridging phenolate.

Another factor to consider is the impact of the phenolate itself on the electronics of the ligand. Comparison of the aromatic protons of aniline, δH_{ar} = 7.07 - 7.14 ppm,[241] and 4-aminophenolate, δH_{ar} = 6.21 - 6.36 ppm,[242] shows there is only a 11 % change in the chemical shifts as a result of the addition of the *para*-phenolate. Therefore, it is believed that not only the presence of the phenolate on the ring can describe the differences observed between **3.4·Eu2** and ***m*-xylyl·Eu2**, the phenolate must also play a role in the structure of the complex in solution.

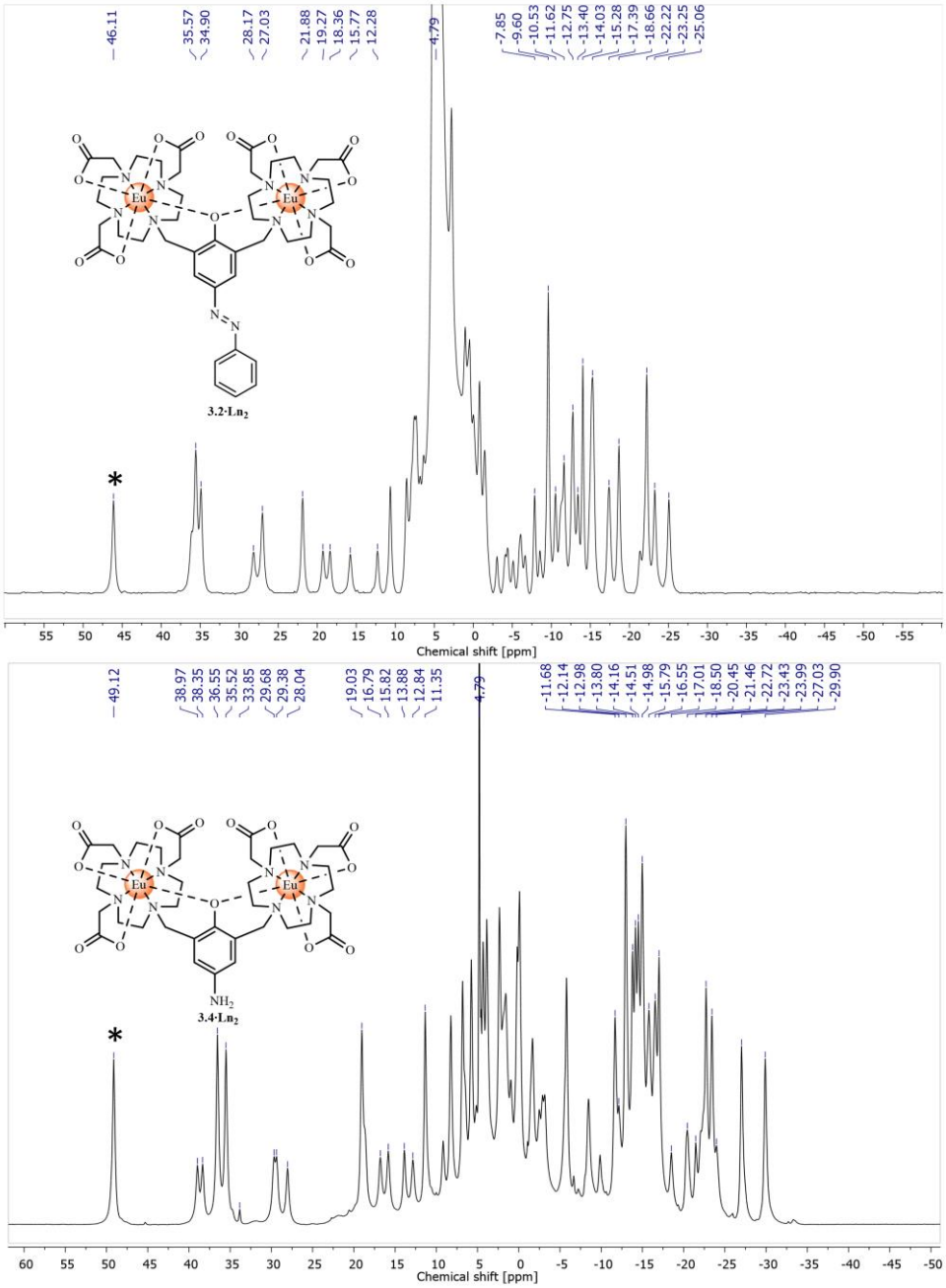


*Figure 3.4: [1]H NMR spectra of **3.2·Eu2** and **3.4·Eu2** (400 MHz, D2O). * denotes the axial proton environment.*

In both **3.2·Eu2** and **3.4·Eu2** the deprotonated phenolate can directly coordinate to both Eu(III) centres within the complex, therefore the distance between the Eu(III) centres is reduced in comparison to ***m*-xylyl·Eu2**. As a result, it is believed that each proton environment experiences a contribution to the effective magnetic field from both Eu(III) centres and thus the chemical shift of the protons is shifted to higher ppm, outwith the usually expected range for Eu(III) complexes. Additionally, the proton environment labelled as '*' is particularly shifted. The

crystal structure of the related complex in Figure 3.2 shows an axial carbon which sits directly between both Eu(III) centres. It is believed that the proton on this carbon, which is directed towards the Eu(III) centres, is heavily influenced by two paramagnetic Eu (III) centres and thus shifted to the highest chemical shift.[73]

3.4.1.1 Influence of *para*-Substituents on the ^{1}H NMR of Binuclear Eu(III) Complexes

To understand the influence of the *para*-substituent on the ^{1}H NMR of all complexes in the series, **3.1·Eu$_2$**, **3.2·Eu$_2$** **3.3·Eu$_2$** and **3.4·Eu$_2$**, were compared (Figure 3.5). Interestingly, within the series the position of the axial proton shifts to higher chemical shifts with increasingly activating groups in the *para*-position on the ring. Normally in organic compounds, the increasing electron donating capability of a group increases the electron density on the ring, leading to increased shielding and an upfield shift (lower chemical shifts). However, in this system the heavily shifted proton environment relates to the axial protons on the ligand, not the ring protons. For this series of Eu(III) complexes the axial protons shift downfield upon increasingly electron donating behaviour of the *para*-substituent.

To explain this trend, the anisotropy of the Eu(III) centres must be considered, in particular the anisotropy of the individual m_J states. The gap between the ground ($^{7}F_0$) and the first excited state ($^{7}F_1$) of Eu(III) is small and therefore the excited state can be thermally populated. The excited state is split into individual m_J states (J = -1, 0, 1), where the non-zero states are influenced by paramagnetic effects. These states are further split by the crystal field and therefore the Boltzmann population of each m_J state is dependent on the crystal field. By increasing the electron density on the ring, the crystal field is altered. This results in changes in the individual Boltzmann population of the individual m_J states. This in turn alters the anisotropy of the Eu(III) centres and thus the chemical shift of the axial proton is shifted. The more electron density on the ring, the greater the change in anisotropy and thus the larger

change in chemical shift is observed. Regardless, the shift in this axial proton is a handle to monitor the reduction of the probes **3.1·Eu$_2$**, **3.2·Eu$_2$** and **3.3·Eu$_2$** to **3.4·Eu$_2$.**

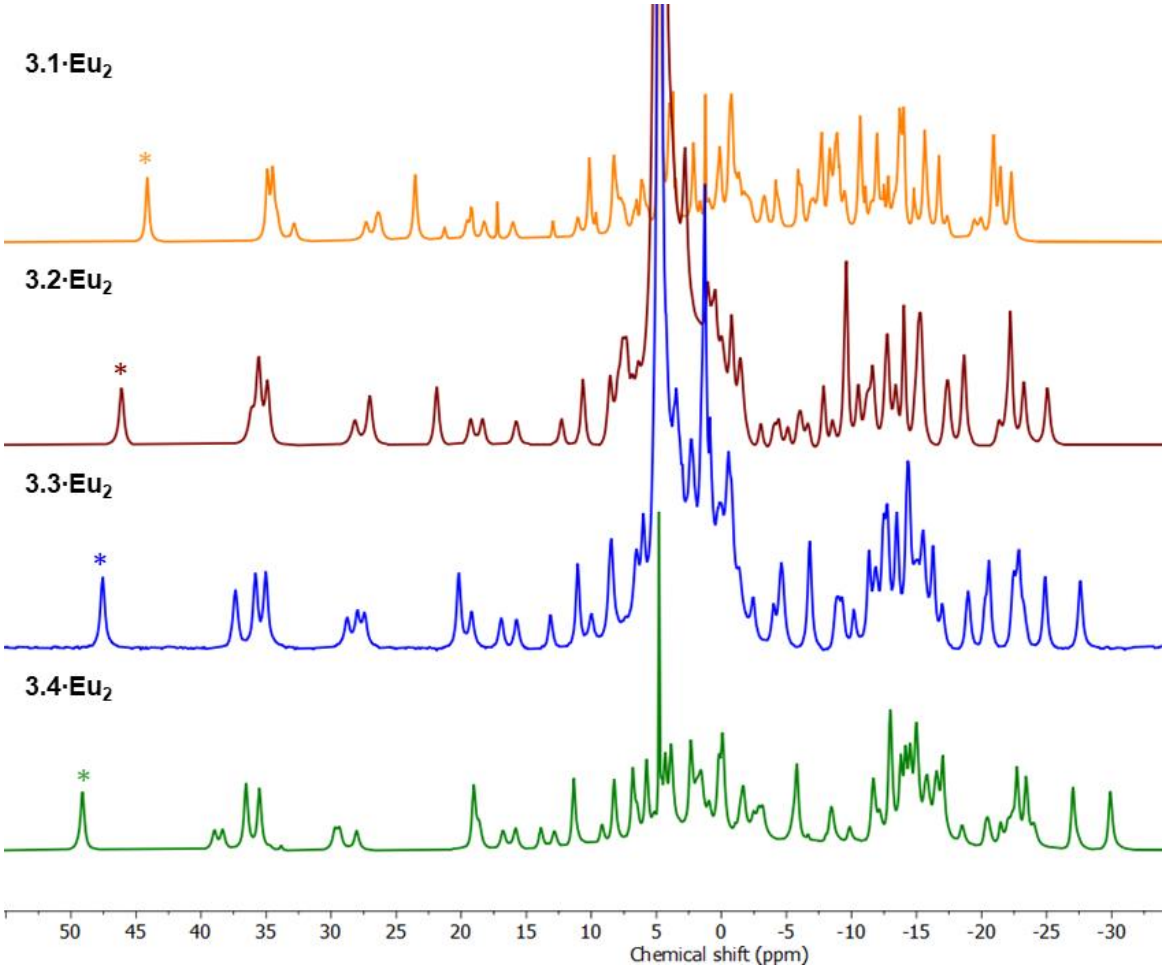


*Figure 3.5: ^{1}H NMR of Eu(III) analogues, **3.1·Eu$_2$**, **3.2·Eu$_2$** **3.3·Eu$_2$** and **3.4·Eu$_2$** (400 MHz, 298K). * Represents the axial DO3A protons.*

3.4.2 High Performance Liquid Chromatography (HPLC)

HPLC was used to determine the purity of the Ln(III) complexes. Figure 3.6 shows the HPLC traces of **3.2·Ln$_2$** (Ln = Tb, Gd and Eu), under the conditions defined by method 2, detailed in **Chapter 7**.

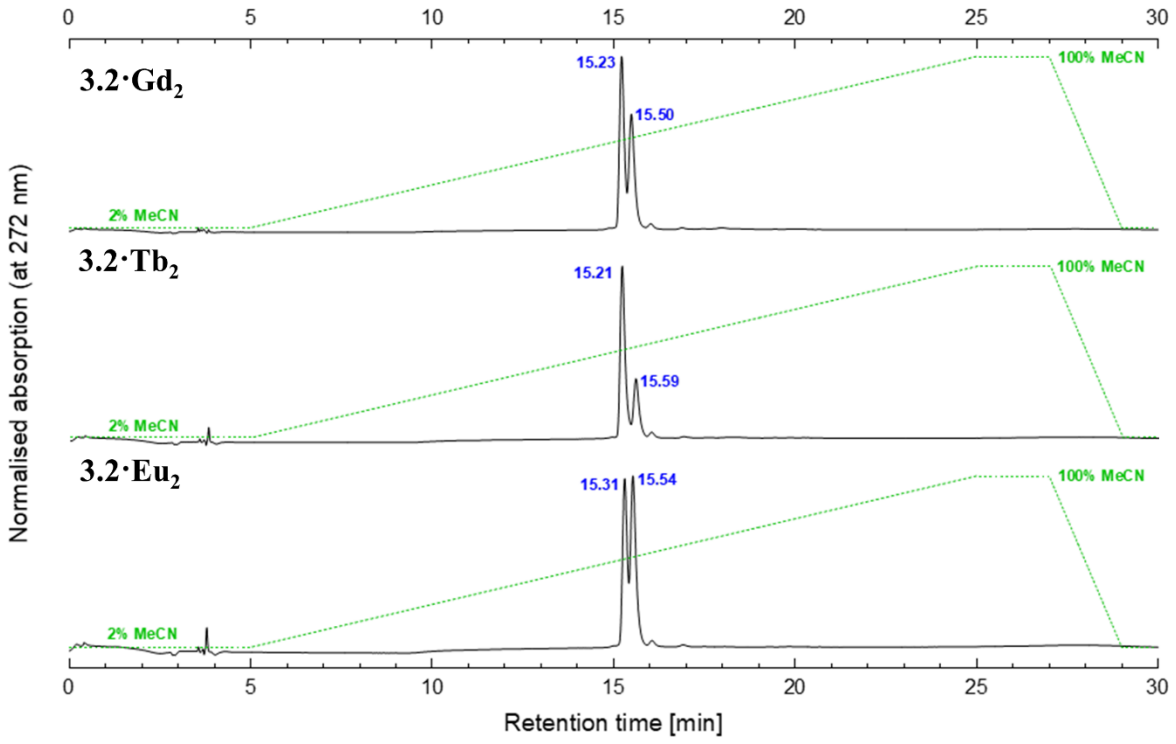


*Figure 3.6: HPLC traces of complexes **3.2·Tb**$_2$, **3.2·Eu**$_2$ and **3.2·Gd**$_2$ using method 2, the secondary peaks represent E and Z isomers, as determined by absorbance spectra of each peak.*

The presence of two significant peaks in each trace, with similar retention times, can be assigned to both *E* and *Z* isomers of each complex in solution, which was identified by the absorbance spectra recorded for each peak. Both isomers are similar in polarity only differing by the geometry of the N=N bond, as a result the two isomer co-elute. Interestingly, within the ligand series the retention times differed depending on the coordinated Ln(III).

3.5 Relaxivity

To explore the potential of the Gd(III) analogues as magnetic resonance probes the relaxivity, r_1, was determined in collaboration with Dr Lina Hacker in the Department of Oncology. The relaxivity is quantified as the variation of the water-proton relaxation rate (T_1^{-1}) normalised to the concentration of the paramagnetic complex in solution.[243] All Gd(III) complexes, **3.1·Gd**$_2$, **3.2·Gd**$_2$ **3.3·Gd**$_2$ to **3.4·Gd**$_2$ were investigated in PBS at pH 7.4 with a 7 T magnet. The T_1

values of the complexes were measured and plotted as a function of Gd(III) concentration, (Figure 3.7a), the calculated r_1 values for each complex are recorded in Table 3.1.

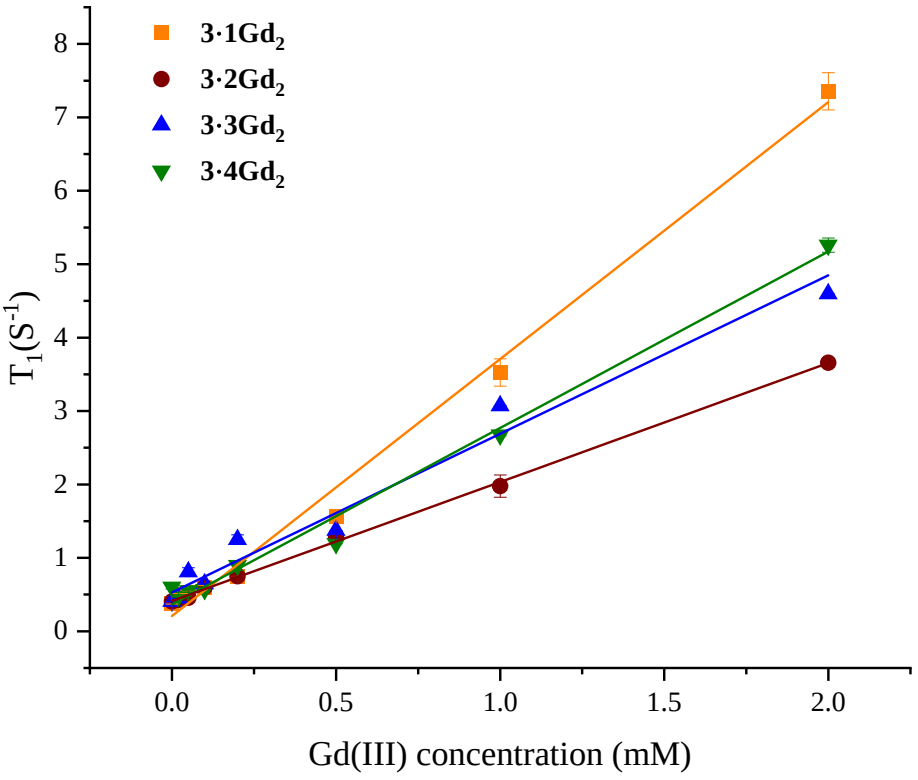


*Figure 3.7: a) T_1 of Gd(III) analogues **3.1·Gd₂**, **3.2·Gd₂** **3.3·Gd₂** to **3.4·Gd₂** as a function of Gd(III) concentration measured at 7 T at 298 K in PBS pH 7.4 b) Change in r_1 compared to **3.4·Gd₂** demonstrating the turn-on/off capabilities upon reduction of probes **3.1·Gd₂**, **3.2·Gd₂** **3.3·Gd₂**,.*

*Table 3.1: r_1 of Gd(III) analogues **3.1·Gd₂**, **3.2·Gd₂** **3.3·Gd₂** to **3.4·Gd₂** measured at 7 T at 298 K in PBS pH 7.4.*

	r_1 (7 T) ($S^{-1}mM^{-1}$)
3.1·Gd₂	3.47 ± 0.13
3.2·Gd₂	1.64 ± 0.02
3.3·Gd₂	2.10 ± 0.14
3.4·Gd₂	2.43 ± 0.11

A linear fit was reported for the relaxivity of all Gd(III) complexes, indicating that each complex is stable in solution and r_1 does not change as a result of the local environment. Interestingly, the longitudinal relaxivity of the nitro derivative **3.1·Gd$_2$** (3.47 s^{-1} mM^{-1}) is comparable to the clinically available Gd-DOTA which has a r_1 of 2.8 s^{-1} mM^{-1} at 7 T.[244] The aniline, **3.4·Gd$_2$** (2.43 s^{-1} mM^{-1}), exhibits a decrease in relaxivity compared to **3.1·Gd$_2$**: this system therefore acts as a turn-off MRI sensor upon reduction of **3.1·Gd$_2$** to **3.4·Gd$_2$** (43% change). In contrast, the reduction of the azo complex **3.2·Gd$_2$** (1.64 s^{-1} mM^{-1}) to **3.4·Gd$_2$** (48% change). leads to an increase in relaxivity and hence acts as a turn-on MR probe. The negligible difference in the r_1 of **3.3·Gd$_2$** and **3.4·Gd$_2$**, suggests that upon reduction, minimal change in the magnetic resonance signal was observed (Figure 3.7b). Therefore, both **3.1·Gd$_2$** and **3.2·Gd$_2$** are promising MR probes which respond to the presence of reductive environments. Ideally a turn on probe with a significant change in relaxivity is preferred for ease of detection, therefore **3.2·Gd$_2$** is currently the most promising candidate.

3.6 Luminescent Properties of Tb(III) Analogues

3.6.1 Absorbance Spectra

The absorbance spectra of **3.1·Tb$_2$**, **3.2·Tb$_2$** **3.3·Tb$_2$** to **3.4·Tb$_2$** were recorded at 90 mM in PBS (pH 7.4) scanning from 240 nm to 700 nm (Figure 3.8). For all complexes, the absorbance spectra was dominated by the organic transitions of the ligand, no observable absorptions directly relating to the Tb(III) metal transitions were recorded.

The absorption of **3.1·Tb$_2$** (Figure 3.8, orange) is defined by the ligand centred transitions of the nitro-phenyl antenna. **3.1·Tb$_2$** absorbs well between 300 - 450 nm (λ_{max} = 349 nm) corresponding to the overlap of both $\pi \rightarrow \pi^*$ and $n \rightarrow \pi^*$ transitions of the nitro-phenol. The absorbance of **3.2·Tb$_2$** (red) is dominated by the electronic transitions of the azobenzene. The λ_{max} (364 nm), corresponds to the $\pi \rightarrow \pi^*$ transition of the azobenzene, the shoulder observed

around 450 - 500 nm corresponds to the n → π^* transition. Both **3.1·Tb$_2$** and **3.2·Tb$_2$** are highly absorbing in the blue/green region of visible light in comparison to **3.3·Tb$_2$** and **3.4·Tb$_2$** which absorb UV light. The nitro-phenyl and the azobenzene both contain electron withdrawing groups in the para-position of the phenol ring, therefore the transitions related to the aromatic ring are red shifted to longer wavelengths. In comparison, the absorbance of the organic transitions of both the azide and aniline are comparatively blue shifted (240 - 300 nm), with no absorbance between 350 - 500 nm. This is a result of the electron donating groups in the *para*-position on the aromatic ring.

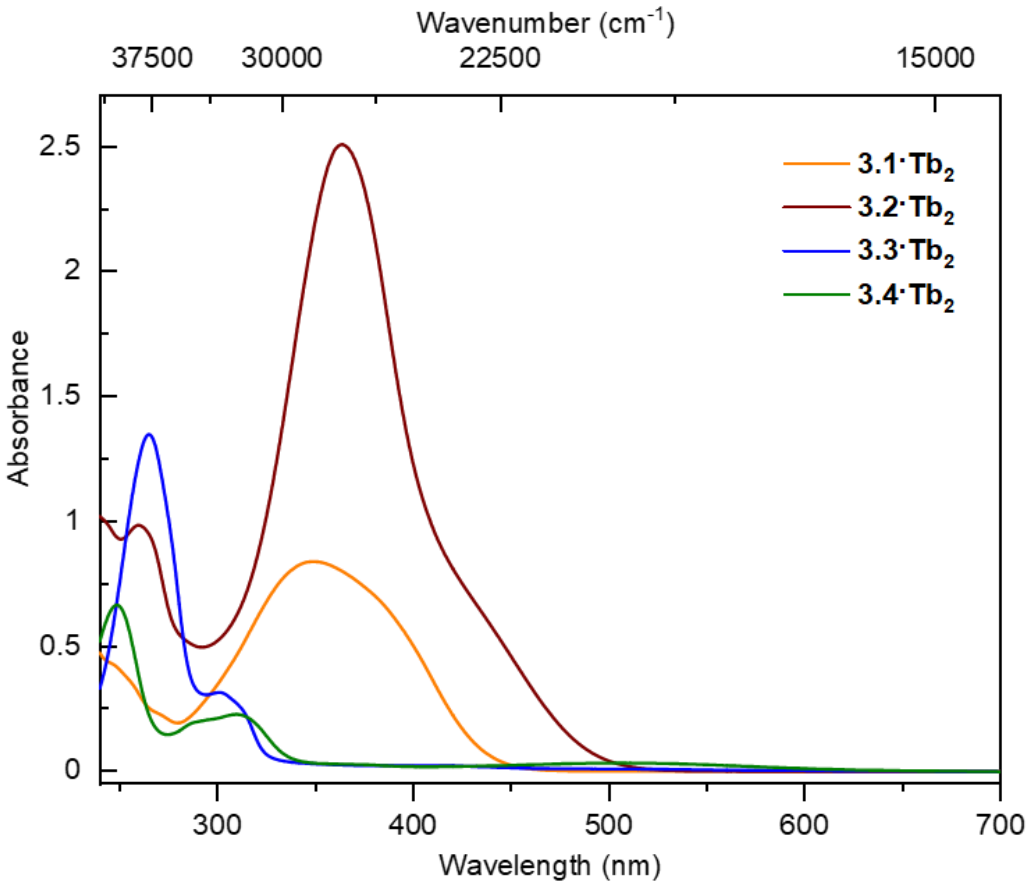


*Figure 3.8: The absorbance of **3.1·Tb$_2$**, **3.2·Tb$_2$**, **3.3·Tb$_2$** to **3.4·Tb$_2$** were recorded at 90 mmol in PBS at pH 7.4 at 298 K.*

3.6.2 Steady State Spectra

The steady state emission and excitation spectra focussing on the Tb(III) luminescence of each complex were recorded at 298 K unless stated otherwise. To record the emission spectra,

Tb(III) was directly excited into the $^7F_6 \rightarrow {}^5D_4$ transition (λ_{ex} = 488 nm), emission and excitation slits were fixed at 1 and 5 nm respectively with a step size of 0.5 nm and integration time of 0.5 s. To record the excitation spectra, the $^5D_4 \rightarrow {}^7F_5$ transition was monitored (λ_{em} = 545 nm), emission and excitation slits were set at 5 and 1 nm respectively, the step size was 0.5 nm and the integration time 0.5 s.

3.6.2.1 Emission Spectra

Excitation of complex **3.2·Tb$_2$** via the π → π* and n → π* transitions resulted in negligible emission. Therefore, direct excitation into the Tb(III) $^7F_6 \rightarrow {}^5D_4$ transition (λ_{ex} = 488 nm) was investigated. This allowed for direct comparison of the non-radiative decay pathways available in each complex, negating the influence of the antenna effect.

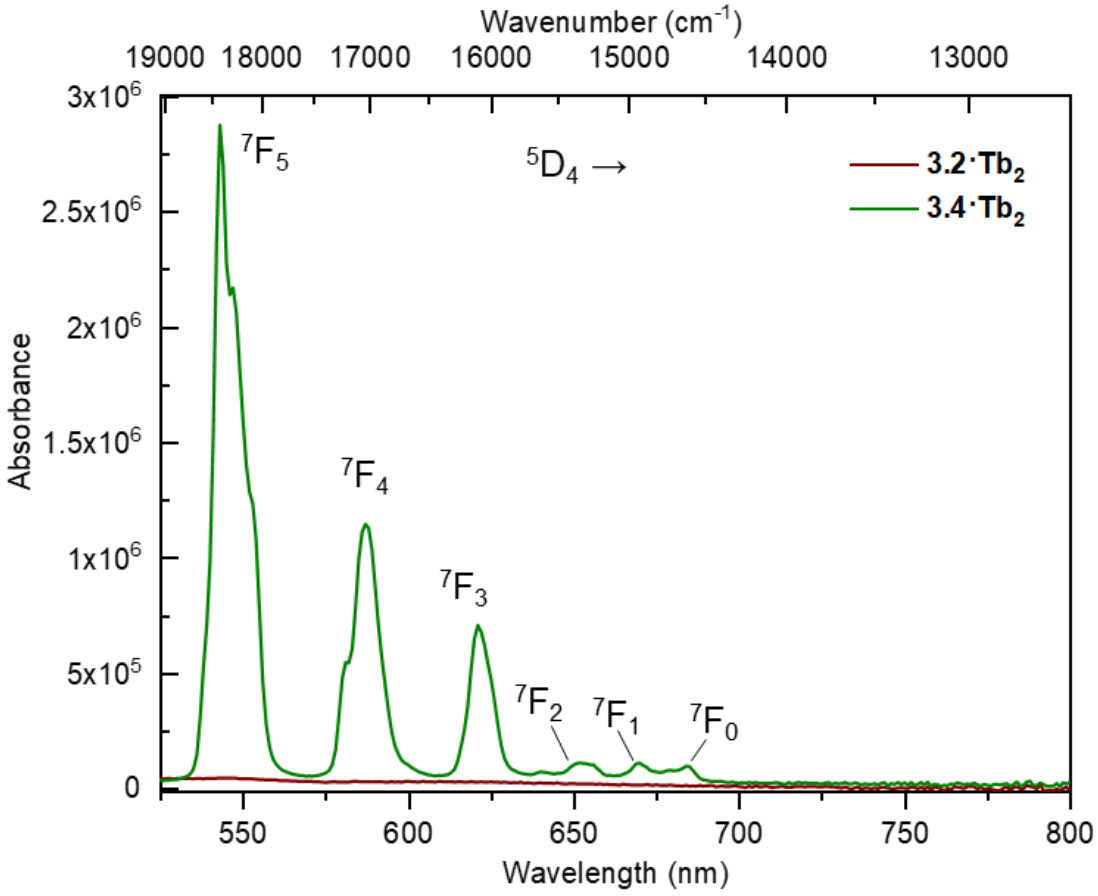


*Figure 3.9: Emission spectra of **3.2·Tb$_2$** (maroon) and **3.4·Tb$_2$** (green) upon excitation at 488 nm, emission slit 1 nm, excitation split 5 nm, integration time 0.5 s.*

The emission spectra recorded for **3.2·Tb2** (maroon) and **3.4·Tb2** (green) when directly excited into the Tb(III) $^7F_6 \rightarrow {}^5D_4$ transition (λ_{ex} = 488 nm) are shown in Figure 3.9. The emission spectrum of **3.4·Tb2** describes clearly the radiative Tb(III) transitions from the emissive $^5D_4$ state to the lower lying ^7F_J (J = 5, 4, 3, 2, 1, 0). The splitting observed for each $^5D_4 \rightarrow {}^4F_J$ transition relates to the various electronic states of the emissive $^5D_4$ state (9 electronic states). Due to the high number of electronic states in the principle emissive state of Tb(III) the spectra contains over 400 individual transitions; the resolution of the spectrometer is not high enough to resolve these individually, therefore bands are observed. Notably, the emission observed for **3.2·Tb2** is almost non-existent and the shape does not resemble the characteristic Tb(III) emission. Since **3.2·Tb2** was directly excited into the Tb(III) $^7F_6 \rightarrow {}^5D_4$ transition (λ_{ex} = 488 nm) the emission spectrum recorded does not report on the antenna capabilities of the ligand, but rather on the availability and efficiency of non-radiative decay pathways. In the complex **3.2·Tb2**, rapid isomerisation around the N=N bond acts as a non-radiative sink, as a result, the azobenzene ligand acts as an impressive quencher of Tb(III) luminescence.[184]

3.6.2.2 Excitation Spectra (λ_{em} = 545 nm)

To understand more about the luminescent properties of the Tb(III) complexes, their excitation spectra were recorded between 240 – 450 nm, monitoring the intensity of the $^5D_4 \rightarrow {}^7F_5$ emission at 545 nm (Figure 3.10). This range allowed for investigation of the emission observed at 545 nm as a result excitation *via* the organic ligand. Comparisons between the absorption and excitation spectra illuminated the photophysical processes underpinning the efficiency of the ligands on **3.2·Tb2** and **3.4·Tb2** to act as antennas for Tb(III) emission.

The excitation spectrum of **3.4·Tb2** (green) shows two clear ligand centred transitions, which efficiently sensitise the Tb(III) excited state *via* energy transfer. However, in the excitation spectrum recorded for **3.2·Tb2** (maroon) there is no observable contribution from the

azobenzene ligand as a sensitiser for Tb(III) centred emission at any wavelength investigated (Figure 3.10).

The comparison between the absorbance and the excitation spectra (λ_{em} = 545 nm) for **3.2·Tb$_2$** and **3.4·Tb$_2$** is shown in Figure 3.11. Interestingly, **3.2·Tb$_2$** strongly absorbs across all regions in which the excitation spectra was measured, however there is no observable contribution from the ligand to the Tb(III) emission. Therefore, regardless of the efficiency of the azobenzene ligand to absorb light, energy transfer to the Tb(III) excited state was not observed. Therefore, it is believed that the absorbed energy is dissipated non-radiatively, particularly through the photoisomerisation of the azobenzene. This is in agreement with the observations of other azobenzene containing lanthanide complexes **2·L$_a$Eu** and **2·L$_b$Eu$_2$**, discussed in **Chapter 2**.

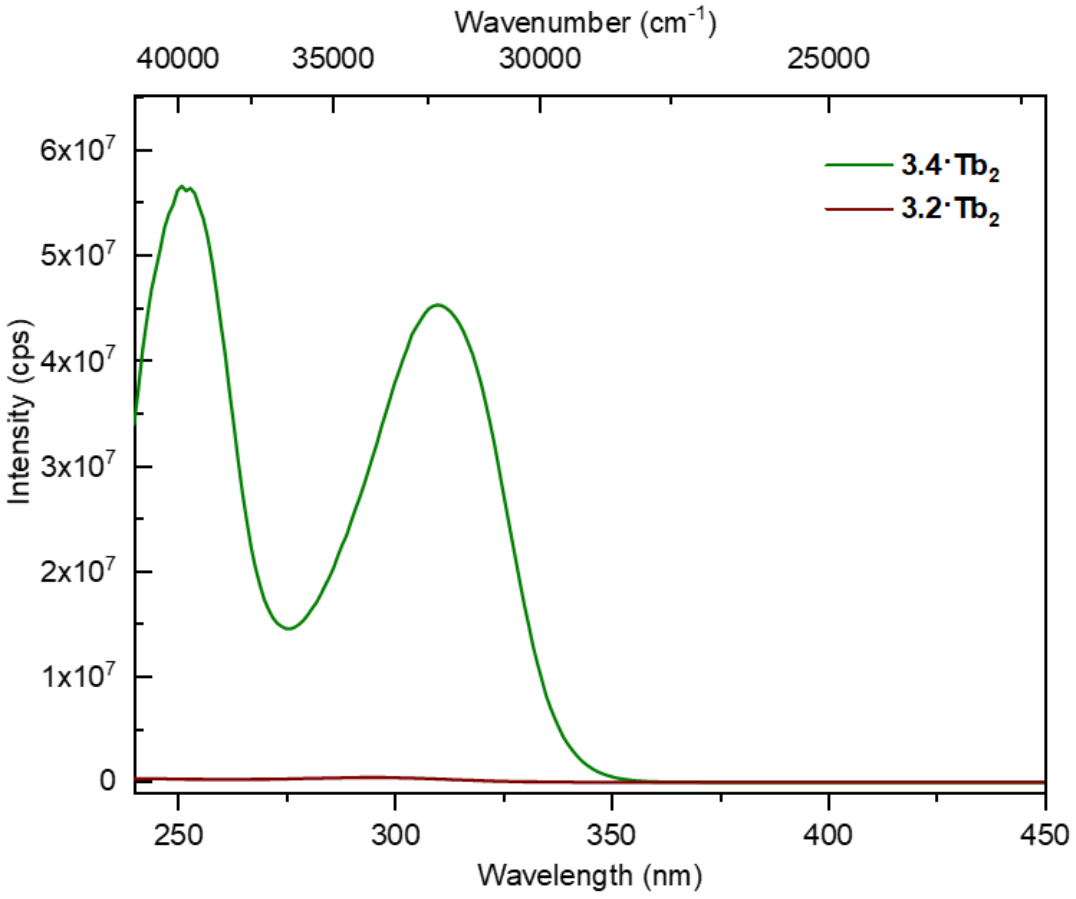


*Figure 3.10: Excitation spectra of **3.2·Tb$_2$** (maroon) and **3.4·Tb$_2$** (green) upon emission at 545 nm, emission slit 5 nm, excitation split 1 nm, integration time 0.5 s.*

However, for **3.4·Tb$_2$**, the excitation spectrum mirrors the absorbance spectrum almost exactly (Figure 3.11), therefore excitation into both the n → π^* and π→ π^* transitions of the organic aniline lead to efficient energy transfer and population of the Tb(III) $^5D_4$ excited state. Importantly, in the application of responsive probes for reductive environments it is advantageous to have good contrast between the OFF and the ON state. In this example, the azobenzene containing **3.2·Tb$_2$** (OFF state) is essentially dark at all excitation wavelengths, however, **3.4·Tb$_2$** (ON state) emits strong bright green light. It is conceivable that *in-situ* reduction of **3.2·Tb$_2$** to **3.4·Tb$_2$** would reveal an efficient luminescent turn on-probe for the sensing of reductive environments.

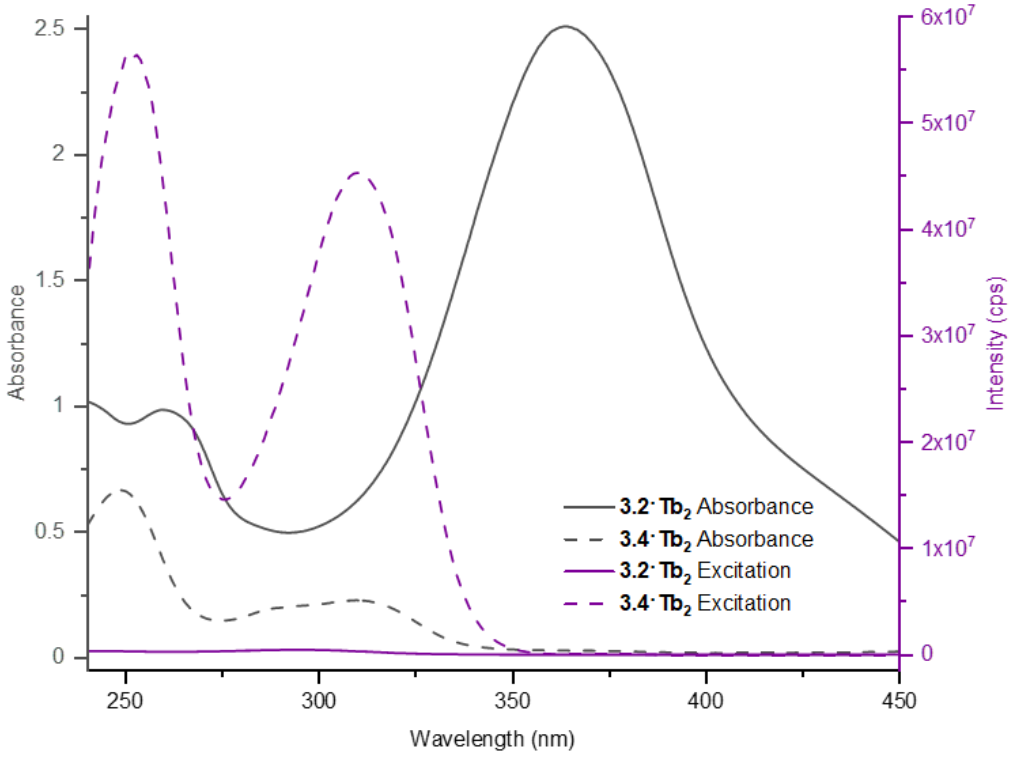


*Figure 3.11: Absorbance (black) and excitation (purple) spectra for both of **3.2·Tb$_2$** (solid line) and **3.4·Tb$_2$** (dashed line). λ_{max} = 545 nm, emission slit 5 nm, excitation slit 1 nm, integration time 0.5 s.*

3.6.2.3 Comparison of Luminescent Properties of Binuclear Tb(III) Complexes

To evaluate the series of related Tb(III) complexes, the luminescent properties of **3.2·Tb$_2$** and **3.4·Tb$_2$** were compared to that of the previously synthesised **3.1·Tb$_2$** and **3.3·Tb$_2$**. Both the

emission (λ_{ex} = 488 nm) and excitation (λ_{em} = 545 nm) spectra for all Tb(III) complexes are shown in Figure 3.12. Importantly, all of the redox activatable optical probes, **3.1·Tb$_2$**, **3.2·Tb$_2$** and **3.3·Tb$_2$** were found to be considerably less emissive than **3.4·Tb$_2$** when excited directly into the $^7F_6 \rightarrow {}^5D_4$ transition (λ_{ex} = 488 nm) of Tb(III).

Comparison of the proportion of light emitted for each complex, to the light emitted from the ON state **3.4·Tb$_2$** (100%), both **3.1·Tb$_2$** (1.73 %), **3.2·Tb$_2$** (8.72 %) shows impressive contrast between OFF and ON states, thus highlighting the utility of the Tb(III) complexes as promising optical probes for the investigation of reductive environments. Notably, **3.3·Tb$_2$** (11.73 %) was found to be the most emissive of the activatable probes, as a result of photo-reduction to **3.4·Tb$_2$** *in situ*.

The excitation spectra for all Tb(III) complexes shown in Figure 3.12 describes the emission intensity (λ_{em} = 545 nm) upon excitation at a particular wavelength. Both **3.1·Tb$_2$** and **3.2·Tb$_2$** are essentially flat lines, close to the baseline and therefore do not sensitise Tb(III) emission at any wavelength investigated. These essentially dark states show promise as highly efficient OFF states for responsive optical imaging.

Repeated excitation of **3.3·Tb$_2$** with 488 nm revealed increased intensity of the Tb(III) emission upon successive excitation. This suggests that the excitation itself is influencing the photophysical properties of **3.3·Tb$_2$**. Additionally, the excitation spectrum of **3.3·Tb$_2$** is almost identical in shape to that of **3.4·Tb$_2$** albeit with a lower intensity, under the same experimental conditions. Therefore, it is believed that **3.3·Tb$_2$** can be photoreduced *in situ* to form **3.4·Tb$_2$**.

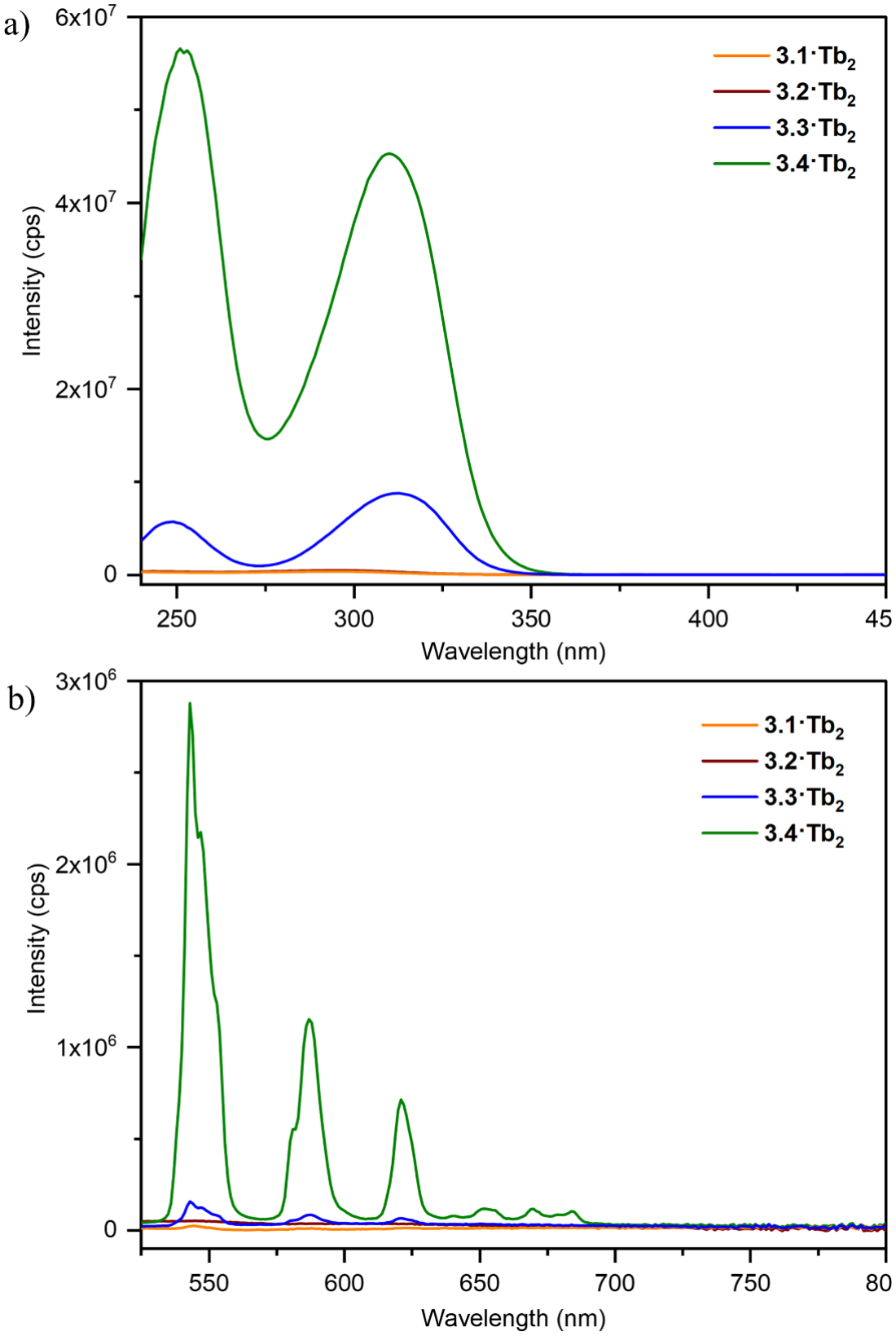


*Figure 3.12: Luminescent properties of Tb(III) complexes **3.1·Tb₂** (orange), **3.2·Tb₂** (maroon), **3.3·Tb₂** (blue) and **3.4·Tb₂** (green) a) Excitation spectra where λ_{em} = 545 nm, ex slit = 1 nm, em slit = 5 nm, intergration time = 0.5 s b) Emission spectra where λ_{ex} = 488 nm, ex slit = 5 nm, em slit = 1 nm, intergration time = 0.5s.*

3.6.2.4 Quantum Yields

As **3.4·Tb$_2$** was highly emissive, the quantum yield was measured upon excitation at 313 nm, by Dr Daniel Kovacs. 313 nm was chosen as it was the excitation wavelength which corresponds to the maximum observed Tb(III) emission as a result of sensitisation *via* the aniline ligand. Emission spectra of **3.4·Tb$_2$** (λ_{ex} = 313 nm) and the reference compound quinine sulphate (Φ = 59.0 %)[245, 246] were recorded under the same experimental conditions. Integrations of the area under each emission spectrum were calculated and using equation 3.1 the quantum yield of **3.4·Tb$_2$** was determined.

$$\Phi_s = \frac{I_s}{I_{ref}} \cdot \frac{f_{A_{ref}}}{f_{A_s}} \cdot \frac{(n_s)^2}{(n_{ref})^2} \Phi_{ref}$$

(3. 1)

In this system the second term is disregarded since the absorption of both **3.4·Tb$_2$** and reference quinine sulphate is identical. The third term is also removed as both the reference and complex are in dilute conditions in the same solvent and so the refractive index is assumed to be equal simplifying equation 3.1 to equation 3.2.

$$\Phi_s = \frac{I_s}{I_{ref}} \cdot \Phi_{ref}$$

(3. 2)

Using equation 3.2 the quantum yield of **3.4·Tb$_2$** was found to be 45.2%. The quantum yield of **3.4·Tb$_2$** is extremely high for Tb(III) emission and compares well to the most emissive Tb(III) complexes in the literature in which a maximum quantum yield was found to be 54 %.[64, 247, 248] This is believed to be as a result of a lack of solvent molecules in the inner coordination sphere, as evidenced from the solid state structure in Figure 3.2. A demonstration of the brightness of **3.4·Tb$_2$** was performed with a qualitative experiment in which all complexes at 90 mmol in PBS (pH 7.4) were excited with a UV lamp at 254 nm and then

photographed (Figure 3.13). **3.4·Tb$_2$** is extremely bright to the naked eye, **3.3·Tb$_2$** can also be seen (as a result of photoreduction) whereas both **3.1·Tb$_2$** and **3.2·Tb$_2$** are non-emissive.

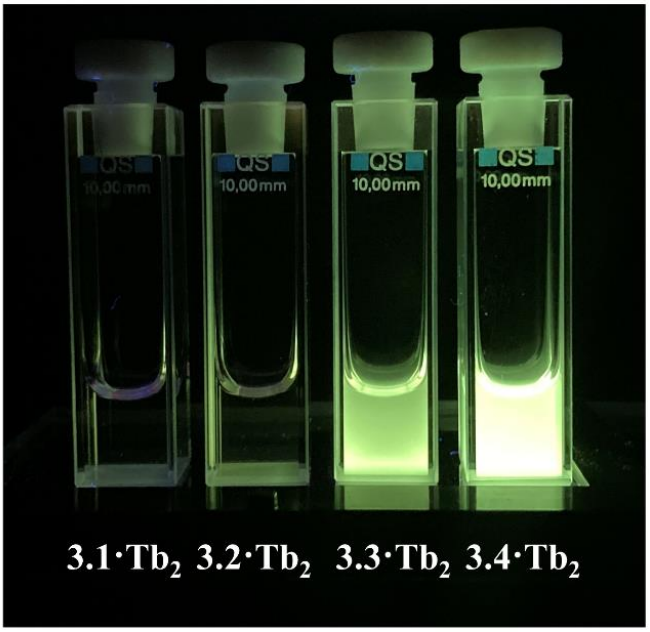


Figure 3. 13: Visualisation of the difference in emission intensity of all Tb(III) probes upon excitation with 254 nm light as taken with a camera.

3.6.3 Time-gated Luminescence

3.6.3.1 Luminescence Lifetimes

The luminescence lifetimes of complexes **3.1·Tb$_2$**, **3.2·Tb$_2$**, **3.3·Tb$_2$** and **3.4·Tb$_2$** were measured upon excitation at 488 nm at 90 μM in PBS buffered H_2O (pH 7.4) with a 50 μs time delay (Figure 3.14).

From Figure 3.14a, the Tb(III) complexes **3.1·Tb$_2$, 3.3·Tb$_2$** and **3.4·Tb$_2$** were found to have similar profiles. Only upon plotting against a logarithmic scale the differences could be more clearly observed (Figure 3.14b). In contrast, the luminescence lifetime of **3.2·Tb$_2$** differed significantly from the related complexes: it was found to be significantly shorter. At 298 K, a monoexponential decay profile was recorded for complexes **3.1·Tb$_2$**, **3.3·Tb$_2$** and **3.4·Tb$_2$** in water, whilst **3.2·Tb$_2$** exhibited a biexponential decay profile. This is indicative of the presence

of two distinct species in solution, corresponding to the *E* and *Z* isomers of the azobenzene fragment of **3.2·Tb$_2$**.[172, 173, 186]

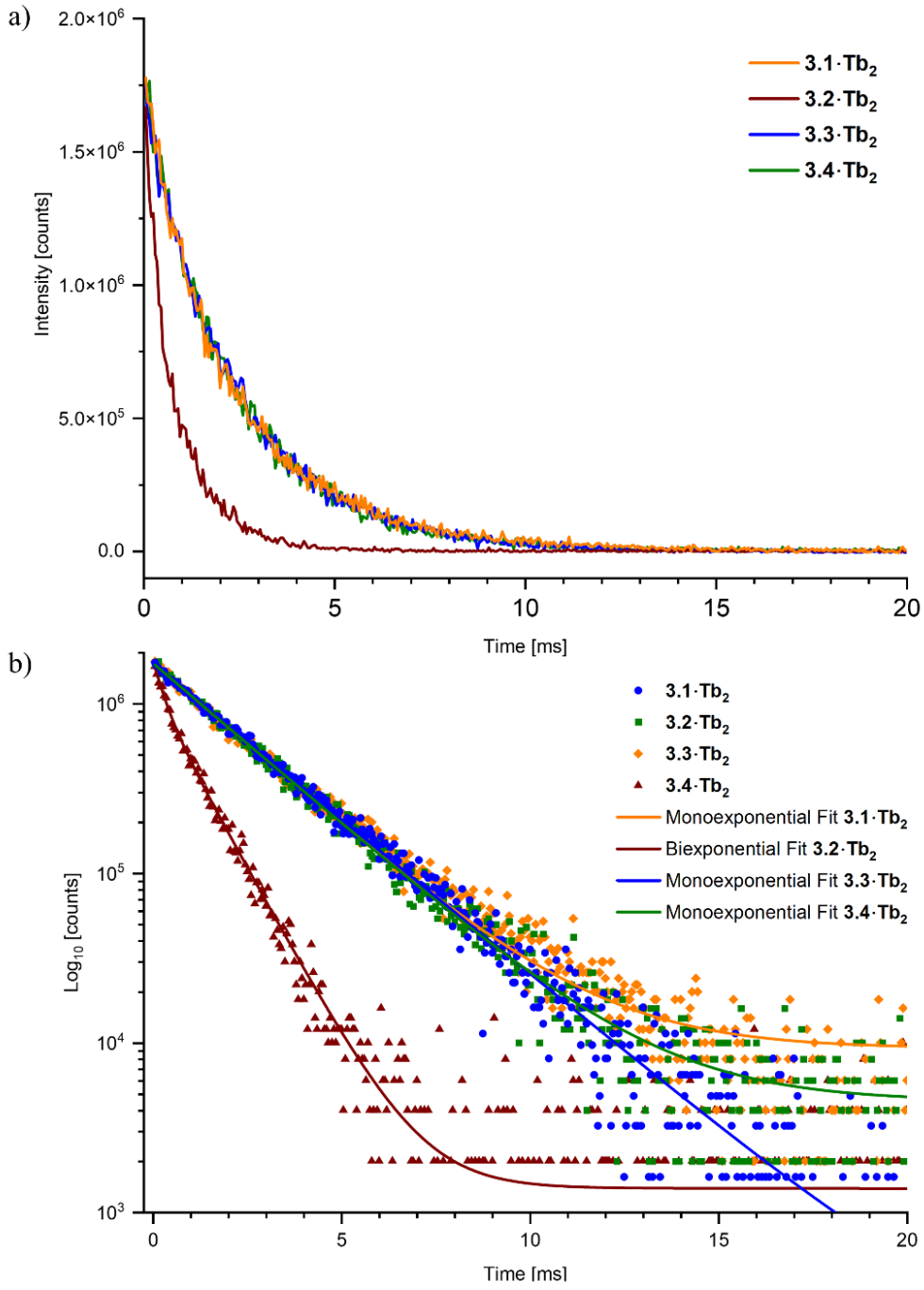


*Figure 3.14: a) Exponential decays of the complexes **3.1-4·Tb$_2$** b) Decay profile on log scale of the complexes **3.1-4·Tb$_2$**. Complexes were measured at 90 µM in 10 mM PBS buffer at pH 7.4 (orange – **3.1·Tb$_2$**, λ_{exc} = 294 nm, λ_{em} = 545 nm, Front slit: 29.00 nm, Exit slit: 14.50 nm, time delay: 50 µs; maroon – **3.2·Tb$_2$**, λ_{exc} = 294 nm, λ_{em} = 545 nm, Front slit: 19.0 nm, Exit slit: 6.00 nm, time delay: 50 µs; blue – **3.3·Tb$_2$**, λ_{exc} = 310 nm, λ_{em} = 545 nm, Front slit: 13.0 nm, Exit slit: 1.00 nm, time delay: 50 µs; green – **3.4·Tb$_2$**, λ_{exc} = 294 nm, λ_{em} = 545 nm, Front slit: 29.00 nm, Exit slit: 2.00 nm, time delay: 50 µs).*

The luminescence lifetime of each complex in D_2O (pD 7.4 (pH + 0.45)) was also measured and the corresponding *q* values (number of bound solvent) were calculated using the modified Horrocks equation (3.3). Here, A = 5.0 and B = 0.06 in water and k_H and k_D (in ms^{-1}) correspond to the rate constant of the lifetime decay in the given solvent and the corresponding deuterated solvent.[68]

$$q = A(k_H - k_D - B)$$

(3. 3)

*Table 3.2: Luminescent lifetimes of **3.1-4·Tb₂** in PBS buffered H_2O (pH 7.4) and D_2O (pD 7.4 (pH + 0.45)) upon excitation at 488 nm, 0.5 s time delay and the corresponding q values (number of bound solvent) as calculated by the modified Horrocks equation. *__3. 2·Tb₂__ fit to a biexponential lifetime.*

	T (H_2O) (ms)	**T (D_2O) (ms)**	q_{Tb}
3.1·Tb₂	2.28	2.85	~0
3.2·Tb₂	1.00, 0.20	0.85	-
3.3·Tb₂	2.38	2.54	~0
3.4·Tb₂	2.28	2.49	~0

Luminescent lifetimes for **3.1·Tb₂**, **3.3·Tb₂** and **3.4·Tb₂** ranged between 2.2-2.4 ms in water, increasing modestly to 2.5-2.8 ms in D_2O, suggesting a contribution from an outer sphere oscillator effect.[67] This is supported by calculation of the number of water molecules directly bound to the metal centre (q) using the modified Horrocks equation.[66] The value of ~0 for the Tb(III) complexes suggest that both Tb(III) centres are not coordinated to a solvent molecule, which agrees with the solid state structure determined for the related complex shown in Figure 3.2. There, the Tb(III) centres are each coordinatively saturated by the ligand, particularly the bridging phenolate. This lack of inner sphere solvent in both solid and solution state allows for the intense brightness observed for **3.4·Tb₂** in solution. Effectively, the Tb(III) centres are caged from the external environment by the binuclear ligand.

3.7 Chemical Reduction

The responsive capabilities of probes **3.1·Ln$_2$**, **3.2·Ln$_2$** and **3.3·Ln$_2$** were investigated with the *in-situ* chemical reduction of each probe. This transformation was monitored by ^{1}H NMR and luminescence.

3.7.1 ^{1}H NMR Response

Complexes **3.1·Eu$_2$** and **3.2·Eu$_2$** were reduced in the presence of zinc and a proton source (either NH_4Cl or NH_4HCO_2) in D_2O. ^{1}H NMR was used to investigate the reduction over time, particularly monitoring the chemical shift of the axial proton on the cyclen ring, denoted with a '*'. Figure 3.15 shows the reduction of **3.1·Eu$_2$** to **3.4·Eu$_2$** over the course of 18 hours. Between 6-12 hours a mixture of both **3.1·Eu$_2$** and **3.4·Eu$_2$** is observed, which is clearly described by the presence of both axial proton peaks at 49.1 (**3.1·Eu$_2$**) and 44.1 ppm (**3.4·Eu$_2$**). After 18 hours, **3.1·Eu$_2$** is no longer observable in the ^{1}H NMR spectrum, which is identical to **3.4·Eu$_2$** in D_2O. As expected, over time the axial proton shifts downfield, indicative of the formation of **3.4·Tb$_2$**.

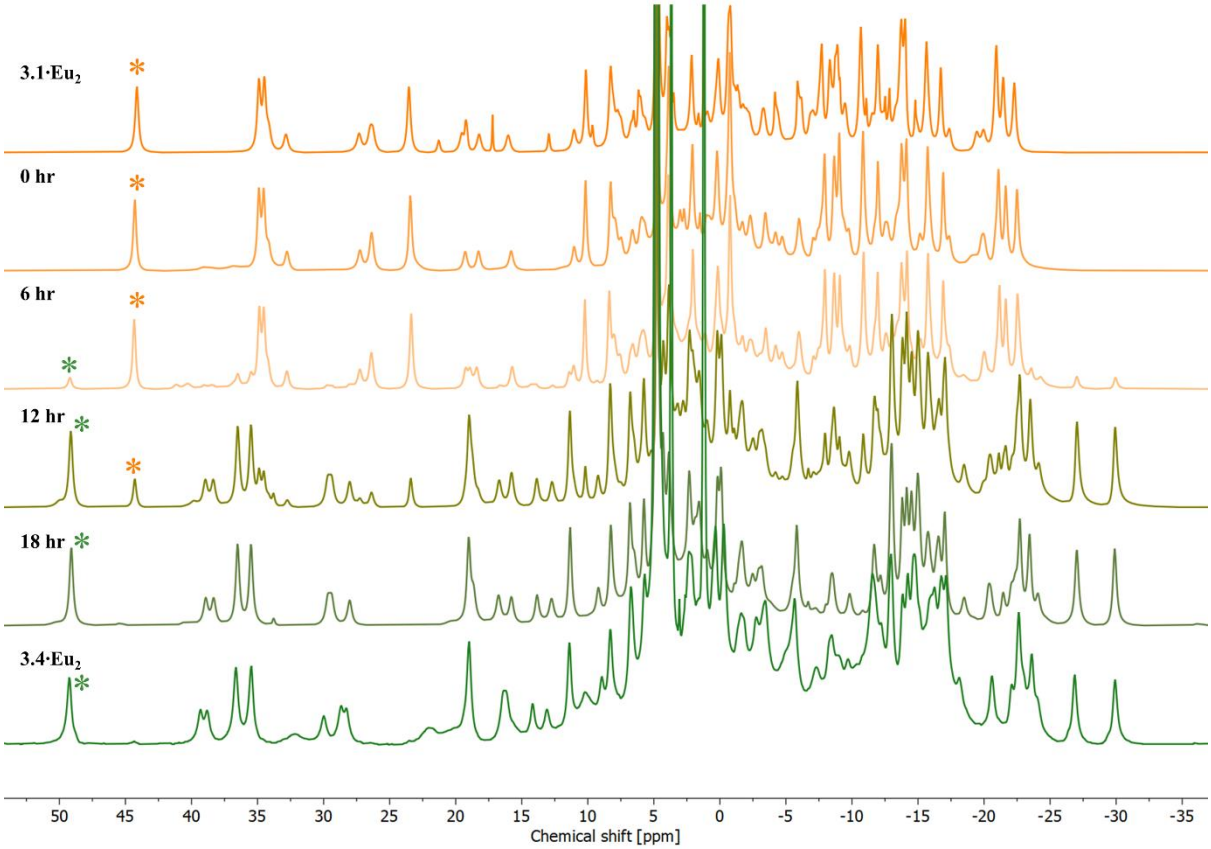


*Figure 3.15: ^{1}H NMR of the in situ chemical reduction of **3.1·Eu$_2$** to **3.4·Eu$_2$** with Zn and NH_4Cl over the course of 18 hours in D_2O at 400 MHz.*

Figure 3.16 shows the *in-situ* chemical reduction of **3.2·Eu$_2$** to **3.4·Eu$_2$** with zinc and ammonium formate. The reduction of **3.2·Eu$_2$** was slower compared to that of **3.1·Eu$_2$** under the same conditions, reaching completion after 48 hours. As with **3.1·Eu$_2$** the progress of the reduction could be monitored by the presence and intensity of the axial proton environment. At 24 hours, the solution contained a mixture of **3.2·Eu$_2$** (H_{ax} = 46.1 ppm) and **3.4·Eu$_2$** (H_{ax} = 49.1 ppm) in solution. After 48 hours, only **3.4·Eu$_2$** was present.

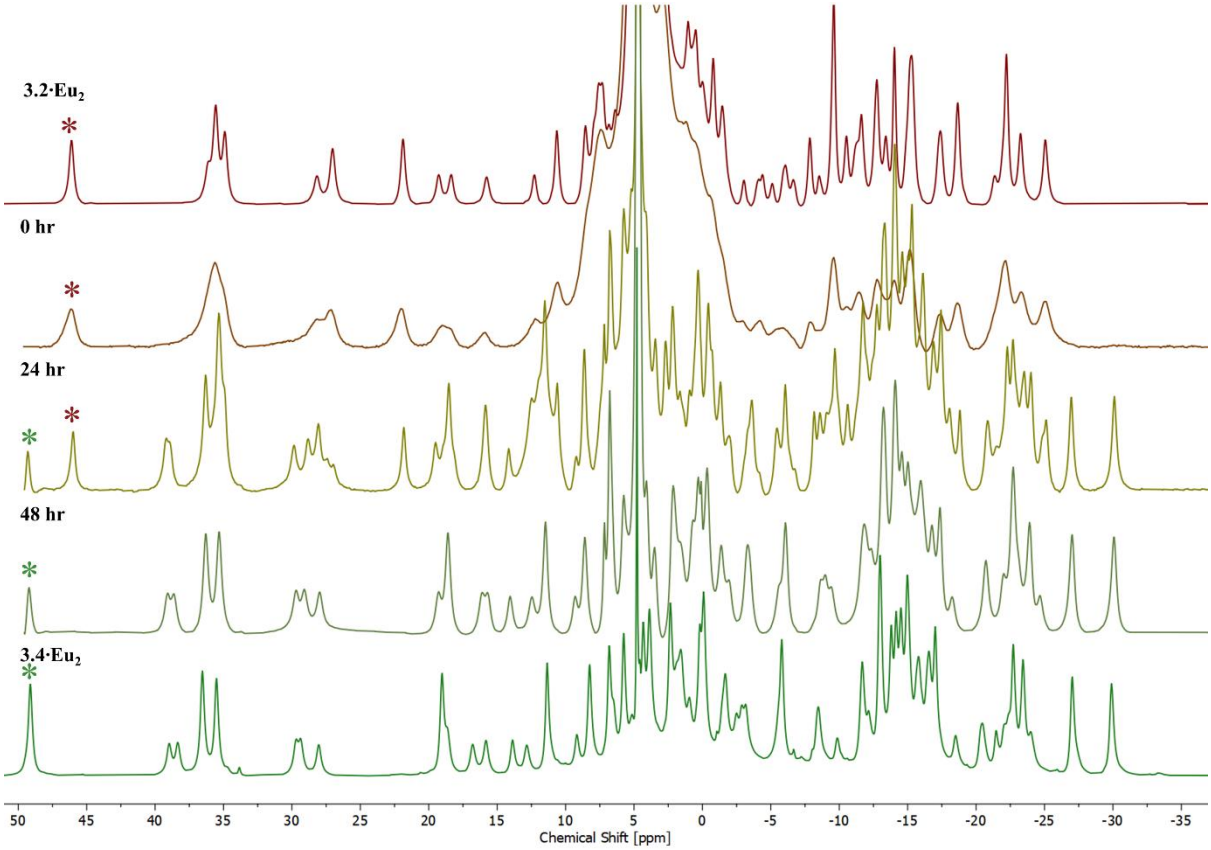


*Figure 3.16: ^{1}H NMR of the in-situ chemical reduction of **3.2·Eu$_2$** to **3.4·Eu$_2$** with Zn and NH_4HCO_2 over the course of 48 hours in D_2O at 400 MHz.*

3.3·Eu$_2$ was reduced *in-situ* with NaSH in D_2O. This reduction was much quicker comparatively and the reaction had gone to completion after just 2 hours (Figure 3.17). Notably, the reduction had already started after 5 minutes, and at 1 hour a mixture of both **3.3·Eu$_2$** (δH_{ax} = 47.6 ppm) and **3.4·Eu$_2$** (δH_{ax} = 49.1 ppm) in solution was observed. Upon complete reduction after 2 hours only **3.4·Eu$_2$** was present in solution.

The formation of **3.4·Eu$_2$** upon reduction of each of the activatable probes **3.1·Eu$_2$**, **3.2·Eu$_2$** and **3.3·Eu$_2$** was supported by HR-ESI mass spectrometry (See **Chapter 7**). Upon complete reduction, samples were taken from the NMR tubes, diluted with water and run on the HR-ESI mass spectrometer. For each complex the fingerprint for **3.4·Eu$_2$** was recorded, confirming the reduction did in fact yield the proposed aniline complex.

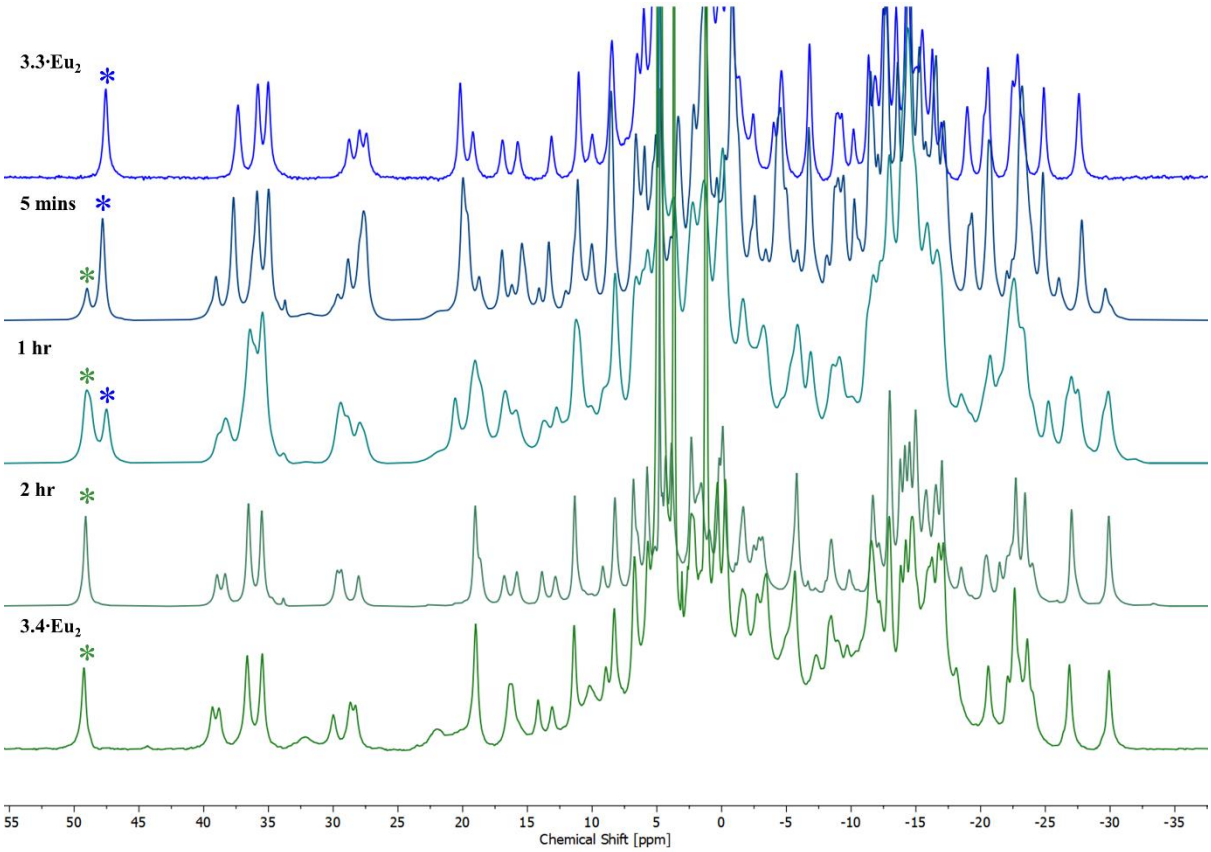


*Figure 3.17: ^{1}H NMR of the in situ chemical reduction of **3.3·Eu2** to **3.4·Eu2** with NaSH over the course of 2 hours in D_2O at 400 MHz.*

3.7.2 Luminescence Response

The luminescent "turn-on" response of optical probes **3.1·Tb2**, **3.2·Tb2** and **3.3·Tb2** upon *in-situ* chemical reduction with zinc and ammonium formate were investigated using a Tecan infinite M1000 Pro Plate reader. To each well varying concentrations of each complex **3.1·Tb2**, **3.2·Tb2**, **3.3·Tb2** and **3.4·Tb2** were added (0.01 M, 0.001 M and 0.0001 M) in MES buffer (0.1 M pH 6.0). To each sample 10 µl of 1 M zinc and 20 µl of 1 M ammonium formate was added. Additionally, all complexes were measured under the same conditions in the absence of the reducing agents. For each sample, a spectrum was recorded every 30 minutes for 16 hours, samples were shaken before each measurement. λ_{ex} = 280 nm, emission slit = 2.5 nm, excitation slit = 2.5 nm, gain = 165, integration time 0.2 ms.

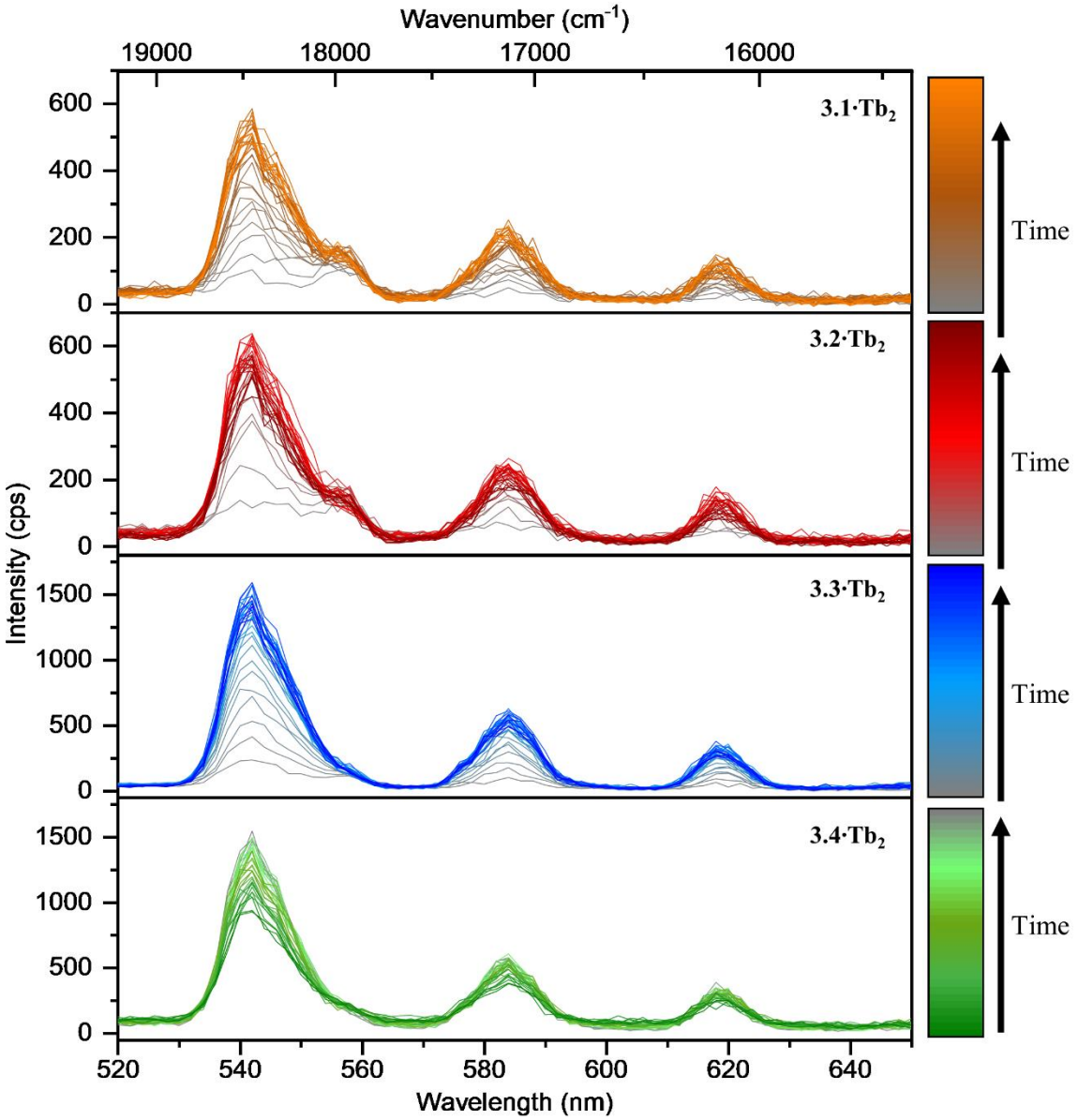


*Figure 3.18: Emission spectra **3.1·Tb₂** (orange), **3.2·Tb₂** (red), **3.3·Tb₂** (blue) and **3.4·Tb₂** (green) (0.01 M in MES (0.1 M)) upon exposure to Zn and ammonium formate. λ_{ex} = 280 nm, emission slit = 2.5 nm, excitation slit = 2.5 nm, gain = 165, integration time 0.2 ms.*

Figure 3.18 shows the change in Tb(III) emission, upon excitation at 280 nm, in the presence of zinc and ammonium formate over 16 hours for complexes **3.1·Tb₂**, **3.2·Tb₂**, **3.3·Tb₂**, and **3.4·Tb₂**. For each activatable probe, **3.1·Tb₂**, **3.2·Tb₂** and **3.3·Tb₂**, the emission intensity increases significantly over the progression of the experiment. Upon reduction, the radiative $^5D_4 \rightarrow {}^7F_J$ (J = 5, 4, 3) transitions of the Tb(III) metal centre are observed, corresponding to the formation of the emissive complex **3.4·Tb₂**. Interestingly, the emission intensity of **3.4·Tb₂** changes slightly over time, decreasing in intensity over the progression of the experiment. This

is attributed to photobleaching upon extended periods of exposure to UV light. Importantly, **3.1·Tb$_2$**, **3.2·Tb$_2$** and **3.3·Tb$_2$** measured under the same conditions, in the absence of reductive chemicals, showed negligible change in the emission intensity over time. Therefore, the change observed in Figure 3.18 is directly correlated to the *in-situ* reduction of each optical probe, thus all three Tb(III) complexes demonstrate a significant increase in the emission of green light upon exposure to a reductive environment.

3.8 Electrochemical Reduction

The electrochemical reduction of complexes **3.1·Tb$_2$**, **3.2·Tb$_2$** and **3.3·Tb$_2$** were measured in collaboration with the Vincent group by Euan Sarson. Analysis of the experimental spectra was completed in collaboration. To further understand the redox activity of probes **3.1·Tb$_2$**, **3.2·Tb$_2$** and **3.3·Tb$_2$** the electrochemical reduction of each probe was investigated by cyclic voltammetry. Cyclic voltammograms were run with a step potential = -0.00244 V and a scan rate = 0.02 V/s, with 3 cycles recorded for each complex. The set-up included a working electrode of glassy carbon (1 mm diameter), a counter electrode of graphite, and an Ag/AgCl reference electrode. The cell was set up under a N_2 atmosphere in a glove box (O_2 < 2 ppm). The Ag/AgCl reference electrode was calibrated *vs* SHE. The cathodic onset potential, the measure by which the probes were compared, was defined by the potential at which the current in the baseline-corrected voltammogram begins to increase exponentially and exceeds a threshold value of 10 nA. This procedure is adapted from a method used to define onset potentials for a range of nitro-compounds from the current at a rotating disk electrode.[249] A stationary electrode was used here due to the smaller sample requirement in the cell.

*Table 3.3: Cathodic onset potentials (V) of **3.1·Tb₂**, **3.2·Tb₂** and **3.3·Tb₂** in both TRIS (pH 7.4) and MES (pH 6.0) vs SHE.*

Cathodic Onset Potential vs SHE (V)

	Tris pH 7.4	MES pH 6.0
3.1·Tb₂	-0.413	-0.240
3.2·Tb₂	-0.394	-0.258
3.3·Tb₂	-	-

The cyclic voltammogram was recorded for each probe in both TRIS (pH 7.4) and MES (pH 6.0) and the cathodic onset potentials determined are shown in Table 3.3. Both pH 7.4 and 6.0 were investigated. Tumour environments can often become acidic and in extreme examples can reach pH 6.0, therefore understanding the redox capability of the Tb(III) complexes was required to investigate any pH dependence.[250]

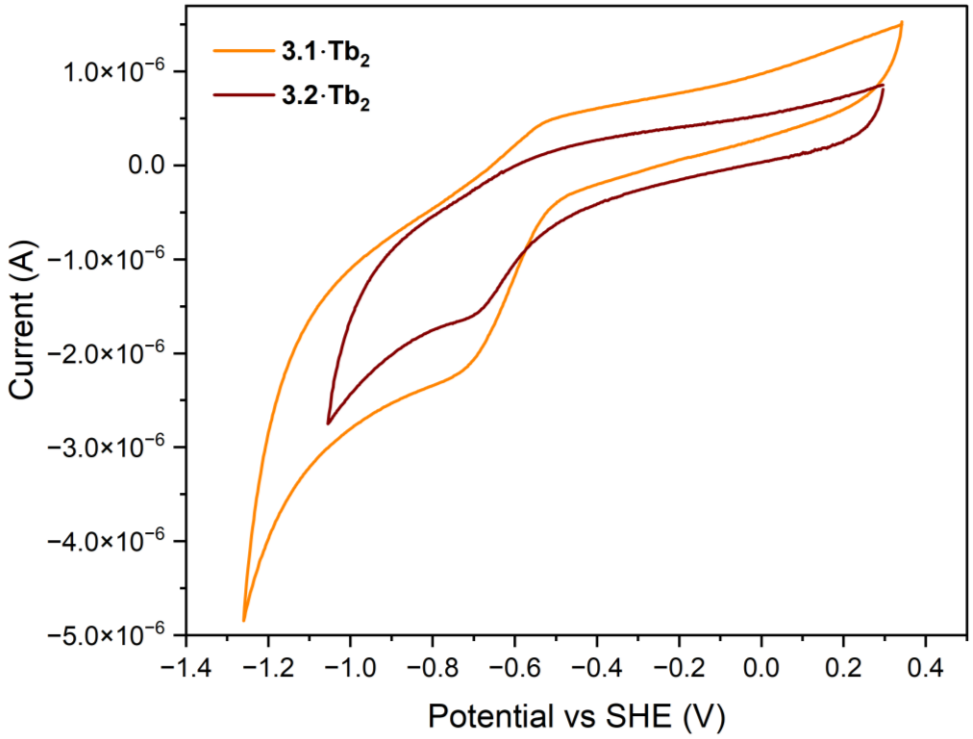


*Figure 3.19:Cyclic voltammogram of **3.1·Tb₂** and **3.2·Tb₂** in TRIS (pH 7.4) vs SHE.*

3.1·Tb$_2$ and **3.2·Tb$_2$** produced clear cyclic voltammograms at pH 7.4, containing a single reduction peak upon exposure to increasingly negative potentials. Upon subsequent treatment to increasingly positive potentials (0.4 V), no oxidation was observed (Figure 3.19). This suggests that the reduction of both **3.1·Tb$_2$** and **3.2·Tb$_2$** is irreversible under electrochemical conditions. The presence of only one reduction peak for each complex suggests that all mechanistic steps for the complete reduction of both **3.1·Tb$_2$** and **3.2·Tb$_2$** occur within the boundaries of each peak and thus must represent the six electrons required for the reduction of both the nitroaryl and the azobenzene complexes. The cathodic onset potentials of **3.1·Tb$_2$** and **3.2·Tb$_2$** at pH 7.4 were determined as -0.41 and -0.39 V (*vs* SHE), respectively, consistent with the redox potential of related nitrophenyl and azobenzene compounds.[249, 251, 252]

The electrochemical reduction of **3.1·Tb$_2$** and **3.2·Tb$_2$** was also measured at pH 6.0 in MES reported in the cyclic voltammograms shown in Figure 3.20. This allowed for investigations into the influence of pH on the electrochemical potential at which the reduction of both the nitroaryl and azobenzene occurs. The electrochemical behaviour observed for **3.1·Tb$_2$** at pH 6.0 differs to that at pH 7.4, the cathodic onset potential is reduced to -0.24 V vs SHE and the electrochemical reduction remains irreversible at pH 6.0. Additionally, the electrochemical reduction of **3.2·Tb$_2$** also occurred at a more positive cathodic onset potential -0.26 V *vs* SHE, again the reduction remained irreversible at lower pH. The possible increase in cathodic onset potential for both **3.1·Tb$_2$** and **3.2·Tb$_2$** was perhaps due to the increased ease of protonation of the ligands at pH 6.0.

The onset potential of **3.3·Tb$_2$** could not be determined, perhaps due to the instability of the azide functional group to electrochemical conditions. The subtle difference in onset potential of **3.1·Tb$_2$** and **3.2·Tb$_2$** and their pH dependence is promising for the utility of the compounds in investigating a range of redox potentials in solution, given that the redox potential of hypoxic tissues has been found to be between -0.25 and -0.4 V (*vs* SHE).[253, 254]

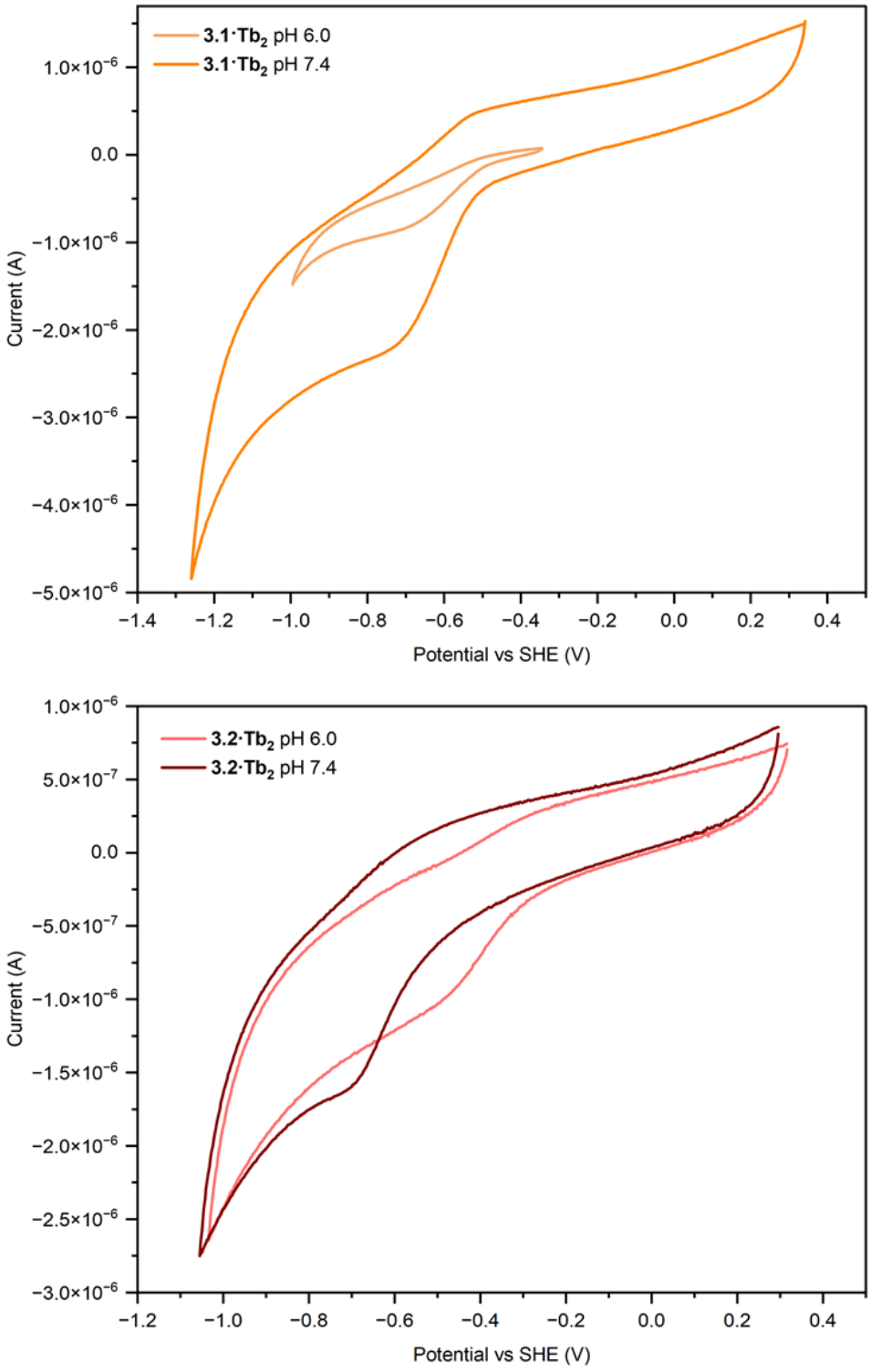


*Figure 3.20: Cyclic voltammogram of top)**3.1·Tb₂** in TRIS (pH 7.4) and MES (pH 6.0) bottom) **3.2·Tb₂** in TRIS (pH 7.4) and MES (pH 6.0) vs SHE*

3.9 Detecting Hydrogen Sulphide in Solution

Hydrogen sulphide can accumulate in hypoxic tissue and inhibit mitochondrial respiration. By understanding the levels of hydrogen sulphide in hypoxic environments the mechanism of hypoxia itself can be further understood.[255]

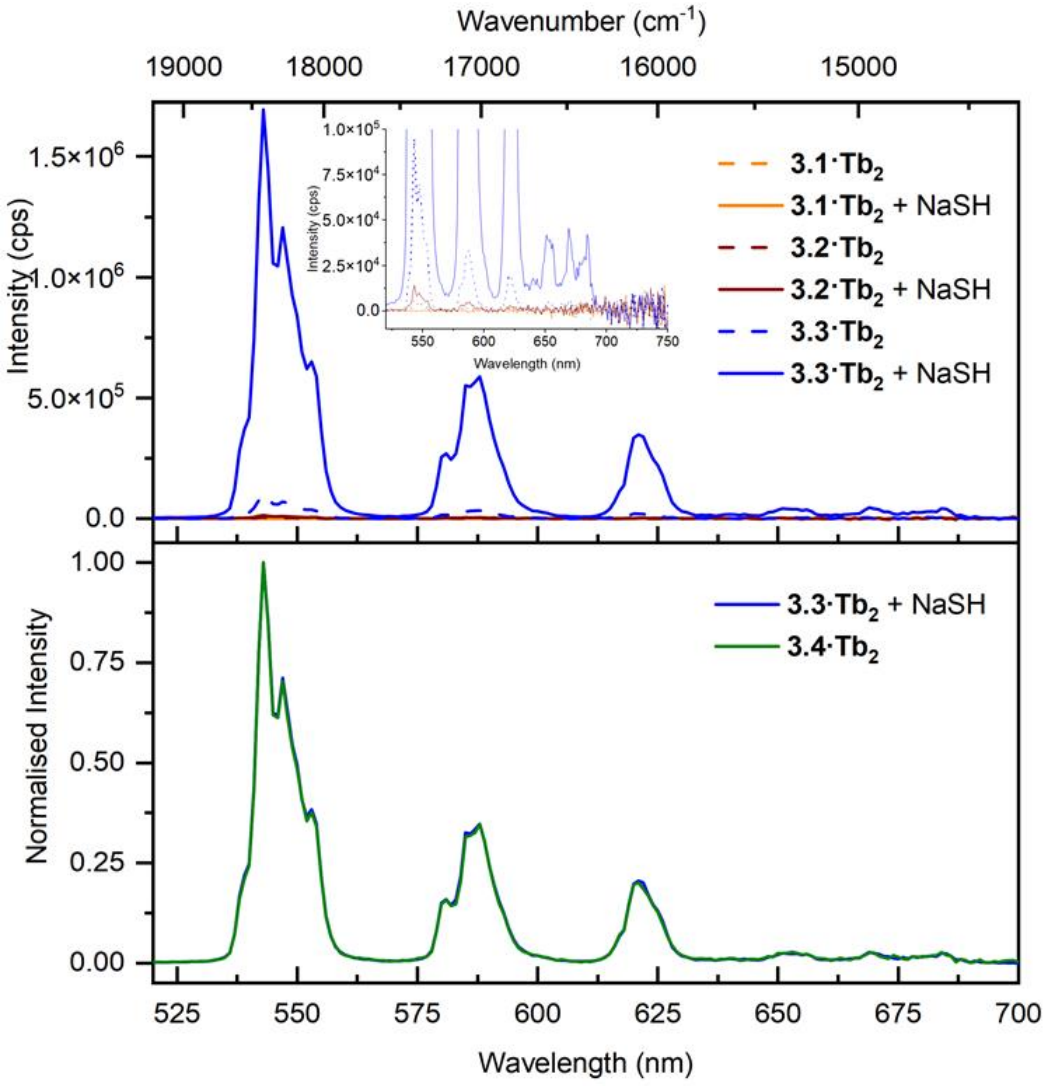


*Figure 3.21: Emission spectra of redox-activatable probes **3.1-3·Tb2** (90 µM in PBS at pH 7.4) upon exposure to NaSH (250 µM) (top) Emission spectra of **3.1-3·Tb2** before and after exposure to NaSH (λ_{ex} = 318 nm, emission slits: 1 nm, excitation slits: 1 nm, integration time 0.5 s) (bottom) Normalised emission spectra of **3.3·Tb2** (blue) after exposure to NaSH and **3.4·Tb2** (green).*

To investigate the redox sensitive optical probes **3.1·Tb2**, **3.2·Tb2** and **3.3·Tb2** as sensors for hydrogen sulphide each complex was exposed to NaSH for 10 minutes in PBS buffered to pH 7.4. The emission spectra (λ_{ex} = 318 nm) were compared before and after the addition of

hydrogen sulphide (Figure 3.21). Probes **3.1·Tb$_2$** and **3.2·Tb$_2$** remained dark and showed no observable Tb(III) centred emission upon exposure to NaSH. However, **3.3·Tb$_2$**, which contains an aryl-azide functional group, displayed a 20-fold increase in the emission intensity upon addition of NaSH. The emission observed was characteristic of Tb(III) emission, displaying the distinctive $^5D_4 \rightarrow {}^7F_J$ (J = 5, 4, 3, 2, 1, 0) transitions. Importantly, by comparison of the normalised emission spectrum of **3.3·Tb$_2$** after reduction with NaSH, with **3.4·Tb$_2$** the crystal field splitting of the Tb(III) is identical. This suggests that upon reduction of **3.3·Tb$_2$** with NaSH the aniline **3.4·Tb$_2$** is formed.

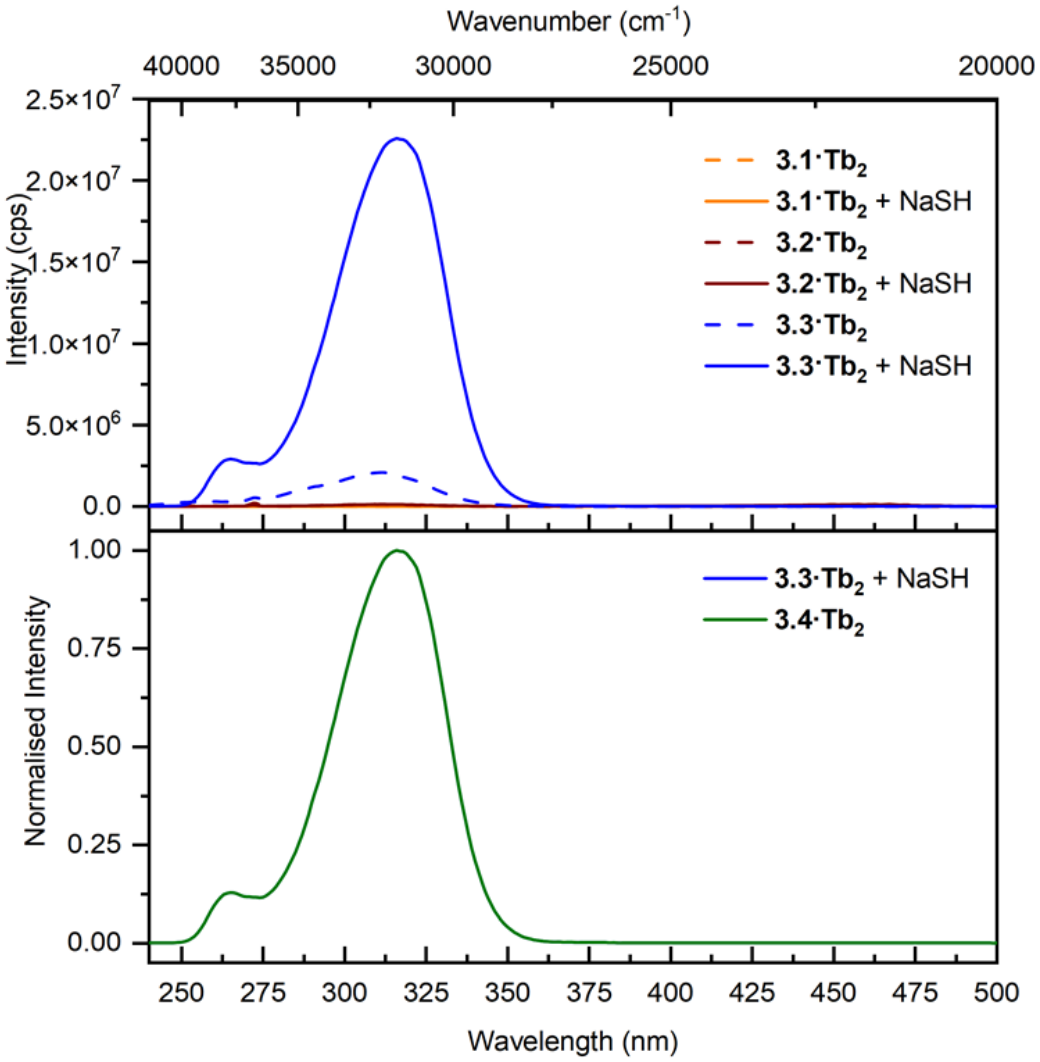


*Figure 3.22: Excitation spectra of redox-activatable probes **3.1-3·Tb$_2$** (90 µM in PBS at pH 7.4) upon exposure to NaSH (250 µM) (top) Excitation spectra of **3.1-3·Tb$_2$** before and after exposure to NaSH (λ_{em} = 545 nm, emission slits: 5 nm, excitation slits: 1 nm, integration time 0.5 s) (bottom) Normalised excitation spectra of **3.3·Tb$_2$** (blue) after exposure to NaSH and **3.4·Tb$_2$** (green).*

Additionally, the excitation spectra were recorded for each probe (λ_{ex} = 545 nm) before and after exposure to NaSH, Figure 3.22. Again, **3.1·Tb$_2$** and **3.2·Tb$_2$** displayed minimal sensitising efficiency for Tb(III) emission, both before and after the addition of NaSH. However, the excitation spectrum recorded after the addition of NaSH for **3.3·Tb$_2$** increased significantly. Normalised excitation spectra of **3.3·Tb$_2$** after exposure to NaSH and **3.4·Tb$_2$** were found to be identical, further supporting that reduction of the aryl-azide **3.3·Tb$_2$** converts it to the aniline **3.4·Tb$_2$**. Of all the binuclear redox sensitive Tb(III) probes investigated only the aryl-azide probe, **3.3·Tb$_2$**, is selective for reduction by NaSH. These results show that **3.3·Tb$_2$** is extremely promising as an optical "turn-on" probe for the detection of NaSH in solution.

3.10 Biocatalytic Reduction

An exciting new technology, developed by the Vincent group, investigates the bioreduction of compounds containing nitro functional groups using hydrogenanse enzymes immobilized on a carbon support. Their systems have been found to work well for simple organic compounds, however they are yet to be tested on more complex inorganic complexes, with a range of reducible groups. To explore the possibility of biocatalytic reduction of the three redox sensitive optical probes, a carbon-immobilised hydrogenase enzyme was investigated in collaboration with the Vincent group, particularly Dr Daria Sokolova.[256-258] The catalyst developed in the Vincent group which consists of a nickel-iron hydrogenase, Hyd-1, adsorbed onto a carbon-black support (Hyd-1/C), has previously been shown to facilitate the reduction of a wide range of substrates containing nitro-aryl groups. [249, 259-261] Therefore, it was a promising catalyst for the bioreduction of optical probes **3.1·Tb$_2$**, **3.2·Tb$_2$** and **3.3·Tb$_2$**.

Accordingly, **3.1·Tb$_2$**, **3.2·Tb$_2$** and **3.3·Tb$_2$** (10 mM) in PBS (50 mM, pH 6.0) were treated with Hyd-1/C (C:Hyd-1 = 40:1 mass ratio, 0.53 mg of C, 13 μg of Hyd-1 per reaction) at pH 6.0 in water (10% DMSO) under 30 mL/min flow of H_2 for 24 hours at room temperature (for full

experimental details see **Chapter 7**). Under these conditions only the reduction of **3.2·Tb$_2$** was observed by emission spectroscopy (Figure 3.23b), characterized by the radiative transitions from the $^5D_4$ emissive state of Tb(III). This is the first example of an azobenzene complex being reduced in the presence of a hydrogenase biocatalyst.

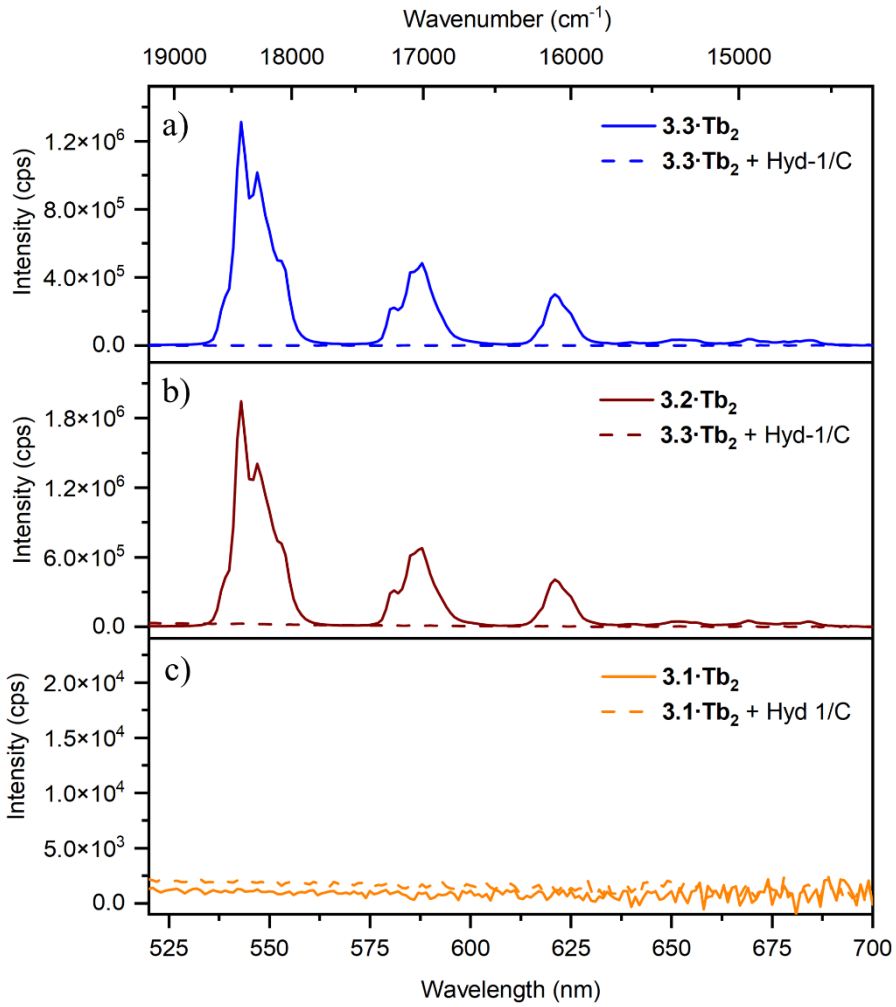


*Figure 3.23: Emission properties of redox-activatable probes **3.1-3·Tb$_2$** (90 µM in PBS at pH 6.0) upon exposure to Hydrogenase -1 on carbon support a) **3.3·Tb$_2$** before and after exposure to 1.06 mg of C, 26 µg of Hyd-1 b) **3.2·Tb$_2$** before and after exposure to 0.53 mg of C, 13 µg of Hyd-1 c) **3.1·Tb$_2$** before and after exposure to 1.06 mg of C, 26 µg of Hyd-1. (λ_{ex} = 318 nm, emission slits: 3 nm, excitation slits: 1 nm, integration time 0.5s*

Upon increased catalyst loading (1.06 mg of C, 26 µg of Hyd-1 per reaction) and reaction time (72 hours) the reduction of **3.3·Tb$_2$** could be achieved (Figure 3.23a). Notably, the nitro-aryl complex, **3.1·Tb$_2$** was not reduced, even under extended reaction times (72 hours) and increased enzyme loading (1.06 mg of C, 26 µg of Hyd-1 per reaction) (Figure 3.23c). Previous work has found that a *para*-phenolate can inhibit the reduction of the aryl-nitro group with

Hyd-1/C, perhaps due to the electron density available on the aromatic ring and the availability of resonance stabilization. Much like the azobenzene complex, this is only one of a handful of examples of the reduction of azides with a hydrogenase biocatalyst. Thus, the field of biocatalytic reduction using Hyd-1 immobilized on carbon is expanded to the possibility of investigating the reduction of a variety of new classes of compound.

3.11 Cell Studies

Investigations into the viability of each probe in cellular environments, particularly in hypoxic cancer cells, were carried out in collaboration with Dr Lina Hacker and the Hammond group in the Department of Oncology at the University of Oxford.

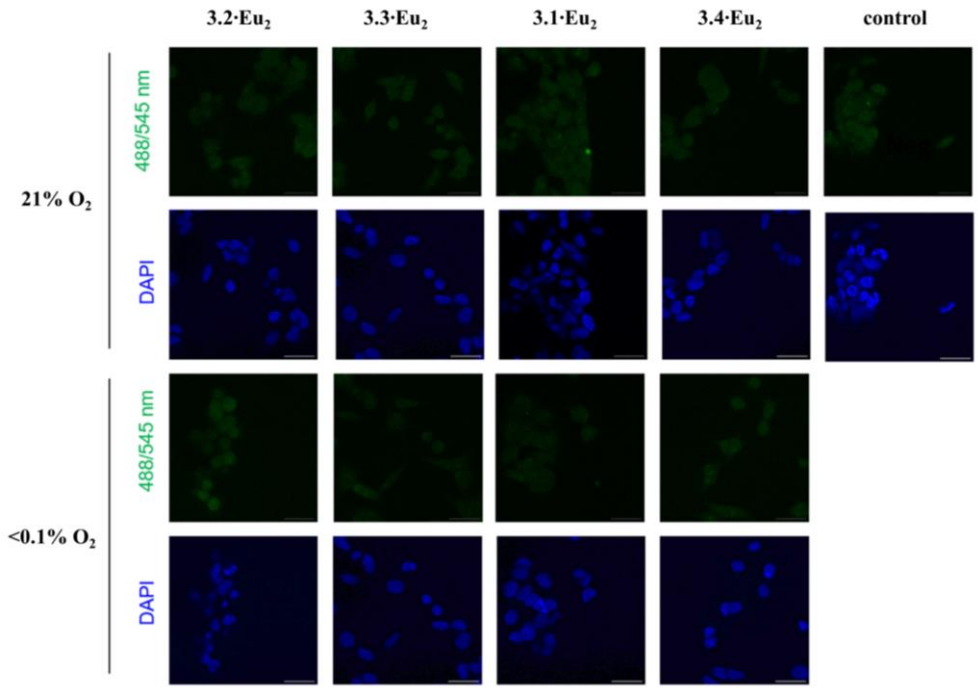


Figure 3.24: Fluorescence microscopy of complexes. Representative fluorescence images of HCT116 cells treated with ***3.1·Tb2****,* ***3.2·Tb2****,* ***3.3·Tb2*** *, or* ***3.4·Tb2*** *(500 μM) for 16 h in the oxygen conditions indicated (exc. 488 nm / em. 545 nm). Scale bar represents 12 μM; blue colour represents DAPI stain.*

Unfortunately, preliminary cellular uptake studies of all Tb(III) complexes, **3.1·Tb2**, **3.2·Tb2**, **3.3·Tb2** and **3.4·Tb2**, into colorectal cell line HCT116 under both normoxic (21 % O_2) and hypoxic (<0.1 % O_2) conditions showed no Tb(III) emission (Figure 3.24) upon direct

excitation into the $^7F_6 \rightarrow {}^5D_4$ transition (λ_{ex} = 488 nm). This included the control complex **3.4·Tb$_2$** with a quantum yield of 45.2%. From control experiments, Tb(III) emission can be observed under the conditions of the experiment. Therefore, the lack of Tb(III) emission is likely due to the lack of uptake of probes into the cell caused by the neutrality and polarity of the lanthanide compounds.[262]

3.12 Conclusions

In summary, this chapter describes the design, synthesis and applications of a family of redox activatable probes **3.1·Ln$_2$**, **3.2·Ln$_2$** and **3.3·Ln$_2$**. Judicious choice of coordinating lanthanide within the 3 distinct ligand systems allowed for responsive probes for both MR and optical imaging to be developed.

Gd(III) analogues were utilised for MR imaging presenting both turn-on and turn-off capabilities upon reduction. The relaxivity of **3.1·Gd$_2$** is greater than that of **3.4·Gd$_2$**, thus upon reduction a turn-off contrast probe is realised. Contrastingly, the relaxivity of **3.2·Gd$_2$** is lower than **3.4·Gd$_2$**, therefore reduction would correspond to a turn-on probe. Interestingly, the longitudinal relaxivity of the nitro derivative **3.1·Gd$_2$** is comparable to the clinically available Gd-DOTA.

The complex **3.4·Tb$_2$** displayed particularly favourable properties for imaging, with excitation wavelengths as high as 488 nm strong emission in the green region and long-lived luminescence lifetimes (ms). Importantly, the redox-activatable probes **3.1·Tb$_2$**, **3.2·Tb$_2$** and **3.3·Tb$_2$** are essentially dark under the same conditions. This allowed for a significant turn-on luminescent response upon reduction. Importantly, this reduction can be monitored by changes in the emission intensity, absorbance spectra and ^{1}H NMR spectra. It was found that the largest change in the emission intensity upon reduction occurred upon the reduction of **3.1·Tb$_2$**, where a 60-fold increase in the emission intensity was observed. Also, the reduction of **3.2·Tb$_2$** was

found to correspond to an increase in emission intensity of ~12-fold. The smallest changes, ~8-fold increase in emission intensity, were observed upon reduction of **3.3·Tb$_2$**, which was found to photoreduce under prolonged exposure to light. Notably, each probe presents a significant turn-on of bright green light emission upon excitation with visible light (488 nm) when exposed to reductive conditions.

Additionally, electrochemical reduction was successful for **3.1·Tb$_2$** and **3.2·Tb$_2$**, revealing an irreversible reduction peak potential with cathodic onset potentials within the range of previously measured redox potentials of hypoxic cells. This suggests that the reduction of both probes could be achieved under the redox potential afforded by hypoxic environments, allowing insight into the mechanisms of hypoxia. Futhermore, **3.3·Tb$_2$** was found to be specific for the optical sensing of hydrogen sulfide in solution, a biomarker for hypoxia. Therefore, with **3.2·Tb$_2$** the mechanism and role of hydrogen sulfide in hypoxic environments can be further understood. Finally, biocatalytic reduction was demonstrated using Hyd-1/C for **3.2·Tb$_2$** and **3.3·Tb$_2$** in water and monitored by changes in the Tb(III) emission intensity. This demonstrates the first examples of both azobenzene and azide compounds being reduced by a hydrogenase biocatalyst, opening up new avenues for the catalytic reduction of important classes of compounds.

These results demonstrate the unique fundamental properties of lanthanide complexes for redox imaging applications. The reductive orthogonality of the complexes suggests that such systems could allow for the development of probes to establish the precise nature of reductive stress. With improved deliverability into cells, probes based on the design principles described in this chapter will aid in the understanding of the mechanisms, diagnosis and treatment of hypoxia and reductive biological environments more broadly.

3.13 References for Chapter 3

1. H. Sies, R. J. Mailloux and U. Jakob, *Nat. Rev. Mol. Cell Biol.*, 2024, **25**, 701–719
2. K. C. Heathcote, T. P. Keeley, M. Myllykoski, M. Lundekvam, N. McTiernan, S. Akter, N. Masson, P. J. Ratcliffe, T. Arnesen and E. Flashman, *Nat. Commun.*, 2024, **15,** 5360
3. E. U. Hammarlund, E. Flashman, S. Mohlin and F. Licausi, *Science*, 2020, **370**, 421.
4. E. H. Sarsour, M. G. Kumar, L. Chaudhuri, A. L. Kalen and P. C. Goswami, *Antioxid. Redox Signal*, 2009, **11**, 2985-3011.
5. J. D. Watson, *Lancet*, 2014, **383**, 841-843.
6. A. F. Cumpstey, A. D. Clark, J. M. Santolini, A. A. Jackson and M. Feelisch, *Antioxid. Redox Signal*, 2021, **35**, 1226-1268.
7. Y. M. Lee, W. F. He and Y. C. Liou, *Cell Death Discov.*, 2021, **12**.
8. E. M. Hammond, M. C. Asselin, D. Forster, J. P. B. O'Connor, J. M. Senra and K. J. Williams, *Clin. Oncol.*, 2014, **26**, 277-288.
9. J. A. Maybin, A. A. Murray, P. T. K. Saunders, N. Hirani, P. Carmeliet and H. O. D. Critchley, *Nat. Commun.*, 2018, **9**.
10. K. Pham, K. Parikh and E. C. Heinrich, *Front. Physiol.*, 2021, **12**.
11. J. A. Horscroft, A. O. Kotwica, V. Laner, J. A. West, P. J. Hennis, D. Z. H. Levett, D. J. Howard, B. O. Fernandez, S. L. Burgess, Z. Ament, E. T. Gilbert-Kawai, A. Vercueil, B. D. Landis, K. Mitchell, M. G. Mythen, C. Branco, R. S. Johnson, M. Feelisch, H. E. Montgomery, J. L. Griffin, M. P. W. Grocott, E. Gnaiger, D. S. Martin and A. J. Murray, *Proc. Nat. Acad, Sci.*, 2017, **114**, 6382-6387.
12. A. J. Peacock, *Br. Med. J.*, 1998, **317**, 1063-1066.
13. P. S. Chen, W. T. Chiu, P. L. Hsu, S. C. Lin, I. C. Peng, C. Y. Wang and S. J. Tsai, *J Biomed. Sci.*, 2020, **27**, 63.
14. W. R. Wilson and M. P. Hay, *Nat. Rev. Cancer*, 2011, **11**, 393-410.
15. G. Delaney, S. Jacob, C. Featherstone and M. Barton, *Cancer*, 2005, **104**, 1129-1137.
16. E. Janczy-Cempa, O. Mazuryk, A. Kania and M. Brindell, *Cancers*, 2022, **14**, 2686.
17. P. du Souich and C. Fradette, *Expert Opin. Drug Metab. Toxicol.*, 2011, **7**, 1083-1100.
18. C. Fradette and P. du Souich, *Curr. Drug Metab.*, 2004, **5**, 257-271.
19. J. Zhang, H. W. Liu, X. X. Hu, J. Li, L. H. Liang, X. B. Zhang and W. H. Tan, *Anal. Chem.*, 2015, **87**, 11832-11839.
20. B. Brennecke, Q. Wang, Q. Zhang, H. Y. Hu and M. Nazaré, *Angew. Chem. Int, Ed.*, 2020, **59**, 8512-8516.
21. A. Ryan, *Br. J. Pharmacol.*, 2017, **174**, 2161-2173.
22. R. B. P. Elmes, *Chem. Commun.*, 2016, **52**, 8935-8956.
23. S. Kizaka-Kondoh and H. Konse-Nagasawa, *Cancer Sci.*, 2009, **100**, 1366-1373.
24. L. J. O'Connor, I. N. Mistry, S. L. Collins, L. K. Folkes, G. Brown, S. J. Conway and E. M. Hammond, *ACS Cent. Sci.*, 2017, **3**, 20-30.
25. S. S. Wang, X. J. Wu, Y. Q. Zhang, D. Zhang, B. Y. Xie, Z. X. Pan, K. F. Ouyang and T. Peng, *Org. Biomol. Chem.*, 2021, **19**, 3469-3478.
26. S. Karan, M. Y. Cho, H. Lee, H. S. Park, E. H. Han, Y. Song, Y. Lee, M. Kim, J. H. Cho, J. L. Sessler and K. S. Hong, *J. Med. Chem.*, 2022, **65**, 7106-7117.
27. S. Kuang, F. M. Wei, J. Karges, L. B. Ke, K. Xiong, X. X. Liao, G. Gasser, L. N. Ji and H. Chao, *J. Am. Chem. Soc.*, 2022, **144**, 4091-4101.
28. J. L. Sun, Z. L. Liu, H. C. Yao, H. L. Zhang, M. F. Zheng, N. Shen, J. J. Cheng, Z. H. Tang and X. S. Chen, *Adv. Mater.*, 2023, e202207733.
29. L. J. O'Connor, C. Cazares-Korner, J. Saha, C. N. G. Evans, M. R. L. Stratford, E. M. Hammond and S. J. Conway, *Nat. Protoc.*, 2016, **11**, 781-794.

30. S. Apte, F. T. Chin and E. E. Graves, *Curr. Org. Synth.*, 2011, **8**, 593-603.
31. A. L. D. Wallabregue, H. Bolland, S. Faulkner, E. M. Hammond and S. J. Conway, *J. Am. Chem. Soc.*, 2023, **145**, 2572-2583.
32. H. A. Henthorn and M. D. Pluth, *J. Am. Chem. Soc.*, 2015, **137**, 15330-15336.
33. E. Marutani, M. Morita, S. Hirai, S. Kai, R. M. H. Grange, Y. Miyazaki, F. Nagashima, L. Traeger, A. Magliocca, T. Ida, T. Matsunaga, D. R. Flicker, B. Corman, N. Mori, Y. Yamazaki, A. Batten, R. Li, T. Tanaka, T. Ikeda, A. Nakagawa, D. N. Atochin, H. Ihara, B. A. Olenchock, X. Shen, M. Nishida, K. Hanaoka, C. G. Kevil, M. Xian, D. B. Bloch, T. Akaike, A. G. Hindle, H. Motohashi and F. Ichinose, *Nat. Commun.*, 2021, **12**, 3108.
34. Y. Yao, L. Delgado-Rivera, H. Samareh Afsari, L. Yin, G. R. J. Thatcher, T. W. Moore and L. W. Miller, *Inorg. Chem.*, 2018, **57**, 681-688.
35. M. Tropiano and S. Faulkner, *Chem. Commun.*, 2014, **50**, 4696-4698.
36. J. F. Desreux, *Inorg. Chem.*, 1980, **19**, 1319-1324.
37. J. Lohrke, T. Frenzel, J. Endrikat, F. C. Alves, T. M. Grist, M. Law, J. M. Lee, T. Leiner, K. C. Li, K. Nikolaou, M. R. Prince, H. H. Schild, J. C. Weinreb, K. Yoshikawa and H. Pietsch, *Adv. Therap.*, 2016, **33**, 1-28.
38. H. Li and T. J. Meade, *J. Am. Chem. Soc.*, 2019, **141**, 17025-17041.
39. M. C. Heffern, L. M. Matosziuk and T. J. Meade, *Chem. Rev.*, 2014, **114**, 4496-4539.
40. J. Wahsner, E. M. Gale, A. Rodríguez-Rodríguez and P. Caravan, *Chem. Rev.*, 2019, **119**, 957-1057.
41. Y. Liu, L. L. Zhang, M. Nazare, Q. Q. Yao and H. Y. Hu, *Acta Pharm. Sin. B*, 2018, **8**, 401-408.
42. M. M. Rashid, B. A. Corbin, P. Jella, C. J. Ortiz, M. A. Samee, R. G. Pautler and M. J. Allen, *J. Am. Chem. Soc.*, 2022, **144**, 23053-23060.
43. S. A. A. S. Subasinghe, J. Ortiz, Caitlyn, J. Romero, L. Ward, Cassandra, G. Sertage, Alexander, L. Kurenbekova, T. Yustein, Jason, G. Pautler, Robia and J. Allen, Matthew, *Proc. Nat. Acad. Sci.*, 2023, **120**.
44. D. Parker, J. D. Fradgley and K.-L. Wong, *Chem. Soc. Rev.*, 2021, **50**, 8193-8213.
45. U. Cho and J. K. Chen, *Cell Chem. Biol.*, 2020, **27**, 921-936.
46. D. M. D. Leguerrier, R. Barré, J. K. Molloy and F. Thomas, *Coord. Chem. Rev.*, 2021, **446**.
47. C. A. Gould, *Science*, 2022, **378**, 1181-1181.
48. D. Maniaki, A. Sickinger, L. A. B. Moreno, D. Aguilà, O. Roubeau, N. S. Settineri, Y. Guyot, F. Riobé, O. Maury, L. A. Galán and G. Aromí, *Inorg. Chem.*, 2023, **62**, 3106-3115.
49. L. Münzfeld, S. Gillhuber, A. Hauser, S. Lebedkin, P. Hädinger, N. D. Knöfel, C. Zovko, M. T. Gamer, F. Weigend, M. M. Kappes and P. W. Roesky, *Nature*, 2023, **620**, 92.
50. T. J. Sørensen, L. R. Hill, J. A. Tilney, O. A. Blackburn, M. W. Jones, M. Tropiano and S. Faulkner, *Eur. J. Inorg. Chem.*, 2014, **2014**, 2520-2528.
51. L. R. Hill, T. J. Sørensen, O. A. Blackburn, A. Brown, P. D. Beer and S. Faulkner, *Dalton Trans.*, 2013, **42**, 67-70.
52. C. Alexander, J. A. Thom, A. M. Kenwright, K. E. Christensen, T. J. Sørensen and S. Faulkner, *Chem. Sci.*, 2023, **14**, 1194-1204.
53. O. A. Blackburn, M. Tropiano, L. S. Natrajan, A. M. Kenwright and S. Faulkner, *Chem. Commun.*, 2016, **52**, 6111-6114.
54. M. P. Placidi, L. S. Natrajan, D. Sykes, A. M. Kenwright and S. Faulkner, *Helv. Chim. Acta*, 2009, **92**, 2427-2438.
55. S. Concilio, L. Sessa, A. Petrone, A. Porta, R. Diana, P. Iannelli and S. Piotto, *Molecules*, 2017, **22**, 875.

56. E. J. Corey and A. Venkateswarlu, *J. Am. Chem. Soc.*, 1972, **94**, 6190-+.
57. P. Gupta, P. Yadav, B. Rana, B. Ghosh, R. S. Dhaka and K. Manna, *Eur. J. Inorg. Chem.*, 2024, **27**.
58. U. Geiger, Y. Haas and D. Grinstein, *J. Photochem. Photobiol. A*, 2014, **277**, 53-61.
59. D. Parker, E. A. Suturina, I. Kuprov and N. F. Chilton, *Acc. Chem. Res.*, 2020, **53**, 1520-1534.
60. N. Bloembergen, E. M. Purcell and R. V. Pound, *Phys. Rev.*, 1948, **73**, 679-712.
61. Y. Shen, F. L. Goerner, C. Snyder, J. N. Morelli, D. Hao, D. Hu, X. Li and V. M. Runge, *Investig. Radiol.*, 2015, **50**, 330-338.
62. A. Chevalier, C. Massif, P. Y. Renard and A. Romieu, *Chem. Eur. J.*, 2013, **19**, 1686-1699.
63. D. F. Eaton, *Pure Appl. Chem.*, 1988, **60**, 1107-1114.
64. D. F. Eaton, *J. Photochem. Photobiol. B*, 1988, **2**, 523-531.
65. A. Aebischer, F. Gumy and J.-C. G. Bünzli, *Phys. Chem. Chem. Phys.*, 2009, **11**, 1346.
66. Z. Zhao, M. Bian, C. Lin, X. Fu, G. Yu, H. Wei, Z. Liu, Z. Bian and C. Huang, *Sci. China Chem.*, 2021, **64**, 1504-1509.
67. M. Rajendran and W. Miller, Lawrence, *Biophys. J.*, 2015, **109**, 240-248.
68. J. Isokuortti, K. Kuntze, M. Virkki, Z. Ahmed, E. Vuorimaa-Laukkanen, M. A. Filatov, A. Turshatov, T. Laaksonen, A. Priimagi and N. A. Durandin, *Chem. Sci.*, 2021, **12**, 7504-7509.
69. S. Monti, E. Gardini, P. Bortolus and E. Amouyal, *Chem. Phys. Lett.*, 1981, **77**, 115-119.
70. K. Kuntze, J. Viljakka, E. Titov, Z. Ahmed, E. Kalenius, P. Saalfrank and A. Priimagi, *Photochem. Photobiol. Sci.*, 2022, **21**, 159-173.
71. R. M. Supkowski and W. D. Horrocks, *Inorg. Chim. Acta*, 2002, **340**, 44-48.
72. W. D. Horrocks and D. R. Sudnick, *J. Am. Chem. Soc.*, 1979, **101**, 334-340.
73. A. Beeby, I. M. Clarkson, R. S. Dickins, S. Faulkner, D. Parker, L. Royle, A. S. de Sousa, J. A. G. Williams and M. Woods, *J. Chem. Soc. Perkin Trans. 2*, 1999, 493-503.
74. D. Sokolova, T. Lurshay, J. Rowbotham, G. Stonadge, H. Reeve, S. Cleary, T. Sudmeier and K. Vincent, *Nat. Commun.*, 2024, **15**, 7297.
75. X. C. Zheng, H. Mao, D. Huo, W. Wu, B. R. Liu and X. Q. Jiang, *Nat. Biomed. Eng.*, 2017, **1**.
76. M. I. M. P.C Martins, P.Parpot, C.Ralha, T.S. Rocha, *Portugaliae Electrochim. Acta*, 1997, **15**, 401-405.
77. A. Eriksson and L. Nyholm, *Electrochim. Acta*, 1999, **44**, 4029-4040.
78. J. Jiang, C. Auchinvole, K. Fisher and C. J. Campbell, *Nanoscale*, 2014, **6**, 12104-12110.
79. H. Johnston, P. Dickinson, A. Ivens, A. H. Buck, R. D. Levine, F. Remacle and C. J. Campbell, *Proc. Nat. Acad. Sci.* 2019, **116**, 19753-19759.
80. C. E. Cooper and G. C. Brown, *J. Bioenerg. Biomembr.*, 2008, **40**, 533-539.
81. C. Zhu, Z. Zou, C. Huang, J. Zheng, N. Liu, J. Li and R. Yang, *Chem. Commun,*, 2019, **55**, 3235-3238.
82. D. D. Ma, C. X. Huang, J. Zheng, W. Y. Zhou, J. R. Tang, W. J. Chen, J. S. Li and R. H. Yang, *Anal. Chem.*, 2019, **91**, 1360-1367.
83. L. Sun, G. Li, X. Chen, Y. Chen, C. Jin, L. Ji and H. Chao, *Sci. Rep.*, 2015, **5**, 14837.
84. H. A. Reeve, L. Lauterbach, P. A. Ash, O. Lenz and K. A. Vincent, *Chem. Commun.*, 2012, **48**, 1589-1591.
85. H. A. Reeve, L. Lauterbach, O. Lenz and K. A. Vincent, *Chem. Cat. Chem.*, 2015, **7**, 3480-3487.

86. J. S. Rowbotham, M. A. Ramirez, O. Lenz, H. A. Reeve and K. A. Vincent, *Nat. Commun.*, 2020, **11**.
87. E. Mathieu, A. Sipos, E. Demeyere, D. Phipps, D. Sakaveli and K. E. Borbas, *Chem. Commun.*, 2018, **54**, 10021-10035.

Chapter 4

Investigating the Structure of Kinetically Stable Nd(III) Complexes in Solution

4.1 Introduction

This chapter details the techniques used to investigate the structure and speciation of a near infra-red (NIR) emitting, kinetically stable, Nd(III) complex in solution. This project focusses on the observation of two isomers of the Nd(III) complex, which adopt either the twisted square antiprismatic (TSAP) or the square antiprismatic (SAP)geometries. The distribution of both isomers in solution were independently determined by ^{1}H NMR and detailed luminescence spectroscopic analysis. Additionally, the spectroscopic profiles of each isomer were deconvoluted from the recorded experimental spectra, with the aid of principal component analysis. This work is in partnership with Villads R. M. Nielsen, in the group of Prof. Thomas Just Sørensen at the University of Copenhagen, Villads performed the PCA analysis and spectral fitting, discussion of the results of this fitting were done in collaboration.

4.1.1 Lanthanides in Solution

Lanthanides are now ubiquitous in society as a result of their impressive optical and magnetic properties.[263] Applications in biology, sensors and for recycling/processing of lanthanides rely upon lanthanide complexes in solution.[264] However, understanding the chemistry and structure of lanthanide complexes in solution is challenging and common solid state characterisation techniques such as x-ray diffraction cannot be applied. Therefore, utilising the luminescent and magnetic properties of lanthanides, their solution state structure can be investigated with NMR and optical techniques.[11, 12, 265-267] These techniques allow for a deeper understanding of the

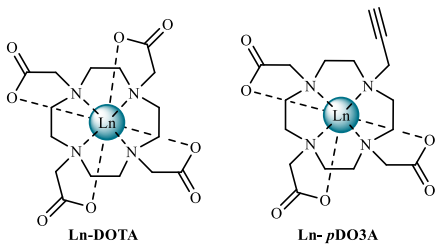
behaviour of lanthanide complexes in solution, which in turn, aids the design of next generation lanthanide complexes.

4.1.2 Neodymium Properties and Applications

Neodymium is a crucial element for the development of permanent magnets,[268, 269] and high-powered lasers.[270, 271] In order for these applications to be achieved, Nd(III) must first be processed from ore or recycled, both procedures require neodymium to be dissolved in solution. Therefore, greater understanding of Nd(III) in solution is required to improve such processes and lead to more sustainable alternatives.[272-274]

Nd(III) cations have interesting optical properties, the intrinsic transitions are highly absorbing ($\varepsilon(Nd(III))$ = 0.1–16 $M^{-1}\,cm^{-1}$), in comparison to other lanthanides such as Europium, ($\varepsilon(Eu(III))$ = 0.05–1.5 $M^{-1}\,cm^{-1}$).[164, 275] Additionally Nd(III) ions emit in the near infra-red (NIR) region with characteristic lifetimes (ns).[17, 165] These are particularly advantageous properties for the development of NIR probes for *in vivo* applications.[276, 277] The long luminescent lifetimes allow for the use of time resolved imaging methods, negating any background autofluorescence in biological media,[278] and the emission of non-ionising NIR light, increases the penetration depth and reduces damage to biological tissues.[279]

4.1.3 Kinetic Stability of Ln(III) Complexes



Scheme 4.1: Chemical structure of kinetically stable Ln(III) complexes based on the DOTA and propargyl-DO3A(pDO3A) ligands.

Aqueous Ln(III) cations can disrupt cellular processes and present toxicity issues in biological tissues.[280] Therefore, for use *in vivo*, it is important that Ln(III) cations are contained within a kinetically stable complex. This is achieved with highly chelating, preorganised, macrocyclic ligands, such as the octadentate DOTA framework (Scheme 4.1).[281] However, for the design of responsive Ln(III) complexes, often a heptadentate DO3A system is employed, where the vacant amine is functionalised depending on the required application.[106, 167] A common and simple example of such a system is the propargyl DO3A (*p*DO3A) ligand, often utilised in click chemistry (Scheme 4.1).[115, 116, 119]

The propargyl DO3A ligand is widely utilised in Ln(III) chemistry for a plethora of applications. It has been used in the development of an optical probe for the detection of Cu(I) in solution,[115] for post complex modification and the sensing of biologically important molecules,[116, 118, 124] and in the formation of impressive multi-metallic and supramolecular Ln(III) complexes.[121, 282]

4.1.4 Structure Property Relationships of Isomers

The complexation of lanthanide(III) cations within DOTA and DO3A based ligands, results in a distribution of isomers in solution. The Ln(III) complexes can adopt either the square antiprismatic (SAP) or the twisted square antiprismatic (TSAP) structures, which interconvert in solution (Figure 4.1). [77, 283]

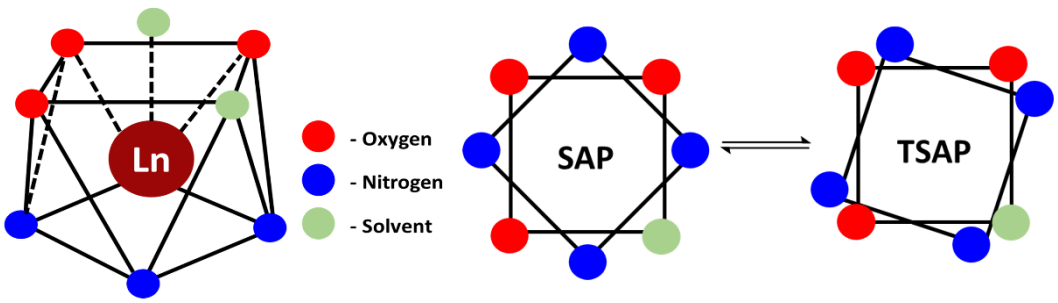


Figure 4.1 Schematic representation of the coordination of Lanthanide (III) ions within DO3A-based ligands.

The distribution of TSAP and SAP isomers in solution can have a significant impact on the optical and magnetic properties of the Ln(III) complex.[76, 78, 183] For example, the clinically approved contrast agent, Gd(DOTA) which is used in MRI imaging, adopts both TSAP and SAP forms, in a 1:4 ratio, where the SAP geometry is the major isomer present in solution.[77, 284] However, the minor TSAP isomer is known to exchange water in the axial position of Gd(DOTA) at a rate 50 times faster than that of the SAP isomer.[285] Therefore, the TSAP isomer acts as a considerably better contrast agent, even though it is the least dominant isomer in solution. A common technique to improve Gd(III) contrast agents is to force the structure into entirely the TSAP isomer, usually by the addition of sterically bulky groups on to the ligand.[106, 223, 225] This highlights the importance of determining the speciation and structure of Ln(III) complexes in solution, and the resulting structure-property relationships.

4.1.5 Speciation of Ln(III) Complexes in Solution

Proton NMR can be a useful technique to investigate speciation in solution, for systems where the interconversion between species is slower than the timescale of the NMR experiment. For paramagnetic Ln(III) complexes, geometric isomers of symmetric and coordinatively saturated complexes can be easily investigated with NMR, as detailed in **Chapter 1, Section 1.3.2.2**.[286] However, complexities arise upon using NMR to determine speciation for heptadentate, unsaturated Ln(III) complexes which produce broad and overlapping peaks, as a result of fluxionality in the complex.[106, 183, 287]

Experimentally recorded luminescence spectra can also be used to investigate the speciation and structure in solution of Ln(III) complexes.[36, 72, 76, 81, 88, 162, 163, 274, 288] This technique requires high resolution spectra from which the population and position of the Ln(III) transition energies, dictated by the crystal field splitting, can be determined. As a result, information detailing the geometry and environment of the Ln(III) complex in solution can be directly

determined from the fine optical spectrum.[2] However, for complicated systems in which more than one species is present, understanding the speciation is not trivial.[76, 234] Often, the experimentally recorded spectra describe a weighted average of the species in solution, where the spectra of individual species overlap. Therefore, a method to deconvolute the spectroscopic fingerprints of individual species in solution would allow for a detailed investigation into the structure-property relationships of Ln(III) species in solution.

4.1.6 Principal Component Analysis (PCA)

Principal component analysis (PCA) is a dimensionally reductive statistical method which characterises a dataset by its common features, called principal components. The principal components account for the total variance observed in the initial data set. For example, for large data sets with multiple variables, the data could be represented in multiple dimensions. However, by defining the principal components, the dataset can be represented by plotting the individual data points as a function of these defined principal components. Thus reducing the number of dimensions, and allowing the data to be more easily visualised and interpreted, Figure 4.2.[289]

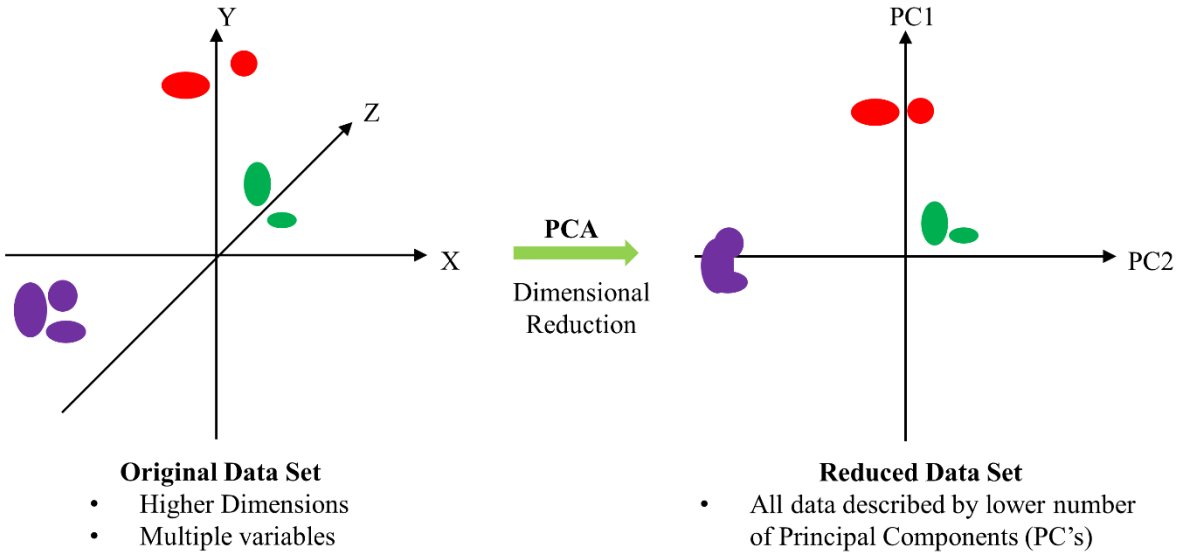


Figure 4.2: Schematic to describe how principal component analysis (PCA) reduces larger dimensional datasets into principal components for easier visualisation and interpretation.

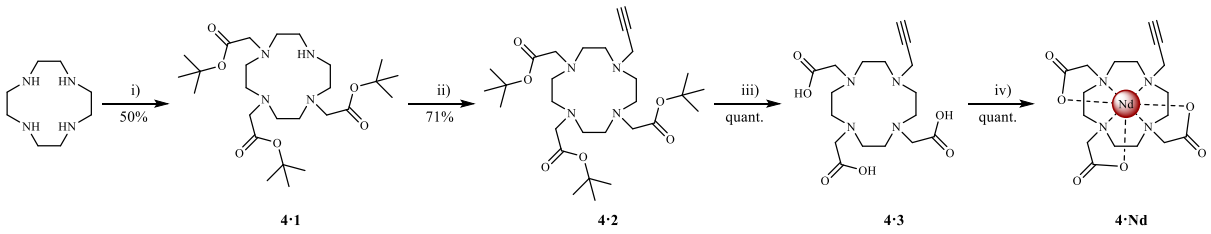
In chemistry, PCA has been utilised to investigate a plethora of data sets, from the analysis of Red Wine and Whisky,[290, 291] to more sophisticated examples such as examining data collected from molecular dynamics simulations of biological macromolecules.[292]

4.1.7 Aims

The work described in this chapter aims to present a detailed investigation into the optical properties of the kinetically stable, Nd(III) propargyl-DO3A complex in solution. Focussing on the speciation in solution and influence of geometric isomers (TSAP and SAP) on the luminescent properties. PCA was employed to aid in the determination of species in solution and their contribution to the observed experimental spectra.

4.2 Synthesis of Nd(III) propargyl-DO3A

Nd(III) propargyl-DO3A (**4·Nd**) was synthesised according to a previously reported procedure as shown in Scheme 4.2.[293] Full experimental details and characterisation can be found in **Chapter 7**.



*Scheme 4.2: Synthetic procedure for the synthesis of **4·Nd** i) tert-butyl bromoacetate, sodium bicarbonate, acetonitrile, rt 72 hours ii) propargyl bromide, potassium carbonate, acetonitrile, rt, 24 hours iii) TFA:DCM (1:1), rt, 24 hours iv) $Nd(OTf)_3$, NaOH, H_2O, 45 ℃, 72 hours.*

Dropwise addition of *tert*-butyl bromoacetate (3 equivalents) to the macrocycle, under basic conditions, afforded **4·1** as a crystalline white powder in moderate yield (53 %). Following this, **4·1** was treated with 1 equivalent of propargyl bromide, in the presence of potassium carbonate. Propargyl bromide reacted with the protonated nitrogen on the cyclen ring *via* an S_N2 mechanism and purification by hot filtration, in acetonitrile, led to the successful isolation

of **4·2** in good yield (71 %). Subsequently, the *tert*-butyl ester protected arms of the macrocycle were hydrolysed upon treatment with trifluoroacetic acid (TFA), as a result the carboxylate groups on the flanking arms of the macrocycle were liberated to produce **4·3** in quantitative yield. Following this, **4·3** was dissolved in water and heated to 45 °C, to this $Nd(OTf)_3$, 1.05 eq., was added and the pH adjusted to pH 10 with sodium hydroxide (1 M). The reaction was left for 3 days, upon which the precipitate was removed after centrifugation and the remaining solution dialysed with Milli-Q water for 3 days, removal of the solvent allowed for the isolation of **4·Nd** in quantitative yield.

4.3 Characterisation of Nd(III) propargyl-DO3A

This section details the characterisation techniques evidencing the successful synthesis of **4·Nd**. The complex was confirmed by HR-ESI mass spectrometry and ^{1}H NMR, full details can be found in **Chapter 7**.

4.3.1 Solid State Structure of Ln(III) propargyl-DO3A

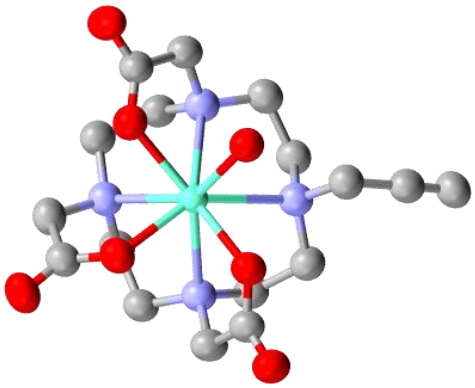


Figure 4.3 Crystal structure of Eu(III) propargyl-DO3A, reproduced with permission from Faulkner and co-workers.[293] Hydrogens omitted for clarity.

In an investigation into the influence of anion binding on the properties of Ln(III) complexes in solution, Faulkner and co-workers isolated the solid state crystal structure of Eu(III) propargyl-DO3A, Figure 4.3.[293] The geometry adopted in the crystal structure reported is that

of the square antiprismatic (SAP) geometry, (O-N twist angle is ≈ 40 degrees) suggesting that the SAP isomer the thermodynamic product. No crystal structure of the corresponding TSAP isomer has been reported, however the TSAP structure of the closely related DOTA variant has been isolated by Sørensen and co-workers.[294]

4.3.2 ^{1}H NMR Spectrum

The ^{1}H NMR spectra of **4·Nd** is shown in Figure 4.4. The chemical shifts of the proton environments extend up to ± 35.00 ppm, indicative of the formation of a mononuclear Nd(III) complex, in which the protons on the ligand experience the influence of the paramagnetic Nd(III) centre. Upon complexation, the Nd(III) metal centre in **4·Nd** adopts a heptadentate coordination, dictated by the seven donor atoms on the ligand. Therefore, it is coordinatively unsaturated and 1-2 solvent molecules reversibly coordinate to the Nd(III) metal centre, this fluxionality results in the broad lines observed in Figure 4.4.

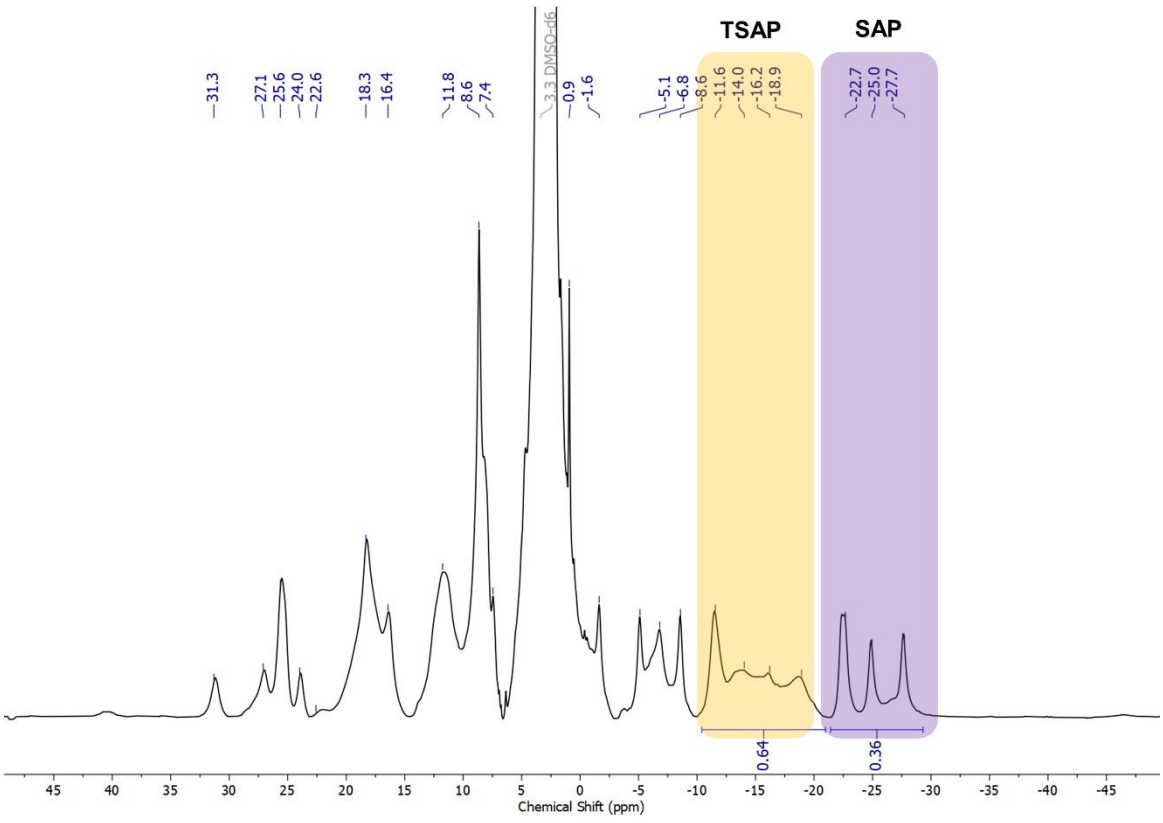


*Figure 4.4: ^{1}H NMR spectrum of compound **4·Nd** (DMSO-d_6), 400 MHz, 298 K.*

Additionally, the ^{1}H NMR shows the presence of both TSAP and SAP isomers of **4·Nd** which interconvert on the timescale of the experiment.[76] The electron density of Nd(III) is oblate in nature and therefore the proton environments in the square antiprismatic (SAP) isomer are shifted downfield in comparison to the same proton environments in a twisted square antiprismatic (TSAP) geometry. In the case of **4·Nd**, the peaks between -21.4 and -29.0 represent the axial protons, on the macrocycle, of the SAP isomer and the peaks between -10.4 and -20.9 represent the corresponding proton environments in the TSAP isomer, as shown in Figure 4.4. Integration of each set of peaks, normalised to 1, results in the estimated percentage distribution of isomers in solution, SAP (36 %) and TSAP (64 %).

The rate of exchange between TSAP and SAP isomers of heptadentate Ln(III) complexes, such as DO3A based complexes, was found to be fast on the NMR timescale at pH 5.0 in water (**Chapter 7**, Figure 7.18), where the signals coalesce as an averaged spectrum.[295] Therefore, the observed distinction between TSAP and SAP isomers, in slow exchange on the NMR timescale seen in Figure 4.4, suggests that the interconversion is slower in DMSO-d_6, as the signals are more defined. It is proposed that carbonate, from the atmosphere, can bind in a bidentate manner to the axial positions of heptadentate Ln(III) complexes.[99, 296] Upon binding it is proposed that the interconversion between TSAP and SAP isomers is restricted and the two species become visible on the timescale of the ^{1}H NMR experiment. Therefore, it is important to consider the influence of carbonic acid in the distribution of TSAP and SAP isomers in this system.

4.3.3 Optical Spectroscopy

Nd(III) steady state emission and excitation spectra were recorded at 298 K and 77 K in DMSO. For emission spectra, Nd(III) was directly excited into the $^{4}I_{9/2} \rightarrow {}^{4}G_{5/2}, {}^{2}G_{7/2}$ transition (λ_{ex} = 583 nm), a long-pass filter of 800 nm was used, and the centre wavelength of the detector set

to 880 or 1050 nm for the two regions of interest. The laser power was set to 90% with the maximum repetition rate (78 MHz). A 750B grating was used for measurements below 950 nm, and a 1200B grating was used for measurements above 950 nm. The emission spectra were obtained upon excitation with wavelengths scanning from 490 nm to 770 nm, spectra were taken at an interval of 0.5 nm, providing a total of 560 spectra, where each spectrum was background corrected to the spectra recorded for the solvent under the same conditions. The excitation spectra were composed upon integration of peaks in the emission spectra. The integration was plotted against excitation wavelength and corrected to the lasing power at that wavelength. For samples recorded at 77 K, a constant nitrogen flow in the sample chamber was maintained to avoid condensation on the quartz NMR tubes.

The luminescent properties of **4·Nd** at both 298 K and 77 K are shown in Figure 4.5. At both temperatures, the excitation spectrum of **4·Nd** describes the intrinsic electronic transitions of Nd(III) arising from the $^4I_{9/2}$ ground state to the excited states ($^2K_{13/2}$, $^4G_{9/2}$, $^4G_{5/2}$, $^2G_{7/2}$, $^2S_{3/2}$, $^4F_{7/2}$). The excitation spectrum is entirely described by the transitions of the Nd(III) cation, with no contribution from an antenna. This is unsurprising as the organic ligand proparyl-DO3A is lacking in a motif that can absorb light as high as 490 nm.

The emission spectrum of **4·Nd** was recorded upon direct excitation into the $^4I_{9/2} \rightarrow {}^4G_{5/2}$, $^2G_{7/2}$ transition (583 nm), resulting in the radiative emission from the principle emissive state $^4F_{3/2}$ to the ground state $^4I_{9/2}$ (Figure 4.5). The observation of crystal field splitting in the emission spectra, results from the degeneracy of the primary emissive state, $^4F_{3/2}$, which contains, 2 levels and the lowest energy multiplet which contains 5 levels. Therefore, in the emission spectrum corresponding to the $^4F_{3/2} \rightarrow {}^4I_{9/2}$ transition, 10 individual transitions can maximally be observed in the spectrum for a single emissive species, in the absence of a magnetic field (See **Chapter 2 Section 2.6.3**). Both the excitation and emission spectra were also recorded at 77 K, the transitions observed in the spectra are sharper in comparison to that recorded at 298 K,

with slight changes to the spectra. This is as a result of reduced Boltzmann population of higher energy states and reduced rate of interconversion of isomers (TSAP and SAP) in solution.

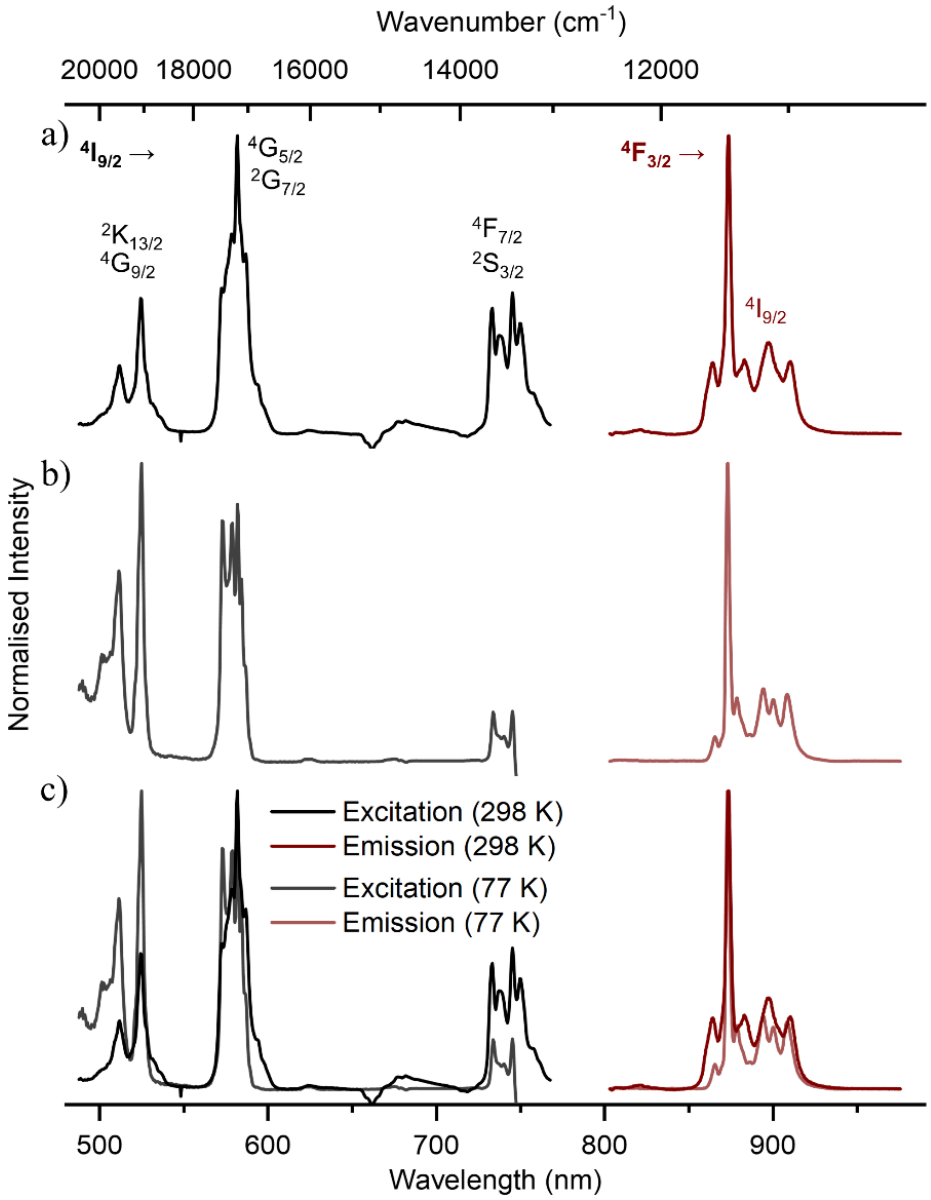


*Figure 4.5: a) Excitation and emission spectra of **4·Nd** at 298 K b) at 77 K. c) comparison of the normalised excitation and emission spectra at both 298 K and 77 K. λ_{ex} = 583 nm.*

4.4 Determination of Multiple Species in Solution

4.4.1 Steady State Luminescence

The changes in crystal field splitting observed between both the emission and excitation spectra recorded at 298 K and 77 K, warranted further investigation to determine if multiple species in

solution were present. To investigate this further, the shape and intensity of each individual emission spectra recorded across the $^4I_{9/2} \rightarrow {}^4G_{5/2}$, $^2G_{7/2}$ excitation band (centred around ~580 nm) were interrogated, Figure 4.6.

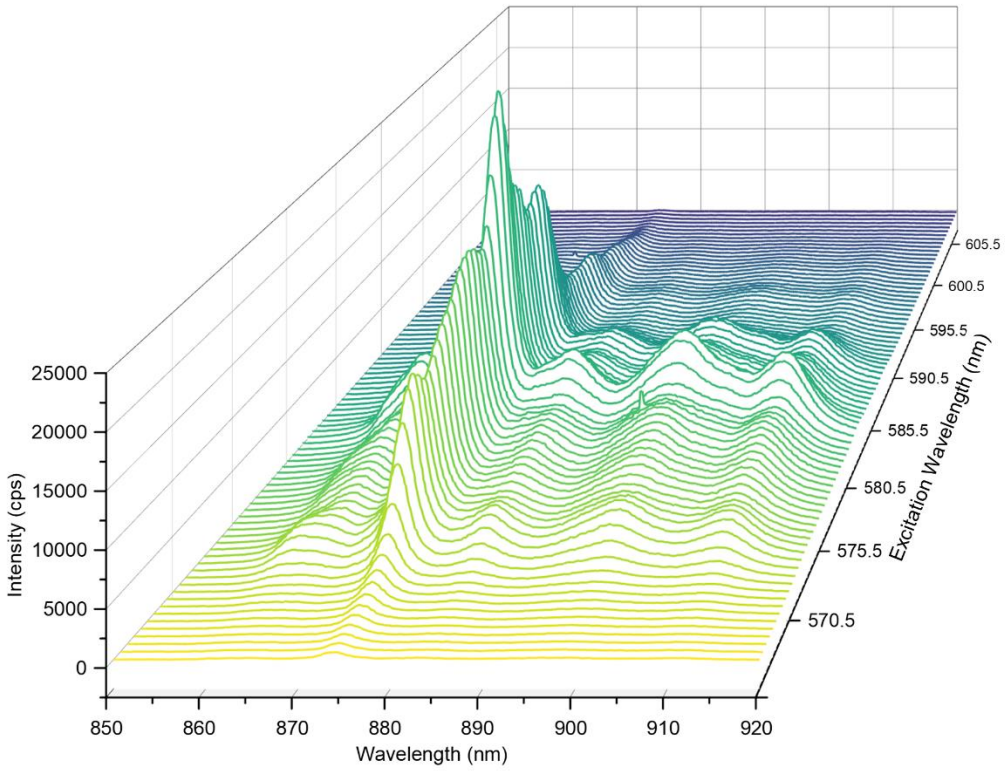


*Figure 4.6: Waterfall plot of the emission spectra recorded of **4·Nd** upon excitation from 566 to 606 nm across the $^4I_{9/2} \rightarrow {}^4G_{5/2}$, $^2G_{7/2}$ transition at 298 K.*

The waterfall plot shows the evolution of the excitation band centred around 880 nm at different excitation wavelengths, changes are observed in both the intensity and crystal field splitting of the emission spectra. The changes observed in the individual emission spectra recorded across an excitation band describe the efficiency of a particular excitation wavelength at populating the $^4F_{3/2}$ excited state of a species, the efficiency of emission from this excited state and the number of Nd(III) containing species in solution. The efficiency of an excitation wavelength to populate the $^4F_{3/2}$ excited state differs for individual Nd(III) containing species as it is dependent on the geometry and electronic structure of that species. Therefore, if multiple Nd(III) containing species are present in solution, then the emission spectra recorded represents

a weighted average of all species in solution as a function of the excitation wavelength. This is highlighted in Figure 4.7, where the emission spectra corresponding to two excitation wavelengths, one at the beginning of the band (572 nm) and one at the end of the band (597 nm) are compared.

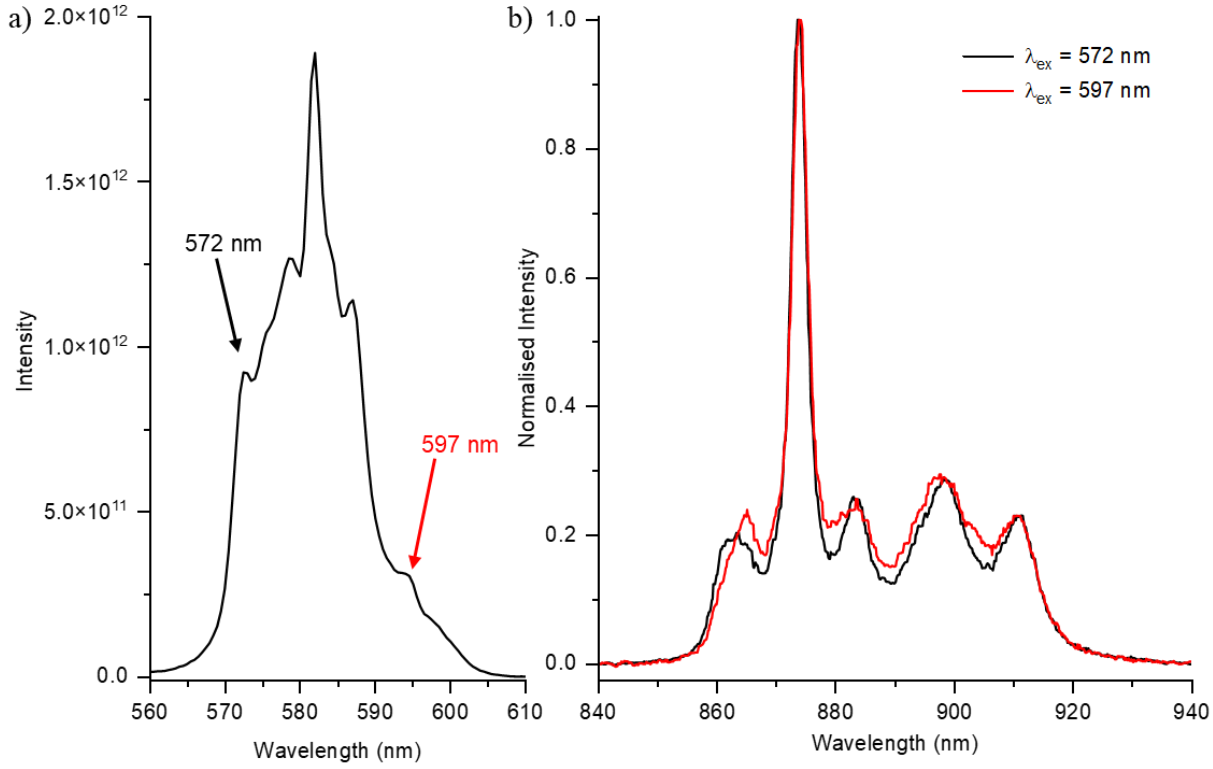


*Figure 4.7: a) excitation spectra of **4·Nd** at 298 K b) emission spectra of **4·Nd** upon excitation at 572 nm (black) and 597 nm (red) at 298 K.*

Excitation of **4·Nd** with 572 and 597 nm light, reveals corresponding emission spectra with distinct profiles and different crystal field splitting. The difference observed is slight, suggesting that the unique species in solution are similar and likely relate to the TSAP and SAP isomers of **4·Nd** in solution, as observed in the ^{1}H NMR spectrum (Figure 4.4). Importantly, as with the proton NMR, the spectroscopic analysis was carried out in the presence of carbonate, from the atmosphere. Therefore, these spectra describe the weighted average of both TSAP and SAP isomers of **4·Nd** in the presence of axially bound carbonate. The observation of small changes supports the notion that carbonate restricts the rotation and interconversion

between geometric isomers in solution. The variation in these spectra across the excitation band relate to the varying efficiency of the two wavelengths investigated in populating the $^4F_{3/2}$ excited state of each structurally distinct Nd(III) species. Therefore, the true "clean" spectra for each species in solution cannot be identified purely from experimentation alone.

4.4.2 Time-gated Luminescence

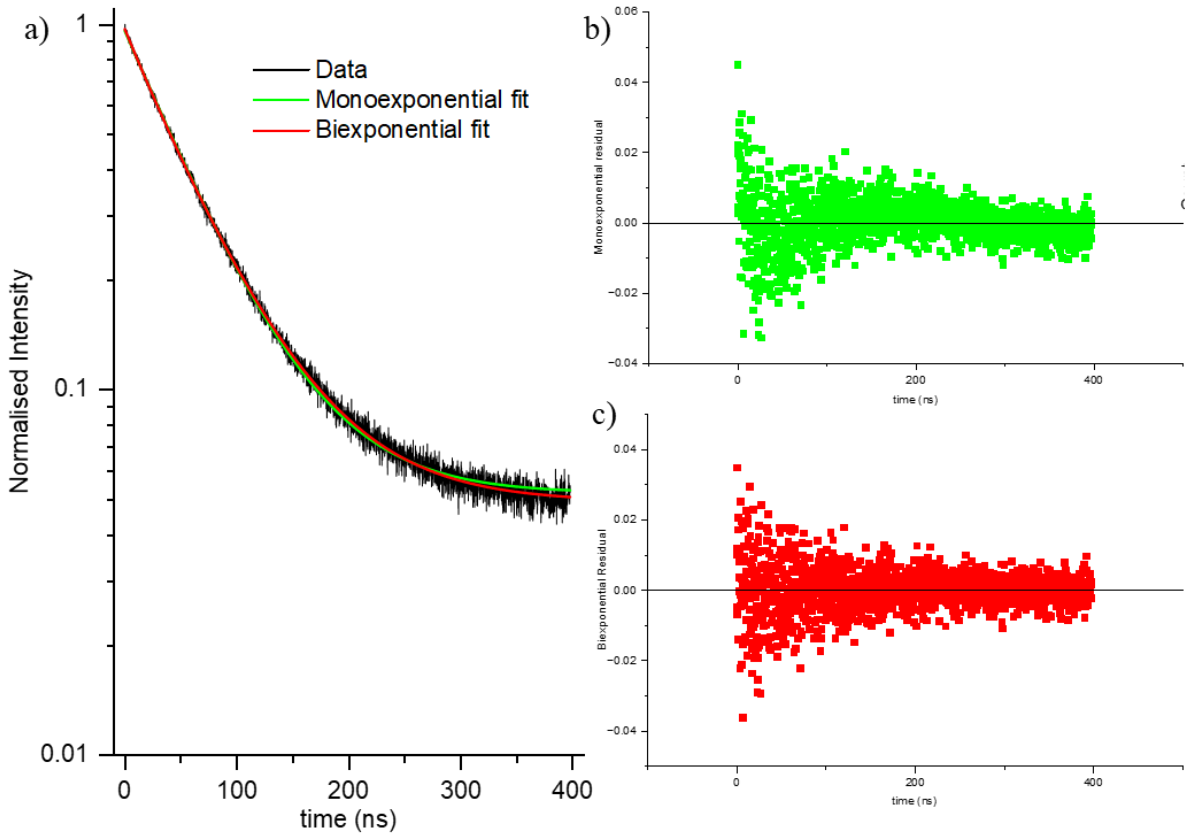


*Figure 4.8: a) luminescent lifetime of **4·Nd** upon excitation at 580 nm, fitted to both a monoexponential (green) and biexponential fit (red) b) residuals from monoexponential fit c) residuals from biexponential fit. Measured by Mikkel Baldtzer Liisberg at the University of Copenhagen.*

To further investigate the optical properties of **4·Nd**, the time-gated luminescent lifetime was measured upon direct excitation into the $^4I_{9/2} \rightarrow {}^4G_{5/2}$, $^2G_{7/2}$ transition (λ_{ex} = 580 nm), Figure 4.8. Upon attempts to fit the experimental data recorded, a monoexponential decay fit was not sufficient to fully describe the data and a biexponential fit was required. The residuals from the monoexponential fit as shown in Figure 4.8b, are skewed compared to the almost symmetrical residuals of the biexponential fit (Fig. 4.8c). The need for a biexponential fit to properly

describe the data supports the presence of two species in solution at 298 K. The lifetimes derived from the biexponential fit are recorded in Table 4.1, and are within the expected range for Nd(III) complexes in solution (ns).[165]

*Table 4.1: Luminescence lifetimes (τ) of **4·Nd** at 298 K (λ_{ex} = 580 nm) fitted to a biexponential decay.*

	τ_1 (ns)	τ_2 (ns)
4·Nd	33.8	63.9

4.5 Principal Component Analysis

To further investigate the presence of two species in solution, principal component analysis (PCA) was used. The PCA analysis was performed by Villads R. M. Nielsen, in the group of Prof. Thomas Just Sørensen at the University of Copenhagen. The results of the PCA were discussed and analysed in collaboration.

A PCA program implemented in python using the Scikit-Learn[297] which assesses 2 principle components was used in all cases. PCA was used to identify the principal components required to described the emission data, and then for spectral reconstruction of the "clean" emission spectra of each species in solution. The input data supplied to the PCA is pre-processed with background subtraction of the solvent spectra recorded under the same conditions. The emission spectra investigated using PCA was recorded for **4·Nd** in DMSO at 298 K and 77 K, each emission band, $^4F_{3/2} \rightarrow {}^4I_{9/2}$ (~880 nm) and $^4F_{3/2} \rightarrow {}^4I_{11/2}$ (~1060 nm) were analysed independently, along with the corresponding excitation bands, $^4I_{9/2} \rightarrow {}^4G_{5/2}$, $^2G_{7/2}$ (~ 580 nm) and $^4I_{9/2} \rightarrow {}^4F_{3/2}$ (~860 nm). For PCA analysis of all investigated bands at both 298 K and 77 K, see **Chapter 7**.

Figure 4.9 describes the results from the principal component analysis of the experimentally observed emission spectra corresponding to the $^4F_{3/2} \rightarrow {}^4I_{9/2}$ (~880 nm) transition at 77 K. The

excitation spectra (Fig 4.9a) shows two distinct excitation bands. The band centred around ~580 nm relates to the $^4I_{9/2} \rightarrow {}^4G_{5/2}, {}^2G_{7/2}$ transition and the band centred around ~740 nm corresponds to the $^4I_{9/2} \rightarrow {}^4F_{7/2}, {}^2S_{3/2}$ transition of Nd(III). The normalised emission spectra recorded as a result of excitation into each of the bands observed in the excitation spectra, is shown in Fig. 4.9b. Upon excitation across varying wavelengths, the crystal field splitting of the emission spectra changes. These normalised emission spectra were fed into the PCA, which determined two principal components, PC1 and PC2, describing 68% and 12% of the variance in the emission spectra, respectively (Fig. 4.9c).

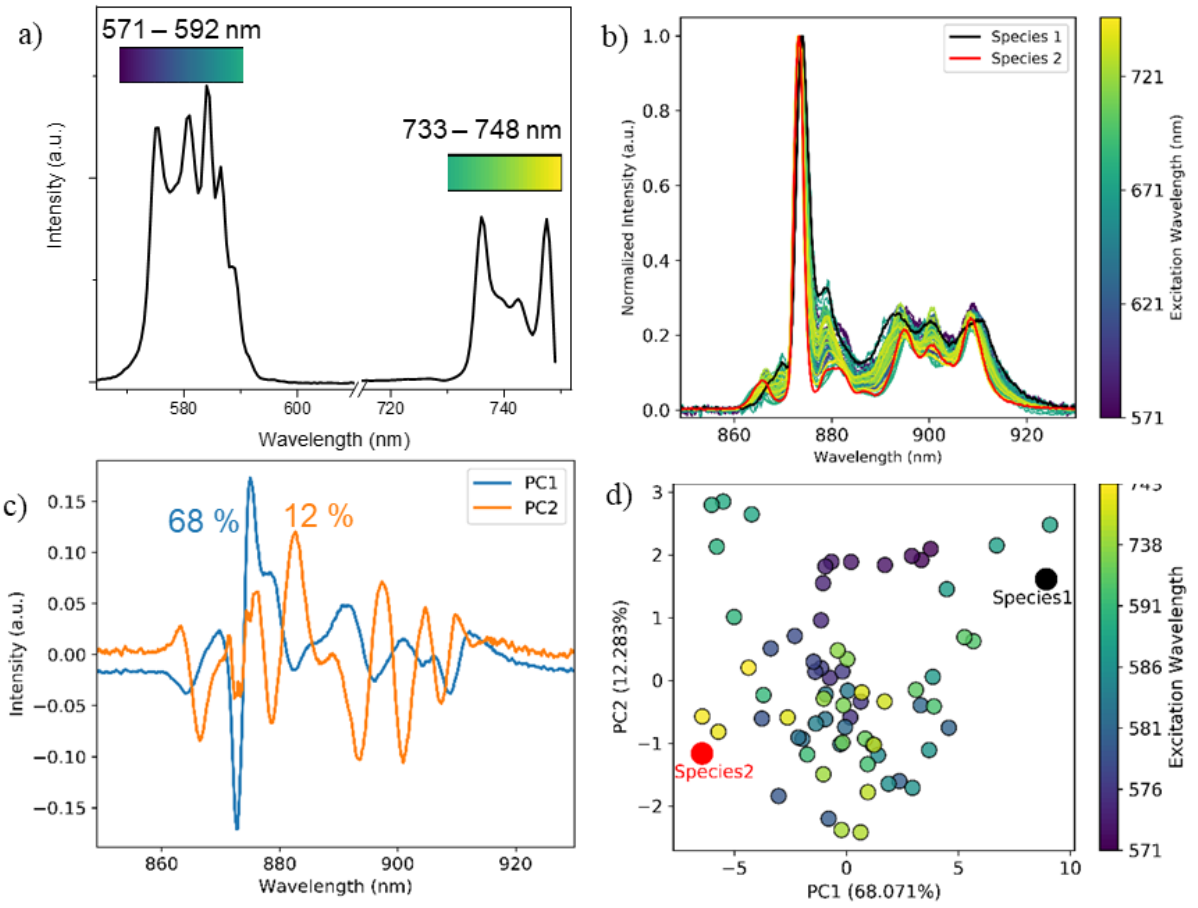


*Figure 4.9: a) Excitation spectra of **4·Nd** in DMSO as determined from the emission spectra centred around the 880 nm transition b)Emission spectra of **4·Nd** in DMSO with varying excitation wavelengths and the clean species determined from the PCA, Species A (black) and Species B (red) c) The emission spectra plotted as a function of the variance in data according to the 2 Principle components determined, PC1 and PC2 d) The principle components determined, PC1 (blue) and PC2 (orange) as a function of intensity and emission wavelength. Created by Villads R. M. Nielsen.*

As PC1 describes the largest variance in the dataset, the emission spectra which are most dissimilar in terms of PC1 were taken to be the most different spectra (Fig. 4.9d). This was validated by using the PCA to reconstruct the spectra of the two most dissimilar species, which is in agreement with the experimental data. Therefore, PCA was used to construct the "clean" spectra of the two individual species that contribute to the emission spectra based on the principal components defined from the input data, Fig. 4.9b. The calculated "clean" spectra for species A and B describes the extremes of the experimental emission data well and are clearly distinct from each other, with differing crystal field splitting and varying intensities of the transitions relating to the microstates in Nd(III).

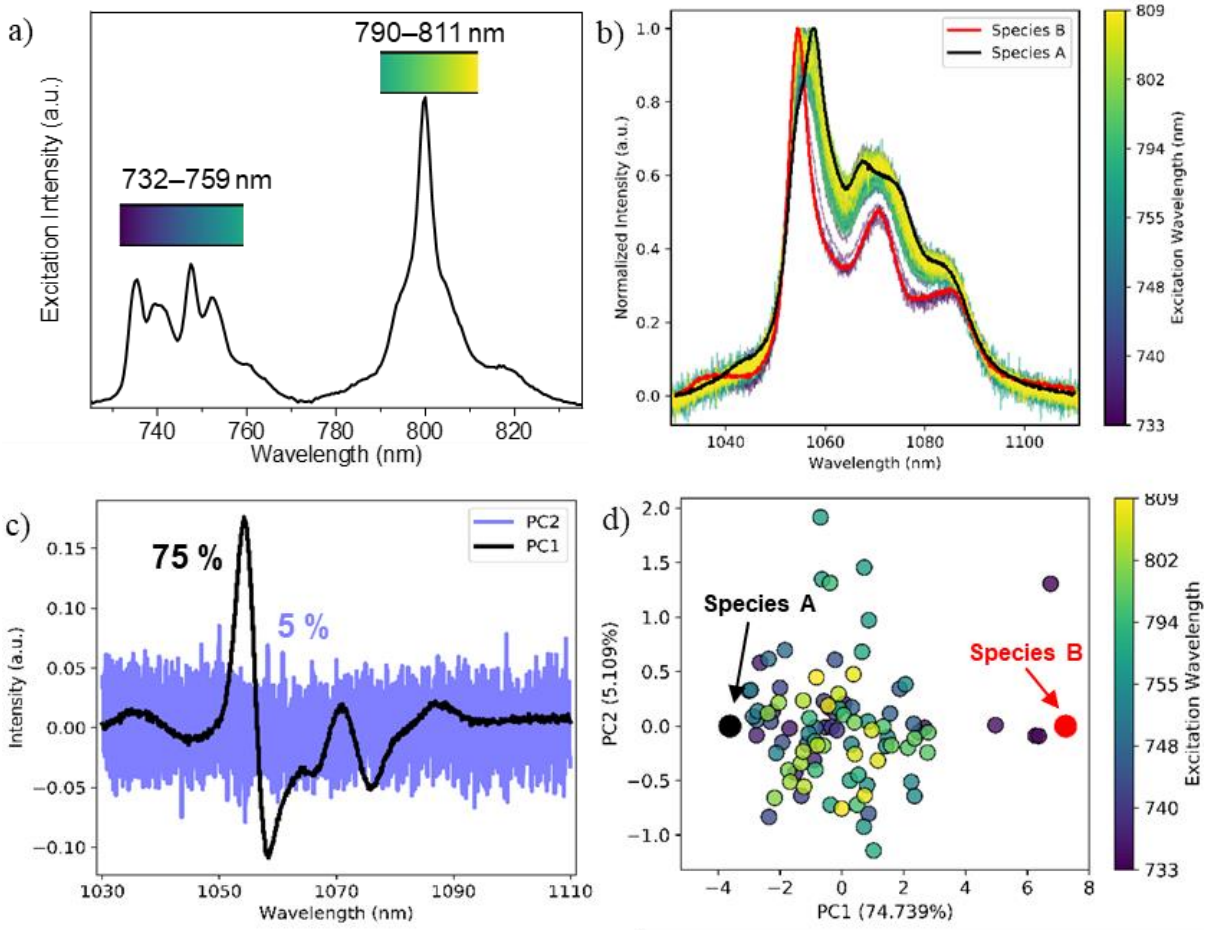


*Figure 4.10: a) Excitation spectra of **4·Nd** in DMSO as determined from the emission spectra centred around the 1060 nm transition b)Emission spectra of **4·Nd** in DMSO with varying excitation wavelengths and the clean species determined from the PCA, Species 1 (black) and Species 2 (red) c) The emission spectra plotted as a function of the varience in data according to the 2 Principle components determined, PC1 and PC2 d) The principle components determined, PC1 (blue) and PC2 (orange) as a function of intensity and emission wavelength. Created by Villads R. M. Nielsen.*

Using the same PCA procedure, the emission spectrum recorded for the $^4F_{3/2} \rightarrow {}^4I_{11/2}$ (~1060 nm) transition at 77 K was analysed (Figure 4.10). In this case, the excitation spectra focussed on both the $^4I_{9/2} \rightarrow {}^4F_{7/2}$, $^2S_{3/2}$ transition (~740 nm) and the $^4I_{9/2} \rightarrow {}^4F_{3/2}$ (~860 nm). The principal components defined by the PCA, as shown in Fig. 4.10c describe the shape (PC1, 75 %) and the noise (PC2, 5%) of the individual emission spectra recorded. PCA was then used again to reconstruct the clean spectra of Species A and Species B for the $^4F_{3/2} \rightarrow {}^4I_{11/2}$ transition, Fig. 4.10b, which again describe the variance in the experimental data well and are distinct from each other.

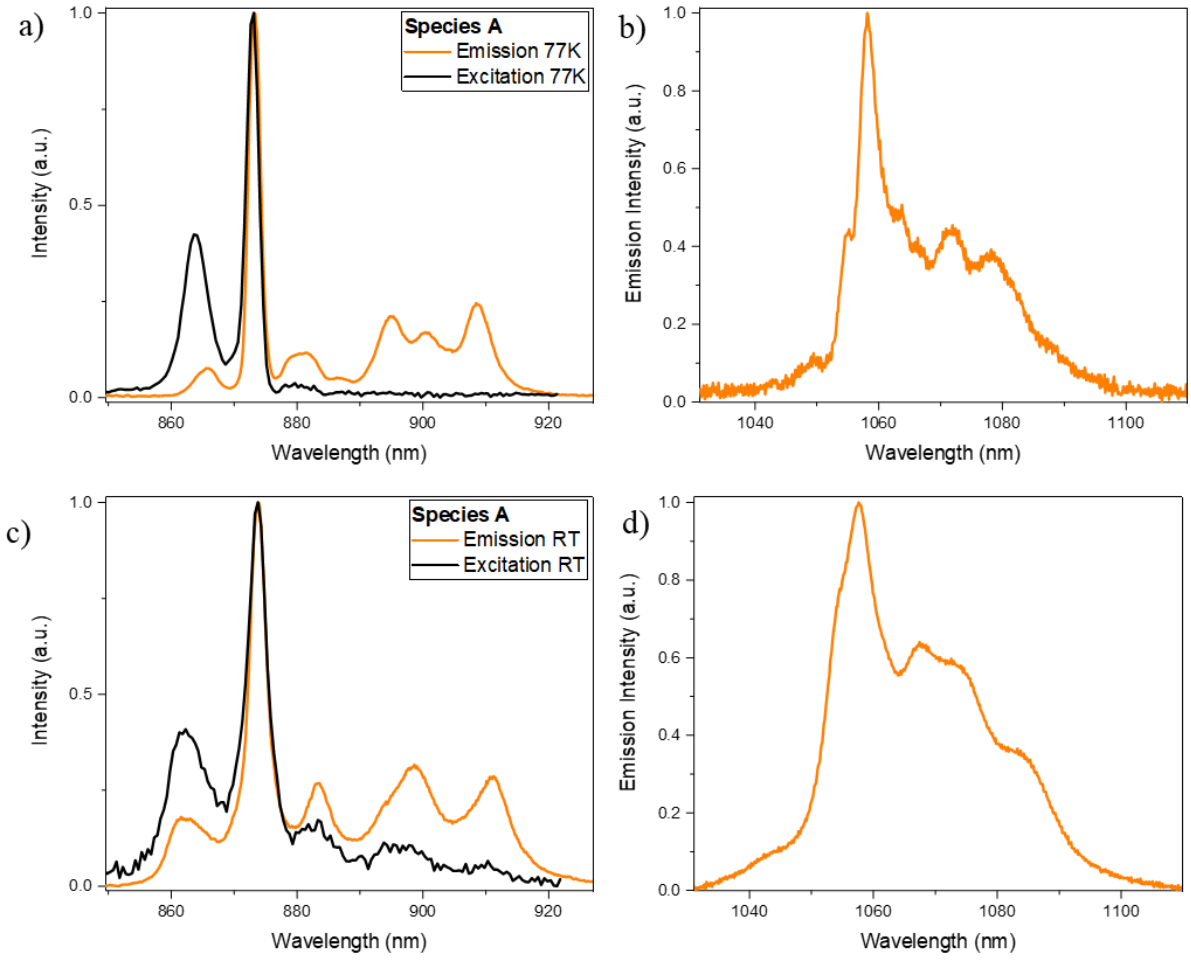


Figure 4.11: Constructed spectra for Species A using PCA a) Emission (orange) and excitation (black) spectra, centred on the $^4I_{9/2} \rightarrow {}^4F_{3/2}$ transition at 77 K b) Emission (orange) spectra, centred on the $^4F_{3/2} \rightarrow {}^4I_{11/2}$ transition at 77 K c) Emission (orange) and excitation (black) spectra, centred on the $^4I_{9/2} \rightarrow {}^4F_{3/2}$ transition at 298 K d) Emission (orange) spectra, centred on the $^4F_{3/2} \rightarrow {}^4I_{11/2}$ transition at 298 K. Created by Villads R. M. Nielsen.

This analysis was repeated for all datasets, including the excitation spectra. Using PCA both the "clean" excitation and the emission spectra of species A (Figure 4.11) and Species B (Figure 4.12) at both 298 K and 77 K could be reconstructed. Normalised spectra of the excitation and emission spectra relating to the $^4I_{9/2} \rightarrow {}^4F_{3/2}$ transition for both Species A and B, at both temperatures agree well with each other, agreeing that the PCA analysis was robust. Therefore, the PCA constructed spectra were used to determine the contribution of each species to the experimental spectra.

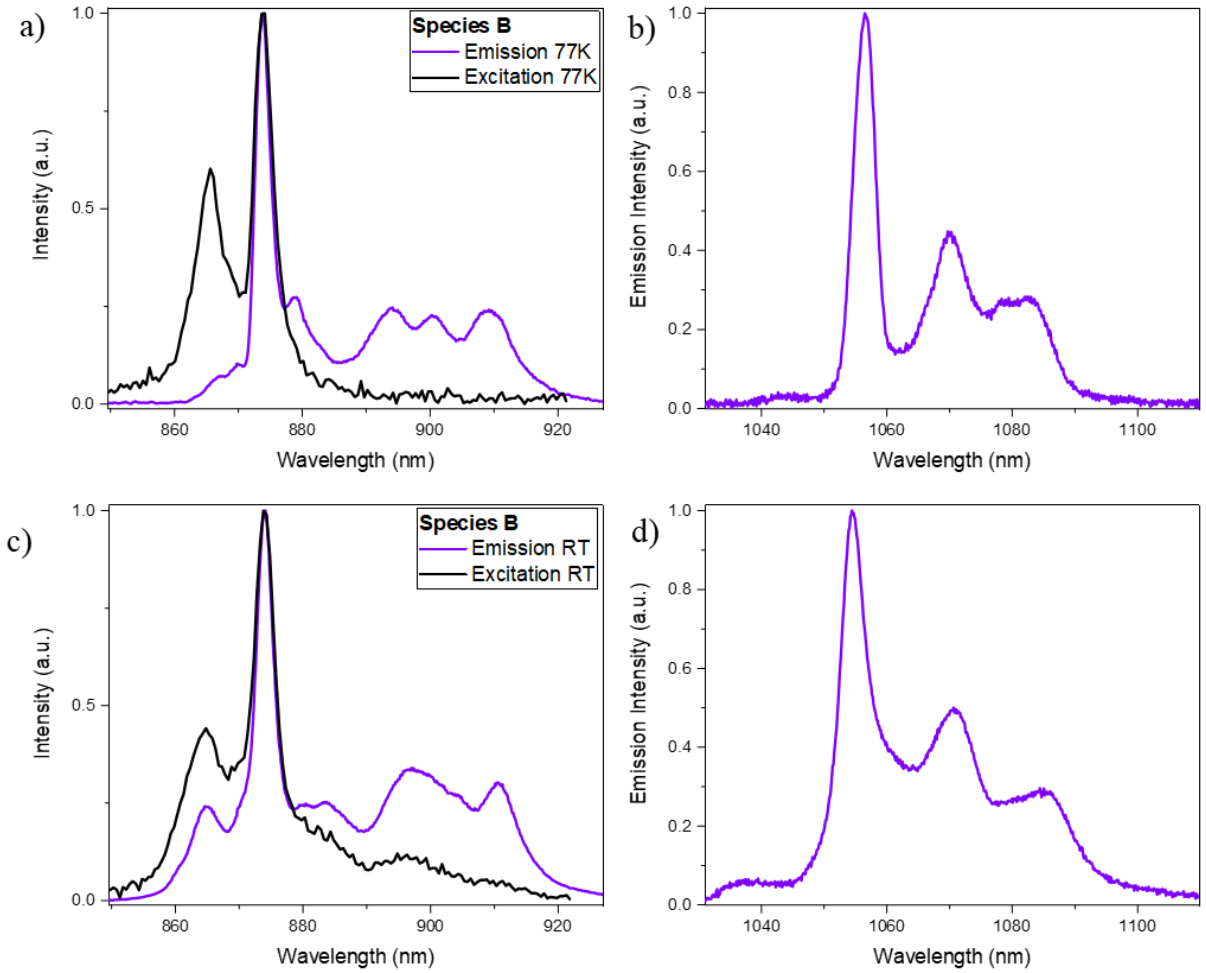


Figure 4.12: Constructed spectra for Species B using PCA a) Emission (purple) and excitation (black) spectra, centred on the $^4I_{9/2} \rightarrow {}^4F_{3/2}$ transition at 77 K b) Emission (purple) spectra, centred on the $^4F_{3/2} \rightarrow {}^4I_{11/2}$ transition at 77 K c) Emission (purple) and excitation (black) spectra, centred on the $^4I_{9/2} \rightarrow {}^4F_{3/2}$ transition at 298 K d) Emission (purple) spectra, centred on the $^4F_{3/2} \rightarrow {}^4I_{11/2}$ transition at 298 K. Created by Villads R. M. Nielsen.

4.6 Spectral Fitting and Isomeric Distribution

The "clean" spectra of Species A and Species B reconstructed from the PCA, were subsequently used to fit each individual, experimentally recorded, emission spectra as a linear contribution of both Species A and Species B, Figure 4.13. Initially, the individual emission spectra of the 880 nm band, upon excitation with wavelengths across $^4I_{9/2} \rightarrow {}^4F_{3/2}$ (~860 nm) excitation band, were fitted as a linear combination of species A and B. Upon excitation of **4·Nd** with 863 nm light, the experimental emission spectra recorded, when fitted to a linear combination of the PCA constructed spectra, is almost entirely described by Species B (Blue), with only a small contribution from Species A (orange). However, upon excitation of **4·Nd** with 859 nm light, the contribution of Species A (orange) dominates the description of the experimental data. Notably, by scanning from 859 nm to 863 nm and recording an emission spectrum at every integer excitation wavelength, the contribution of species A and species B from fitting the experimental data varies from one extreme to the other. The linear combination fit, using the PCA constructed spectra (red), describes the experimental data well and therefore each emission spectra could be described as a percentage contribution from both Species A and B.

By repeating this fitting for each emission spectra recorded across an entire excitation band, excitation spectra corresponding of the "clean" Species A and Species B could be constructed. Thus, by fitting the experimental excitation data by a linear combination of the two excitation spectra constructed, the percentage contribution of each species in solution was determined. Resulting in the percentage contribution of species A and species B as 66 % and 34 % respectively. The same fitting procedure was repeated for both 880 nm and 1060 nm emission bands at both 298 K and 77 K, for which the percentages of Species A and B are tabulated in Table 4.2. For details, see **Chapter 7**.

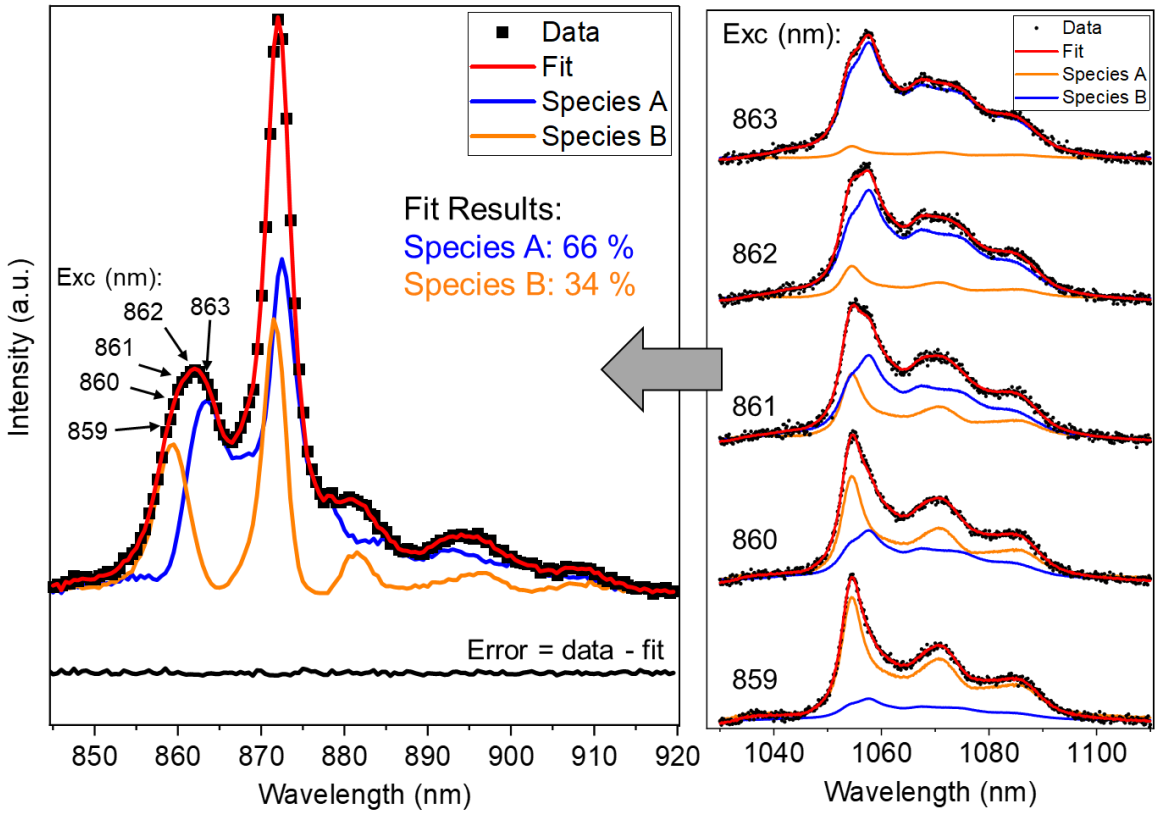


Figure 4.13: Fitting procedure of the experimentally determined emission spectra using a linear contribution of the PCA constructed spectra of species A and B, where the determined proportions of each species in the emission spectra reported on the overall contribution to the excitation spectra. Created by Villads R. M. Nielsen.

Table 4.2: Percentage distribution of Species 1 and Species 2 from both the PCA and fitting performed at 298 K and 77 K for both emission transitions recorded, $^4F_{3/2} \rightarrow {}^4I_{11/2}$ (~1060 nm) and $^4F_{3/2} \rightarrow {}^4I_{9/2}$ (880 nm).

Emission Transition		PCA (298 K)	PCA (77 K)
$^4F_{3/2} \rightarrow {}^4I_{11/2}$	***Species 1***	65.2	48.0
	Species 2	35.1	52.0
$^4F_{3/2} \rightarrow {}^4I_{9/2}$	***Species 1***	65.7	47.6
	Species 2	34.3	52.4

For all emission spectra analysed at both 298 K and 77 K, the percentage distribution of Species A and B in solution determined by both the PCA and the linear combination fitting are in agreement with each other. Importantly, for a given temperature, the percentage of each species determined from both the emission bands ($^4F_{3/2} \rightarrow {}^4I_{9/2}$ and $^4F_{3/2} \rightarrow {}^4I_{11/2}$) are in agreement. At 298 K, Species A is dominant in solution, (65.2 %) whereas at 77 K the distribution of Species A and B is effectively equal (Species A, 51.4 % and Species B, 48.6 %), therefore at higher

temperatures the equilibrium between the two species shifts towards the formation of Species A in solution.

At 298 K, the percentage distribution of TSAP and SAP isomers of **4·Nd**, in DMSO-d_6 were determined by proton NMR to be 64 % and 36 % respectively. In comparison, the spectroscopic analysis of **4·Nd** in DMSO, determined the percentage distribution of Species A and B as 65.2 % and 34.8 % respectively. However, it must be considered that this only stands if the luminescent lifetimes are much shorter than the rotational tumbling observed in NMR spectroscopy and that the extinction coefficients and quantum yield of each isomer are the same. With this in mind, it can be estimated that, not only do species A and B correspond to the geometric isomers in solution, but that Species A is the TSAP isomer and Species B is the SAP isomer.

4.7 Spectral Reconstruction

The entire excitation and emission spectra of both Species A and Species B, at 298 K and 77 K, was reconstructed using PCA, Figure 4.14. This corresponds to the individual luminescent spectra for the twisted square antiprismatic geometry of **4·Nd** in DMSO (orange) and the square antiprismatic geometry (purple). Importantly, using principal component analysis, similar but distinct species in solution can be spectroscopically mapped as individual components, for detailed analysis and understanding of speciation of emissive Nd(III) complexes in solution.

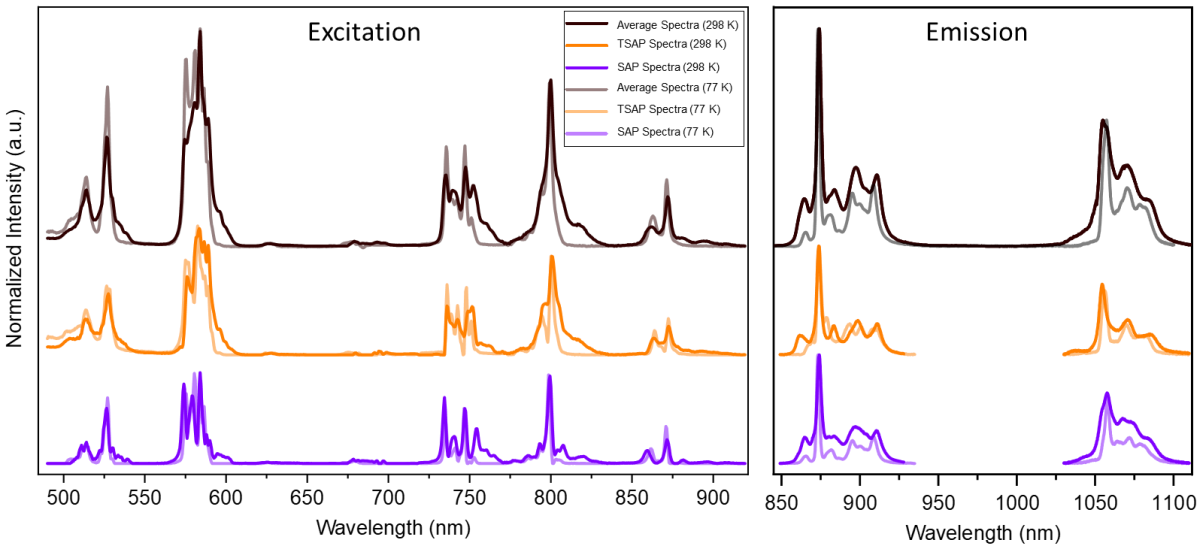


*Figure 4.14: Reconstructed spectra from PCA of the excitation anf emission spectra of TSAP and SAP isomers of **4·Nd** in DMSO. Created by Villads R. M. Nielsen.*

4.8 Determination of Energy levels

The complete reconstruction of both the excitation and emission spectra of the geometric isomers of **4·Nd** in DMSO allowed for the determination of the ground and first excited state energies of both the TSAP and SAP isomers in solution. To reduce the influence of Boltzmann distributions, the reconstructed spectra at 77 K were analysed for each species, Figure 4.15. Voigt functions were used to fit the observed transitions of both the $^4F_{3/2}$ excited state and the $^4I_{9/2}$ ground state, of the reconstructed spectra of both TSAP and SAP isomers. First, the emission spectra were fitted to describe the 5 microstates of the $^4I_{9/2}$ ground state, the gaussian broadness was shared between each individual peak (instrumental) whereas the Lorentzian broadness was refined for the individual line broadness of each peak. Using the parameters determined by fitting the emission spectra, the excitation spectra was fitted to describe the 2 microstates of the $^4F_{3/2}$ excited state. This was in accordance with the procedure developed by Sørensen and co-workers.[163] The individual Voigt fitting of each observed transition was combined as a cumulative fit (red), which described the dataset well for both emission and excitation spectra of both isomers. The individual peak position corresponds to the energy of

the microstate, where the intensity of this transition is described by the overall area of the peak. Determination of the individual peak positions (in wavenumbers) were determined for both species and are shown in Figure 4.16.

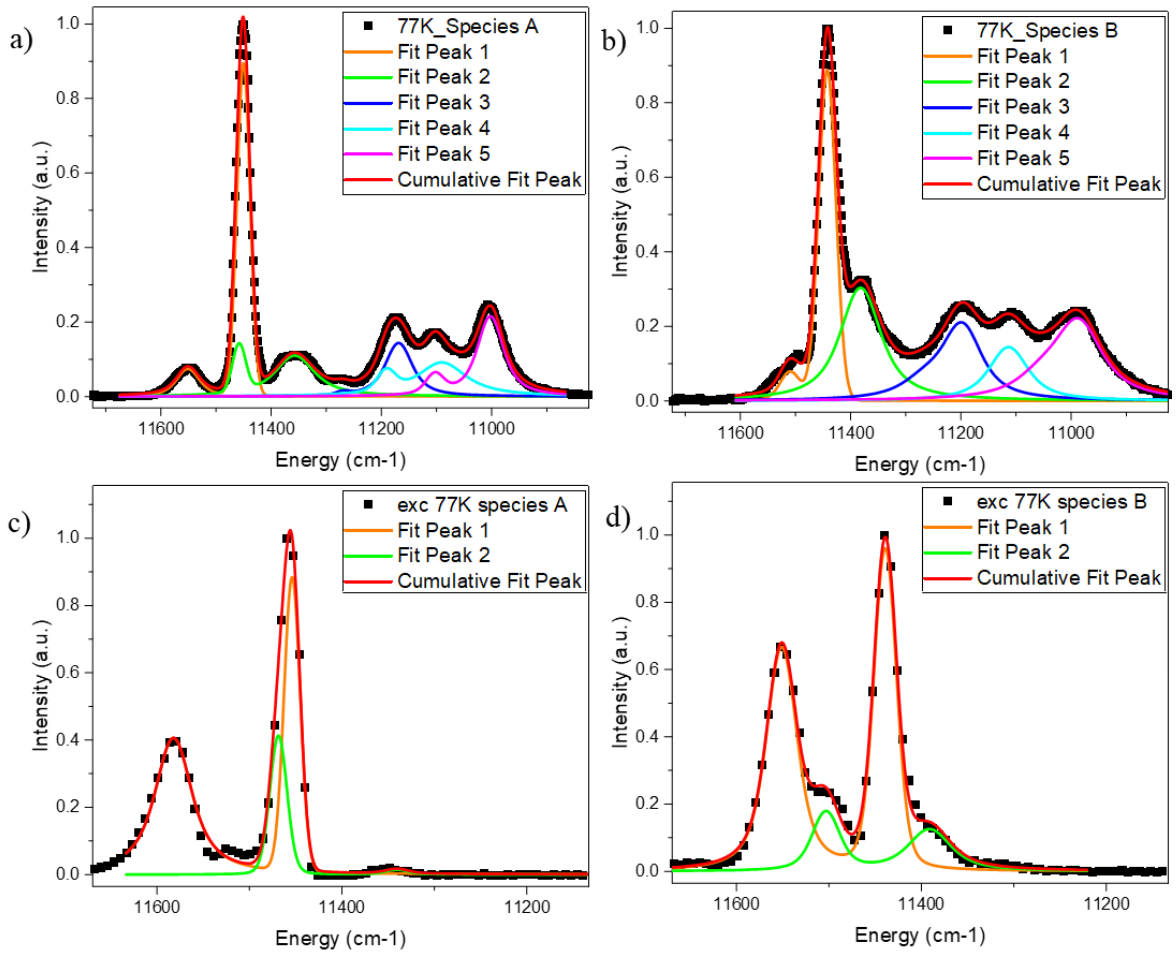


*Figure 4.15: a) Voight fitting of the PCA constructed emission spectra of the a) TSAP and b) SAP isomerand the PCA constructed excitation spectra of the TSAP c) and SAP b) isomers of **4·Nd** in DMSO. Created by Villads R. M. Nielsen.*

The calculated energies of each individual microstate, for both the ground and first excited state manifold of the geometric isomers are close in energy. However, the energies of the TSAP isomer are slightly more destabilised than the SAP isomer. This is in agreement with the previously reported the crystal structure of **4·Eu** (Section **4.3.1**), where only the SAP isomer was isolated as the thermodynamic product.

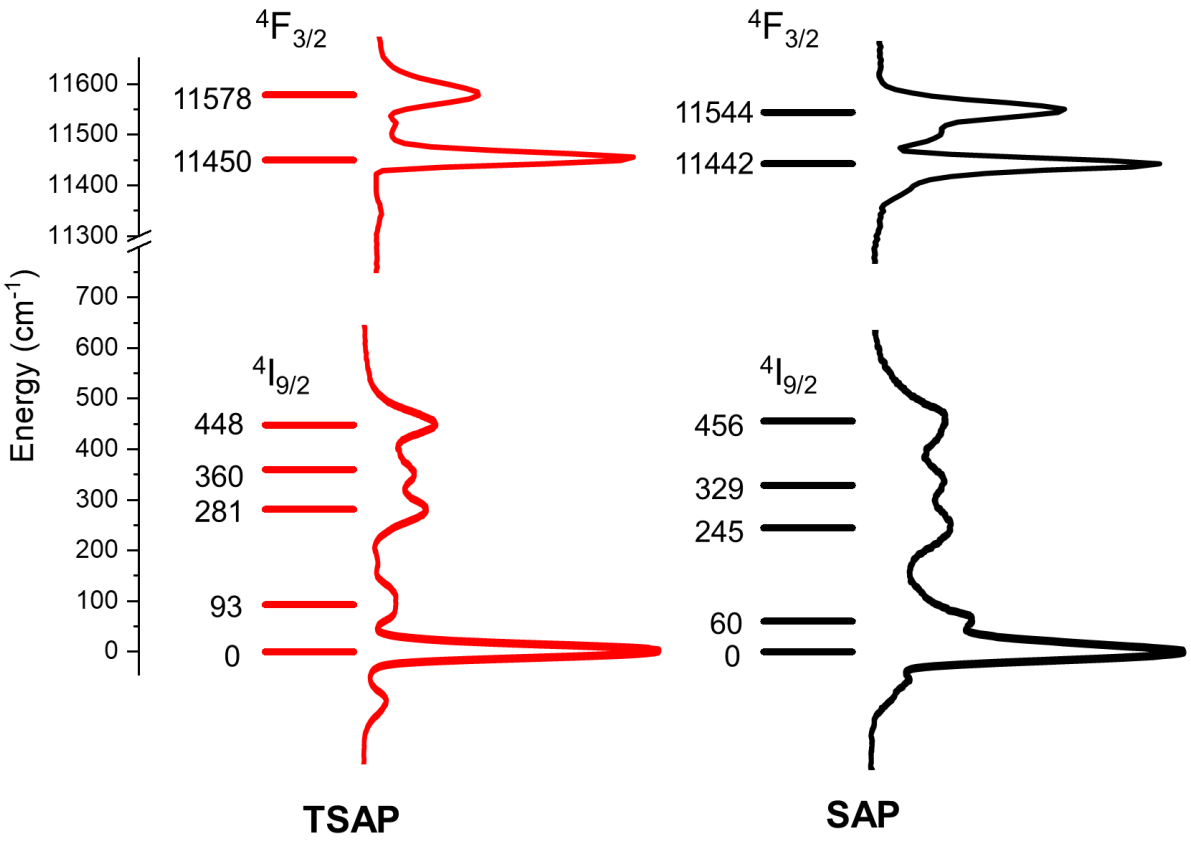


*Figure 4.16: Calculated energies of the microstates of the ground and first excited state manifold for both TSAP and SAP isomers of **4·Nd** in DMSO, from fitting the PCA constructed spectra with Voigt functions. Created by Villads R. M. Nielsen.*

4.9 Conclusions

To conclude, the work in this chapter describes the speciation of a kinetically stable heptadentate Nd(III) complex, **4·Nd**, in solution by both ^{1}H NMR and detailed spectroscopic analysis. Analysis by both techniques were in agreement that the distribution of geometric isomers (TSAP and SAP) of **4·Nd** was determined in solution to be 64 -66 % TSAP and 36-34 % SAP at 298 K. Additionally, spectral reconstruction using PCA allowed for the isolation of individual excitation and emission spectra of both TSAP and SAP isomers to de deconvoluted from an experimental (averaged) spectrum. Voigt fitting of the reconstructed spectra at 77 K, determined the distinct energies of the Nd(III) microstates of the ground and first excited state manifolds. Revealing, that in solution at 298 K, although the TSAP isomer is the major isomer, the SAP isomer is more thermodynamically stable.

Importantly, the work in this chapter highlights the need for investigating Ln(III) emission across an excitation band, if only a single emission spectrum is recorded, at a single excitation wavelength, the spectra might describe weighted average of multiple species in solution. Only by scanning across the band and observing any changes in the emission spectra, can speciation be fully understood. This work also highlights the importance of pH when investigating coordinatively unsaturated Nd(III) complexes, it must be assumed that at neutral pH, carbonate will occupy the axial positions in heptadentate Nd(III) complexes.

Having demonstrated the capability and validity of using PCA analysis in determining the speciation in solution of **4·Nd**, it is proposed that principal component analysis of luminescence spectra could be a useful tool used to determine the speciation of more complicated systems in solution.

4.10 References for Chapter 4

1. J. C. G. Bunzli, *Acc. Chem. Res.*, 2006, **39**, 53-61.
2. J. G. O'Connell-Danes, B. T. Ngwenya, C. A. Morrison and J. B. Love, *Nat. Commun.*, 2022, **13**.
3. B. Bleaney, *J. Magn. Reson.*, 1972, **8**, 91-&.
4. B. Bleaney, R. J. P. Williams, A. V. Xavier, R. B. Martin, B. A. Levine and C. M. Dobson, *Chem. Commun.*, 1972, 791.
5. K. B. Yatsimirskii and N. K. Davidenko, *Coord. Chem. Rev.*, 1979, **27**, 223-273.
6. G. R. Choppin and D. R. Peterman, *Coord. Chem. Rev.*, 1998, **174**, 283-299.
7. N. Kofod, M. Storm Thomsen, P. Nawrocki and T. J. Sørensen, *Dalton Trans.*, 2022, **51**, 7936-7949.
8. M. Sagawa, S. Fujimura, N. Togawa, H. Yamamoto and Y. Matsuura, *J. Appl. Phys.*, 1984, **55**, 2083-2087.
9. S. Sugimoto, *J. Phys. D Appl. Phys.*, 2011, **44**.
10. C. A. Haynam, P. J. Wegner, J. M. Auerbach, M. W. Bowers, S. N. Dixit, G. V. Erbert, G. M. Heestand, M. A. Henesian, M. R. Hermann, K. S. Jancaitis, K. R. Manes, C. D. Marshall, N. C. Mehta, J. Menapace, E. Moses, J. R. Murray, M. C. Nostrand, C. D. Orth, R. Patterson, R. A. Sacks, M. J. Shaw, M. Spaeth, S. B. Sutton, W. H. Williams, C. C. Widmayer, R. K. White, S. T. Yang and B. M. Van Wonterghem, *Appl. Optics*, 2007, **46**, 3276-3303.
11. J. H. Campbell and T. I. Suratwala, *J. Non-Cryst. Solids*, 2000, **263**, 318-341.
12. J. Sherwood, G. T. Gongora and A. P. M. Velenturf, *J. Clean. Prod.*, 2022, **376**.
13. J. M. D. Coey, *Engineering-PRC*, 2020, **6**, 119-131.

14. V. R. M. Nielsen, M. Grasser, S. S. Mortensen, B. Le Guennic and T. J. Sorensen, *Inorg. Chem.*, 2024, **63**, 40, 18596–18607
15. P. R. Nawrocki and T. J. Sørensen, *Phys. Chem. Chem. Phys.*, 2023, **25**, 19300-19336.
16. H. A. Hussain, A. A. Ansari and K. Iftikhar, *Spectrochim. Acta A*, 2004, **60**, 873-884.
17. W. T. Carnall, P. R. Fields and K. Rajnak, *J. Chem. Phys.*, 1968, **49**, 4424-4442.
18. A. Beeby and S. Faulkner, *Chem. Phys. Lett.*, 1997, **266**, 116-122.
19. Z. Guo, S. Park, J. Yoon and I. Shin, *Chem. Soc. Rev.*, 2014, **43**, 16-29.
20. J. C. G. Bünzli and S. V. Eliseeva, *J. Rare Earth*, 2010, **28**, 824-842.
21. Y. Y. Ning, M. L. Zhu and J. L. Zhang, *Coord. Chem. Rev.*, 2019, **399**.
22. R. Jouclas, S. Laine, S. V. Eliseeva, J. Mandel, F. Szeremeta, P. Retailleau, J. He, J. F. Gallard, A. Pallier, C. S. Bonnet, S. Petoud, P. Durand and É. Tóth, *Angew. Chem. Int. Ed.*, 2024, **136**.
23. A. Palasz and P. Czekaj, *Acta Biochim. Pol.*, 2000, **47**, 1107-1114.
24. X. Y. Wang, T. Z. Jin, V. Comblin, A. Lopezmut, E. Merciny and J. F. Desreux, *Inorg. Chem.*, 1992, **31**, 1095-1099.
25. J. D. Routledge, M. W. Jones, S. Faulkner and M. Tropiano, *Inorg. Chem.*, 2015, **54**, 3337-3345.
26. M. C. Heffern, L. M. Matosziuk and T. J. Meade, *Chem. Rev.*, 2014, **114**, 4496-4539.
27. M. Tropiano, A. M. Kenwright and S. Faulkner, *Chem. Eur. J.*, 2015, **21**, 5697-5699.
28. G. J. Stasiuk and M. P. Lowe, *Dalton Trans.*, 2009, 9725.
29. R. F. H. Viguier and A. N. Hulme, *J. Am. Chem. Soc.*, 2006, **128**, 11370-11371.
30. H. Akiba, J. Sumaoka, K. Tsumoto and M. Komiyama, *Anal. Chem.*, 2015, **87**, 3834-3840.
31. N. Candelon, N. D. Hădade, M. Matache, J.-L. Canet, F. Cisnetti, D. P. Funeriu, L. Nauton and A. Gautier, *Chem. Commun.*, 2013, **49**, 9206.
32. T. J. Sorensen and S. Faulkner, *Acc. Chem. Res.*, 2018, **51**, 2493-2501.
33. C. Allain, P. D. Beer, S. Faulkner, M. W. Jones, A. M. Kenwright, N. L. Kilah, R. C. Knighton, T. J. Sorensen and M. Tropiano, *Chem. Sci.*, 2013, **4**, 489-493.
34. S. Aime, M. Botta and G. Ermondi, *Inorg. Chem.*, 1992, **31**, 4291-4299.
35. S. Hoeft and K. Roth, *Chem. Ber.*, 1993, **126**, 869-873.
36. L. G. Nielsen and T. J. Sorensen, *Inorg. Chem.*, 2020, **59**, 94-105.
37. K. J. Miller, A. A. Saherwala, B. C. Webber, Y. Wu, A. D. Sherry and M. Woods, *Inorg. Chem.*, 2010, **49**, 8662-8664.
38. S. Aime, A. Barge, J. I. Bruce, M. Botta, J. A. K. Howard, J. M. Moloney, D. Parker, A. S. de Sousa and M. Woods, *J. Am. Chem. Soc.*, 1999, **121**, 5762-5771.
39. S. Aime, M. Botta, M. Fasano, M. P. M. Marques, C. F. G. C. Geraldes, D. Pubanz and A. E. Merbach, *Inorg. Chem.*, 1997, **36**, 2059-2068.
40. D. Parker, R. S. Dickins, H. Puschmann, C. Crossland and J. A. K. Howard, *Chem. Rev.*, 2002, **102**, 1977-2010.
41. J. Wahsner, E. M. Gale, A. Rodríguez-Rodríguez and P. Caravan, *Chem. Rev.*, 2019, **119**, 957-1057.
42. J. Lohrke, T. Frenzel, J. Endrikat, F. C. Alves, T. M. Grist, M. Law, J. M. Lee, T. Leiner, K. C. Li, K. Nikolaou, M. R. Prince, H. H. Schild, J. C. Weinreb, K. Yoshikawa and H. Pietsch, *Adv. Therap.*, 2016, **33**, 1-28.
43. Y. G. Gorbunova, A. G. Martynov, K. P. Birin and A. Y. Tsivadze, *Russ. J. Inorg. Chem.*, 2021, **66**, 202-216.
44. A. K. R. Junker, M. Tropiano, S. Faulkner and T. J. Sorensen, *Inorg. Chem.*, 2016, **55**, 12299-12308.
45. V. R. M. Nielsen, P. R. Nawrocki and T. J. Sorensen, *J. Phys. Chem. A*, 2023, **127**, 3577-3590.

46. M. S. Thomsen, P. R. Nawrocki, N. Kofod and T. J. Sorensen, *Eur. J. Inorg. Chem.*, 2022, **2022**.
47. M. Storm Thomsen, H. O. B. Andersen and T. J. Sørensen, *Dalton Trans.*, 2022, **51**, 14118-14124.
48. P. R. Nawrocki, N. Kofod, M. Juelsholt, K. M. Ø. Jensen and T. J. Sørensen, *Phys. Chem. Chem. Phys.*, 2020, **22**, 12794-12805.
49. N. Kofod, R. Arppe-Tabbara and T. J. Sorensen, *J. Phys. Chem. A*, 2019, **123**, 2734-2744.
50. O. A. Blackburn, J. D. Routledge, L. B. Jennings, N. H. Rees, A. M. Kenwright, P. D. Beer and S. Faulkner, *Dalton Trans.*, 2016, **45**, 3070-3077.
51. K. Binnemans, *Coord. Chem. Rev.*, 2015, **295**, 1-45.
52. J. C. G. Bünzli and C. Piguet, *Chem. Soc. Rev.*, 2005, **34**, 1048-1077.
53. T. J. Sørensen, L. R. Hill, J. A. Tilney, O. A. Blackburn, M. W. Jones, M. Tropiano and S. Faulkner, *Eur. J. Inorg. Chem.*, 2014, **2014**, 2520-2528.
54. M. Greenacre, P. J. F. Groenen, T. Hastie, A. I. D'Enza, A. Markos and E. Tuzhilina, *Nat. Rev. Method Primers*, 2023, **3**.
55. R. Bro and A. K. Smilde, *Anal. Methods*, 2014, **6**, 2812-2831.
56. W. Kew, I. Goodall and D. Uhrín, *Food Chem.*, 2019, **298**.
57. J. Palma and G. Pierdominici-Sottile, *Chemphyschem*, 2023, **24**.
58. C. Alexander, J. A. Thom, A. M. Kenwright, K. E. Christensen, T. J. Sorensen and S. Faulkner, *Chem. Sci.*, 2023, **14**, 1194-1204.
59. M. S. Thomsen, S. Parsons and T. J. Sorensen, *Dalton Trans.*, 2022, **51**, 15725-15733.
60. A. Takács, R. Napolitano, M. Purgel, A. C. Bényei, L. Zékány, E. Brücher, I. Tóth, Z. Baranyai and S. Aime, *Inorg. Chem.*, 2014, **53**, 2858-2872.
61. J. I. Bruce, R. S. Dickins, L. J. Govenlock, T. Gunnlaugsson, S. Lopinski, M. P. Lowe, D. Parker, R. D. Peacock, J. J. B. Perry, S. Aime and M. Botta, *J. Am. Chem. Soc.*, 2000, **122**, 9674-9684.
62. D. Parker, *Coord. Chem. Rev.*, 2000, **205**, 109-130.
63. F. Pedregosa, G. Varoquaux, A. Gramfort, V. Michel, B. Thirion, O. Grisel, M. Blondel, P. Prettenhofer, R. Weiss, V. Dubourg, J. Vanderplas, A. Passos, D. Cournapeau, M. Brucher, M. Perrot and É. Duchesnay, *J. Mach. Learn. Res.*, 2011, **12**, 2825–2830.

Chapter 5

Speciation of Binuclear Ln(III) Complexes in Solution

5.1 Introduction

This chapter describes the ^{1}H NMR studies of previously investigated binuclear Ln(III) complexes, described in **Chapter 3**. The work described in this chapter focusses on the influence of pH on the structure and speciation of the binuclear Ln(III) complexes in solution. Using the information afforded from optical and magentic studies, the structure and properties of binuclear Ln(III) complexes can be elucidated.

5.1.1 Binuclear Ln(III) Complexes

Binuclear Ln(III) complexes have underpinned some of the most important advances in f-element chemistry in recent years,[118, 146, 233, 235-237, 298-300] particularly the development of high-temperature single molecule magnets (SMMs).[231, 301, 302] Binuclear complexes have also shown considerable potential in solution.[57, 58, 166, 234, 235, 237, 238, 293, 303-306] As discussed in **Chapter 3** of this thesis, binuclear Ln(III) complexes are exciting probes for the investigation of redox conditions in solution. Binuclear Ln(III) complexes have been demonstrated as luminescence sensors for bi-dentate carboxylates,[94, 234, 235] in cell imaging and recognition,[307] and in the development of multimetallic arrays,[121] and hybrid d-f systems.[57, 58, 153]

Optical spectroscopy of binuclear Ln(III) complexes revealed that additional photophysical processes become feasible, including the energy transfer between individual Ln(III) centres, providing there is sufficient spectral overlap between the two ions.[305, 308, 309] This energy transfer is dependent on the energy levels of the cations, and the distance detween them in

solution.[62, 63] Therefore, by understanding their structures in solution, more can be understood about the optical properties of mulitmetallic Ln(III) systems. NMR spectroscopy can be a useful tool for the structural investigations of Ln(III) complexes in solution.[286] However, although there are numerous investigations into the optical properties of kinetically stable binuclear Ln(III) complexes, there are only a handful of examples that present the corresponding investigations in ^{1}H NMR.[237, 310]

5.1.2 Influence of Paramagnetic Ions on ^{1}H NMR Spectra

The presence of a paramagnetic ion contributes to the magnetic field experienced by other nuclei within the complex, and thus influences the ^{1}H NMR spectra accordingly. The observed chemical shift of a nucleus is defined by the contact shift, pseudocontact (paramagnetic contribution) and diamagnetic contribution, as described in equation 5.1.

$$\Delta_{obs} = \Delta_c + \Delta_p + \Delta_d$$

(5. 1)

Contact shift (Δ_c) describes the interaction of electron density through bonds, the diamagnetic shift (Δ_d) describes the influence of nearby paired electrons on the chemical shift, and the pseudocontact shift (Δ_p) describes a through space interaction as a result of nearby unpaired electrons. For Ln(III) ions, where many are paramagnetic and where the bonding is dominated by electrostatic interactions, the pseudocontact shift dominates the experimentally observed ^{1}H NMR. The pseudocontact shift for axially symmetric complexes, as derived by Bleaney, is defined by equation 5.2.[11, 12]

$$\Delta_p = C \left(\frac{(3\cos 2\theta - 1)}{r^3} \right)$$

(5. 2)

In equation 5.2, C is a proportionality constant related to the anisotropy and electronic structure of the Ln(III) ion, r and θ are spherical coordinates of the observed nucleus with respect to a Ln(III) ion at the origin.[11, 12]

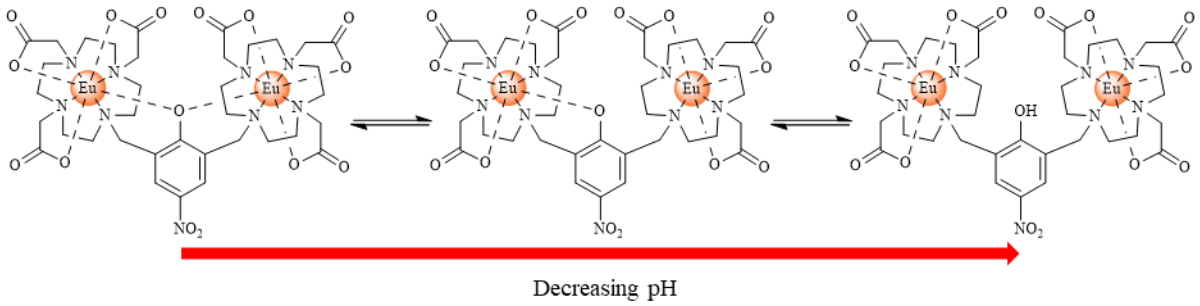
The shape of the ground state distribution of the f-electrons in Ln(III) complexes can range between oblate and prolate. In this chapter, Tb(III) and Eu(III) complexes are investigated, where the ground state anisotropy is oblate and, as a result, the principle axis is perpendicular to the net direction of the spin density. Therefore, protons in the equatorial positions are more significantly perturbed by the pseudocontact shift than those in the axial positions. Additionally, there is a vector component to the pseudocontact shift which depends on the distance and angle of the proton from the net spin density. This means that some proton environments are shifted in one direction, while others are moved in the opposite, resulting in both positive and negative chemical shifts being observed.[73] The range of chemical shifts varies with the Ln(III) ion investigated and is dependent on the magnetic properties of the individual Ln(III) ion, as described by Bleaney.[12] Tb(III) is highly paramagnetic, as a result of the J-levels of the lowest energy multitplets (J = 6), leading to increased chemical shifts close to ± 500.00 ppm; whereas Eu(III) is moderately paramagnetic, and thus only perturbs the proton environment up to around ± 50.00 ppm.

Importantly, the anisotropy of the ground state of the Ln(III) cation is not enough to fully describe the ^{1}H NMR spectrum of the Ln(III) complex, it is also heavily dependent on the crystal field splitting. When the crystal field splitting is larger than the kT of the system, this leads to the breakdown of the Bleaney theory.[73, 311] Bleaney theory also negates the influence of higher order ligand field terms, anisotropic electron distribution and any variation in position of the principal magnetic axis.[312]

Furthermore, the peaks observed in the ^{1}H NMR spectra of paramagnetic complexes are often significantly broadened, in comparison to that of diamagnetic complexes. The close proximity of the paramagnetic ions to the proton environments enhances both the transverse (τ_1) and longitudinal (τ_2) relaxivity, thus resulting in the observed line broadening. Therefore, detailed analysis of ^{1}H NMR spectra can elicit important information about the structure of Ln(III) complexes in solution, particularly the influence of symmetry and crystal field effects.

5.2 Aims

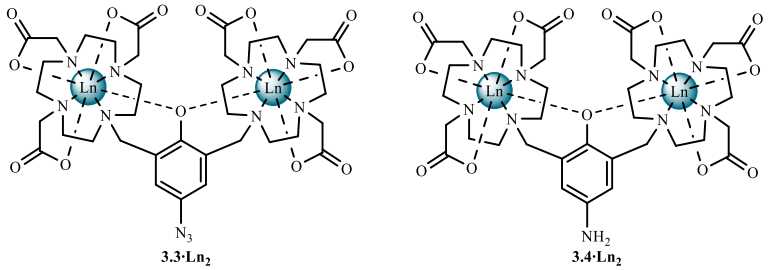
The impressive optical and magnetic properties of the binuclear Ln(III) complexes investigated in **Chapter 3** warranted a detailed analysis into the structure and speciation of the binuclear Ln(III) complexes in solution, with a focus on the influence of pH on these characteristics. This investigation builds on the work previously reported by Faulkner and co-workers on the pH dependence of **3.1·Eu$_2$**. Here, the structure in solution of **3.1·Eu$_2$** was dependent on the protonation of the phenolate, resulting in three species, as shown in Scheme 5.1. Each of these species corresponded to a change in both the luminescence spectrum and the ^{1}H NMR spectrum.[237]



*Scheme 5.1: Schematic to describe the speciation in solution of **3.1·Eu$_2$** as a function of pH, reproduced with permission.[237]*

From the work described in **Chapter 3**, the complex of interest is the highly luminescent **3.4·Tb$_2$**, which at pH 7.4 in PBS buffer was shown to have a quantum yield of 45.2%. **3.4·Tb$_2$** contains multiple pH sensitive functional groups; the carboxylate arms, bridging phenolate and

the amine *para* to the phenolate on the aromatic ring. To fully understand the structure of **3.4·Tb$_2$** in solution, the pKa of each pH sensitive functional group needs to be determined; consequently, **3.4·Tb$_2$** and **3.4·Eu$_2$** were investigated by ^{1}H NMR, at varying pDs. As a control, **3.3·Tb$_2$** was also investigated as the azide group *para* to the phenolate on the aromatic ring is not pH sensitive, thus allowing for investigations into the pH dependence of the phenol and carboxylate groups to be verified with an isostructural analogue (Scheme 5.2).



Scheme 5.2: Structures of the binuclear Ln(III) complexes investigated in this chapter.

5.3 ^{1}H NMR of Binuclear Ln(III) Complexes

5.3.1 Experimental Details

All complexes were dissolved in D_2O (0.8 mL) and added to a quartz NMR tube. To this, 0.1 M NaOD was added to reach an alkaline pD (~ 10). All other pD values were reached upon sequential addition of DCl (0.1 or 0.01 M). An extended sweep range of ± 750.00 ppm was used to investigate the Tb(III) complexes, and an extended sweep range of ± 60.00 ppm was used to investigate the Eu(III) complexes.

As the investigations were carried out in D_2O, the pD was measured. pD is related to pH using equation 5.3.[313]

$$pD = pH + 0.4$$

(5. 3)

5.3.2 Tb(III) Binuclear Complexes

3.3·Tb$_2$ was investigated by ^{1}H NMR at varying pDs. **3.3·Tb$_2$** contains an azide functional group in the *para* position of the aromatic ring and, unlike the highly emissive **3.4·Tb$_2$**, which contains an amine in this position, the azide is not sensitive to pH. Therefore, ^{1}H NMR analysis of **3.3·Tb$_2$** allowed for a detailed investigation into the pD dependence of the phenolate and carboxylic acids within the complex.

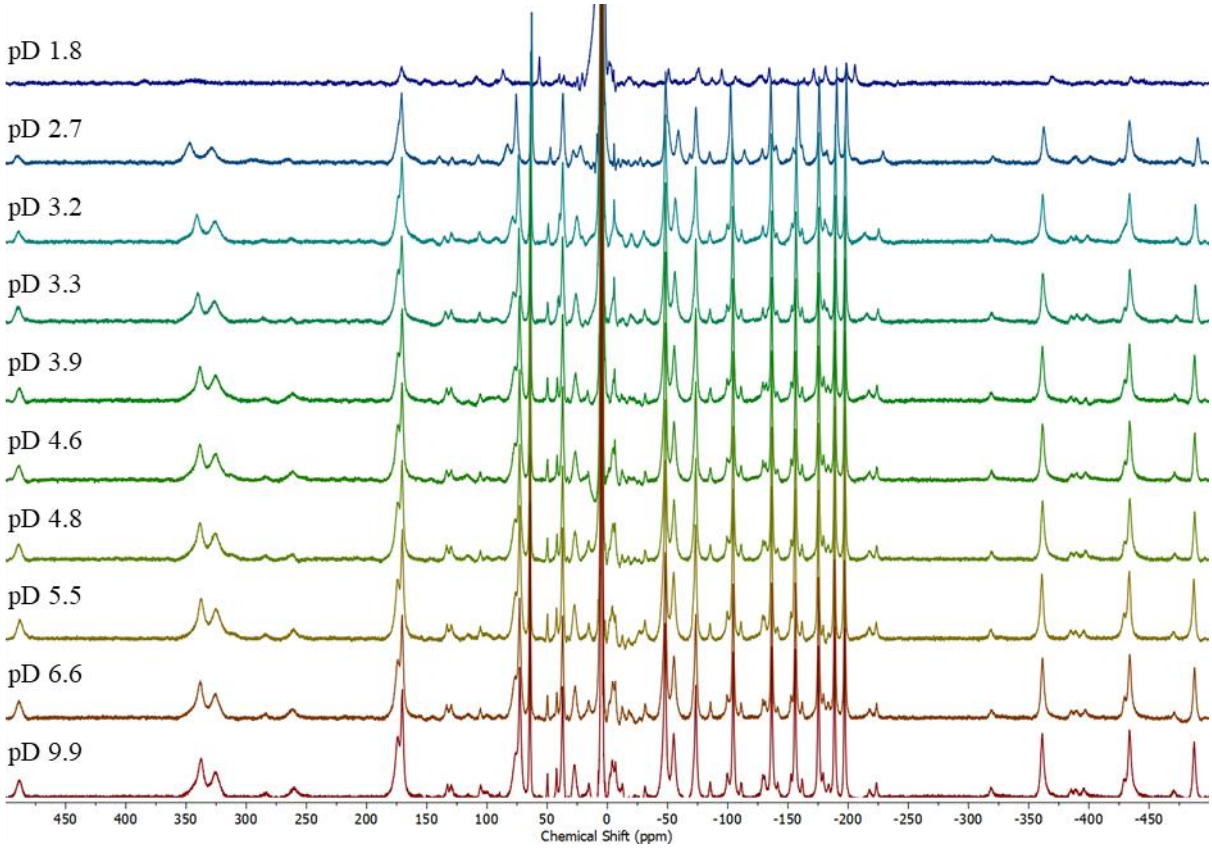
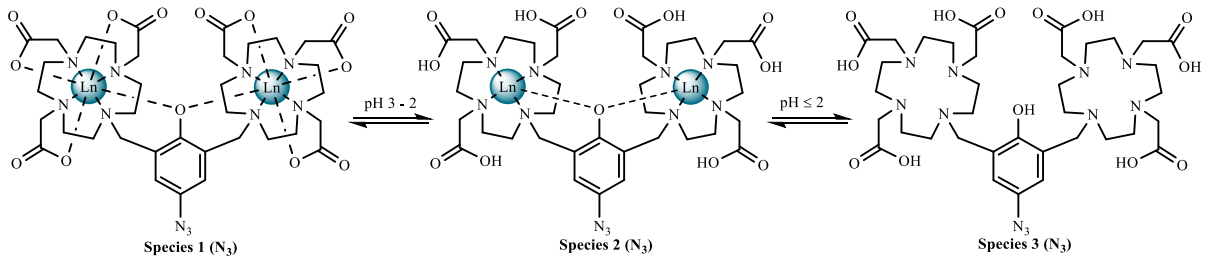


*Figure 5.1:Stacked ^{1}H NMR spectra (400 MHz) of **3.3·Tb$_2$** at different pDs in D_2O.*

From the stacked spectra displayed in Figure 5.1, there is no significant change observed in the ^{1}H NMR spectra of **3.3·Tb$_2$** between pD 9.9 and pD 3.2. The spectra within this region are indicative of a Tb(III) complex, confirmed by the presence of proton environments occurring up to ± 500.00 ppm. The stability of **3.3·Tb$_2$** within this pD range, where the phenolate and carboxylate arms are expected to be deprotonated, suggests that the spectra recorded correspond to Species 1 (N_3), see Scheme 5.3. In Species 1 (N_3), the phenolate is deprotonated

and can coordinate to both Ln(III) centers; in this case the Ln(III) ions are close in distance and influence the contact shift of the oxygen on the phenolate. Additionally, the spectra observed in this range shows that the SAP isomer of **3.3·Tb$_2$** is the dominant species in solution, with negligible peaks relating to the TSAP isomer, see Figure 5.2. For Tb(III) complex, it is postulated that the SAP geometry is stabilized by the coordination of the phenolate to both Tb(III) centers.



*Scheme 5.3: Schematic describing the structures in solution proposed for **3.3·Tb$_2$** at varying pD.*

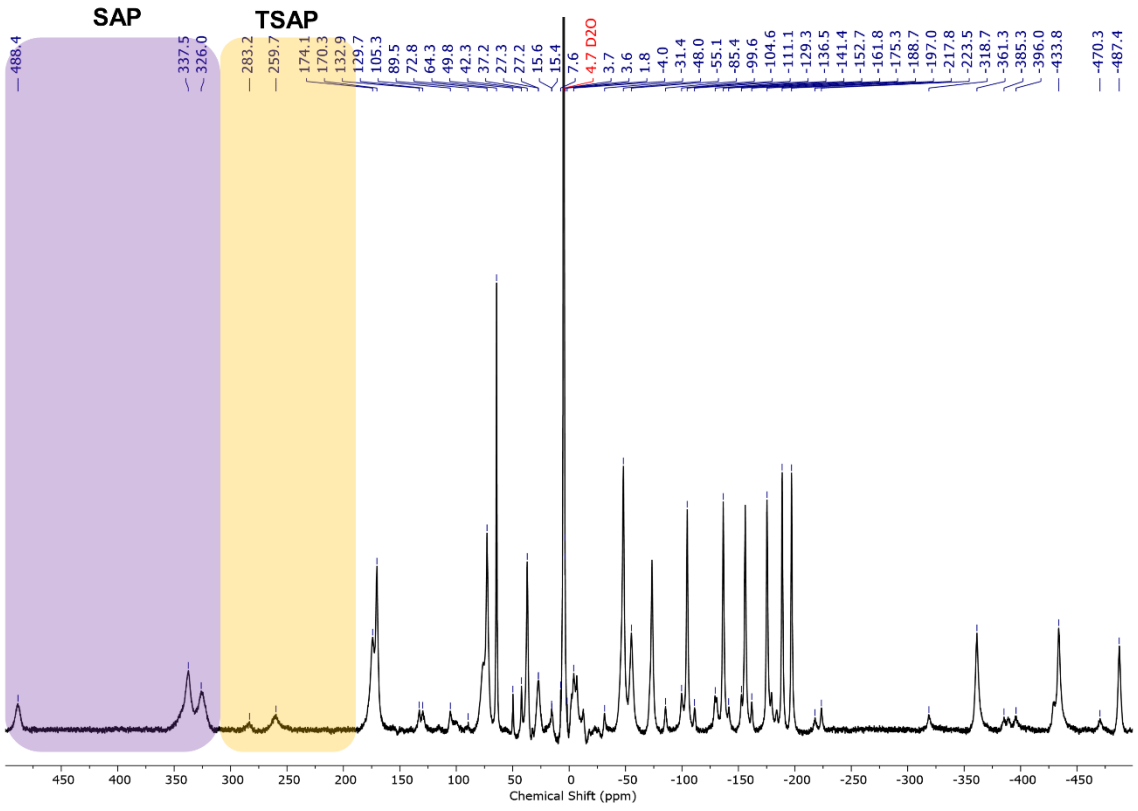


*Figure 5.2: ^{1}**3.3·Tb$_2$** in D$_2$O at pD 9.9, regions of TSAP and SAP isomers are highlighted.*Upon decreasing the pD to 2.7, a change in peak shift is observed in the ^{1}H NMR spectrum. This is highlighted in Figure

5.2 where the proton environment at ~ 340 ppm shifts downfield with increasing pD. By plotting the chemical shift, as a function of pD, three distinct regions can be defined (red, green and blue). As discussed earlier, the red region describes the region in which Species 1 dominates. This is followed by the changes in chemical shifts, in the blue region, observed between pD 3.2 and pD 2.7. This change potentially derived from the protonation of the carboxylic acids, hence corresponding Species 2 (N_3).[314]

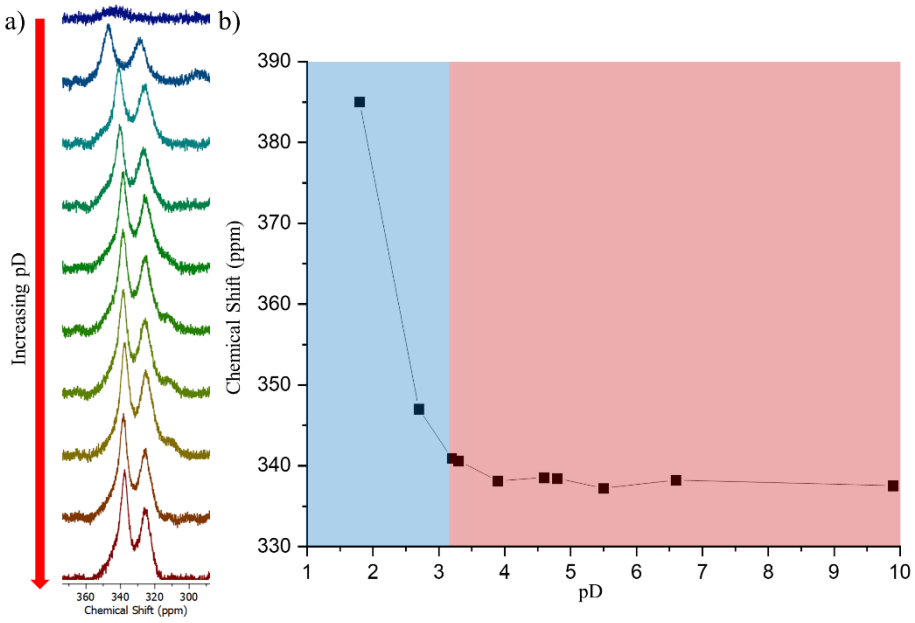


*Figure 5.3: a) Stacked ^{1}H NMR of **3.3·Tb**$_2$ at varying pDs, focussed on the chemical shift of the proton environment at ~340 ppm b) Plot of chemical shift vs pD, highlighting the defined regions (blue and red) in which each species dominates.*

Upon further decreasing the pD to 1.8, a drastic change in the spectrum is observed. At this pD, species 1 and 2 are no longer observed. Peaks are observed at differing chemical shifts, and the intensity of the proton signals is diminished. This is attributed to the protonation of the carboxylic acid groups resulting in Tb(III) ions leaching from the complex and thus resulting in the formation of Species 3 (N_3). It is believed that upon protonation of the carboxylic acids, the rigid structure shown in the crystal structure (see **Chapter 3** Figure 3.2) is lost, and the phenol is protonated and no longer protected. The spectrum at pD 1.8 is likely made up from a contribution of Species 2 (N_3) and Species 1 (N_3) in equilibrium, with intermediate species

such as the corresponding mononuclear complex. The exact pKa for each functional group in D_2O for **3.3·Tb$_2$** could not be determined, but it is estimated that the protonation of the carboxylic acids and phenolate occur below pD 3.2. This is in agreement with the literature on the pH stability of similar Ln(III) complexes.[70, 315]

Upon excitation *via* the sensitizing ligand, **3.4·Tb$_2$** is a highly emissive complex with a quantum yield of 45.2% in PBS buffer at pH 7.4. However, the aniline, which is believed to be a reason for this impressive sensitizing efficiency (See **Chapter 3**) is pH dependent, and thus the influence of varying pD on **3.4·Tb$_2$** was investigated by ^{1}H NMR.

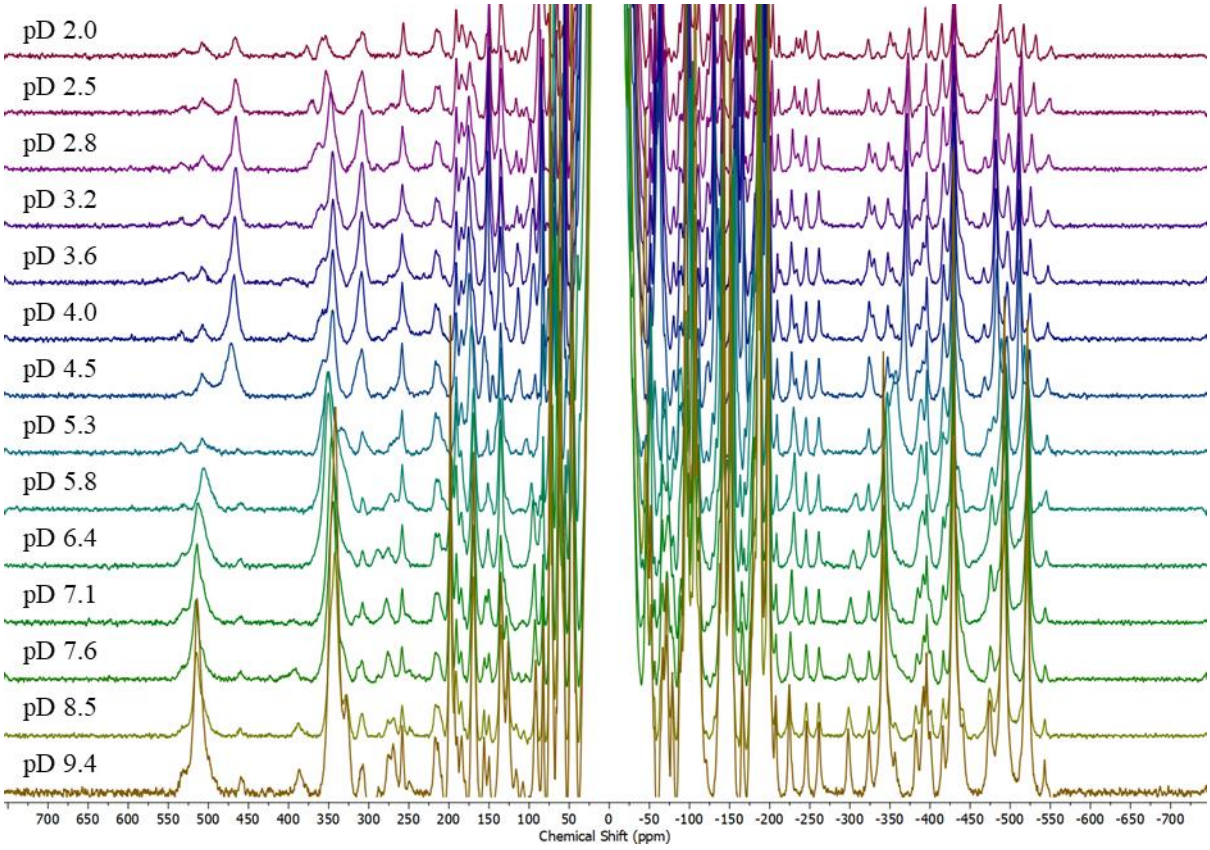


*Figure 5.4: Stacked ^{1}H NMR spectra (499.9 MHz) of **3.4·Tb$_2$** at different pDs in D_2O.*

The stacked spectra shown in Figure 5.4 show the ^{1}H NMR of **3.4·Tb$_2$** is largely unchanged between pD 9.4 and pD 7.1. At around pD 7.1, the proton environments begin to shift and split, changing the profile of the spectrum considerably, so that by pD 4.5 the spectrum is drastically different. Between pD 4.5 and pD 2.8, the spectrum is stable and remains largely unchanged;

however, at pD 2.5, and below, the signal intensities of the present proton environments become diminished and new peaks appear in the spectrum.

Unlike the structurally analogous complex **3.3·Tb$_2$**, a change is observed in the ^{1}H NMR spectrum of **3.4·Tb$_2$** between pD 9.4 and pD 2.8. It is believed that this significant change relates to the protonation of the amine in the *para* position to the phenolate on the ring. This is supported by the pD curve shown in Figure 5.5 where, upon plotting the chemical shift of the proton environment at ~ -340 ppm of **3.4·Tb$_2$** as a function of pD, the most significant change in chemical shift occurs between pD 9.4 and pD 2.8. Additionally, Figure 5.5 shows that there is an equivalence point in this region which, upon fitting the curve to a sigmoidal dose response function (see **Chapter 7** for details), was found to occur at pD 5.3. Using equation 5.3, it is estimated that the pKa of this protonation occurs at pH 4.9, this is in agreement with literature values of the pKa of aniline.[316]

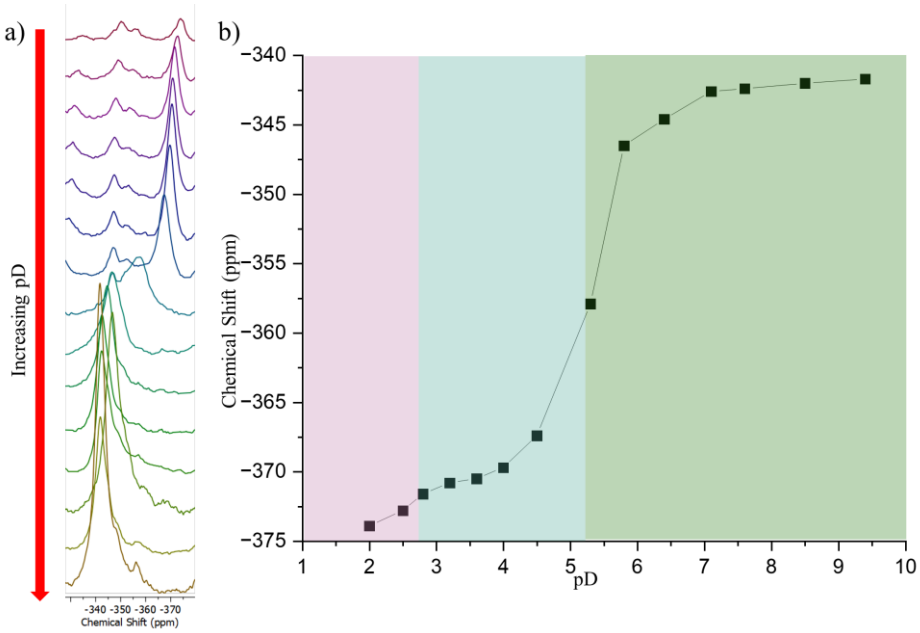
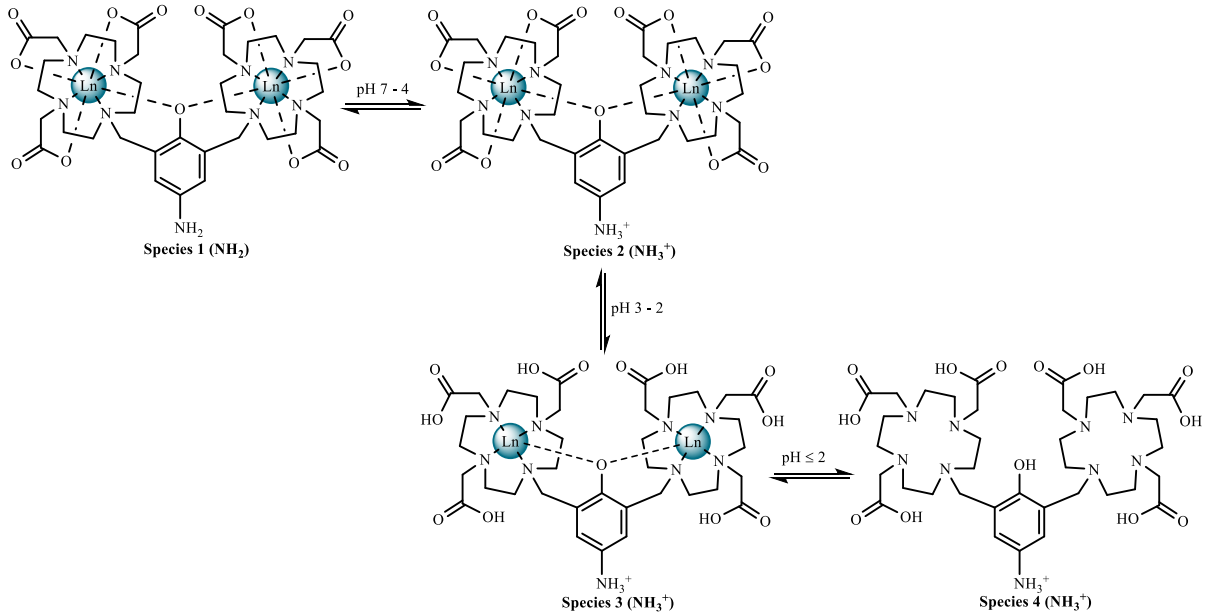


*Figure 5.5: a) Stacked ^{1}H NMR of **3.4·Tb$_2$** at varying pDs, focussed on the chemical shift for the proton environment at ~ -340 ppm b) Plot of chemical shift vs pD, highlighting the defined regions (pink, blue and green) in which each species dominates.*

Therefore, it is proposed that between pD 9.4 and pD 7.1 Species 1 (NH_2), as shown in Scheme 5.4, dominates, where the aniline is deprotonated. Below pD 7.1, Species 1 (NH_2) is in

equilibrium with Species 2 (NH_3^+) and the ^{1}H NMR spectrum represent a weighted averaged of both species in solution. Between pD 5.3 and pD 2.8, Species 2 (NH_3^+) dominates in solution. Below pD 2.8, the changes observed in the ^{1}H NMR spectra are similar to those observed in the same range for **3.3·Tb$_2$**, representing the protonation of the carboxylic acids in solution (Species 3 (NH_3^+)), and the subsequent leaching of Tb(III) ions from the complex and the protonation of the phenolate (Species 4 (NH_3^+)).



*Scheme 5.4: Schematic describing the structures in solution proposed for **3.4·Tb$_2$** at varying pDs.*

Interestingly, Species 1 (N_3) of **3.3·Tb$_2$** and Species 1 (NH_2) of **3.4·Tb$_2$** are structurally analogous, with the only difference arising from the azide and amine functional groups present on the aromatic ring of the ligand framework. However, comparison between the ^{1}H NMR spectra of both complexes at pD 9.9 shows that the proton environments in **3.4·Tb$_2$** are considerably downshifted in comparison to that of **3.3·Tb$_2$**, particularly that of the most downshifted environment which occurs at 514.1 ppm for **3.4·Tb$_2$** and at 488.4 ppm for **3.3·Tb$_2$**. This difference corresponds to a 5% change and is a direct consequence of the molecular orbitals on the ligand and the influence of the functional group present. As explained in detail in **Chapter 3**, by altering the position and amount of electron density on the ring, this perturbs

the f-electron density of the individual m_j states anisotropically for the Ln(III) complex, resulting in a change in the relative energies and the Boltzmann distribution.

5.3.3 Eu(III) Binuclear complexes

To support the speciation investigated in the Tb(III) complexes, the pD dependence of the ^{1}H NMR of Eu(III) complex, **3.4·Eu$_2$**, was also investigated, as shown in Figure 5.6. The stacked ^{1}H NMR spectra of **3.4·Eu$_2$** differed from that of the analogous Tb(III) complex in the maximum chemical shift being recorded at 48.7 ppm, indicative of the formation of a Eu(III) complex. Similarly to Tb(III) complex, there was a negligible change in the ^{1}H NMR spectra between pD 10.3 and pD 7.1; whereas upon decreasing the pD to 3.7, a significant change in the spectrum was observed.

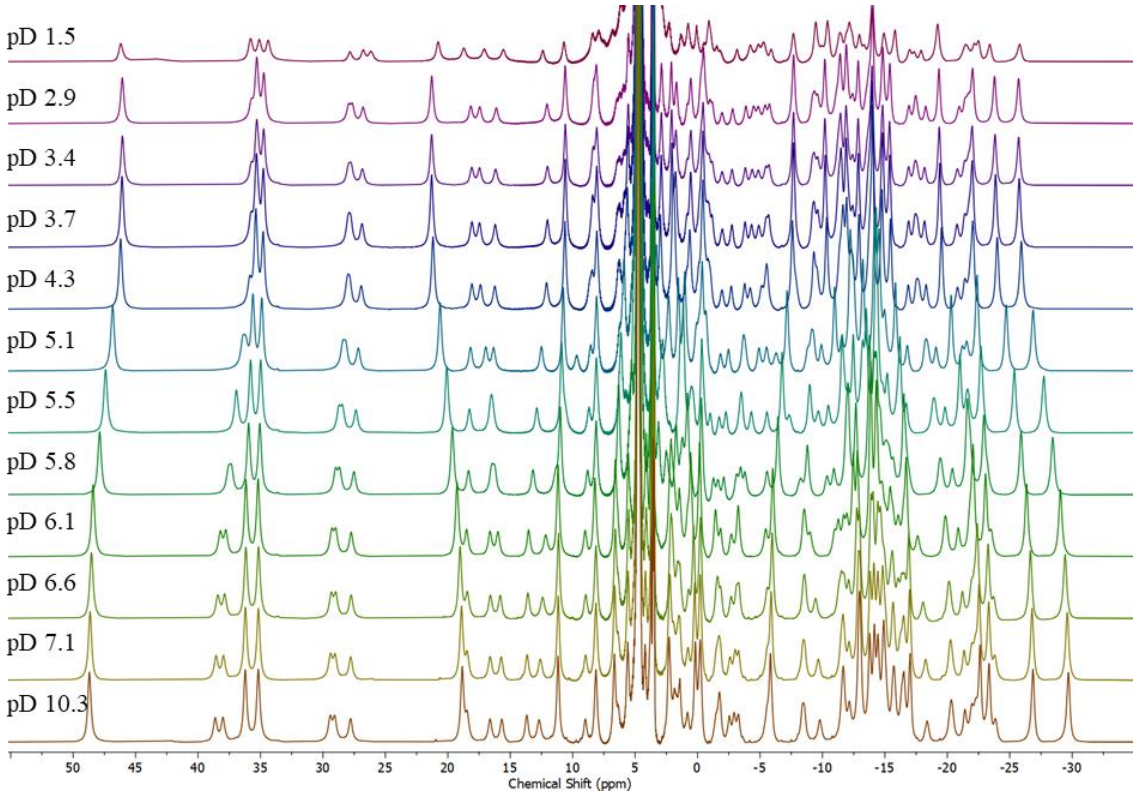


*Figure 5. 6: Stacked ^{1}H NMR spectra (499.9 MHz) of **3.4·Eu$_2$** at different pDs in D_2O.*

The pKa in D_2O for **3.4·Eu$_2$** was determined to occur at pD 5.5 (pH = 5.1), in accordance with the pKa determined for the isostructural Tb(III) analogue. Again, upon decreasing the pD

further, to pD 2.0, additional peaks are observed and the intensity of the peaks diminish as a result of Eu(III) ions leaching out of the complex.

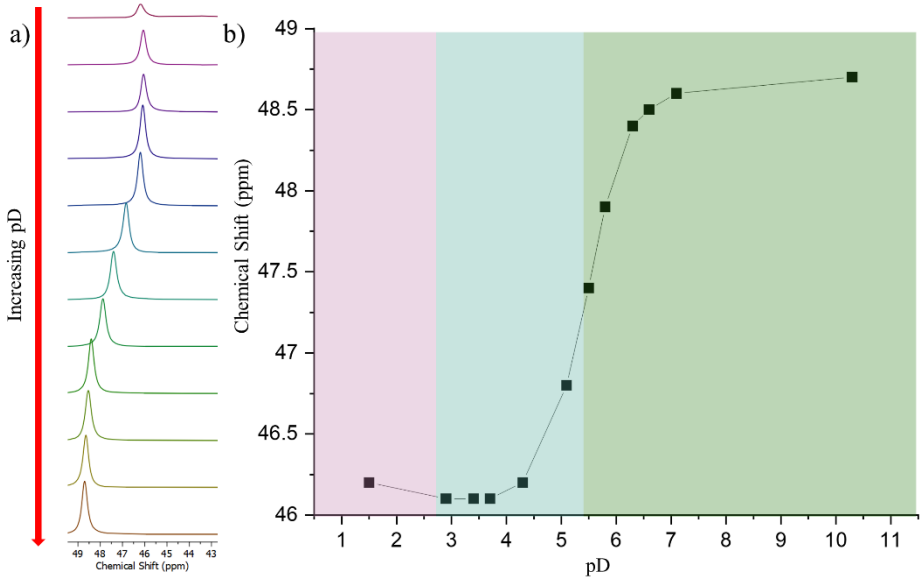


*Figure 5. 7: a) Stacked ^{1}H NMR of **3.4·Eu$_2$** at varying pDs, focussed on the chemical shift for the proton environment at ~ 47 ppm b) Plot of chemical shift vs pH, highlighting the defined regions (red, blue and green) in which each species dominates.*

5.4 Conclusions

In conclusion, the work in this chapter demonstrates the utility of investigating the ^{1}H NMR of paramagnetic Ln(III) complexes in determining the structure and speciation of binuclear complexes in solution. The ^{1}H NMR of **3.3·Tb$_2$** showed that the structure in solution remained stable between pD ~10.0 and pD ~3.0, only at pD <3.0 significant changes were observed. At pD values below 3.0, it is believed that the carboxylates on the macrocycle become protonated, and subsequently Tb(III) leaches from the complex, resulting in the formation of multiple related species in solution and resulting in a loss of signal intensity. This trend was observed also for **3.4·Tb$_2$** and **3.4·Eu$_2$** at pD <3.0, suggesting that speciation below pD 3.0 is shared across the isostructural series. However, unlike **3.3·Tb$_2$**, the ^{1}H NMR spectrum of **3.4·Tb$_2$** and **3.4·Eu$_2$** significantly changed between pD ~10.0 and pD ~3.0, corresponding to the protonation of the aniline present in the *para*-position of the aromatic ring. The pKa was determined to be

~4.9 – 5.0, in agreement with the literature.[316] As a result of these ^{1}H NMR studies, the speciation in solution of important binuclear complexes were further understood, allowing for improved design of the next generation complexes.

5.5 References for Chapter 5

1. C. Alexander, J. A. Thom, A. M. Kenwright, K. E. Christensen, T. J. Sørensen and S. Faulkner, *Chem. Sci.*, 2023, **14**, 1194-1204.
2. Y.-G. Wang, Y.-Q. Li, H.-H. Tang, L.-R. Lin and L.-H. Ma, *ACS Omega*, 2018, **3**, 5480-5490.
3. O. A. Blackburn, M. Tropiano, L. S. Natrajan, A. M. Kenwright and S. Faulkner, *Chem. Commun.*, 2016, **52**, 6111-6114.
4. H. Akiba, J. Sumaoka, K. Tsumoto and M. Komiyama, *Anal. Chem.*, 2015, **87**, 3834-3840.
5. L. R. Hill, T. J. Sørensen, O. A. Blackburn, A. Brown, P. D. Beer and S. Faulkner, *Dalton Trans.*, 2013, **42**, 67-70.
6. S. G. Reis, M. Briganti, S. Soriano, G. P. Guedes, S. Calancea, C. Tiseanu, M. A. Novak, M. A. del Aguila-Sánchez, F. Totti, F. Lopez-Ortiz, M. Andruh and M. G. F. Vaz, *Inorg. Chem.*, 2016, **55**, 11676-11684.
7. B. E. Klamm, T. E. Albrecht-Schmitt, R. E. Baumbach, B. S. Billow, F. D. White, S. A. Kozimor, B. L. Scott and A. M. Tondreau, *Inorg. Chem.*, 2020, **59**, 8642-8646.
8. J. Q. Nguyen, J. W. Ziller and W. J. Evans, *Inorganics*, 2023, **11**.
9. L. Münzfeld, S. Gillhuber, A. Hauser, S. Lebedkin, P. Hädinger, N. D. Knöfel, C. Zovko, M. T. Gamer, F. Weigend, M. M. Kappes and P. W. Roesky, *Nature*, 2023, **620**, 92.
10. C. A. Gould, *Science*, 2022, **378**, 1181-1181.
11. S. D. R. De, A. Mondal, S. R. Giblin and R. A. Layfield, *Angew. Chem. Int. Ed.*, 2024, **63**.
12. P. Zhang, F. Benner, N. F. Chilton and S. Demir, *Am. Chem.*, 2022, **8**, 717-730.
13. C. Simms, V. R. M. Nielsen, T. J. Sørensen, S. Faulkner and M. J. Langton, *Phys. Chem. Chem. Phys.*, 2024, **26**, 18683-18691.
14. C. Alexander, J. A. Thom, A. M. Kenwright, K. E. Christensen, T. J. Sorensen and S. Faulkner, *Chem. Sci.*, 2023, **14**, 1194-1204.
15. T. J. Sørensen and S. Faulkner, *Acc. Chem. Res.*, 2018, **51**, 2493-2501.
16. T. J. Sørensen, A. M. Kenwright and S. Faulkner, *Chem. Sci.*, 2015, **6**, 2054-2059.
17. T. J. Sørensen, L. R. Hill, J. A. Tilney, O. A. Blackburn, M. W. Jones, M. Tropiano and S. Faulkner, *Eur. J. Inorg. Chem.*, 2014, **2014**, 2520-2528.
18. M. Tropiano, C. J. Record, E. Morris, H. S. Rai, C. Allain and S. Faulkner, *Organometallics*, 2012, **31**, 5673-5676.
19. S. Faulkner and D. Sykes. (2010). Lanthanide Assemblies and Polymetallic complexes. In: Hänninen, P., Härmä, H. (eds) Lanthanide Luminescence. Springer Series on Fluorescence, vol 7. Springer, Berlin, Heidelberg. https://doi.org/10.1007/4243_2010_3
20. M. P. Placidi, L. S. Natrajan, D. Sykes, A. M. Kenwright and S. Faulkner, *Helv. Chim. Acta*, 2009, **92**, 2427-2438.

21. S. J. A. Pope, B. J. Coe, S. Faulkner, E. V. Bichenkova, X. Yu and K. T. Douglas, *J. Am. Chem. Soc.*, 2004, **126**, 9490-9491.
22. S. J. A. Pope, A. M. Kenwright, S. L. Heath and S. Faulkner, *Chem. Commun.*, 2003, 1550-1551.
23. J. A. Tilney, T. J. Sørensen, B. P. Burton-Pye and S. Faulkner, *Dalton Trans.*, 2011, **40**, 12063.
24. Y. O. Fung, W. Q. Wu, C. T. Yeung, H. K. Kong, K. K. C. Wong, W. S. Lo, G. L. Law, K. L. Wong, C. K. Lau, C. S. Lee and W. T. Wong, *Inorg. Chem.*, 2011, **50**, 5517-5525.
25. T. J. Sorensen and S. Faulkner, *Acc. Chem. Res.*, 2018, **51**, 2493-2501.
26. E. Di Piazza, L. Norel, K. Costuas, A. Bourdolle, O. Maury and S. Rigaut, *J. Am. Chem. Soc.*, 2011, **133**, 6174-6176.
27. S. Faulkner and S. J. A. Pope, *J. Am. Chem. Soc.*, 2003, **125**, 10526-10527.
28. T. Ala-Kleme, M. Latva and K. Haapakka, *Anal. Chim. Acta*, 2000, **403**, 161-171.
29. D. L. Dexter, *J. Chem. Phys.*, 1953, **21**, 836-850.
30. T. FöRster, *J. Biomed. Optics*, 2012, **17**, 011002.
31. Y. G. Gorbunova, A. G. Martynov, K. P. Birin and A. Y. Tsivadze, *Russ. J. Inorg. Chem.*, 2021, **66**, 202-216.
32. L. S. Natrajan, P. L. Timmins, M. Lunn and S. L. Heath, *Inorg. Chem.*, 2007, **46**, 10877-10886.
33. B. Bleaney, *J. Magn. Reson.*, 1972, **8**, 91-&.
34. B. Bleaney, R. J. P. Williams, A. V. Xavier, R. B. Martin, B. A. Levine and C. M. Dobson, *Chem. Commun.*, 1972, 791.
35. D. Parker, E. A. Suturina, I. Kuprov and N. F. Chilton, *Acc. Chem. Res.*, 2020, **53**, 1520-1534.
36. J. Kowalewski, L. Nordenskiold, N. Benetis and P. O. Westlund, *Prog. Nucl. Magn. Reson. Spectrosc.*, 1985, **17**, 141-185.
37. M. E. Boulon, G. Cucinotta, J. Luzon, C. Degl'Innocenti, M. Perfetti, K. Bernot, G. Calvez, A. Caneschi and R. Sessoli, *Angew. Chem. Int. Ed.*, 2013, **52**, 350-354.
38. A. Krezel and W. Bal, *J. Inorg. Biochem.*, 2004, **98**, 161-166.
39. M. Tosato, L. Lazzari and V. Di Marco, *ACS Omega*, 2022, **7**, 15596-15602.
40. E. Toth, E. Brucher, I. Lazar and I. Toth, *Inorg. Chem.*, 1994, **33**, 4070-4076.
41. E. Toth and E. Brucher, *Inorg. Chim. Acta*, 1994, **221**, 165-167.
42. A. Albert and E. P. U. Serjeant, *Ionization constants of acids and bases : a laboratory manual*, 1962.

Chapter 6

Conclusions and Future Work

Chapter 2 discusses the first reported examples of kinetically stable, photoswitchable and emissive lanthanide complexes. This system can be controlled and interrogated using orthogonal wavelengths of visible and near-IR light. Notably, the photoswitching of these complexes is entirely decoupled from the emission and excitation of their trivalent lanthanide cations. This is of significance in relation to applications in optical information storage, in particular for read-write processes.

Chapter 3 investigates the development of a family of redox-activated probes for magnetic resonance and optical imaging. Gadolinium(III)-based probes displayed potential as both turn on and turn off probes for MR imaging. Terbium(III)-based probes displayed impressive optical properties, possessing ON states with high quantum yields. This family of activatable Ln(III) complexes consists of a range of compound classes that reduce under different conditions and at different redox potentials. However, these complexes were found to suffer from poor cell permeability, hindering biological applications thus far. Work is currently ongoing to enable the delivery of these lanthanide complexes into cells *via* a variety of methods. The "trojan horse" methodology" aims to deliver facilitate the complex delivery through vesicle encapsulation. After crossing the cell-membrane, the loaded vesicles release their contents upon sonication.[317, 318] Another method is to modify the complexes themselves to improve cellular uptake, either by increasing their charge and lipophilicity or by adding targeting peptides that facilitate delivery into cells.

Chapter 4 details the structure and speciation of common heptadentate Ln(III) complexes in solution. In particular, the determination of the isomeric distribution of twisted square antiprismatic (TSAP) and square antiprismatic (SAP) geometries at 298 K is discussed in depth. ^{1}H NMR and detailed optical spectroscopic studies were fully consistent with one another, with the isomeric distribution of TSAP and SAP isomers found to be 64-66% and 36-34% respectively. Importantly, this chapter demonstrates the ability of PCA analysis and spectral fitting to facilitate the analysis of small changes in the optical spectra. However, all experiments were carried out in DMSO, in which carbonate is formed upon the dissolution of atmospheric CO_2. It is hypothesised the binding of carbonate to the lanthanide complex reduces the rate of interconversion between TSAP and SAP isomers, therefore influencing the isomeric distribution in solution. To investigate this hypothesis, all experiments and analysis should be repeated in water at a pH below the pK_a of carbonic acid (< pH 6.0) to understand the influence of bound carbonate on both the distribution and spectroscopic properties of the geometric isomers.

Chapter 5 describes the utility of ^{1}H NMR spectroscopy as a tool for probing changes in the solution-phase speciation and structures of binuclear Ln(III) complexes across a range of pH values. The optical properties of each complex at different pH values should be assessed to enable a full understanding of the speciation processes and structure-property relationships observed thus far.

In summary, the results described herein demonstrate the different ways in which ligand modification can enable the manipulation of Ln(III) luminescence, and showcase the importance of investigating the solution-phase structures of Ln(III) complexes to illuminate their structure-property relationships. This has enabled the development and application of a range of Ln(III) complexes in a number of applications, spanning optical information storage and the optical detection of redox environments.

Chapter 7

Experimental Procedures

7.1 General Methods and Reagents

7.1.1 Synthesis and Purification

Unless stated otherwise, experiments were performed at 25 °C using reagents and solvents purchased commercially and used without further purification. Anhydrous solvents were acquired by passing them through an MBraun MPSP-800 column followed by degassing with nitrogen. Triethylamine was distilled from and stored over potassium hydroxide. Deionised, microfiltered water was obtained from a Milli-Q™ Millipore machine. Merck silica gel 60 under nitrogen pressure was used for silica gel flash column chromatography. Thin layer chromatography was performed on silica-coated (60G F254) aluminium plates from Merck and aluminium oxide coated with 254 nm fluorescent indicator aluminium plates from Merck. Samples were visualized by UV-light (254 and 365 nm) and/or using permanganate stain. Solvent systems containing a mixture of solvents are reported as a ratio by volume of each solvent.

Float-A-Lyzer® G2 dialysis tubes (500, 1000 MWCO) equipped with regenerated cellulose were purchased from Spectrum and used to purify the lanthanide complexes. The dialysis tube was activated by 10 % ethanol or isopropanol solution followed by Milli-Q type 1 deionised water before being used. The corresponding complexes were dissolved in water and transferred into a dialysis tube. The dialysis tube was placed in a 2.5 L-beaker filled with Milli-Q type 1 deionised water. The dialysis lasts for at least two days under stirring and the deionised water was replaced with fresh deionised water more than three times during dialysis.

7.1.2 Characterisation Information

7.1.2.1 Mass Spectrometry

Mass spectra were carried out on a Waters BioAccord LC-MS system; flow injection analysis was performed on an ACQUITY I-Class PLUS UPLC System (Waters, Millford, MA, USA) coupled to an AQUITY RDa mass spectrometer (Waters, Milford, MA, USA) equipped with an ESI probe, in positive ion mode. The flow rate was set to 0.300 mL/min using 50 % methanol (aq) + 0.1 % formic acid eluent. Scan parameters were set as follows: analyser mode, full scan; scan range 50-2000 m/z; scan rate, 2 Hz; cone voltage, 40 V; capillary voltage, 0.8 kV; desolvation temperature, 550 °C; and intelligent data capture, on.

7.1.2.2 NMR Spectrometry

NMR spectra were obtained using a Bruker Avance III HD nanobay NMR equipped with a 9.4 T magnet (^{1}H 400.2 MHz, ^{19}F 376.5 MHz, ^{13}C 100.6 MHz), Bruker Avance NMR equipped with a 11.75 T magnet and a ^{13}C detect cryoprobe (^{1}H 500.3 MHz, ^{13}C 125.8 MHz) and Bruker NEO 600 with broadband helium cryoprobe (^{1}H 600.4 MHz, ^{13}C 151.0 MHz). Chemical shifts were referenced to residual solvent peaks and are given as follows: chemical shift (δ, ppm), multiplicity (s, singlet; br, broad; d, doublet, t, triplet; q, quartet; m, multiplet), coupling constant (J, Hz), integration. All NMR spectra were recorded at 298K, unless stated otherwise.

7.1.2.3 Liquid Chromatography Mass Spectrometry (LCMS)

LCMS (ESI) results were recorded on a Waters LCT Premier bench-top orthogonal acceleration time-of-flight LC-MS system, connected to a CTC Analytics HTS PAL Sample Manager, Acquity PDA Detector, Acquity Column Heater/Cooler, Acquity Binary Solvent Manager. Samples (5 µL; 10 µL sample loop) were injected onto an ACE equivalence C_{18} (50 ´ 2.1 mm) column.

7.1.2.4 High Performance Liquid Chromatography (HPLC)

All HPLC analysis were carried out on a Thermo Scientific Vanquish Core HPLC on an analytical Discovery® Cyano 25 cm × 4.6 mm, 5µm column fitted with a Discovery® Cyano 2 cm × 4.0 mm, 5µm guard column. All samples were filtered using a fisherbrand PTFE filter with 0.2um pore size. Unless otherwise stated HPLC traces were monitored at 272 nm. Methods are detailed below. All solvent systems contained 0.1 % Formic Acid.

Method 1: [95:5 H_2O: MeCN; → 50:50 H_2O: MeCN: 55 min; 2 min hold; → 95:5 H_2O: MeCN: 5 min;; 1 mL/min].

Method 2: [98:2 H_2O: MeCN; 5 min hold → 0:100 H_2O: MeCN: 20 min; 2 min hold; → 98:2 H_2O: MeCN: 2 min; 5 min hold; 1 mL/min].

7.1.2.5 Absorption Spectra

Absorption spectra were recorded on a Jasco V-770 UV-Visible/NIR Spectrophotometer equipped with Peltier temperature controller and stirrer using quartz cuvettes of 1 cm path length. Experiments were conducted at 25°C unless otherwise stated.

7.1.2.6 Optical Spectroscopy

Steady state emission spectra

Steady State excitation and emission spectra of organic ligands were recorded on a Horiba Jobin Yvon Fluorolog® 3-12 Fluorometer equipped with a Hamamatsu R928 detector and a double-grating emission monochromator. S1 response was used throughout as luminescence output. Emission and excitation slits were fixed at 5 and 1 nm, respectively the step size was 1 nm and the integration time set to 0.1 s. Excitation were determined by the peaks in the absorbance spectra of each isomer and are detailed in the individual experiment.

Europium(III) excitation and emission spectra were carried out on a PTI QuantaMaster8075 instrument from Horiba Scientific using a xenon arc lamp for excitation. The excitation wavelength was fixed at 395 nm. The temperature was kept constant at 20 °C, with a Koolance EXT-440 liquid cooling system from Horiba Scientific. For samples recorded at 77 K, a constant nitrogen flow in the sample chamber was maintained to avoid condensation on the NMR tube Emission and excitation slits were fixed at 1 and 5 nm, respectively the step size was 0.5 nm and the integration time set to 0.2 s. The emission wavelength was set at 617 nm emission and excitation slits were set at 5 and 1 nm respectively, the step size was 0.5 nm and the integration time was 0.2 s.

Neodymium(III) emission spectra were measured on a custom built spectrometer.[185] The samples were excited by a supercontinuum laser (NKT SuperK Fianium FIU-15) that was coupled to a tuneable bandpass filter (NKT LLTF Contrast VIS/SWIR HP8). The laser power was set to 90% with the maximum repetition rate (78 MHz). A 750B grating was used for measurements below the 950 nm point, and a 1200B grating was used for measurements above 950 nm. The emission slit was set to 25 μm for all measurements. For neodymium(III), the excitation wavelength was set to 580 nm, a long-pass filter of 800 nm was used, and the centre wavelength of the detector set to 880 or 1050 nm for the two regions of interest. For samples recorded at 77K, a constant nitrogen flow in the sample chamber was maintained to avoid condensation on the cuvette.

Neodymium(III) excitation spectra were recorded by changing the wavelength of the excitation source through our own Python code that connects to the tuneable bandpass filter. At each excitation wavelength, an emission spectrum was recorded and integrated by summing all data points spanning the region of interest; the wavelength range chosen. Two different acquisitions were used: (1) the excitation source was scanned from 450 to 835 nm, the exposure time was 100 ms with 1 exposure per frame, and the data points were summed from 840 to 940 nm; (2)

the excitation source was scanned from 773 to 920 nm, the exposure time was 1000 ms with 10 exposures per frame, and the data points were summed from 1040 to 1070 nm.

All spectra are corrected for lamp efficiency and solvent baselines.

Time resolved emission spectra

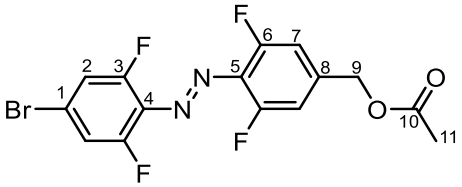
Time-resolved measurements were carried out on a PTI QuantaMaster8075 instrument from Horiba Scientific using a xenon flash lamp as the excitation source. All decay traces were fitted to a monoexponential decay using the Origin 2017 (OriginLab) software. Most lifetimes gave satisfactory fitting using a mono exponential or bi exponential decay fitting.

7.2 Experimental for Chapter 2

7.2.1 Synthesis and Characterisation of Complexes

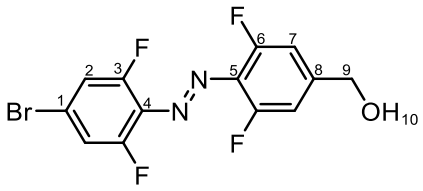
Compounds **2.1**,[319] **2.2**,[168] **2.3**[168], **2.4b**[168] and **2.5b**[168] and **DO3A^{t}Bu**[236] were all synthesised according to previously reported literature procedures.

7.2.1.1 Procedures for Asymmetric Azobenzenes



4-bromo-2,6-difluoroaniline (1.56 g, 12.0 mmol, 1.2 eq.) was dissolved in 48 mL DCM: Acetone (5:1). Oxone (20 g, 65 mmol, 5.5 eq.) was dissolved in water (48 mL) and added to the 2,6-difluoroanaline containing solution. The resulting biphasic solution was stirred overnight at room temperature. The organic layer was separated and reduced under vacuum. The resulting solid was re-dissolved in 50 mL of acetic acid: toluene: TFA (6: 6: 1) solution, to which **3** (2.03 g, 10 mmol, 1.0 eq.) was added. The reaction was stirred for 3 days at room

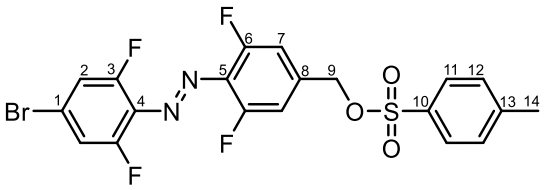
temperature. The solution was concentrated under reduced pressure and purified by silica gel flash column chromatography with DCM to yield an orange crystalline product (0.903 g, 2.77 mmol, 27 %). **^{1}H NMR** (400 MHz, DMSO-d_6) δ: 7.82 – 7.74 (m, 1H, H_2), 7.39 (d, J = 10.6 Hz, 1H, H_7), 5.17 (s, 1H, H_9), 2.14 (s, 1H, H_{11}).**^{13}C NMR** (151 MHz, DMSO-d_6) δ: 170.1 (C_{10}), 155.5 (t, *J* = 5.0 Hz, C_3), 153.8 (d, *J* = 4.9 Hz, C_6), 143.1 (t, *J* = 10.2 Hz, C_8), 129.9 (t, *J* = 9.7 Hz, C_4), 129.7 (d, *J* = 9.8 Hz, C_5), 124.5 (t, *J* = 12.4 Hz, C_1), 117.1 (dd, *J* = 23.3, 3.8 Hz, C_2), 111.8 (dd, *J* = 20.9, 3.3 Hz, C_7), 63.7 (C_9), 20.6 (C_{11}).**^{19}F NMR** (377 MHz, DMSO-d_6) δ: -119.68 (F_2), -120.64 (F_7) **HR-ESI-MS** obsd 404.9855, calcd 404.9856 [$(M + H)^+$, M = $C_{15}H_{10}BrF_4N_2O_2$].



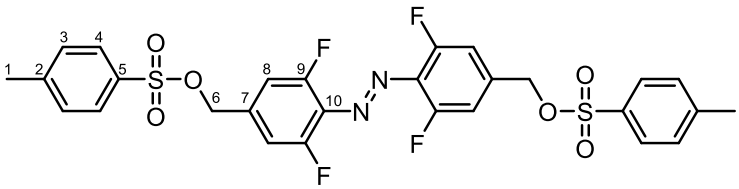
2.4a (900 mg, 2.22 mmol) was dissolved in 250 mL of a solution of 37 % HCl : MeOH (1: 100) and left to stir at 40 °C for 72 hrs. The reaction was diluted with toluene (100 mL) and the solution concentrated under reduced pressure. The crude product was purified by silica gel flash column chromatography eluted with ethyl acetate: DCM (1:5) to yield an orange crystalline solid, **2.5a** (630 mg, 2.76 mmol, 77 %).**^{1}H NMR** (400 MHz, DMSO-d_6) δ 7.80 – 7.72 (m, 2H, H_2), 7.27 (d, *J* = 10.8 Hz, 2H, H_7), 5.63 (t, *J* = 5.8 Hz, 1H, H_{10}), 4.60 (d, *J* = 5.8 Hz, 2H, H_9) ppm. **^{13}C NMR** (151 MHz, DMSO-d_6) δ 156.1 (dd, *J* = 27.4, 4.7 Hz, C_3), 154.3(dd, *J* = 29.7, 4.7 Hz, C_6), 150.9 (t, *J* = 9.2 Hz, C_8), 130.5 (t, *J* = 9.8 Hz, C_4), 129.4 (t, *J* = 9.7 Hz, C_5), 124.6 (t, *J* = 12.4 Hz, C_1), 117.6 (d, *J* = 3.9 Hz, C_2), 110.7 (d, *J* = 3.0 Hz, C_7), 62.0 (d, *J* = 35.3 Hz, C_9) ppm.**^{19}F NMR** (565 MHz, DMSO-d_6) δ -119.93 (d, *J* = 9.9 Hz, F_3), -120.67 (d, *J* = 11.4 Hz, F_6) ppm. **HR-ESI-MS** obsd 362.9750, calcd 362.9751 [$(M + H)^+$, M = $C_{13}H_7BrF_4N_2O$].

7.2.1.2 General Procedure for Tosyl Protection

The corresponding alcohol and 4-toluenesulfonyl chloride (3 eq. (mono protection), 6 eq. (bis protection)) were suspended THF: H_2O (1:3). To this NaOH (3 eq. (mono protection), 6 eq. (bis protection)) was added and the solution was left to stir rapidly at room temperature for 30 mins. The resulting solution was diluted with DCM and washed with water (3 × 50 mL). The organic layer was then concentrated under reduced pressure and purified by silica gel flash column chromatography eluted with DCM to yield a pale orange crystalline solid.



2.6a Yield: 150 mg, 0.34 mmol, (39%). **^{1}H NMR** (400 MHz, DMSO-d_6) (**6**-*E*) δ 7.83 (d, *J* = 8.2 Hz, 2H,H_{11}), 7.78 (d, *J* = 9.2 Hz, 2H, H_2), 7.47 (d, *J* = 8.0 Hz, 2H, H_{12}), 7.27 (d, *J* = 10.4 Hz, 2H, H_7), 5.24 (s, 2H, H_9), 2.40 (s, 3H, H_{14}) ppm. **^{13}C NMR** (151 MHz, DMSO-d_6) (**6**-*E*) δ 155.7 – 155.0 (m, C_6), 154.0 – 153.2 (m, C_3), 145.3 (C_{13}), 139.9 (t, *J* = 10.3 Hz, C_8), 132.3 (C_{10}), 130.6 (t, *J* = 9.9 Hz, C_5), 130.2 (C_{12}), 129.9 – 129.8 (m, C_4), 127.8 (C_{11}), 125.47(C_1), 117.2 (ddd, *J* = 23.3, 6.7, 3.5 Hz, C_2), 112.5 (dd, *J* = 21.2, 3.3 Hz, C_7), 69.7 (C_9), 21.0 (C_{14}) ppm. **^{19}F NMR** (377 MHz, DMSO-d_6) δ -119.56 (F_3), -120.62 (F_6) ppm. **HR-ESI-MS** obsd 518.9817, calcd 518.9819 [$(M + H)^+$, M = $C_{20}H_{13}BrF_4N_2O_3S$].

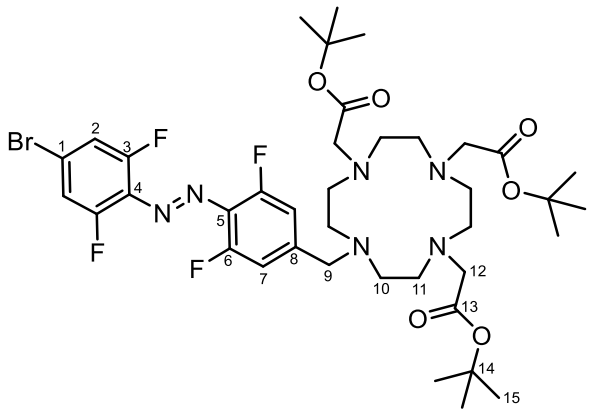


2.6b Yield: 578 mg, 0.93 mmol, 43%). **^{1}H NMR** (600 MHz, DMSO-d_6) δ 7.83 (d, *J* = 8.2 Hz, 4H, **H_4**), 7.49 – 7.45 (m, 4H, **H_3**), 7.26 (d, *J* = 10.5 Hz, 4H, **H_8**), 5.24 (s, 4H, **H_6**), 2.40 (s, 6H, **H_1**) ppm. **^{13}C NMR** (151 MHz, DMSO-d_6) δ 156.2 – 152.6 (m, **C_9**), 145.3 (**C_2**), 140.0 (dt, *J* =

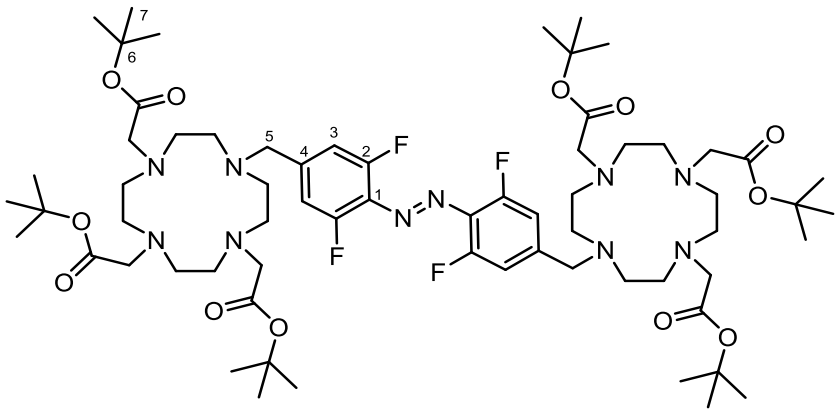
36.3, 10.3 Hz, **C7**), 132.3 (**C5**), 130.6 (t, *J* = 10.0 Hz, **C10**), 130.2 (**C3**), 128.0 (**C4**), 113.1 (dd, *J* = 21.1, 3.5 Hz, **C8**), 69.7 (**C6**), 21.0 (**C1**) ppm. **^{19}F NMR** (565 MHz, DMSO) δ -119.88 (dd, *J* = 555.7, 10.0 Hz, **F9**) ppm. **HR-ESI-MS** obsd 623.0925 , calcd 623.0928 [(M + H)$^+$, M = $C_{28}H_{22}F_4N_2O_6S_2$].

7.2.1.3 General Procedure for *Tert*-butyl Ester Protection

DO3A^{t}Bu.HBr (1.80 eq, **2.6a**, 2.9 eq. **2.6b**) was dissolved in MeCN, followed by the addition of Na_2CO_3 (3.60 eq. **2.6a**, 7.2 eq. **2.6b**). To this either **2.6a** or **2.6b** were added (1.00 eqv) and the reaction mixture was heated at 60°C for 2 days. The resulting suspension was filtered, and the filtrate concentrated under reduced pressure. The red/orange coloured residue was then purified by silica gel flash column chromatography and eluted with DCM (5-10% MeOH).



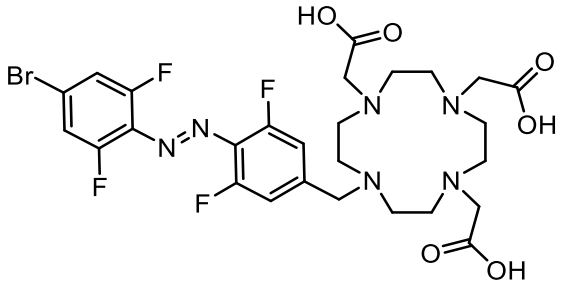
2.7a Yield: 530 mgs, 0.62 mmol, (94 %). **^{1}H NMR** (600 MHz, DMSO) δ: 7.79 – 7.75 (m, 2H, **H2**), 7.49 (d, J = 11.0 Hz, 2H, **H7**).3.61 (m, b, 2H), 3.08 (m, b, 13H), 2.25 (m, b, 7H) (cyclen methylene protons), 1.43 (d, J = 6.2 Hz, 32H, **H15**) ppm. **^{13}C NMR** (151 MHz, DMSO) δ: 173.1 (s, **C13**), 172.6, 155.4 (dd, *J* = 20.6, 4.8 Hz, **C3**) , 153.6 (dd, *J* = 18.5, 4.8 Hz, **C6**), 143.5 (d, *J* = 9.3 Hz, **C8**), 130.0 (t, *J* = 9.8 Hz, **C4**), 129.5 (t, *J* = 9.6 Hz, **C5**), 124.4 (t, *J* = 12.3 Hz, **C1**), 117.2 (s, **C2**), 115.0 (s, **C7**), 81.9 (s, **C14**), 57.2 (cyclen methylene carbons), 55.7 (s, **C12**), 55.4 (s, **C9**), 27.6 (s, **C15**) ppm. **^{19}F NMR** (565 MHz, DMSO) δ -119.01, -120.05, -120.89, -121.10 ppm. **HR-ESI-MS** obsd 691.1497 , calcd 691.1491 [(M + H)$^+$, M = $C_{39}H_{55}BrF_4N_6O_6$].



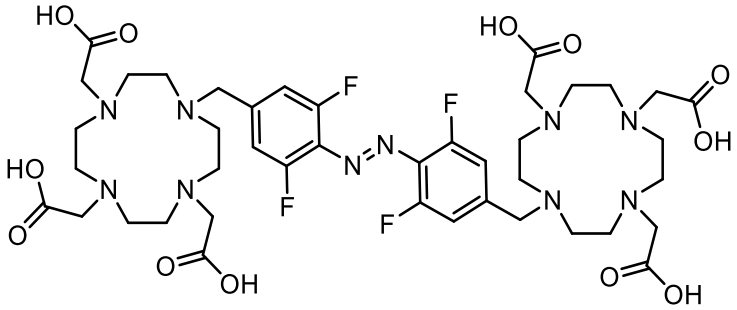
2.7b Yield: 371 mgs, 0.28 mmol, (60%) **^{1}H NMR** (600 MHz, DMSO) δ 7.50 (d, *J* = 11.0 Hz, 4H, **H$_3$**), 3.61 (s, 5H,), 3.20 – 2.63 (m, 24H), 2.41 – 1.71 (m, 15H), 1.44 (s, 56H, H$_a$) ppm. **^{13}C NMR** (151 MHz, DMSO) δ 172.9 (d, *J* = 74.4 Hz), 157.1 – 153.0 (m, **C$_2$**), 143.0 (**C$_1$**), 129.6 (d, *J* = 9.8 Hz, **C$_4$**), 114.9 (d, *J* = 20.0 Hz, **C$_3$**), 81.9, 81.5 (**C$_6$**), 57.1 (**C$_5$**), 55.4, 48.6, 33.5, 27.5 (d, *J* = 13.6 Hz, **C$_7$**), 21.7, 13.9 ppm. **^{19}F NMR** (565 MHz, DMSO) δ -121.95 (d, *J* = 11.4 Hz, **F$_2$**) ppm. **HR-ESI-MS** obsd 1307.7977, calcd 1307.8001 $[(M + H)^+$, M = $C_{66}H_{106}F_4N_{10}O_{12}$].

7.2.1.4 General Procedure for *Tert*-butyl Ester Deprotection

The *tert*-butyl ester protected ligand (1 eqv.) was dissolved in DCM and then TFA was added dropwise (1:1, c = 0.045 M). The reaction mixture was left to stir at room temperature for 18 hours. The reaction mixture was concentrated under reduced pressure and the crude product redissolved in a minimum amount of MeOH (1 volume), this was added dropwise to Et_2O (12 volumes in a falcon tube) and a precipitate formed. The resulting suspension was centrifuged, and the supernatant was decanted. The remaining solid was redissolved in a minimal amount of MeOH. The precipitation-centrifugation procedure was repeated twice more (overall 3 times). The resulting solids were dried to obtain the pure products.



2.L$_a$ in a quantitative yield.**^{1}H NMR** (600 MHz, D_2O) δ 7.31-7.15 (m, 4H, **Aromatic Protons**), 4.82 – 2.3.9 (m, 25 H, **cyclen protons**) ppm. **^{13}C NMR** (151 MHz, D_2O) δ 173.8, 169.2, 155.9, 154.2, 152.0, 150.3,130.2, 129.9, 124.3, 122.7, 116.7, 116.4,116.2, 115.0, 114.5, 62.5, 56.3, 55.6, 53.8, 51.6, 50.3, 49.0, 48.5, 48.0, 47.8, 42.3, 30.1 ppm. **^{19}F NMR** (565 MHz, D_2O) δ -118.23 ppm. **HR-ESI-MS** obsd 693.1472 , calcd 693.1480 $[(M + H)^+$, M = $C_{27}H_{31}BrF_4N_6O_6]$.

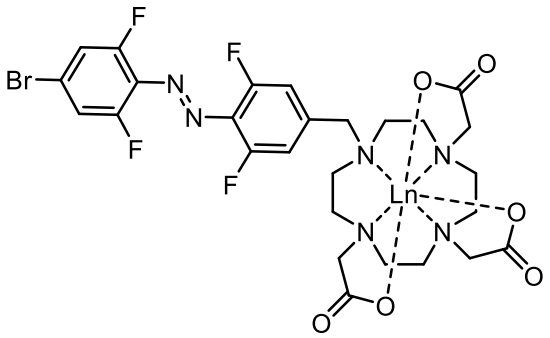


2.L$_b$ in a quantitative yield. **^{1}H NMR** (600 MHz, D_2O) δ 7.43 (d, *J* = 10.6 Hz, 4H, Aromatic Protons), 4.00 – 2.85 (m, 54H, cyclen protons) ppm. **^{13}C NMR** (151 MHz, D_2O) δ 174.5, 169.3, 163.2, 163.0, 156.0, 154.3, 153.5 151.9, 130.3, 117.5, 115.5, 115.2, 115.1, 114.5, 113.8, 56.5, 56.3, 55.5, 53.7, 51.5, 50.7, 49.0, 48.3, 47.9, 27.6, 27.4, 25.3 ppm. **^{19}F NMR** (565 MHz, D_2O) δ -119.92 ppm. **HR-ESI-MS** obsd 971.4246, calcd 971.4245 $[(M + H)^+$, M = $C_{42}H_{58}F_4N_{10}O_{12}]$

7.2.1.5 General Procedure for Lanthanide Coordination

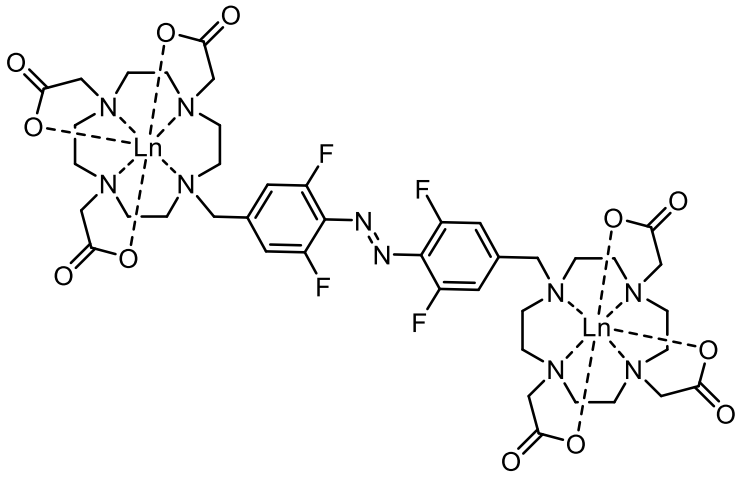
The ligands and $Ln(OTf)_3$ (1.25 eq. (mono), 2.5 eq. (bis)) were added to a HPLC vial and dissolved EtOH:Water (1:1) solution. The vial was sealed, heated to 50 °C and left to stir overnight. To this NaOH (3.5 eq. (mono), 7.0 eq. (bis)) was added portion wise over the next

three hours. The vial was then sealed again and left for 2 days. The precipitate was collected, purified by dialysis and dried to yield an orange solid (quant.) in an orange precipitate forming.



2.EuL$_a$ HR-ESI-MS obsd 841.0453 , calcd 841.0475 [(M + H)$^+$, M = $C_{27}H_{29}BrF_4N_6O_6Eu$]

2.NdL$_a$ HR-ESI-MS obsd 831.0378 , calcd 831.0418 [(M + H)$^+$, M = $C_{27}H_{29}BrF_4N_6O_6Nd$]



2.Eu$_2$L$_b$ HR-ESI-MS obsd 1271.2263 , calcd 1271.2200 [(M + H)$^+$, M = $C_{42}H_{53}F_4N_{10}O_{12}Eu_2$]

2.Nd$_2$L$_b$ HR-ESI-MS obsd 1249.1957 , calcd 1249.1930 [(M + H)$^+$, M = $C_{42}H_{53}F_4N_{10}O_{12}Nd_2$]

7.2.2 Photoswitching experiments

Photo-irradiation of liquid samples was carried out using Thorlabs high-power mounted LEDs; M530L4 (green, 530 nm) and M405L4 (purple, 405 nm) within an in-house custom built set-ups using optical components supplied by Thorlabs.[320] All UV-vis spectra were determined in DMSO. All measurements were performed at room temperature, unless otherwise stated, in a

10 mm quartz cuvette from Starna Scientific (23/Q /10) or Hellma Analytics (SUPRASIL). Electron absorption measurements were recorded on a Jasco V-770 UV-Visible/NIR spectrophotometer operated under Spectra ManagerTM suite. Points were recorded at 0.2 nm interval with UV/Vis bandwidth of 1 nm, UV/Vis response of 0.06 sec in continuous scan mode at the rate of 400 nm/min. For each compound, the *E* isomer sample at 40 μM was irradiated with the appropriate wavelength of light to generate the photo-stationary state, and another spectrum was run, this was repeated until the PSS had been reached. This was repeated for the *Z* isomer.

The photo-stationary states upon irradiation with 405 and 530 nm were determined by HPLC. Each sample was irradiated with either 405 or 530 nm light for 10 minutes. The isosbestic point for each complex was determined from absorbance measurements and found to be at 377 nm. The HPLC spectra were recorded, monitoring the absorbance at 377 nm for each sample. The areas under the peaks integrated to give the relative ratios of each isomer at the PSS. Using the determined ratios after irradiation with both 405 and 530 nm light and the corresponding absorbance spectra, the absorbance of 100% *E*/*Z* was calculated.

$$PSS_E = a[E] + b[Z]$$

$$PSS_Z = c[E] + d[Z]$$

a = percentage of *E* at PSS_E , b = percentage of *Z* at PSS_E , c = percentage of *E* at PSS_z , d = percentage of *Z* at PSS_z.

To calculate the degree of isomerisation upon irradiation to excite the lanthanide the following equation was used:

$$ID = \frac{Abs_{Ex} - Abs_{PSS}}{Abs_{PSS}} \times 100$$

Where ID = Degree of isomerisation (%) Abs_{Ex} = Absorption after excitation of lanthanide, Abs_{PSS} = Abs at PSS (405 or 530 nm). This was calculated at the maximum absorbance wavelength of the n $\rightarrow\pi^*$ transition for both isomers. Once calculated this was compared with the original distribution of isomers in each PSS to give the new isomer distribution.

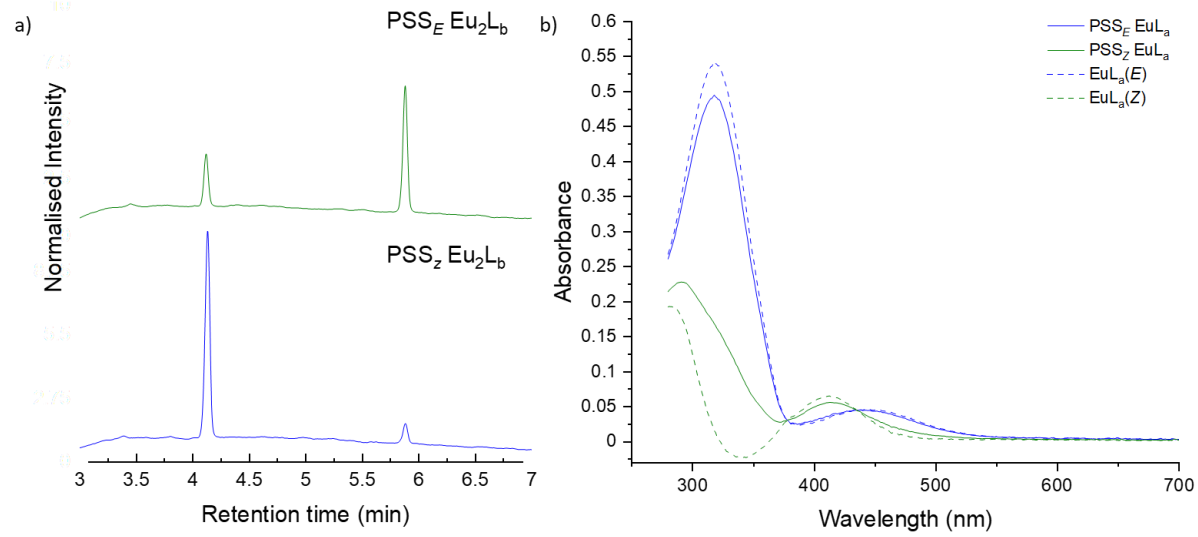


*Figure 7.1: PSS determination for **2.Eu$_2$L$_b$** a) HPLC trace using method 1, PSS$_Z$ (green), PSS$_E$ (blue) b) Absorbance, PSS$_E$ (blue), PSS$_Z$ (green), theoretical spectra for 100% E (dashed blue) and Z (dashed green) isomers.*

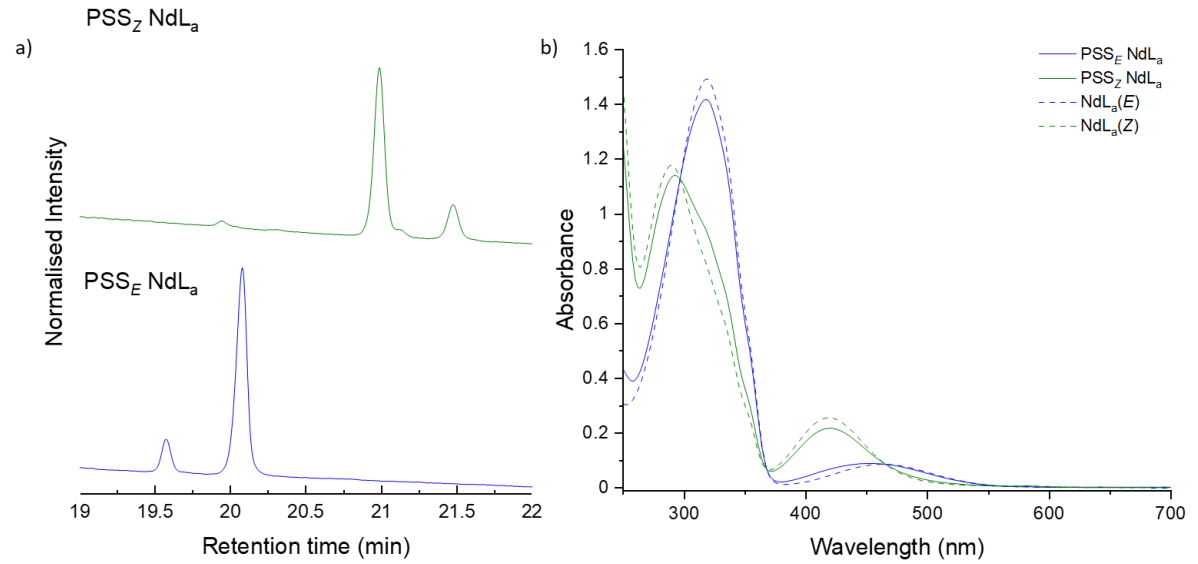


*Figure 7.2 PSS determination for **2.NdL$_a$** a) HPLC trace using method 1, PSS$_Z$ (green), PSS$_E$ (blue) b) Absorbance, PSS$_E$ (blue), PSS$_Z$ (green), theoretical spectra for 100% E (dashed blue) and Z (dashed green) isomers.*

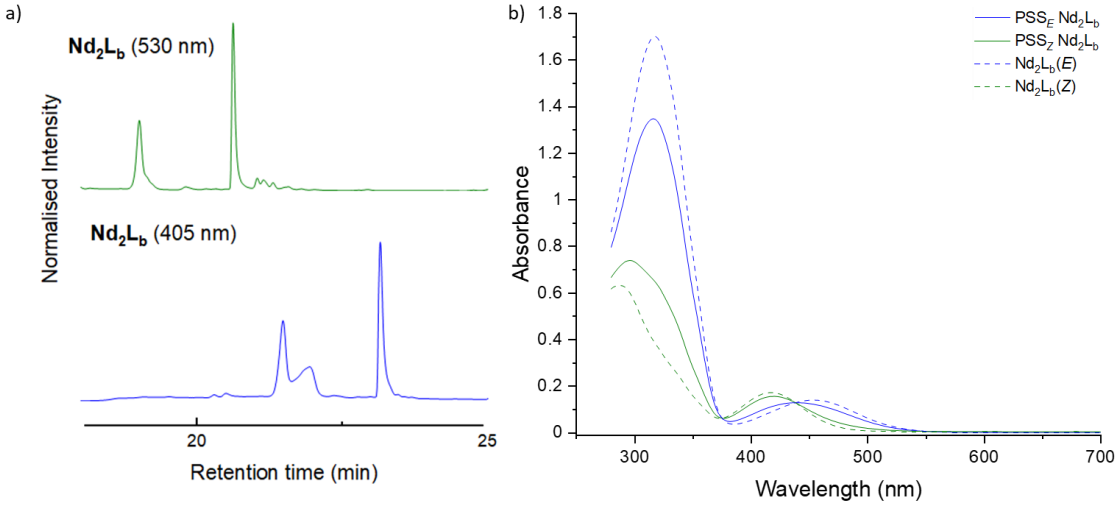


Figure 7.3: PSS determination for ***2.Nd₂L_b*** *a) HPLC trace using method 1, PSS$_Z$ (green), PSS$_E$ (blue) b) Absorbance, PSS$_E$ (blue), PSS$_Z$ (green), theoretical spectra for 100% E (dashed blue) and Z (dashed green) isomers.*

7.2.3 Optical Spectroscopy

Luminescent spectra for Ligands **2.L$_a$** and **2.L$_b$**. For each ligand the emission spectra were recorded upon excitation into both the $\pi \rightarrow \pi^*$ and the $n \rightarrow \pi^*$ transition for each isomer. Absorbance spectra were recorded before and after excitation into each transition, to determine changes in the PSS distribution of isomers.

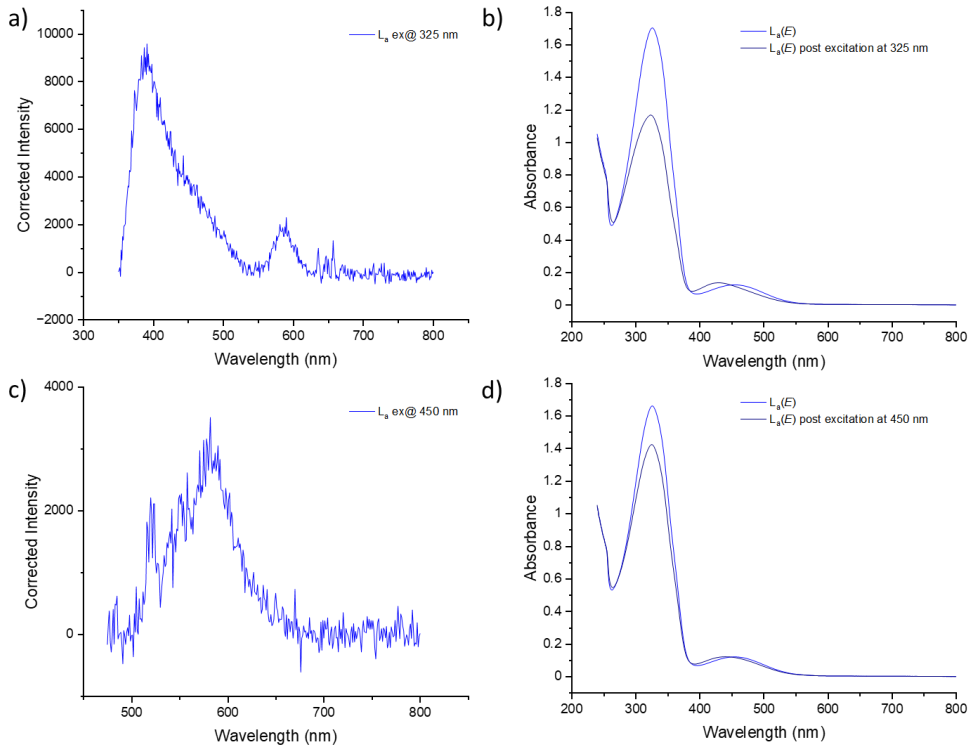


Figure 7.4: Optical spectroscopy of ***2.L$_a$ (E)*** *a) emission upon excitation into the π→π* transition at 325 nm b) Absorbance PSS$_E$ (blue) prior to excitation at 325 nm (navy line) c) emission upon excitation into the n→π* at 450 nm d) Absorbance PSS$_E$ (blue) prior to excitation at 450 nm (navy line). Excitation slit at 5 nm, emission slit at 1 nm, integration time 0.1.*

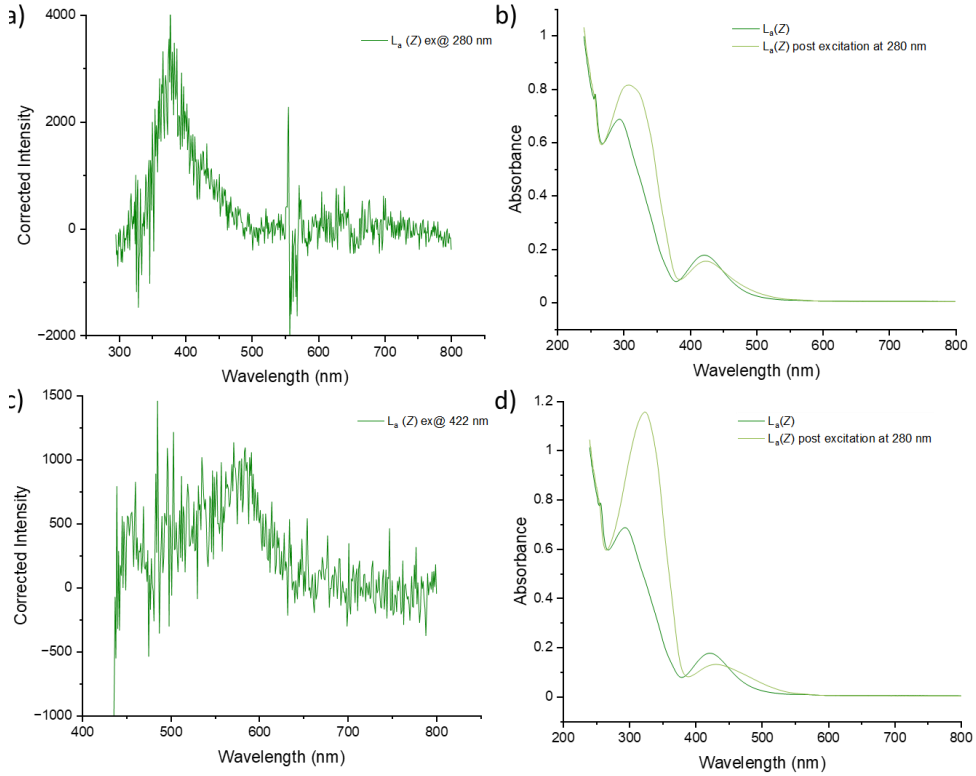


Figure 7.5: Optical spectroscopy of ***2.L$_a$ (Z)*** *a) emission upon excitation into the π→π* transition at 280 nm b) Absorbance PSS$_Z$ (green) prior to excitation at 280 nm (dark green line) c) emission upon excitation into the n→π* at 422 nm d) Absorbance PSS$_z$ (green) prior to excitation at 422 nm (dark green line). Excitation slit at 5 nm, emission slit at 1 nm, integration time 0.1.*

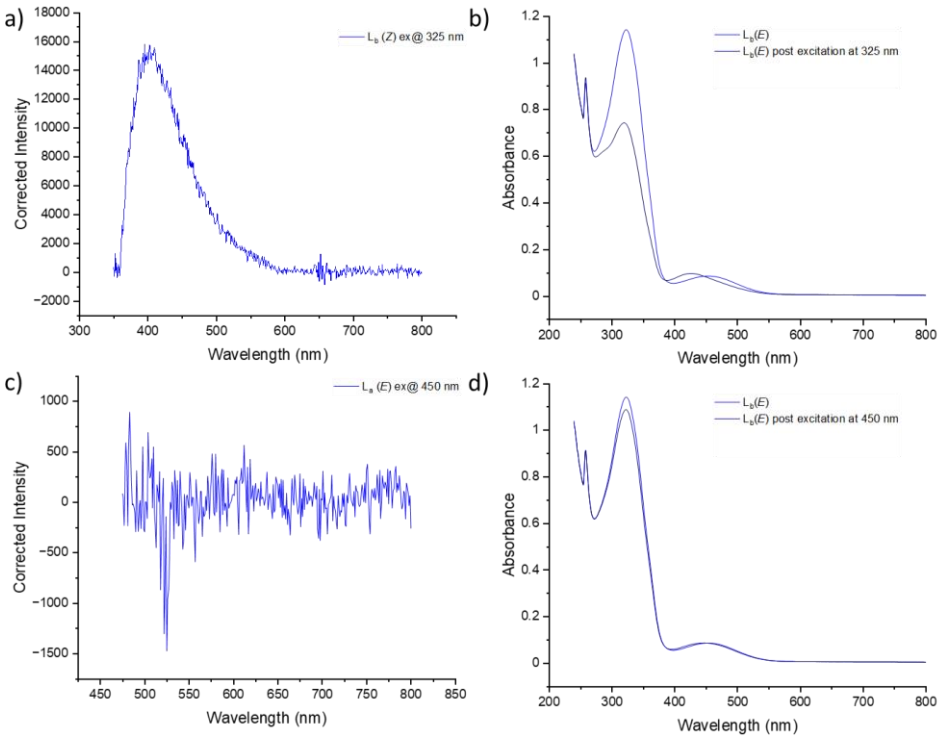


Figure 7.6: Optical spectroscopy of ***2.L$_b$ (E)*** *a) emission upon excitation into the π→π* transition at 325 nm b) Absorbance PSS$_E$ (blue) prior to excitation at 325 nm (navy line) c) emission upon excitation into the n→π* at 450 nm d) Absorbance PSS$_E$ (blue) prior to excitation at 450 nm (navy line). Excitation slit at 5 nm, emission slit at 1 nm, integration time 0.1.*

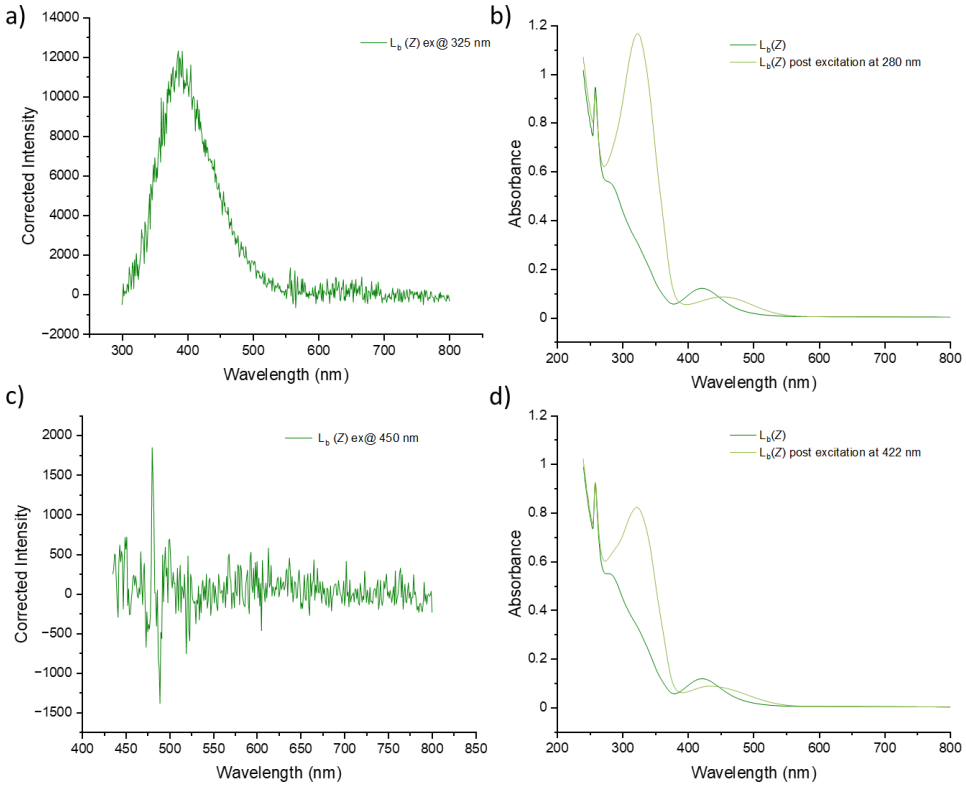


Figure 7.7: Optical spectroscopy of ***2.L$_a$ (Z)*** *a) emission upon excitation into the π→π* transition at 280 nm b) Absorbance PSS$_Z$ (green) prior to excitation at 280 nm (dark green line) c) emission upon excitation into the n→π* at 422 nm d) Absorbance PSS$_z$ (green) prior to excitation at 422 nm (dark green line). Excitation slit at 5 nm, emission slit at 1 nm, integration time 0.1.*

7.2.3.1 Time-Resolved Luminescence Spectroscopy

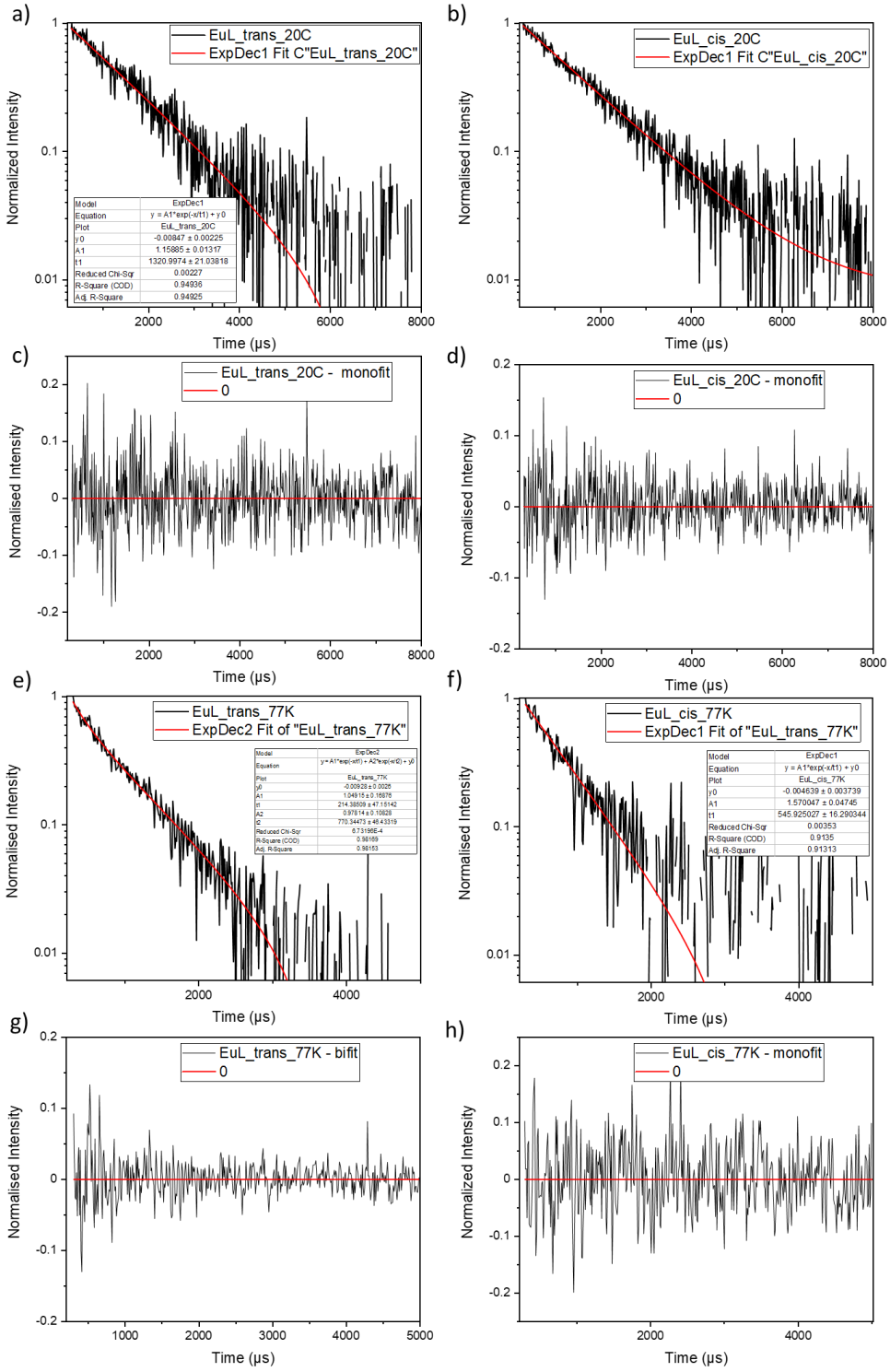


Figure 7.8: Time resolved luminescence decay a) EuL$_a$(E) at 298 (black line), mono-exponential fit (red line) b) EuL$_a$(Z) at 298 K (black line), mono-exponential fit (red line) c)difference plot of mono exponential decay fits determined as the difference from the raw data for EuL$_a$(E) at 298 K d) difference plot of mono exponential decay fits determined as the difference from the raw data for EuL$_a$(Z) at 298 K e) EuL$_a$(E) at 77 K (black line), mono-exponential fit (red line) f) EuL$_a$(Z) at 77K (black line), mono-exponential fit (red line) g)difference plot of mono exponential decay fits determined as the difference from the raw data for EuL$_a$(E) at 77 K h) difference plot of biexponential decay fits determined as the difference from the raw data for EuL$_a$(Z) at 77 K. λ_{ex} = 395 nm, λ_{em} = 616 nm, emission slit = 5 nm, excitation slit = 5 nm, delay time = 10 ms.

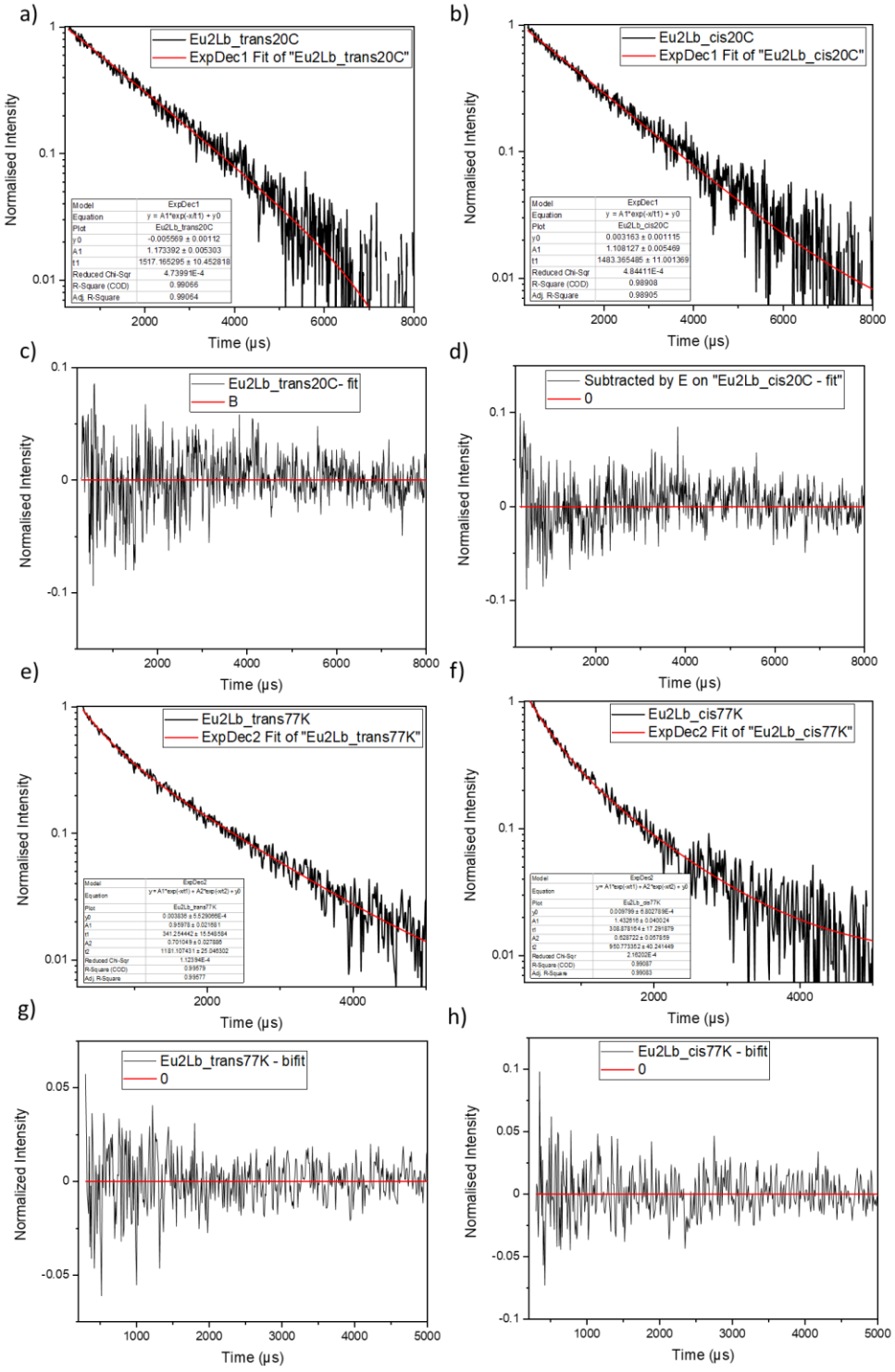


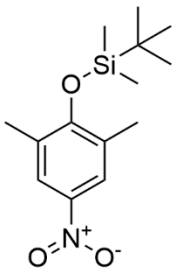
Figure 7.9: Time resolved luminescence decay a) Eu_2L_b(E) at 298 K (black line), mono-exponential fit (red line) b) Eu_2L_b (Z) at 298 K (black line), mono-exponential fit (red line) c) difference plot of mono exponential decay fits determined as the difference from the raw data for Eu_2L_b(E) at 298 K d) difference plot of mono exponential decay fits determined as the difference from the raw data for Eu_2L_b (Z) at 298 K e) Eu_2L_b(E) at 77 K (black line), mono-exponential fit (red line) f) Eu_2L_b(Z) at 77K (black line), biexponential fit (red line) g)difference plot of mono exponential decay fits determined as the difference from the raw data for Eu_2L_b (E) at 77 K h) difference plot of biexponential decay fits determined as the difference from the raw data for Eu_2L_b (Z) at 77 K. λ_{ex} = 395 nm, λ_{em} = 616 nm, emission slit = 5 nm, excitation slit = 5 nm, delay time = 10 ms.

7.3 Experimental for Chapter 3

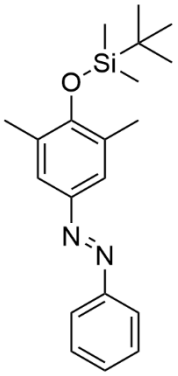
7.3.1 Synthesis and Characterisation

7.3.1.1 General Procedure for TBS Protection

The appropriate phenol (4-iodo-2,6-dimethylphenol, **2a** or **3a**) (1.00 eqv.) and imidazole (4.00 eqv.) were dissolved in DMF (c_{phenol} = 0.7 M), to this TBS-Cl (2.00 eqv.) was added and the reaction mixture was left to stir for 24 hours. The reaction mixture was diluted with Et_2O and washed with brine: H_2O (1:1 mixture, minimum 5 times the volume of DMF used in the reaction) and extracted with Et_2O. After the first extraction the organic phase was further washed with brine. The organic phase was dried over $MgSO_4$, filtered and concentrated under reduced pressure. The crude product was then purified by silica gel flash column chromatography and eluted with petroleum ether: Et_2O (100:0 → 95:5) to obtain the pure product.



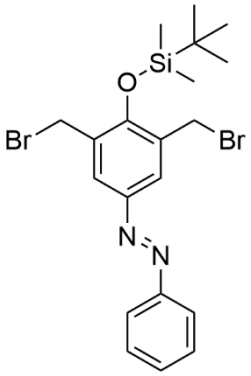
1b. Yield: 6.45 g (96%); R_f = 0.60 (95:5 Pentane/Et_2O); **^{1}H NMR** (400 MHz, $CDCl_3$) δ 7.90 (s, 2H), 2.28 (s, 6H), 1.03 (s, 9H), 0.24 (s, 6H); **^{13}C NMR** (101 MHz, $CDCl_3$) δ 158.4, 141.6, 129.8, 124.5, 26.1, 19.0, 18.1, -2.6; **HR-ESI-MS** obsd 282.1521, calcd 282.1520 [$(M + H)^+$, M = $C_{14}H_{23}NO_3Si$].



2b. Yield: 5.21 g (90%); column conditions: Hexane/EtOAc (98:2); **^{1}H NMR** (600 MHz, $CDCl_3$) δ 7.88 – 7.84 (m, 2H), 7.61 (s, 2H), 7.52 – 7.41 (m, 3H), 2.31 (s, 6H), 1.05 (s, 9H), 0.24 (s, 6H). **^{13}C NMR** (151 MHz, $CDCl_3$) δ 155.5, 153.0, 147.1, 130.4, 129.5, 129.2, 123.8, 122.7, 26.2, 19.0, 18.10, -2.7. **HR-ESI-MS** obsd 341.2044, calcd 341.2044 [$(M + H)^+$, M = $C_{20}H_{28}N_2OSi$].

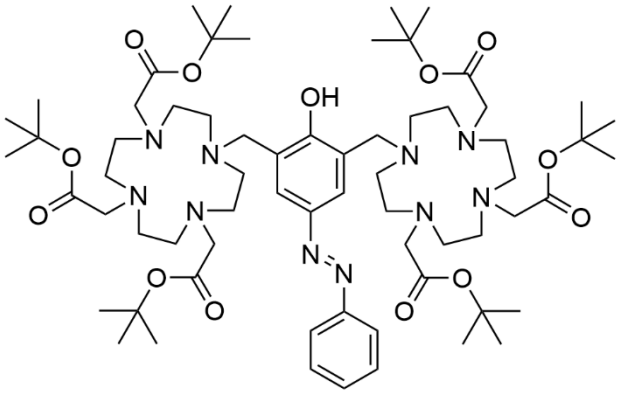
7.3.1.2 General Procedure for Radical Dibromination

The appropriate TBS-protected dimethyl phenol (1.00 eqv.) was dissolved in CCl_4 ($c_{s.m.}$ = 0.1 M) followed by the addition of NBS (2.10 eqv.)). To this benzoyl peroxide was added (0.05 eqv.). The reaction mixture was heated to reflux and left to stir for a minimum of 3 hours. The resulting suspension was left to cool to room temperature and filtered. The filtrate was concentrated under reduced pressure and the crude mixture was then purified by silica gel flash column chromatography and eluted with pentane: Et_2O (100:0 → 99:1 → 98:2 → 97:3 → 96:4 → 95:5 → 90:10 for **1c**) or pentane (isocratic method for **2c** and **3c**) resulted the pure product.



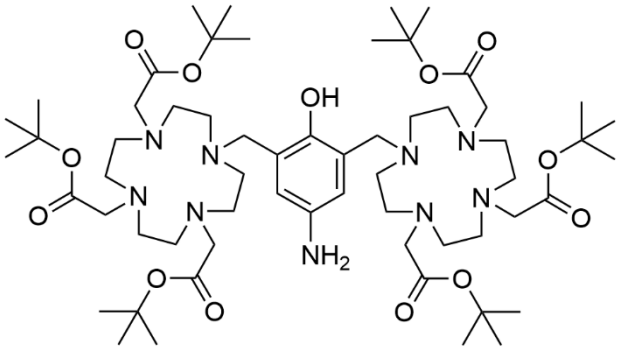
2c. Yield: 1.43 g (42%); R_f = 0.25 (pentane, isocratic); **^{1}H NMR** (600 MHz, $CDCl_3$) δ δ 7.99 (2H) 7.90 – 7.89 (d, 2H), 7.53 – 7.48 (m, 2H), 7.47 – 7.46 (m, 1H), 4.58 (s, 4H), 1.11 (s, 9H), 0.34 (s, 6H). ^{13}C NMR (151 MHz, $CDCl_3$) δ 153.5, 152.7, 147.4, 131.1, 130.2, 129.3, 126.8, 122.9, 34.3, 28.8, 26.2, 22.5, 19.1, 14.2, -3.1. **HR-ESI-MS** obsd 497.0253, calcd 497.0254 [(M + H)$^+$, M = $C_{20}H_{27}Br_2N_2OSi$].

7.3.1.3 Procedures for the Protected Macrocycles



3e. DO3A^{t}Bu.HBr (602 mg, 1.01 mmol, 1.80 eqv) was dissolved in MeCN (14 mL) followed by the addition of Na_2CO_3 (215 mg, 2.02 mmol, 3.60 eqv). To this **3c** (280 mg, 0.56 mmol, 1.00 eqv) was added and the reaction mixture was heated at 60°C for 2 days. The resulting suspension was filtered, and the filtrate concentrated under reduced pressure. The dark red coloured residue was redissolved in a minimum amount of DCM:MeCN (8:2) mixture, then purified by silica gel flash column chromatography and eluted with CH_2Cl_2:MeCN:^{i}PrOH:MeOH (80:20:0:0 → 60:40:0:0 → 60:38:2:0 → 60:30:10:0 →

60:20:20:0 → 60:20:15:5 → 60:20:10:10 → 60:20:0:20 → 60:0:0:40) to obtain the product. The product was redissolved in $CHCl_3$ and was filtered through a membrane filter (Nylon, 0.45 µm pore size) and evaporated to dryness to afford the pure product as a dark orange/red solid. Yield: 435 mg (77%); R_f = 0.20 & 0.30 (60:28:8:4 DCM/MeCN/^{i}PrOH/MeOH); **^{1}H NMR** (400 MHz, $CDCl_3$) δ ppm 8.99 (br, 1H), 8.12 (s, 2H), 7.78 (m, 2H), 7.39 (m, 3H), 4.75–1.67 (m, 48H), 1.66–0.87 (m, 54H); **^{13}C NMR** (101 MHz, $CDCl_3$) δ ppm 173.3, 172.6, 172.1, 170.6, 157.2, 152.7, 147.4, 130.6, 128.8, 126.2, 122.6, 121.9, 82.7, 82.5, 82.4, 56.4, 56.0, 55.8, 55.4, 54.6, 52.5, 51.4, 50.4, 58.0–47.0, 28.3, 28.1, 28.0; **HR-ESI-MS** obsd 1251.8360, calcd 1251.8327 [$(M + H)^+$, M = $C_{66}H_{110}N_{10}O_{13}$].

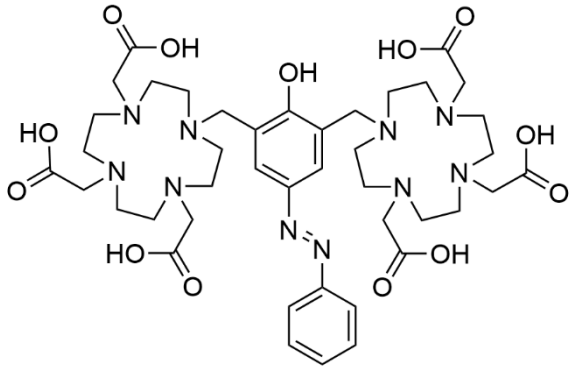


5e. 3e (365 mg, 0.31 mmol) was dissolved in EtOH (5 mL) to this 10% Pd on carbon (55-65% wet, 109 mg, 30 m/m%) was added. The mixture was placed under hydrogen atmosphere and the reaction was left to run at room temperature for 5 days, balloons replaced after 2 days. The resulting suspension was filtered through a pad of Celite and concentrated under reduced pressure. The crude mixture was then purified by silica gel flash column chromatography and eluted with DCM:MeOH (100:0 → 98:2 → 96:4 → 94:6 → 92:8 → 90:10 → 85:15 → 80:20 → 75:25) to obtain the pure product as a brown solid. Yield: 264 mg (74%); R_f = 0.24 (90:10 CH_2Cl_2/MeOH); **^{1}H NMR** (400 MHz, DMSO-d_6) δ ppm 10.24 (s, 1H), 6.55–6.15 (m, 2H), 4.38 (s, 2H), 3.77–1.84 (m, 48H), 1.52–1.34 (m, 54H); **^{13}C NMR** (151 MHz, $CDCl_3$) δ ppm 173.4, 171.9, 107.6, 169.7, 145.1, 141.7, 131.0, 117.9, 82.3, 82.2, 58.2, 57.7–55.8, 55.3, 53.9–

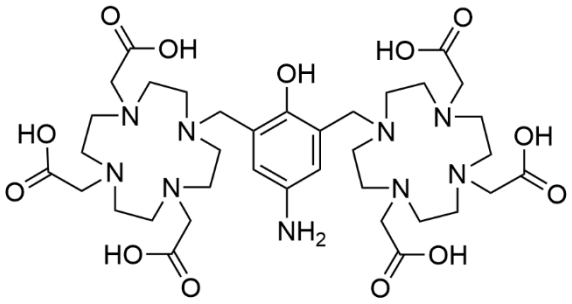
47.0, 31.0, 28.6–27.8; **HR-ESI-MS** obsd 1162.8081, calcd 1162.8061 [$(M + H)^+$, M = $C_{60}H_{107}N_9O_{13}$].

7.3.1.4 General Procedure for *Tert*-butyl Ester Deprotection

The *tert*-butyl ester protected ligand (1 eqv.) was dissolved in DCM and then TFA was added dropwise (1:1, c = 0.045 M). The reaction mixture was left to stir at room temperature for 18 hours. The reaction mixture was concentrated under reduced pressure and the crude product redissolved in a minimum amount of MeOH (1 volume), this was added dropwise to Et_2O (12 volumes in a falcon tube) and a precipitate formed. The resulting suspension was centrifuged, and the supernatant was decanted. The remaining solid was redissolved in a minimal amount of MeOH. The precipitation-centrifugation procedure was repeated twice more (overall 3 times). The resulting solids were dried to obtain the pure products.



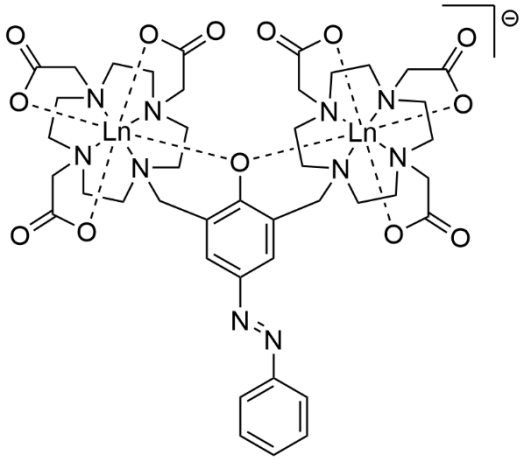
2f. Yield: 293 mg (96%); **^{1}H NMR** (400 MHz, D_2O) δ ppm 8.09 (m, 2H), 7.89 (m, 2H), 7.59 (m, 3H), 4.58–2.48 (m, 48H); **^{13}C NMR** (151 MHz, D_2O) δ ppm 176.8, 175.0, 170.4. 170.1, 169.1, 176.0–169.0, 157.9, 152.5, 146.4, 132.3, 130.2, 123.2, 57.5–47.0, 46.5, 42.9, 41.8. **HR-ESI-MS** obsd 915.4600, calcd 915.4571 [$(M + H)^+$, M = $C_{42}H_{62}N_{10}O_{13}$].



4f. Yield: 124 mg (quant.); **^{1}H NMR** (400 MHz, D_2O) δ ppm 7.56 (s, 2H), 4.53–2.51 (m, 48H); **^{13}C NMR** (151 MHz, D_2O) δ ppm 176.5–169.0, 154.3, 129.4–126.3, 124.1, 57.8–53.4, 53.4–46.1, 43.0. **HR-ESI-MS** obsd 826.4309, calcd 826.4305 [$(M + H)^+$, M = $C_{36}H_{59}N_9O_{13}$].

7.3.1.5 General Procedure for Obtaining the Binuclear Complexes

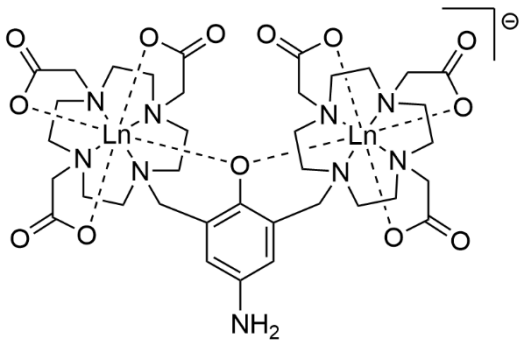
The appropriate ligand (1 eqv.) and the corresponding Ln-triflate (2.4 eqv.) were dissolved in H_2O (c_{ligand} = 0.05M). The reaction mixture was heated to 50 °C and left to stir for 1 day. To this NaOH (1M aqueous solution) was added in portions (3 + 3 + 1(or 2) eqv.) and left to stir at 50 °C for further 2 days. The resulting solution was purified by dialysis (FLOAT-A-LYZER G2 500-1000D CE) for 3 days to remove inorganic contaminants. After the dialysis was complete, the complex solution was concentrated and dried under high vacuum.



2·Eu$_2$. Yield: 35 mg (75%); t_R = 15.31, 15.54 min (CN col., 0.1% HCOOH); **HR-ESI-MS** obsd 1215.2495, calcd 1215.2526 [$(M + H)^+$, M = $C_{42}H_{57}N_{10}O_{13}Eu_2$].

2·Tb$_2$.Yield: 52 mg (81%); t_R = 15.21, 15.59 min (CN col., 0.1% HCOOH); **HR-ESI-MS** obsd 1227.2560, calcd 1227.2608 [(M + H)$^+$, M = $C_{42}H_{57}N_{10}O_{13}Tb_2$].

2·Gd$_2$.Yield: 31 mg (68%); t_R = 15.23, 15.50 min (CN col., 0.1% HCOOH); **HR-ESI-MS** obsd 1225.2581, calcd 1225.2583 [(M + H)$^+$, M = $C_{42}H_{57}N_{10}O_{13}Gd_2$].



4·Eu$_2$. Yield: 35 mg (quant.); t_R= 4.33 min (CN col., 0.1% HCOOH); **HR-ESI-MS** obsd 1124.2194, calcd 1124.2247 [(M + H)$^+$, M = $C_{36}H_{53}N_9O_{13}Eu_2$].

4·Tb$_2$. Yield: 71 mg (quant.); t_R= 4.24 min (CN col., 0.1% HCOOH); **HR-ESI-MS** obsd 1138.2320, calcd 1138.2343 [(M + H)$^+$, M = $C_{36}H_{53}N_9O_{13}Tb_2$].

4·Gd$_2$. Yield: 29 mg (quant.); t_R= 4.28 min (CN col., 0.1% HCOOH); **HR-ESI-MS** obsd 1136.2304, calcd 1136.2318 [(M + H)$^+$, M = $C_{36}H_{53}N_9O_{13}Gd_2$].

7.3.2 X-ray Crystal Structures

Single crystal X-ray structure reported in this work was obtained by Dr Daniel Kovacs, using the vapour diffusion method. The sample were dissolved in a minimal amount of water and acetone was used as an antisolvent.

Low temperature single crystal X-ray diffraction data were collected using a (Rigaku) Oxford Diffraction SuperNova diffractometer, measured by Kirsten Christiansen. Raw frame data were reduced using CrysAlisPro and the structure was solved using 'Superflip' [L. Palatinus and G. Chapuis, J. Appl. Cryst., 2007, 40, 786-790.] before refinement with CRYSTALS [(a) P. Parois, R.I. Cooper and A.L. Thompson, Chem. Cent. J., 2015, 9:30. (b) R.I. Cooper, A.L. Thompson and D.J. Watkin, J. Appl. Cryst. 2010, 43, 1100-1107.] as per the SI (CIF). Crystallographic data have been deposited with the Cambridge Crystallographic Data Centre (CCDC 2370191) and copies of these data can be obtained free of charge via www.ccdc.cam.ac.uk/data_request/cif.

Crystal system / Space group	Monoclinic /	C 2/c
Unit cell dimensions	a = 36.7160(3) Å	α= 90°.
	b = 16.52100(10) Å	β= 101.0464(9)°.
	c = 17.7958(2) Å	γ = 90°.
Volume	10594.67(16) Å^3	
Z	4	
Crystal size	0.25 x 0.07 x 0.05 mm^3	
Temperature	150 K	
Wavelength	1.54184 Å	
Independent reflections	11102 [R(int) = 0.059]	
Data / restraints / parameters	11096 / 0 / 614	
Goodness-of-fit on F^2	0.9335	
Final R indices [I>2sigma(I)]	R1 = 0.0893, wR2 = 0.2262	
R indices (all data)	R1 = 0.0910, wR2 = 0.2317	

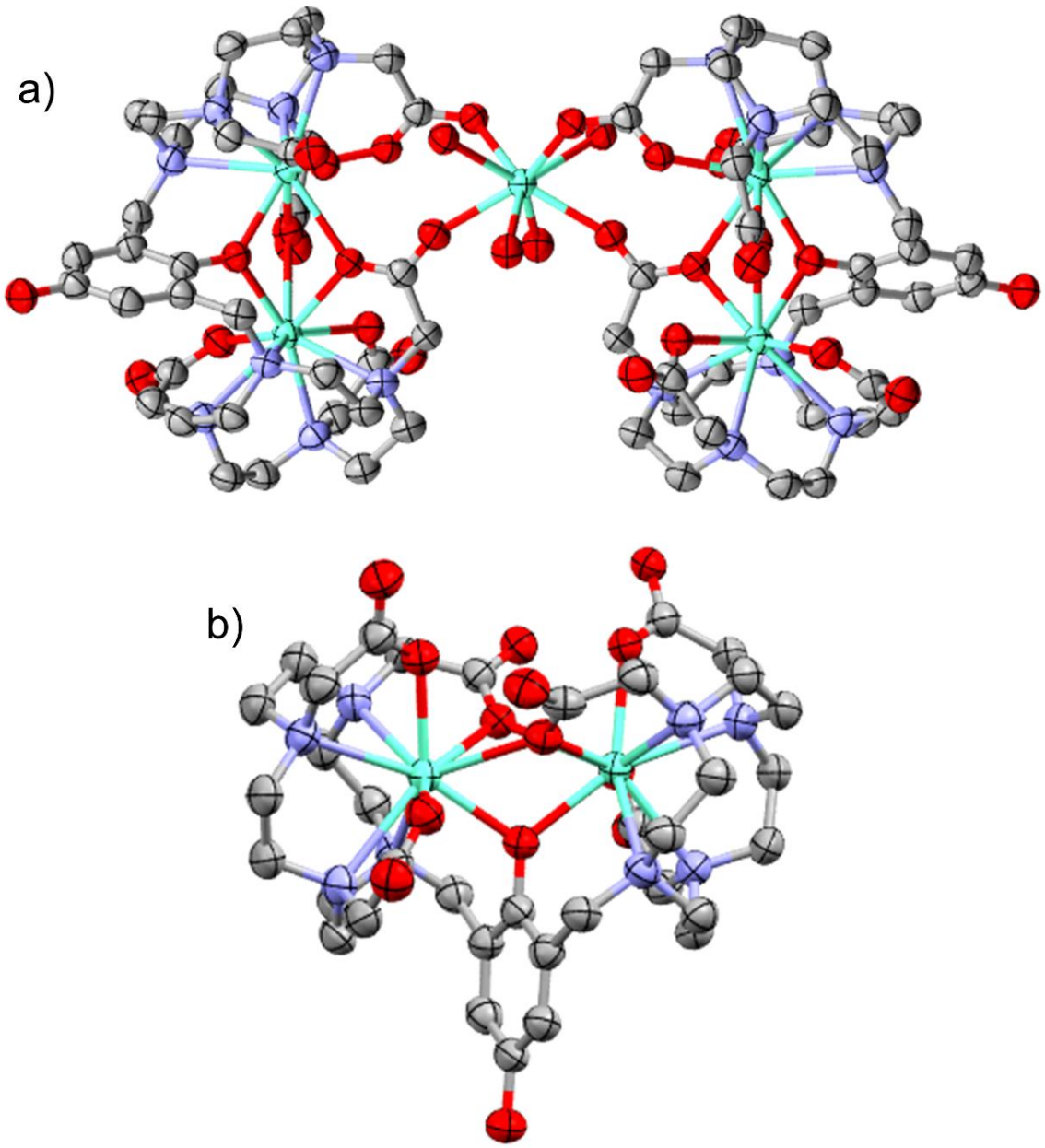


*Figure 7.10; Thermal displacement ellipsoid drawing (50% probability) of a) the full structure of the [[**5·Eu₂**]₂[Eu(H₂O)₄]]⁻ anion, which co-crystallises with a hydrated Na^+ cation (not shown) and b) **5·Eu₂**. All H atoms (excluding OH protons) and non-coordinated solvent molecules have been omitted for clarity. Grown by Dr Daniel Kovacs.*

Table 7. 1: Experimental metrical parameters (bond lengths in Å and angles in °) in ***5·Eu₂****.*

Eu(1)-Eu(31)	3.7698(5)
Eu(1)-O(22)	2.376(5)
Eu(1)-O(48)	2.629(5)
Eu(1)-O(56)	2.345(4)
Eu(1)-O(56)-Eu(31)	107.7(2)
Eu(1)-O(48)-Eu(31)	97.9(2)
Eu(1)-O(22)-Eu(31)	99.3(2)
Eu(1)-O(14)	2.394(5)
Eu(1)-O(18)	2.318(5)
Eu(1)-O(56)	1.7141(9)
Eu(1)-N(11)	2.785(5)
Eu(1)-N(5)	2.648(5)
Eu(1)-N(2)	2.650(6)
Eu(1)-N(8)	2.718(6)
Eu(31)-O(56)	2.324(5)
Eu(31)-O(48)	2.364(5)
Eu(31)-O(22)	2.570(5)
Eu(31)-O(52)	2.385(6)
Eu(31)-O(44)	2.376(5)
Eu(31)-N(38)	2.651(5)
Eu(31)-N(35)	2.699(5)
Eu(31)-N(41)	2.765(6)
Eu(31)-N(32)	2.618(6)

7.3.3 Optical Spectroscopy

7.3.3.1 Steady State Luminescence

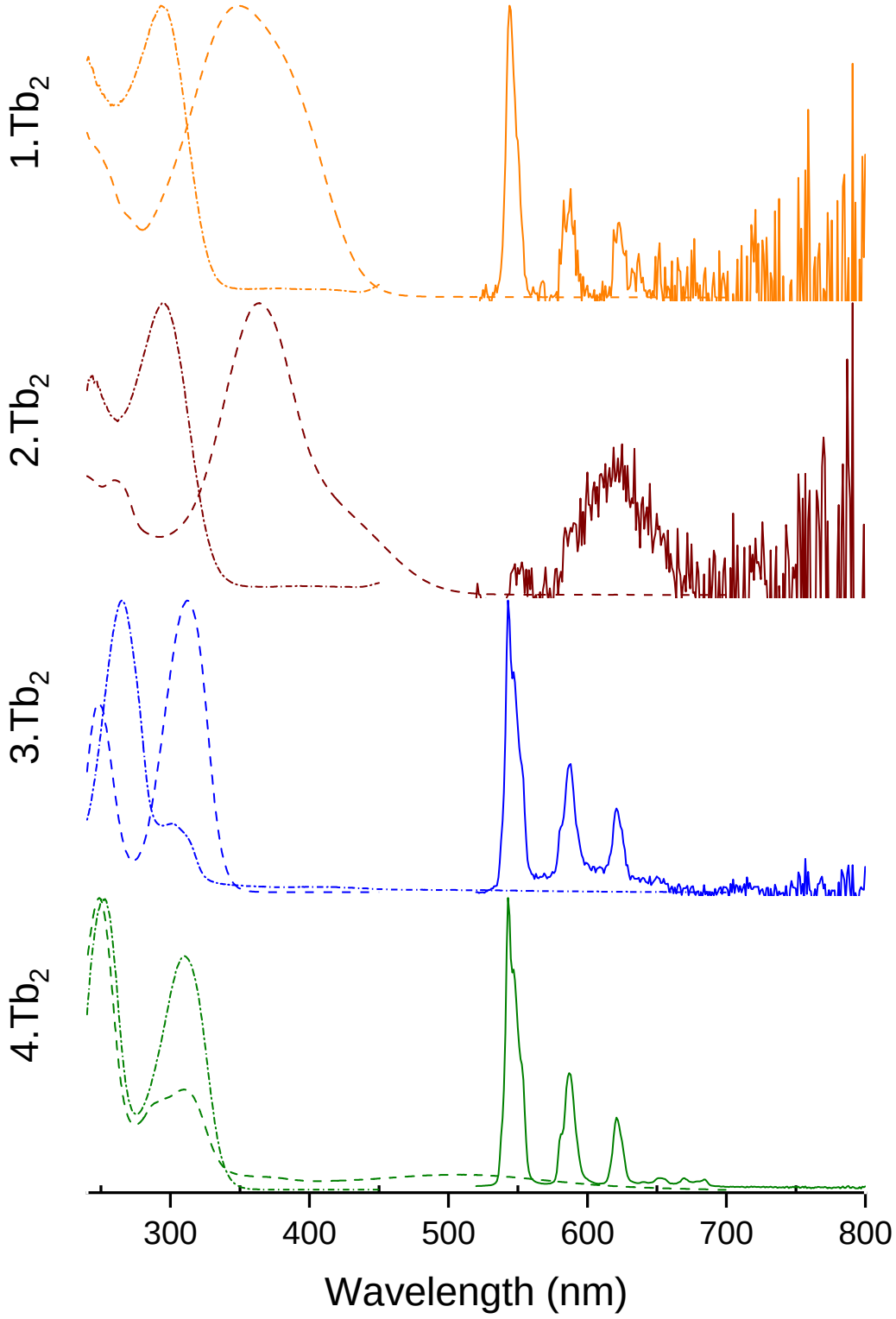


Figure 7.11: Comparison of photophysical properties of compounds ***1-4·Tb₂.*** *Complexes were measured at 90 µM in 10 mM PBS buffer at pH 7.4 at 90 µM in 10 mM PBS buffer at pH 7.4 where short dashed line represents the absorbance, dashed line represents the excitation (λ_{em} = 545 nm), and the solid line represents the emission (λ_{ex} = 488 nm).*

7.3.3.2 Luminescence Lifetimes

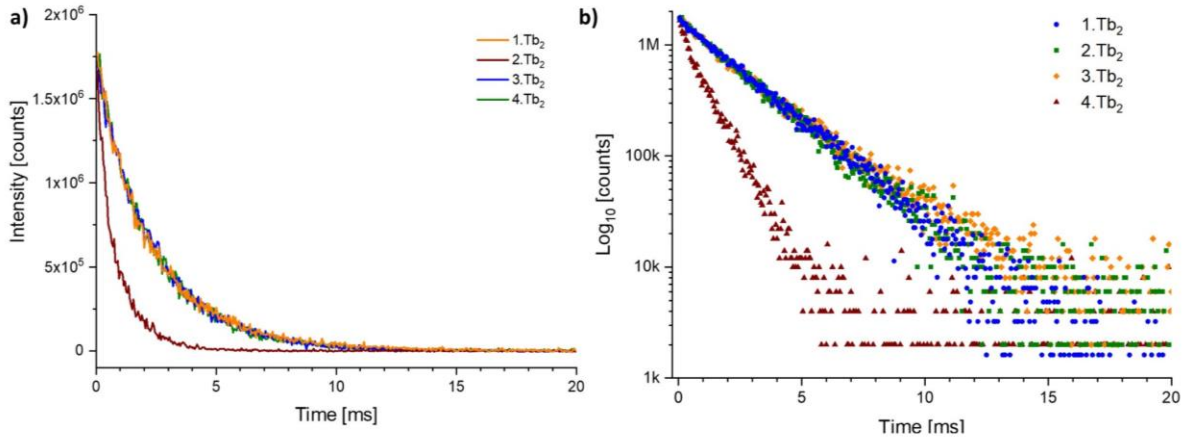


*Figure 7.12: a) Exponential decays of the complexes **3.1-4·Tb₂** b) Decay profile on log scale of the complexes **3.1-4·Tb₂**. Complexes were measured at 90 µM in 10 mM PBS buffer at pH 7.4 at 90 µM in 10 mM PBS buffer at pH 7.4 (orange – **3.1·Tb₂**, λ_{exc} = 294 nm, λ_{em} = 545 nm, Front slit: 29.00 nm, Exit slit: 14.50 nm, t_{int} = 0.1 s, Sample window = 0.50, Time per flash 61.00, FC = 12, time delay: 50 µs; maroon – **3.2·Tb₂**, λ_{exc} = 294 nm, λ_{em} = 545 nm, Front slit: 19.0 nm, Exit slit: 6.00 nm, t_{int} = 0.1 s, Sample window = 0.50, Time per flash 61.00, FC = 4, time delay: 50 µs; blue – **3.3·Tb₂**, λ_{exc} = 310 nm, λ_{em} = 545 nm, Front slit: 13.0 nm, Exit slit: 1.00 nm, t_{int} = 0.1 s, Sample window = 0.50, Time per flash 61.00, FC = 3, time delay: 50 µs; green – **3.4·Tb₂**, λ_{exc} = 294 nm, λ_{em} = 545 nm, Front slit: 29.00 nm, Exit slit: 2.00 nm, t_{int} = 0.1 s, Sample window = 0.50, Time per flash 61.00, FC = 4, time delay: 50 µs)*

7.3.3.3 Triplet Energies

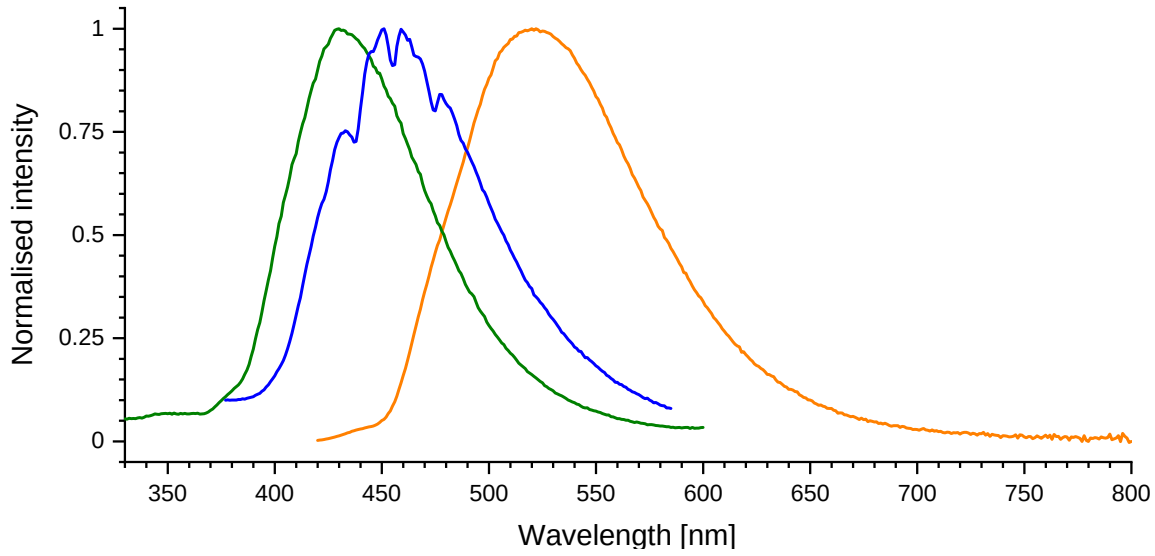


*Figure 7. 13: Normalised steady-state phosphorescence emission of the binuclear Gd complexes (orange – **3.1·Gd₂**, λ_{exc} = 320 nm, Front slit: 5.00 nm, Exit slit: 0.50 nm, t_{int} = 0.5 s , green – **3.3·Gd₂**,, λ_{exc} = 310 nm, Front slit: 3.00 nm, Exit slit: 1.00 nm, t_{int} = 0.2 s, blue – **3.4·Gd₂**,, λ_{exc} = 310 nm, Front slit: 3.00 nm, Exit slit: 1.00 nm, t_{int} = 0.5 s) at 77K measured in 10 mM PBS solution at pH 7.4, with 10% glycerol added. Complex concentrations were at 90 uM. **3.2·Gd₂**, could not be measured due to very low-lying excited states.*

7.3.4 Relaxivity

Relaxivity determination by magnetic resonance imaging (MRI) was conducted using an Agilent 7 T scanner equipped with a DirectDrive console and 400 mT/m imaging gradients (Varian, UK). The RF coil employed was a 72 mm i.d. birdcage resonator (Rapid Biomedical, Germany). T1 measurements were carried out using an inversion recovery spin-echo sequence with the following parameters: slice thickness of 1 mm, field of view (FoV) of 72 x 72 mm, matrix size of 128 x 128, four averages, TR/TE of 10 s/8 ms, and 12 inversion times (Ti) ranging from 0.01 to 6.0 seconds (exponentially spaced). T2 measurements were performed using a spin-echo sequence with the same single-slice sequence as the T_1 measurements: slice thickness of 1 mm, FoV of 72 x 72 mm, matrix size of 128 x 128, four averages, TR of 10 s, and 12 echo times (TE) ranging from 8 to 300 ms (exponentially spaced). All samples were placed in 1 ml syringes (Terumo) in a custom-made 3D-printed phantom holder enabling reproducible measurements. Acquired data was analysed using Matlab (version R2022a).

Note: **3.2·Gd$_2$** was not fully soluble in PBS.

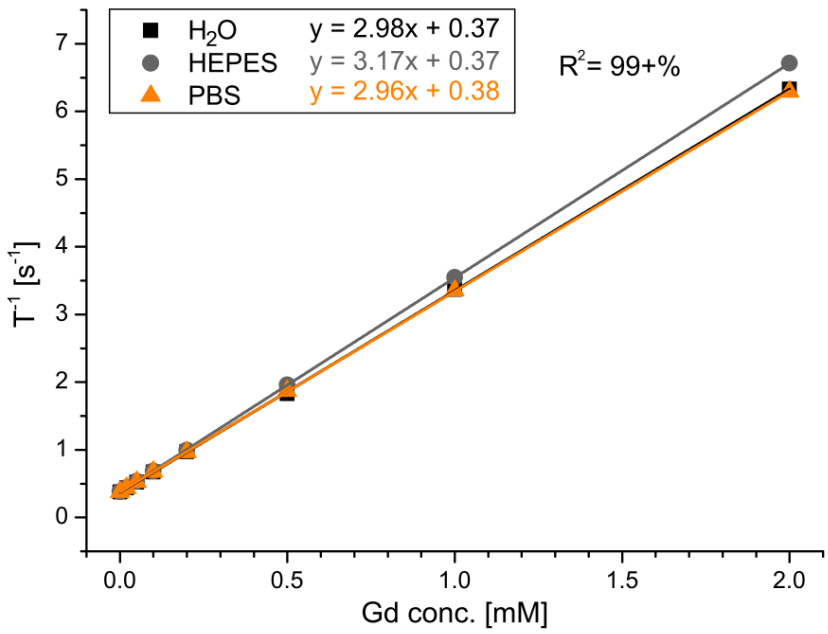


*Figure 7.14: Effect of buffer on T_1 relaxivities. Variation of $1/T_1$ with concentration of **1·Gd$_2$** dissolved in different buffers (at 20 °C, 7 T).*

7.3.5 Cyclic Voltammetry (CV)

CV's were measured in collaboration with the Vincent group, particularly Euan Sarson. The small-volume electrochemical cell consisted of a polyether ether ketone (PEEK) cylinder containing a working electrode of glassy carbon (1 mm diameter), a counter electrode of graphite, and a leak-free Ag/AgCl reference electrode (LF-2-45 model from Alvatek Ltd). The cell was set up under a N_2 atmosphere in a glove box (O_2 < 2 ppm), using 400 μL of a 1 mM solution of complex dissolved in degassed H_2O containing 50 mM Tris and 50 mM NaCl at pH 7.4 or 100 mM MES and 50 mM NaCl at pH 6.0. The air-tight electrochemical cell was then removed from the glove box and connected to an AutoLab 128 N potentiostat (Metrohm) controlled by Nova 2.1.7 software. Cyclic voltammograms were run with step potential = -0.00244 V and scan rate = 0.02 V/s, with 3 cycles recorded for each. The Ag/AgCl reference electrode was calibrated to vs SHE by measuring the cyclic voltammogram of FcMeOH (0.1 mM in 4:1 buffer:EtOH) and comparing to a literature $E_{1/2}$ value of +420 mV vs SHE for FcMeOH.[321] Cathodic onset potentials were calculated as follows: the first linear sweep of the voltammogram of the blank (buffer only) was subtracted from the first linear sweep of the voltammogram of the substrate; a linear baseline in a region of no electrochemical activity was extrapolated across the entire current range; the cathodic onset potential is taken as the potential at which the current in the baseline-corrected voltammogram begins to increase exponentially and exceeds a threshold value of 10 nA (instrument current resolution 0.0003% of current range). This procedure is adapted from a method used to define onset potentials for a range of nitro-compounds from the current at a rotating disk electrode which is typically higher in magnitude, and hence the data from a stationary electrode obtained here are not fully comparable to the earlier data set.[249, 260] A stationary electrode was used here due to the smaller sample requirement in the cell.

*Table 7. 2: Cathodic onset potentials vs SHE (V) of **3.1-3·Tb$_2$**.*

	Cathodic Onset Potential vs SHE / V	
	pH 7.4 (Tris)	**pH 6.0** (MES)
3.1·Tb$_2$	-0.413	-0.240
3.2·Tb$_2$	-0.394	-0.258
3.3·Tb$_2$	/	/

7.3.6 General Procedure for Reduction Assay (Plate Reader)

A Tecan infinite M1000 Pro Plate reader was used to investigate the chemical reduction of probes **3.1-4·Tb$_2$** in a 96 well plate. To each well 100 µl of sample was added. Varying concentrations of compound were added (0.01 M, 0.001 M and 0.0001 M) in MES buffer (0.1 M pH 6.0). To each sample 10 µl of 1 M Zinc and 20 µl of 1M ammonium formate was added. Control samples had 30 µl of MES buffer pH 6.0 added, a spectrum was recorded every 30 minutes for 16 hours, samples were shaken before each measurement. λ_{ex} = 280 nm, emission slit = 2.5 nm, excitation slit = 2.5 nm, gain = 165, integration time 0.2 ms.

7.3.7 General Procedure for Reduction Assay (^{1}H NMR)

3.1·Eu$_2$ and **3.2·Eu$_2$** (0.0138 mmol) was dissolved in 400 µL D_2O followed by the addition of Zn powder (0.248 mmol). To the stirred mixture NH_4Cl (4.5 µL, 0.0082 mmol (10 m/m% solution in D_2O)) was added and the reaction was let to stir at 37 °C for 24 hours. The reaction mixture was centrifuged and the supernatant was decanted and used directly for NMR experiments.

3.1·Eu$_2$ HR-ESI-MS obsd 1124.2069, calcd 1124.2115 [$(M - H)^-$, M = $C_{36}H_{53}N_9O_{13}Eu_2$]

3.2·Eu$_2$ HR-ESI-MS obsd 1126.2298, calcd 1126.2261 [$(M + D)^+$, M = $C_{36}H_{52}N_9O_{13}Eu_2$]

3.3·Eu$_2$ (0.0236 mmol, 1.00 eqv) was dissolved in D_2O (280 µL) followed by the addition of $NaHS \cdot xH_2O$ (141 µL, 0.141 mmol (1 M solution in D_2O), 6.00 eqv) with a micropipette and the reaction was let to stir at 37 °C for 2 hours. In the first 30 mins intense effervescence was observed. The reaction mixture was centrifuged and the supernatant was decanted and used directly for NMR experiments.

3.3·Eu$_2$ HR-ESI-MS obsd 1125.1194, calcd 1125.2182 [$(M + H)^+$, M = $C_{36}H_{52}N_9O_{13}Eu_2$]

7.3.8 NaHS Reduction

A Horiba Jobin Yvon Fluorolog® 3-12 Fluorometer equipped with a Hamamatsu R928 detector and a double-grating emission monochromator was used to investigate the biological reduction of probes **3.1-4·Tb$_2$** with NaHS. The emission of **3.1-4·Tb$_2$** (90 µM, PBS pH 7.4) were recorded upon excitation with 318 nm light, emission and excitation slits were fixed at 1 nm each, the step size was 1 nm and the integration time set to 0.1 s. A pale yellow (455 nm) long pass filter was used. Excitation spectra were recorded by monitoring the emission wavelength at 545 nm where emission and excitation slits were fixed at 5 nm and 1 nm respectively, the step size was 1 nm and the integration time set to 0.1 s. To each sample 250 µM of NaHS was added and the spectra recorded again after 5 minutes.

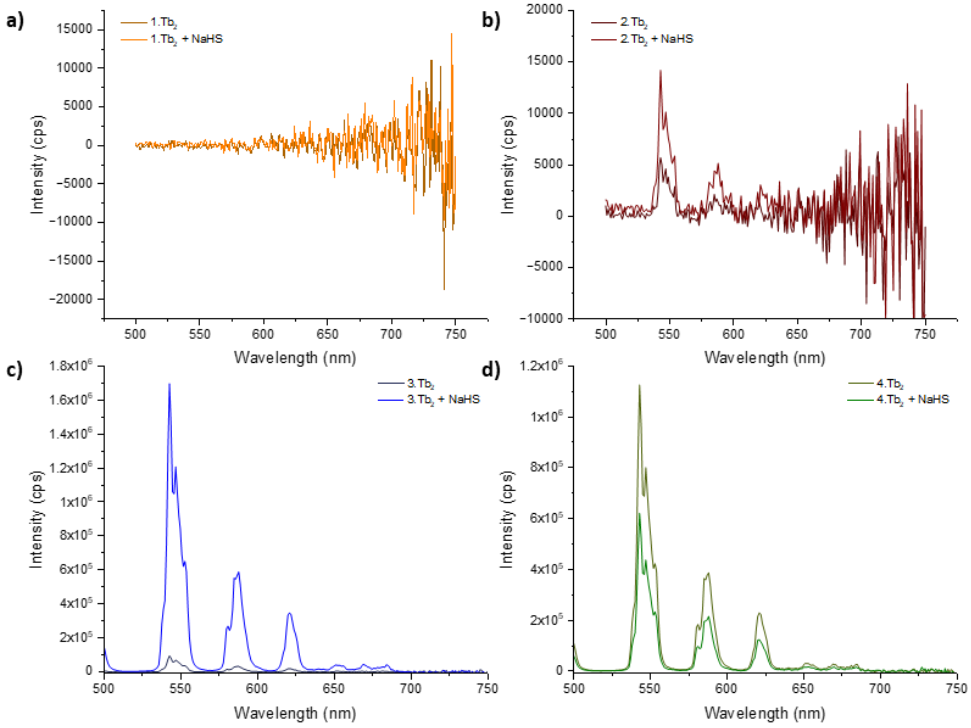


*Figure 7.15: Emission spectra of complexes **3.1-4·Tb2** measured at 90 μM, in PBS at pH 7.4 (λ_{exc} = 318 nm, emission slit:1 nm, exit slit: 1 nm) before and after the addition of NaHS (250 μM).*

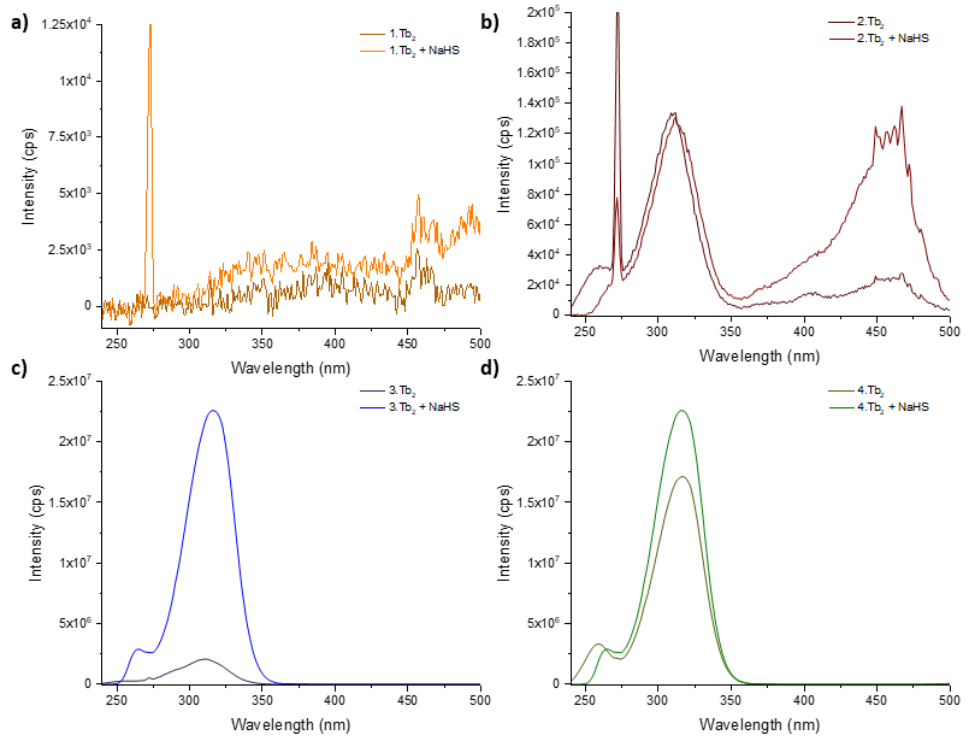


*Figure 7.16: Excitation spectra of complexes **3.1-4·Tb2** measured at 90 μM, in PBS at pH 7.4 (λ_{em} = 545 nm, emission slit: 5 nm, exit slit: 1 nm) before and after the addition of NaHS (250 μM).*

7.3.9 Cell Studies

In collaboration with Dr Lina Hacker in the Hammond group, Department of Oncology.

7.3.9.1 Cell Culture

HCT116 cells were cultured in DMEM medium supplemented with 10% FBS at 37°C, 5% CO_2 in a humidified incubator. All cell lines were routinely mycoplasma tested using a HEK-Blue™ detection kit (Invivogen) and found to be negative.

7.3.9.2 Hypoxia Exposure

Hypoxia treatments at <0.1% O_2 were carried out in a Bactron II Chamber (Shel Laboratory). Oxygen concentrations were periodically validated using anaerobic oxygen indicator strips (ThermoFisher).

7.3.9.3 Fluorescent Microscopy

Cells were seeded onto autoclaved cover slips (Menzel-Glaser) before treatment and hypoxia exposure. Cells were fixed inside the hypoxia chamber in 4% PFA for 10 minutes. Cells were mounted onto microscopy slides (Menzel Glaser) with ProLong™ Gold Antifade Mountant with DAPI to visualise the nucleus (Invitrogen™). Cells were visualised with an LSM780 confocal microscope (Carl Zeiss Microscopy Ltd) at 63x magnification. Excitation and emission wavelengths used were: DAPI 370/470 nm, 488/545 nm.

7.3.10 Biocatalytic Reduction

In collaboration with Dr Daria Sokolova in the Vincent group. Catalyst preparation was carried out in a glove box (Glove Box Technology Ltd.) under a protective N_2 atmosphere (O_2 < 3 ppm). A 20 mg/mL carbon black suspension in PB (50 mM, pH 6.0) was sonicated for 1 hour. For the preparation of the catalyst for four 0.5 mL scale reaction with 10 mM concentration of substrate, 79.2 µL of this suspension was transferred to an Eppendorf tube, 23.1 µL of Hyd-1

solution (1.71 mg/mL) was added (C:Hyd-1 = 40:1 mass ratio), the mixture was gently mixed and left in the fridge (4 °C) for 1 hour. After that, the suspension of the catalyst was centrifuged (3 min, 14500 rpm), the supernatant was removed by pipetting, and the catalyst was resuspended in 75 µL of PB (50 mM, pH 6.0 unless stated otherwise). Resuspension-centrifugation-pipetting steps were repeated 3 times, and then the catalyst was resuspended in 75 µL of PB and directly used for the reaction.

Reaction set-up was carried out in a glove box (Glove Box Technology Ltd.) under a protective N_2 atmosphere (O_2 < 3 ppm). Reactions were run on a 0.5 mL scale with a 10 mM concentration of substrate in PB (50 mM, pH 6.0) or with 10% v/v of DMSO at room temperature under a gentle H_2 flow in an Asynt Octo Mini reactor. A stock solution of substrate in buffer or DMSO was transferred to a reaction vessel, 25 µL of catalyst was added, and the volume was adjusted with the corresponding buffer to a total volume of 0.5 mL. The reactor was closed and removed from the glove box. The H_2 line was connected, and reactions were run at a 30-40 mL/min flow of H_2.

After 24 h of reaction time, the reaction mixture was centrifuged (3 min, 14500 rpm) and the supernatant was transferred, diluted to 90 µM concentration and the fluorescence spectrum was recorded for each sample. Reaction with **3.2·Tb$_2$** (N=N substrate) was complete after 24 hours. Reactions with **3.1·Tb$_2$** (NO_2 substrate) and **3.3·Tb$_2$** (N_3 substrate) were subjected to reaction conditions with freshly prepared catalyst (25 µL of catalyst for each reaction). After 72 h of reaction time **3.3·Tb$_2$** was fully converted to the corresponding amine, which was confirmed by luminescence emission and excitation spectroscopy.

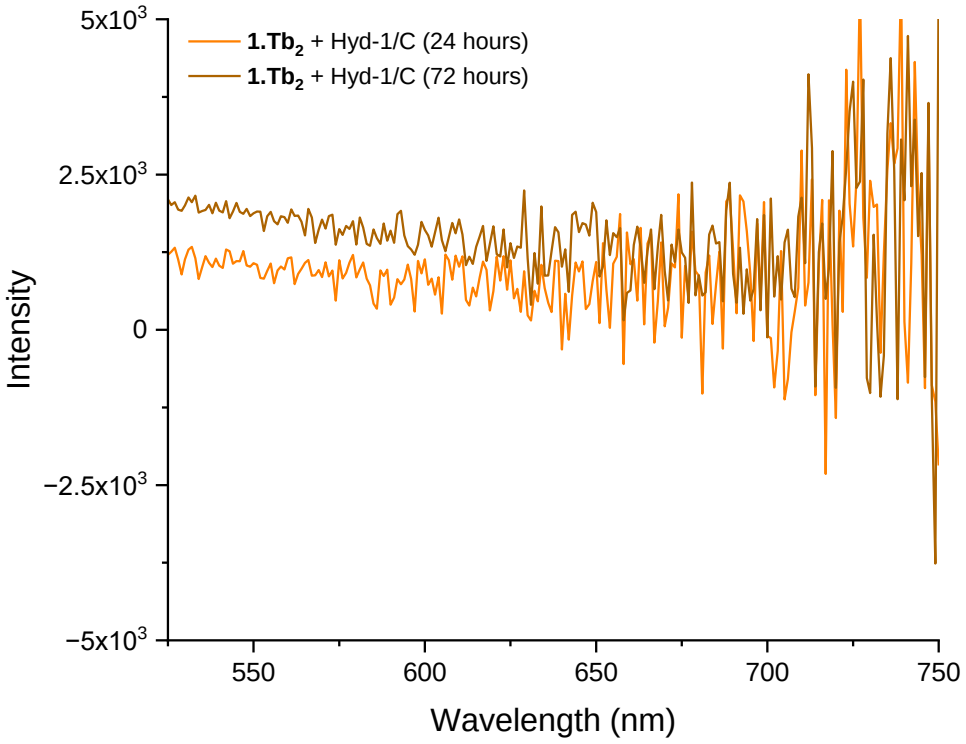


*Figure 7.17: Emission spectra of **3.1·Tb₂** upon exposure to Hyd-1/C under H_2 Fat pH 6.0 λ_{ex} = 318 nm, excitation slit 3 nm, emission slit 1 nm, integration time 0.5 s, with Thorlabs 400 nm bandpass filter.*

7.4 Experimental for Chapter 4

7.4.1 Characterisation 4·Nd

4.Nd ^{1}H NMR (400 MHz, DMSO-d_6) δ 31.63, 27.42, 25.95, 24.30, 22.91, 18.64, 16.75, 12.08, 8.97, 7.77, 1.25, -1.31, -4.79, -6.48, -8.26, -11.23, -13.72, -15.88, -18.60, -22.36, -24.63, -27.40.

HR-ESI-MS obsd 524.0907, calcd 524.0924 [$(M + H)^+$, M = $C_{17}H_{25}N_4O_6Nd$]

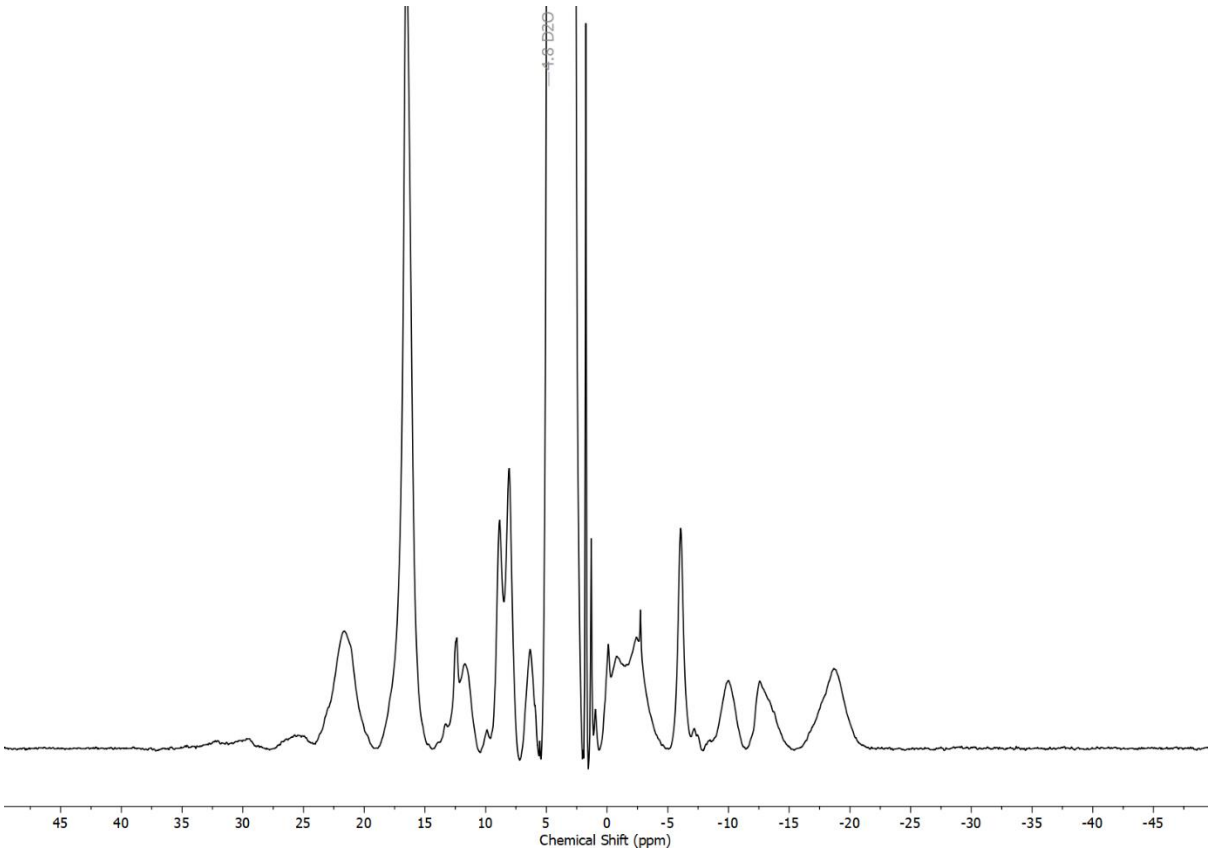


*Figure 7.18: ^{1}H NMR of **4.Nd** in D_2O (400 MHz).*

^{1}H NMR (400 MHz, D_2O) δ 32.08, 29.66, 25.73, 21.64, 16.52, 13.30, 12.41, 11.69, 9.90, 8.87, 8.07, 6.35, 5.55, 4.79, 4.29, 3.76, 3.51, 3.18, 1.97, 1.75, 1.30, 0.95, -0.10, -0.81, -2.44, -2.75, -6.06, -7.19, -9.98, -12.58, -18.68.

7.4.2 PCA for Spectral Reconstruction

In collaboration with Villads R. M. Nielsen in the Sørensen group, University of Copenhagen. For spectral reconstruction, a Principal Component Analysis (PCA) model has been applied on the emission spectra. The PCA is implemented in python using the Scikit-Learn[297] and 2 principle components are used in all cases.

The data given to the PCA is carefully pre-processed. All spectra have been background subtracted with a background spectrum collected for the solvent at the same experimental parameters. For the analysis of the 880 nm centred emission only the 580 nm band is analysed with PCA and for the analysis of the 1070 nm centre emission only the 880 nm band is analysed. The data is selected such that unwanted trends or artefacts in the background have little impact on the PCA results.

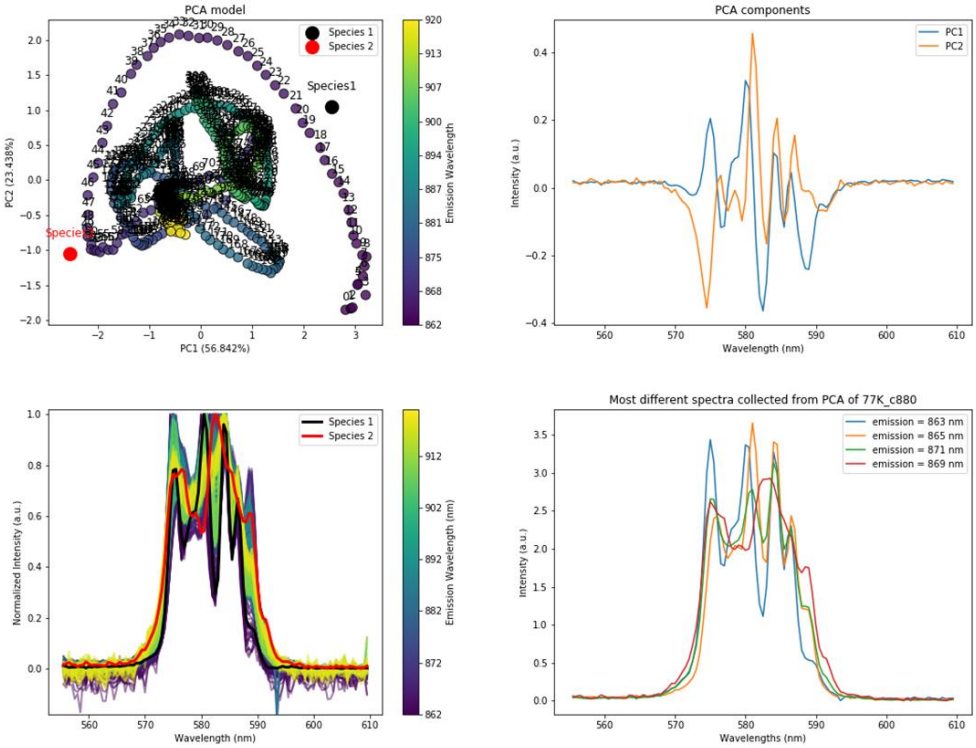


Figure 7.19: PCA analysis of 580 nm excitation band at 77 K. Created by Villads R. M. Nielsen.

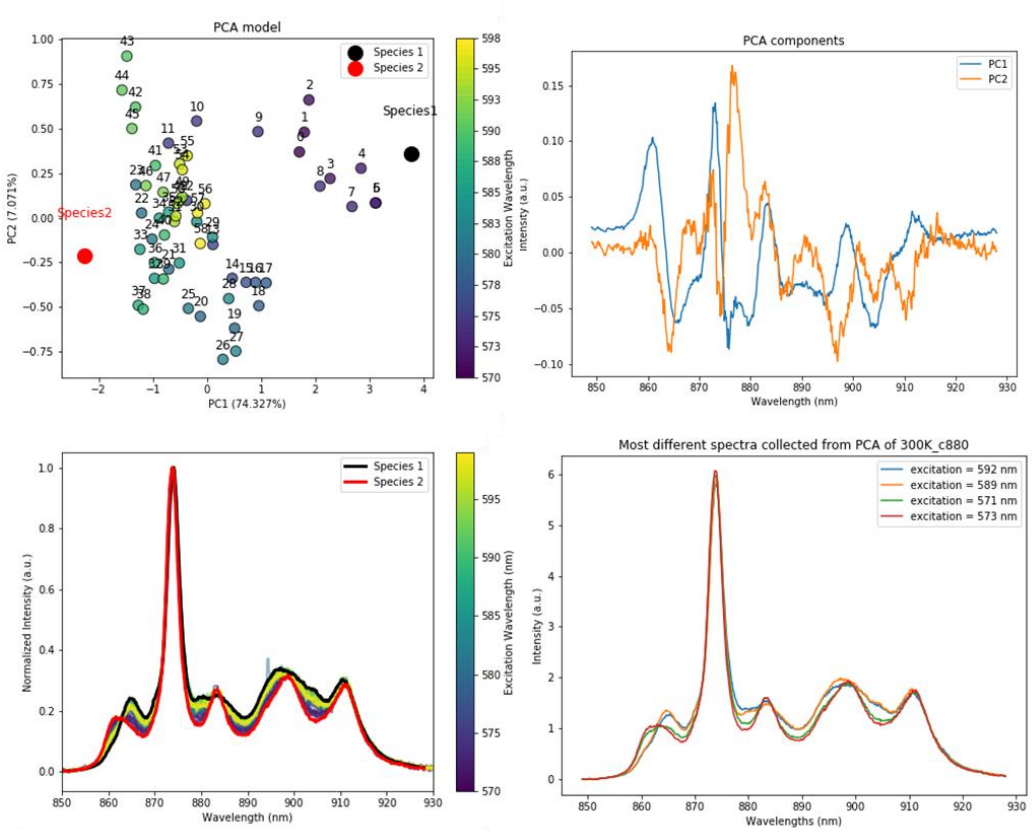


Figure 7.20: PCA analysis of 880 nm emission band at 298 K. Created by Villads R. M. Nielsen.

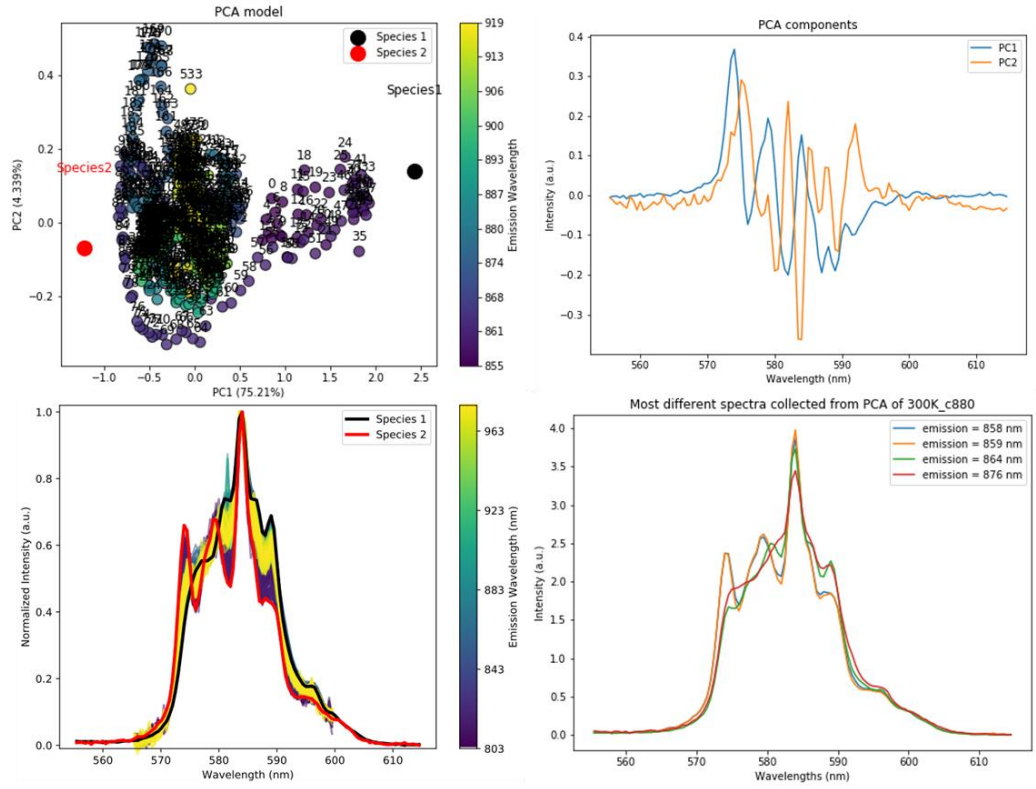


Figure 7.21: PCA analysis of 580 nm excitation band at 298 K. Created by Villads R. M. Nielsen.

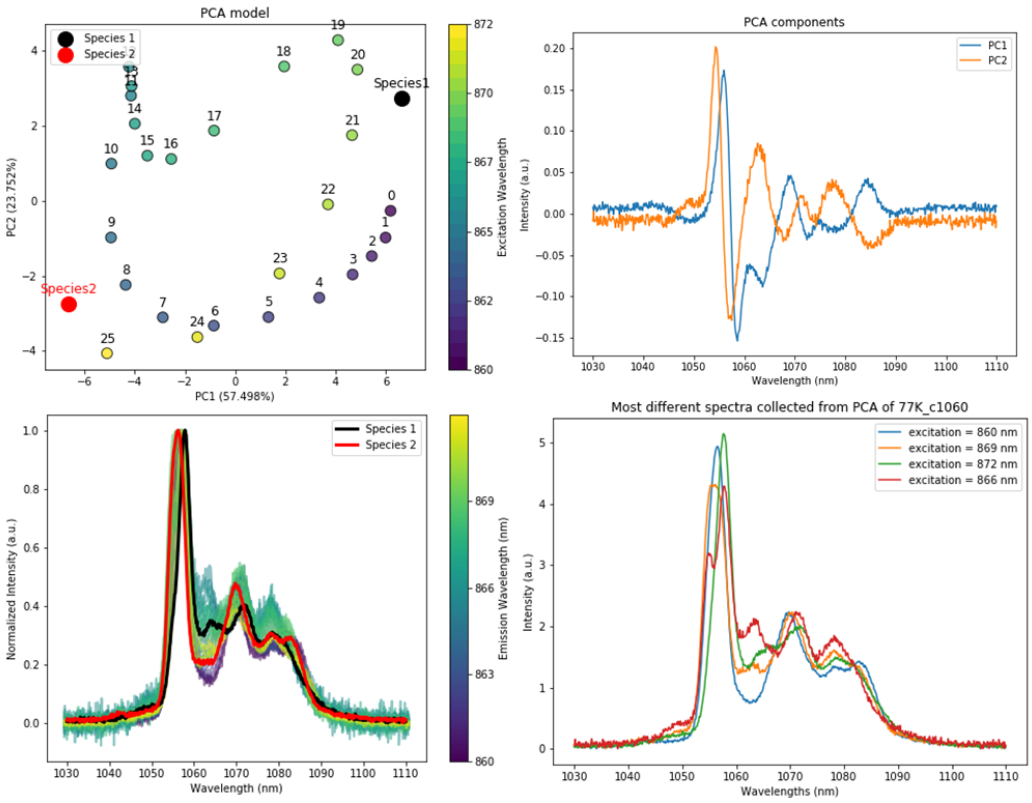


Figure 7.22: PCA analysis of 1060 nm emission band at 298 K. Created by Villads R. M. Nielsen.

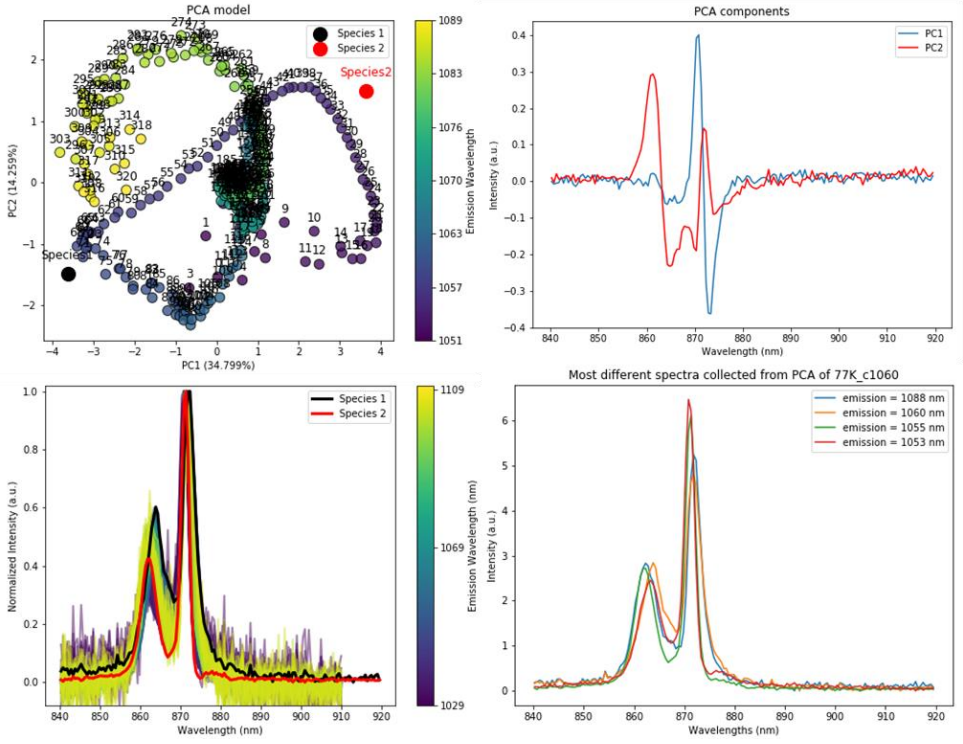


Figure 7.23: PCA analysis of 860 nm excitation band at 77 K. Created by Villads R. M. Nielsen.

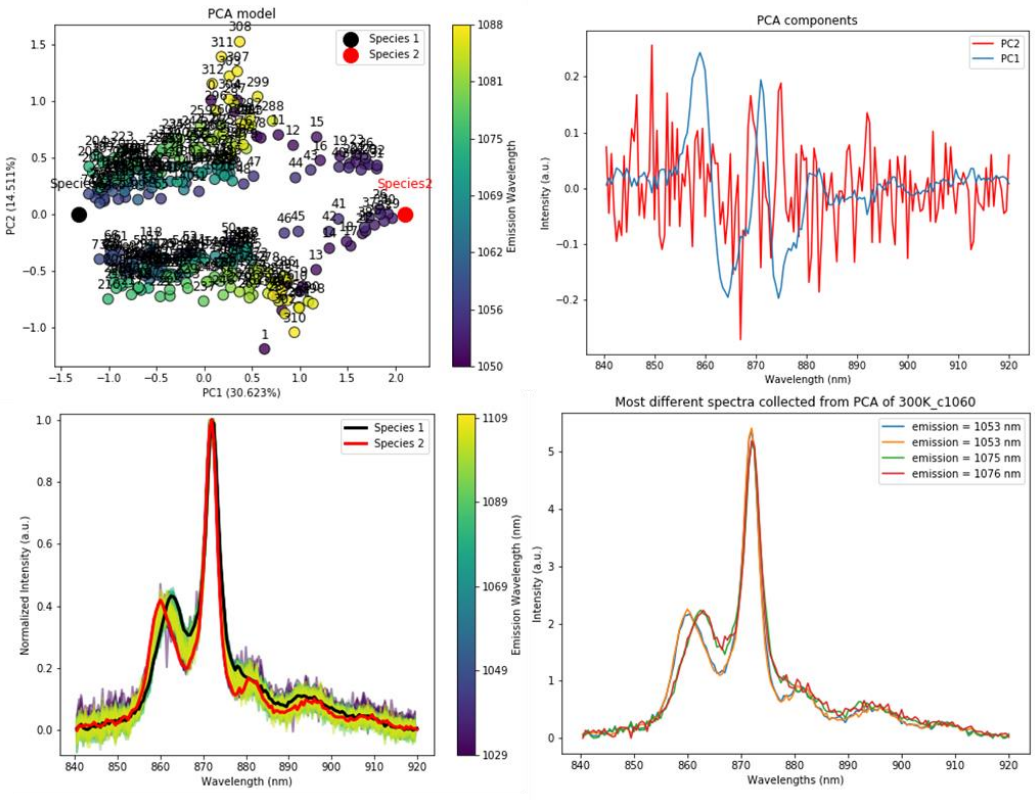


Figure 7.24: PCA analysis of 860 nm excitation band at 298 K. Created by Villads R. M. Nielsen.

7.5 Experimental for Chapter 5

7.5.1 General Method for ^{1}H NMR pH titration

All complexes were dissolved in D_2O (0.8 mL) and added to a quartz NMR tube. To this 0.1 M NaOD was added to reach an alkaline pD (~ 10). All other pD values were reached upon sequential addition of DCl (0.1 or 0.01 M). The pD of each sample was measured with a pH Sensor InLab® NMR**.** The samples were run on either a AVD500 Bruker Avance III NMR equipped with a 11.75 T magnet (^{1}H 499.9 MHz) or a Venus400 (400 MHz) is a Bruker Avance III HD nanobay NMR equipped with a 9.4 T magnet (^{1}H 400.2 MHz). An extended sweep range of ± 750.00 ppm was used to investigate Tb(III) complexes, for Eu(III) the sweep range was extended to ± 60.00 ppm.

7.6 References for Chapter 7

1. P. R. Nawrocki, V. R. M. Nielsen and T. J. Sorensen, *Methods Appl Fluores*, 2022, **10**.
2. A. Kerckhoffs, Z. Bo, S. E. Penty, F. Duarte and M. J. Langton, *Org Biomol Chem*, 2021, **19**, 9058-9067.
3. A. L. Leistner, S. Kirchner, J. Karcher, T. Bantle, M. L. Schulte, P. Gödtel, C. Fengler and Z. L. Pianowski, *Chem-Eur J*, 2021, **27**, 8094-8099.
4. C. Alexander, J. A. Thom, A. M. Kenwright, K. E. Christensen, T. J. Sørensen and S. Faulkner, *Chem Sci*, 2023, **14**, 1194-1204.
5. A. Kerckhoffs, K. E. Christensen and M. J. Langton, *Chem Sci*, 2022, **13**, 11551-11559.
6. P. Rodriguez-Maciá, A. Dutta, W. Lubitz, W. J. Shaw and O. Rüdiger, *Angewandte Chemie International Edition*, 2015, **54**, 12303-12307.
7. D. Sokolova, T. Lurshay, J. Rowbotham, G. Stonadge, H. Reeve, S. Cleary, T. Sudmeier and K. Vincent, unpublished work.
8. H. A. Reeve, L. Lauterbach, O. Lenz and K. A. Vincent, *ChemCatChem*, 2015, **7**, 3480-3487.
9. F. Pedregosa, G. Varoquaux, A. Gramfort, V. Michel, B. Thirion, O. Grisel, M. Blondel, P. Prettenhofer, R. Weiss, V. Dubourg, J. Vanderplas, A. Passos, D. Cournapeau, M. Brucher, M. Perrot and É. Duchesnay, *J. Mach. Learn. Res.*, 2011, **12**, 2825–2830.
10. A. Krezel and W. Bal, *J Inorg Biochem*, 2004, **98**, 161-166.